NEUTRINOS IN COSMOLOGY AND PARTICLE PHYSICS

by

Jun Wu

Bachelor of Science, Beijing Normal University, 2003

Master of Philosophy, The Chinese University of Hong Kong, 2005,

Master of Science, University of Pittsburgh, 2007

Submitted to the Graduate Faculty of

the Department of Physics and Astronomy in partial fulfillment

of the requirements for the degree of

Doctor of Philosophy

University of Pittsburgh

2011

UNIVERSITY OF PITTSBURGH

KENNETH P. DIETRICH SCHOOL OF ARTS AND SCIENCES

This dissertation was presented

by

Jun Wu

It was defended on

November 19, 2011

and approved by

Daniel Boyanovsky, Professor, Department Of Physics & Astronomy

Richard Holman, Professor, Department of Physics

Arthur Kosowsky, Associate Professor, Department of Physics & Astronomy

Adam Leibovich, Associate Professor, Department of Physics

Donna Naples, Associate Professor, Department of Physics

Andrew Zentner, Associate Professor, Department of Physics

Dissertation Director: Daniel Boyanovsky, Professor, Department Of Physics & Astronomy

NEUTRINOS IN COSMOLOGY AND PARTICLE PHYSICS

Jun Wu, PhD

University of Pittsburgh, 2011

This thesis discusses two independent research topics. We first study keV sterile neutrinos as a Warm Dark Matter (WDM) candidate, focusing on their production at temperatures of the electroweak scale and the linear structure growth of WDM particles with arbitrary distribution functions and masses of keV scale. At temperatures of the electroweak scale, the medium effect modifies the mixing angle between sterile and active neutrinos, introducing two narrow Mikheev-Smirnov-Wolfenstein (MSW) resonances that break adiabaticity and enhance the non-thermal production of sterile neutrinos at small momenta. One of the two MSW resonances is in the absence of a lepton asymmetry and occurs only at temperatures around the electroweak scale. By solving the linearized collision-less Boltzmann equation, we obtain a semi-analytical expression of the matter power spectrum for WDM particles with arbitrary distributions agreeing within a few percent error with results from Boltzmann codes. This matter power spectrum depends on the horizon size at matter-radiation equality and the free streaming wave vector k_{fs}, function of mass and distribution of WDM particles. We discover WDM acoustic oscillations at small scales about $k \geq 2k_{fs}$ and an Integrated Sachs-Wolfe (ISW) effect in the Radiation Dominant (RD) era which enhances the matter power spectrum for $k \leq k_{fs}$. A quasi-degeneracy between the mass and distribution function of WDM on the matter power spectrum is identified, suggesting an inherent ambiguity of Lyman-α analysis to constrain WDM parameters. Secondly, based on the observation that neutrinos produced from decay via the charge current interaction are entangled with the corresponding charged leptons, we re-investigate the theory of neutrino oscillations with the focus of the dynamics of the entangled state. We study the dynamics of entanglement

and dis-entanglement explicitly in time, which leads to non-conventional expressions for neutrino oscillation amplitudes and probabilities suggesting possible corrections for short baseline neutrino oscillation experiments. By applying this method to the GSI anomaly, we unambiguously show that the GSI anomaly is not a consequence of neutrino oscillations.

TABLE OF CONTENTS

PREFACE xviii

1.0 OVERVIEW 1

1.1 INSTRUCTION FOR READERS 1

1.2 NEUTRINOS: A WINDOW TO PHYSICS BEYOND THE STANDARD MODEL 2

1.3 SUMMARY OF MAIN RESULTS 5

1.3.1 Part I (Chapters 2 to 4): keV Sterile Neutrinos as a WDM Candidate 6

1.3.2 Part II (Chapters 5 to 7): Theory on Neutrino Oscillations 9

1.3.3 Chapter 8: Conclusion 11

1.4 PUBLICATION LIST 11

2.0 PART I: INTRODUCTION 14

2.1 CONCORDANCE ΛCDM COSMOLOGICAL MODEL 14

2.2 SMALL SCALE PROBLEMS OF ΛCDM MODEL 17

2.2.1 Missing Satellite Problem 19

2.2.2 Cusp Problems in Galaxy Centers 20

2.3 STERILE NEUTRINOS AND OBSERVATIONAL CONSTRAINTS . . . 21

2.3.1 Upper Bound from X-ray Constraints 22

2.3.2 Lower Bond from Phase Space Density of Dwarf Galaxies 22

2.3.3 Constraints From Lyman-α Forest 23

2.4 SUMMARY OF OUR WORK 26

2.4.1 Sterile Neutrinos Produced at the Electroweak Scale 26

2.4.2 Small Scale Aspects of WDM: Power Spectra and Acoustic Oscillations 29

3.0 PART I: STERILE NEUTRINOS PRODUCED AT THE ELECTROWEAK SCALE . . . 35
3.1 THE MODEL . . . 35
3.2 EQUATION OF MOTION . . . 39
3.2.1 One-Loop Self-Energy . . . 40
3.2.2 Propagator: complex poles and propagating modes in the medium . . . 48
3.2.3 Helicity dependence: right-handed sterile neutrinos and standard model interactions . . . 52
3.3 REAL PARTS: MIXING ANGLES AND MSW RESONANCES . . . 53
3.3.1 Mixing angles and MSW resonances: . . . 59
3.3.1.1 Case with vanishing lepton asymmetry . . . 59
3.3.1.2 Case With non-vanishing lepton asymmetry . . . 62
3.4 IMAGINARY PARTS: WIDTHS FROM VECTOR AND SCALAR BOSON DECAY . . . 64
3.4.1 Widths from scalar and vector boson decay: . . . 67
3.4.2 Imaginary parts: from the width to the production rates. . . . 70
3.4.3 Weak or strong damping? . . . 72
3.4.4 Regime of validity of perturbation theory. . . . 73
3.5 NEUTRINO PRODUCTION IN AN EXPANDING UNIVERSE . . . 74
3.6 CONCLUSION . . . 77
4.0 PART I: LINEAR STRUCTURE GROWTH IN THE WDM SCENARIO 80
4.1 COSMOLOGY PRELIMINARIES: FRIEDMAN EQUATION . . . 81
4.2 DENSITY PERTURBATION OF DMS: GENERAL ASPECTS . . . 82
4.2.1 Collision-less Boltzmann Equation . . . 83
4.2.1.1 Unperturbed Collision-less Boltzmann Equation . . . 84
4.2.1.2 Linearly Perturbed Collision-less Boltzmann Equation . . . 86
4.2.2 Formal Solution Of The Linearly Perturbed Collision-less Boltzmann Equation . . . 87
4.2.3 Initial Condition . . . 89
4.2.4 Transfer Function and Super-horizon Mode . . . 92

4.3 CDM AND WDM: DIFFERENT EVOLUTION HISTORIES 93
4.3.1 Our Strategy 96
4.3.2 Free Streaming Distance of CDMs and WDMs 97
4.4 CDM CASE: TIME EVOLUTION AND THE TRANSFER FUNCTION . 101
4.4.1 Density Perturbations of WIMPs in the RD Era 102
4.4.1.1 Density Perturbations of Photons in The RD Era 103
4.4.1.2 Radiation Cross-over 104
4.4.2 Density Perturbations of WIMPs in the MD Era 105
4.4.2.1 2nd-order Legendre Equation 106
4.4.2.2 Transfer Function of WIMPs 108
4.4.2.3 An Alternative Method: To Compare with the WDM Case . 109
4.5 WDM CASE: TIME EVOLUTION OF STERILE NEUTRINO DENSITY PERTURBATIONS 111
4.5.1 Stage I: Relativistic Sterile Neutrinos in the RD Era 112
4.5.2 Stage II and III: Non-relativistic Sterile Neutrinos 115
4.5.2.1 Inhomogeneous Equation for Sterile Neutrino Density Perturbations 117
4.5.2.2 Asymptotic Behavior 118
4.5.2.3 Homogeneous Equation: 2nd-order Associated Legendre Equation 119
4.5.2.4 Green's Function And the Full Solution 121
4.5.2.5 The Born Approximation Of Density Perturbations 123
4.6 WDM CASE: TRANSFER FUNCTION AND POWER SPECTRUM . . . 124
4.6.1 Transfer Function of Sterile Neutrinos 125
4.6.1.1 Numerical Evaluation 127
4.6.1.2 Transfer Function of Sterile Neutrinos With Different Masses And Distributions 129
4.6.1.3 ISW Enhancement 129
4.6.1.4 "Acoustic Oscillations" of WDM 131
4.6.2 Power Spectrum Of Sterile Neutrinos 134

4.6.3 Comparison to Numerical Results From Boltzmann Codes 135
4.6.4 Impact On N-body Simulation And Lyman-α Constraints 137
4.7 SUMMARY AND CONCLUSION 139
5.0 PART II: INTRODUCTION 144
5.1 THEORY OF NEUTRINO OSCILLATION IN PLANE WAVE LIMIT . . 148
5.2 NEUTRINO OSCILLATION UNDER WAVE PACKET TREATMENT . . 151
5.3 SUBTLE ISSUES OF THE THEORY OF NEUTRINO OSCILLATIONS . 156
5.4 SUMMARY OF OUR WORK 159
5.4.1 Dynamics of Disentanglement And Coherence In Neutrino Oscillations 159
5.4.2 Application of the Plane Wave Result to the GSI Anomaly 159
6.0 PART II: DYNAMICS OF DISENTANGLEMENT AND COHERENCE IN NEUTRINO OSCILLATIONS 161
6.1 A MODEL OF "NEUTRINO" OSCILLATIONS 161
6.2 INTERACTION NEAR THE SOURCE 164
6.2.1 Unobserved daughter particles: time evolution of the density matrix 165
6.2.2 Disentangling the neutrino: a two-time measurement 170
6.2.3 Transition amplitudes and event rates 173
6.3 INTERACTION AT THE FAR DETECTOR 173
6.3.1 Transition amplitude and probabilities 174
6.3.2 Factorization of the event rates 176
6.4 DISCUSSIONS 178
6.4.1 Possible corrections for short baseline experiments 178
6.4.2 Wave packet description 179
6.5 CONCLUSION 181
7.0 PART II: IS THE GSI ANOMALY DUE TO NEUTRINO OSCILLATIONS? 183
7.1 INTRODUCTION TO THE GSI ANOMALY 183
7.2 A MODEL FOR THE GSI ANOMALY 186
7.3 NUMBER DENSITIES OF THE PARENT AND THE DAUGHTER PARTICLES 188

7.3.1 Number Density of Daughter Particles 190
7.3.2 Number Density of Parent Particles 194
7.4 CONCLUSION AND DISCUSSIONS 196
8.0 CONCLUSION OF THE THESIS 198
8.1 STERILE NEUTRINO PRODUCED AT THE ELECTROWEAK SCALE 198
8.2 LINEAR STRUCTURE GROWTH IN THE WDM SCENARIO 199
8.3 DYNAMICS OF DISENTANGLEMENT AND COHERENCE IN NEUTRINO OSCILLATION 200
8.4 IS THE GSI ANOMALY DUE TO NEUTRINO OSCILLATIONS? 201
APPENDIX A. APPENDIX FOR STERILE NEUTRINO PRODUCTION 202
A.1 STANDARD MODEL (SM) VECTOR BOSON EXCHANGE 202
A.2 BEYOND STANDARD MODEL (BSM) SCALAR EXCHANGE 203
APPENDIX B. NUMERICAL MANIPULATION OF $I_1(K,U)$ 204
BIBLIOGRAPHY 207

LIST OF TABLES

1 Summary of dark matter particle candidates, their properties, and their potential methods of detection. The particle physics motivations are discussed in Sec. II.B; GHP and NPFP are abbreviations for the gauge hierarchy problem and new physics flavor problem, respectively. In the last five rows, $\surd\surd$ denotes detection signals that are generic for this class of dark matter candidate and $\surd$ denotes signals that are possible, but not generic. "Early Universe" includes phenomena such as BBN and the CMB; "Direct Detection" implies signatures from dark matter scattering off normal matter in the laboratory; "Indirect Detection" implies signatures of late time dark matter annihilation or decay; and "Particle Colliders" implies signatures of dark matter or its progenitors produced at colliders, such as the Large Hadron Collider (LHC). See the text for details. 16

LIST OF FIGURES

1 Comparison of theoretical predicted current density fluctuation power spectrum $P(k)$ with various observational data. The cyan solid line corresponds to the theoretical prediction based on the concordance ΛCDM cosmological model. Other observational data share the same cosmic matter budget parameters. 18

2 Figure from [81]. The allowed region of parameters for DM sterile neutrinos produced via mixing with the active neutrinos (unshaded region). The two thick black lines bounding this region represent production curves for NRP (upper line, $L_6 = 0$) and for RP (lower line, $L^max_6 = 700$) with the maximal lepton asymmetry, attainable in the theoretical model νMSM [257, 201]. L_6 corresponds to 10^6 times the lepton asymmetry. The thin colored curves between these lines represent production curves for (from top to bottom) $L_6 = 8, 12, 16, 25$, and 70. The red shaded region in the upper right corner represents X-ray constraints [78, 77, 209, 74] (rescaled by a factor of two to account for possible systematic uncertainties in the determination of DM content [80, 71]). The black dashed-dotted line approximately shows the RP models with the largest cold component. The black filled circles along this line are compatible with the Lyman-α bounds [73], and the points with $M_1 \leq 4$ keV are also compatible with X-ray bounds. The region below 1 keV is ruled out according to the phase-space density arguments [64, 79]. Abbreviation: BBN, big bang nucleosynthesis. 25

3 (sm) contributions to the self-energy Σ_{sm}. The indices $\{i, j, k\} = \{1, 2\}$ correspond to mass eigenstates, the index f for the intermediate fermion line in the charged current self-energy refers to the charged lepton associated with the active neutrino. 41

4 (bsm) contributions to the self-energy Σ_{bsm}. The indices $\{i,j,k\} = \{1,2\}$ corresponding to mass eigenstates. The dashed line is a scalar propagator either for σ or φ 41

5 Neutral current contribution to the one-loop retarded self-energy Σ_{sm}. The indices $\{i,j\} = \{1,2\}$ and the indices 1 and 2 denote the corresponding mass eigenstate in the intermediate state. 42

6 Scalar exchange contributions to the one-loop self-energy Σ_{bsm}. The indices $\{i,j\} = \{1,2\}$ and the indices 1 and 2 denote the corresponding mass eigenstate in the intermediate state. 43

7 The functions $Af\left(\frac{k}{T},\ \frac{M}{T}\right)$, $Ab\left(\frac{k}{T},\frac{M}{T}\right)$, $Bf\left(\frac{k}{T},\frac{M}{T}\right)$ and $Bb\left(\frac{k}{T},\frac{M}{T}\right)$ with respect to k/T for $M/T = \{1,2,3\}$ in the expression of $\mathrm{Re}\Sigma_{bsm}$. 54

8 The functions $\left(Af(\frac{k}{T},\frac{M}{T}) - Bf(\frac{k}{T},\frac{M}{T})\right)$, $\left(Ab(\frac{k}{T},\frac{M}{T}) - Bb(\frac{k}{T},\frac{M}{T})\right)$ as functions of $\frac{k}{T}$ for $\frac{M}{T} = \{1,2,3\}$ for the case of scalars beyond the SM. 55

9 $Af(\frac{k}{T},\frac{M}{T})$, $Ab(\frac{k}{T},\frac{M}{T})$, $Bf(\frac{k}{T},\frac{M}{T})$ and $Bb(\frac{k}{T},\frac{M}{T})$ as functions of k/T for $\frac{M}{T} = \{1,\ 2,\ 3\}$ for the SM contributions with $\mu = 0$. 57

10 $\left(Af(\frac{k}{T},\frac{M}{T}) - Bf(\frac{k}{T},\frac{M}{T})\right), \left(Ab(\frac{k}{T},\frac{M}{T}) - Bb(\frac{k}{T},\frac{M}{T})\right)$ as functions of k/T for $\frac{M}{T} = \{1,2,3\}$ for the SM contributions with $\mu = 0$. 58

11 The functions $F(m)$, $J(m)$ and $G(m)$ vs $m = M/T$. 59

12 The Cutkosky cut for the imaginary part of the SM and BSM contributions, and the contribution on the mass shell $\omega \simeq k$. 65

13 Perturbed gravitational potential ϕ in the RD era. 89

14 Time evolution of gravitational potential ϕ for super-horizon modes. The dashed line corresponds to the Matter-Radiation equality. 93

15 Summary of time evolution of various perturbations modes of WIMPs and sterile neutrinos. Panel (a) is for WIMPs and panel (b) is for sterile neutrinos. Each λ-value corresponds to one perturbation mode. The scale factor also labels the time arrow. For each case, we demonstrate the important scales involved in the time evolution, as discussed in detail in the context. The shaded regions of panel (a) show the analytically solvable regions, which has been thoroughly studied in [112]. The shaded area in panel (b) emphasizes the perturbation modes experienced different evolution history from that of WIMPs. 96

16 Time evolution of density perturbations of WIMPs in the RD era with respect to its initial value. $x = k\eta/\sqrt{3}$. When $x \simeq 1/\sqrt{3}$, the perturbation mode enters the horizon and start to grow. At late times, the density perturbations grow logarithmically, as shown in Eq. (4.4.13) 103

17 Radiation cross-over for difference perturbation modes. $x_* = k\eta_*/\sqrt{3} = 83.32\ k$. $x_c/x_* \ll 1$ means that the cross-over happens deep in the RD era, which is true for the small scale perturbation modes we are interested in, namely $k \geq 0.2\text{Mpc}^{-1}$. Moreover, for perturbations larger than 30 Kpc, $x \geq 0.1x_* \simeq 8$, the expressions of δ_r and δ under large x limit are well justified. 105

18 Transition of δ from the RD region to the MD region for various perturbation modes. The transition gets better for small scale modes $k < 0.5\text{Mpc}^{-1}$. 108

19 Time evolution of Θ_0 of relativistic sterile neutrinos in the RD universe. Panel (a) shows the early time evolution, where perturbation modes just enter the horizon. The initial growth of the perturbation is due to the ISW effect, reaching maximum around the sound horizon. Eventually these perturbations damp out because of the strong free-streaming suppression of relativistic sterile neutrinos. Panel (b) shows the late time evolution, which is compared with the asymptotic behavior of Eq. (4.5.12). 113

20 Derivative of the gravitational potential ϕ in the RD era with respect to z, which leads to the ISW kick when perturbation modes of relativistic DM particles enter the horizon in the RD universe. 114

21 Homogeneous solutions $g_g(k,u)$ and $g_d(k,u)$ of the homogeneous equation (4.5.31) vs. u for various perturbation modes. The left panel corresponds to the growing mode and the right panel the decaying mode. 121

22 Contribution of the three inhomogeneous terms $I_1(k,u)$, $I_2(k,u)$ and $I_3(k,u)$ to the transfer function defined in Sec. 4.6, up to an overall scaling factor. In this figure, we compare the results of the 1keV DW sterile neutrino (black solid line) and WIMPs for the CDM case (red dashed line). Panel (a) corresponds to the contribution from $I_1(k,u)$, panel (b) to $I_2(k,u)$ and panel (c) to $I_{ISW}(k,u)$. 125

23 $\overline{T}_{B(\mathrm{DW})}(k)$ for DW sterile neutrinos with $m = 1$keV. Panel (a) shows the logarithmic of $T_{B(\mathrm{DW})}$ for a wide range of $k \in (0, 30)$. As $k \to 0$, the WDM and CDM transfer functions coincide with each other for super-horizon modes, consistent with the physical expectation. Panel (b) shows the values of $\overline{T}_{B(\mathrm{DW})}(k)$ for relatively small k from 0 to 10, corresponding to perturbation scales larger than 100Kpc. The WDM transfer function drops quickly with respect to the CDM transfer function as k increases. Panel (c) shows the ratio of the transfer functions for even smaller perturbation modes. The WDM transfer function starts to oscillate with a period about 1Mpc, a new unique feature of WDM density perturbations, which may hint interesting observational signatures. 127

24 Transfer functions of DW and BD sterile neutrinos with $m = 1$keV and $m = 2$keV respectively in linear (left panel) and log (right panel) scales. The thin (thick) solid lines correspond to DW (BD) sterile neutrinos and the black lines are for the case of $m = 1$keV while the red lines for $m = 2$keV. 130

25 ISW contribution to the Born approximated transfer function $\overline{T}_{B(\mathrm{SNs})}(k)$ in Eq. (4.6.6). For simplicity, We only plot the ISW contribution to the integral in the numerator of (4.6.6) for sterile neutrinos with different masses and distribution functions. Solid(dashed) lines correspond to DW(BD) sterile neutrinos. Black ones refer to sterile neutrinos with masses $m = 1$ keV and red ones are for $m = 2$ keV. 131

26 The oscillation feature on the transfer function in Eq. (4.6.6) for $m = 1$keV sterile neutrinos with BD distribution in the left panel and DW distribution in the right panel. Note that oscillations start from different values of ks. 132

27 Comparison of the normalized transfer function for DW with the results from Boltzmann codes. The solid line is the semi-analytical result from Eq. (4.6.6), the (blue) dashed line is the result from the interpolation of non-thermal case in Ref. [274], the (red) dotted line is the result from the interpolating fit in Ref. [165]. For all cases $h = 0.72$, $\Omega_{DM}h^2 = 0.133$ and $g_d = 10.75$. 137

28 $\overline{T}_{B(DW)}(k)$ from the semi-analytical approximation (4.6.6) displaying the acoustic oscillations at small scales $k \geq 2k_{fs} \simeq 10.8, 18.5\ (\text{Mpc})^{-1}$ for $m = 1.0, 1.7$ keV respectively. Note that the horizontal scale is in $(\text{Mpc})^{-1}$ and that vertical scales differ by a factor 5 between the two figures. 138

29 Normalized power spectrum (4.6.13) for DW and BD sterile neutrinos with $m = 1, 2$ keV. 139

30 The matter power spectrum 140

31 An schematic representation of neutrino oscillation experiments in QFT framework. 152

32 Typical experiment in which the charged leptons are measured at a near and far detector and the neutrino is an intermediate state. 163

33 The functions $f_{\pm}(x, t, \Delta)$ vs. x for $t = \{40, 100\}$, $\Delta = 0.1$ 166

34 The products $f_{-}(x, t, \Delta)f_{+}(x, t, \Delta)$ vs. x for $t = \{40, 100\}$,$\Delta = 0.1$ 167

35 The integral $I(t, \Delta) = \int_{-\infty}^{\infty} e^{-x^2} f_{+}(x, t, \Delta)f_{-}(x, t, \Delta)dx$ vs. t for $\Delta = \{0, 0.1, 0.3\}$. 168

36 Figure 3 from [206]. Number of EC decays of H-like ^{140}Pr ions per second as a function of the time after the injection into the ring. The solid and dashed lines represent the fits according to Eq. 1 (without modulation) and Eq. 2 (with modulation) in [206], respectively. The inset shows the Fast Fourier Transform of these data. A clear frequency signal is observed at 0.14 Hz (laboratory frame). 184

37 Figure 5 from [206]. A roomed-in plot of the number of EC decays of H-like ^{142}Pm ions per 0.64 second as a function of the time after the injection into the ring. The solid and dashed lines represent the fits according to Eq. 1 (without modulation) and Eq. 2 (with modulation) in [206], respectively. The inset shows the Fast Fourier Transform of these data. A clear frequency signal is observed at 0.14 Hz (laboratory frame). 185

38 (a) exact interaction of EC decays of a parent particle, (b) approximated interaction of EC decays in our model. 187
39 Self-energy of the parent particle M, the neutrino line corresponds to a propagator of a mass eigenstate. 190

PREFACE

I would like to express my sincere thanks to my supervisor Prof. Daniel Boyanovsky. I benefit a lot from his patient, encouraging and supportive guidance, from his enthusiasms, persistence and discipline in pursuing deeper understandings on physics. I thank him for providing me all possible opportunities to broaden my knowledge of different areas of physics. In particular, I thank him for his understanding and ever-lasting support during my absence from campus in my last year of PhD.

I am also indebted to my committee members Prof. Richard Holman, Prof. Andrew Zentner, Prof. Arthur Kosowsky, Prof. Donna Naples and Prof. Adam Leibovich, for the interesting questions and suggestions during my committee meetings. I have learnt a great deal from the collaboration with Prof. Richard Holman and his student Mr. Jimmy Hutasoit. I thank them for all the helpful discussions. I also thank Prof. Andrew Zentner and Prof. Arthur Kosowsky for their lectures on cosmology, which were inspiring to me. I appreciate the discussions with Prof. Donna Naples on neutrino oscillation experiments.

I thank Prof. Eric Swanson for teaching me quantum field theory and his kind help. I also thank Prof. Xiao-lun Wu for his generosity to allow me work in his Lab to fulfill my curiosity on bio-physics. Furthermore, I thank our secretary Ms. Leyla Hirschfeld for helping me handle many administrative requirements.

I am grateful for all the help from Ms. Li Xie. In particular, I really appreciate her friendship during my visits in Pittsburgh this year. I would like to thank my parents for their supports and love. Finally, I thank my boyfriend Pete. His love and encouragement have helped me go through a lot of difficulties and frustrations. I really appreciate his tolerances of my quick temper when I am under pressure.

1.0 OVERVIEW

1.1 INSTRUCTION FOR READERS

This thesis contains two independent parts. The first part is about our study on sterile neutrinos as a Warm Dark Matter (WDM) candidate, and the second part focuses on several subtle aspects of the theory on neutrino oscillation phenomena. Each part of the thesis has three chapters: Chaps. 2 to 4 belong to the first part, and Chaps. 5 to 7 form the second part of the thesis. These two parts are organized similarly. The first chapter of each part is devoted to an in-depth introduction while the following two chapters contain technical details, each of which is based on a published article. The introduction chapter provides background knowledge on the topic under consideration. To supplement our theoretical work, we pay special attention to the observational/experimental aspects associated with our topic. Each introduction chapter ends with a section containing a detailed summary on the goals, strategy and main results of our research in the corresponding part of the thesis. Finally, we conclude the thesis in Chap. 8 by reviewing the mains results of our work presented here.

Readers who want to quickly get the main ideas of this thesis are suggested to read Secs. 1.2 and 1.3, which briefly introduce the content of the thesis, provide the background information, motivation and main results of our research. Interested readers can then proceed to Chaps. 2 and 5 for an extended introduction of each part of the thesis and summary without too many technical details. The technical details are contained in Chaps. 3 to 4 and Chaps. 6 to 7 for the first and the second parts respectively.

1.2 NEUTRINOS: A WINDOW TO PHYSICS BEYOND THE STANDARD MODEL

There are two "standard" models that frame our current understanding of the physical world. The standard model of particle physics (SM) unifies the strong, weak and electro-magnetic interactions of all known elementary particles, it is very successful and has been confirmed by numerous experimental observations. Another standard model, the concordance ΛCDM cosmological model, explains the cosmic expansion and acceleration, and successfully describes the physics of our universe, including its thermal history, the Big Bang Nucleosynthesis (BBN) and large scale structure formation [194, 112, 281]. According to the ΛCDM model and based on a series of cosmological observations [294, 295, 250, 251, 195, 269, 245, 91, 125, 248, 234, 264], we now know that Dark Matter (DM) is one dominant component of our universe today, occupying 22.7% of the total energy budget [176]. It plays an essential role in determining the cosmic structures we observe today [112, 281]. Since DM is only inferred gravitationally, it can not be explained by any known fundamental particle [112, 281, 124]. Therefore, DM provides a bridge between the two standard models, serving as one of the most direct evidences of the physics beyond the SM.

Sterile neutrinos are a plausible DM candidate well-motivated by the see-saw solution of the neutrino mass problem of the SM [219, 224, 124]. Sterile neutrinos with masses of keV scale feature free streaming lengths of Mpc scales that lie in between those of Cold Dark Matter (CDM) and Hot Dark Matter (HDM), they are usually regarded as a Warm Dark Matter (WDM) candidate. In a pioneering paper in 1994 [113], Dodelson and Widrow first proposed the possibility of sterile neutrinos being a WDM candidate, and studied their production through mixing with active neutrinos in the early universe.

Recently, keV sterile neutrinos have attracted attention because there is accumulating evidence suggesting some potential problems in the standard ΛCDM model at galactic scales [191, 226, 179, 138, 110, 197, 126, 84, 293]. These small scale problems arise from the comparison between numerical simulations and observations of our local group.

They are characterized by the so-called "missing satellite problem" and the "cusp over core" problem. The former refers to the problem that observations on our local group discover almost one order of magnitude fewer dwarf satellite galaxies than the number predicted from numerical simulations based on the ΛCDM scenario [191, 226, 179, 138, 109, 110, 197], while the latter corresponds to the conflict between the predicted cusp type density profiles and the observed shallower core type density profiles toward the center of dwarf galaxies [190, 95, 140, 141, 139, 288, 142, 135, 136, 137, 216, 44, 232, 100]. Together with other small scale problems [266, 267, 253], these discrepancies between simulations and observations suggest that CDM scenario predicts more than enough small structures. Although the small scale problems may be solved by including the baryonic interactions into the N-body numerical simulations, it turns out very challenging to do so not only because the physics associated with galaxy formation is still very unclear but also because it is computationally formidable to include all relevant baryonic processes into the numerical simulations [196, 244]. WDM particles tend to smooth out density perturbations smaller than their free streaming length. Hence, keV sterile neutrinos with free streaming length of Mpc scale provide natural solution to these small scale problems [227, 54, 40, 193, 192, 81]. Moreover, extensions of the SM predict many DM candidates other than the CDM particles [124], and the matter power spectrum at co-moving perturbation scales smaller than 1 Mpc is very sensitive to the existence of WDM [215, 153, 246, 254, 271, 72, 81, 279]. These small scale problems suggest that alternatives to the standard CDM paradigm should be considered.

By decaying into active neutrinos in the SM, sterile neutrinos emit X-ray photons that can be detected by X-ray satellites [75, 78, 69, 81, 5, 279, 80, 289, 74, 209]. Also, the Lyman-α forest in the spectra of far away quasars can be used to constrain sterile neutrino masses and mixing angles [215, 265, 153, 273, 272, 246, 254, 275, 271, 72, 75, 76, 78, 69, 279]. By combining these data, it was found that keV sterile neutrinos with small mixing angles $\theta \leq 10^{-4}$ are proper WDM candidates [81]. Moreover, keV sterile neutrinos also provide an explanation for the observed pulsar kicks via the anisotropic neutrino emission of newly born neutron stars [198, 50]. Intriguingly, the LSND neutrino oscillation experiment observed an anomaly which suggests that there exists at least one sterile neutrino with mass of eV order

[35, 36, 37, 39, 38]. The LSND result was recently confirmed by observations at MiniBooNE [11] in anti-neutrino mode. Thus, these observations do not rule out the possibilities to have sterile neutrinos with higher masses.

Although the existence of DM implies new physics beyond the SM, the first evidence of the incompleteness of the SM actually came from the phenomenon of neutrino oscillations dating back to the mid-20th century. The idea of neutrino oscillations was first proposed by Pontecorvo in 1957 in analogy with the K^0-$\bar{K}^0$ oscillations [241]. Soon, it was used to successfully explain the deficit of the solar neutrino flux, referring to the famous solar neutrino problem [242, 155]. Now, neutrino oscillations are widely supported by solar neutrino experiments [90, 6, 20, 12, 263], atmospherical neutrino experiments [169, 185, 34, 19, 22] and terrestrial neutrino oscillation experiments [37, 11, 18, 25, 57, 26]. Active neutrinos in the SM are massless, however, they are required to be massive by the phenomenon of neutrino oscillations. This conflict is called the neutrino mass problem of the SM [148]. It is one of the major tasks of extensions beyond the SM to solve this problem. Sterile neutrinos are ubiquitous in these extensions because they can generate masses of the active neutrinos through the see-saw mechanism [219, 224].

The phenomena of neutrino oscillations provide useful and important opportunities to study many fundamental properties of neutrinos, including their mass differences, mixing angles, mass hierarchy, CP violating phases, etc [148]. Furthermore, these phenomena have profound applications in particle physics, astrophysics and cosmology. As mentioned previously, the resonant flavor mixing between electron and muon neutrinos in the sun explains the solar neutrino problem [242, 155, 283, 218]. During BBN, neutrino oscillations may lead to distortion of the electron neutrino distribution, hence change neutron to proton ratio, affecting the abundance of light elements in the universe [114].

The simplest theoretical description of neutrino oscillations is analogous to the two-state quantum mechanical Rabi oscillations with all particles described by plane waves [241, 214], capturing the essential ingredients of neutrino oscillation phenomena, that is the coher-

ent mixing of neutrino mass eigenstates. Though simple and intuitive, this model is not self-consistent because the exact energy-momentum conservation during neutrino production and detection forbids two massive neutrinos to interfere coherently. To solve this controversy, the wave packet nature of the neutrino states in an oscillation experiment was pointed out by Nussinov [231] and Kayser [180]. Based on the wave packet idea, a more complete and realistic picture of neutrino oscillations was developed within the framework of quantum field theory automatically including neutrino production and detection [149, 152, 143, 159, 160, 48, 15]. Neutrino oscillation formulas obtained under these considerations provide the guidelines for current data analyses on neutrino oscillation experiments [148]. Recently, it was recognized that neutrinos produced via decay through the charge current weak interaction are actually entangled with the corresponding charge leptons. It was further argued that it is necessary to dis-entangle the entangled state in order to maintain the coherent interference of neutrino mass eigenstates and enable their oscillations [92]. These new observations have stimulated debates on the validity of current theory on neutrino oscillations and its relation with the entanglement issue [92, 17, 184].

1.3 SUMMARY OF MAIN RESULTS

We divide the thesis into two parts. The first part focuses on keV sterile neutrinos as a WDM candidate, motivated by the potential small scale problems in the ΛCDM model. The second part of the thesis is devoted to studying the theory of neutrino oscillations, with the focus of the dynamics of entanglement and dis-entanglement aspects that was missed in most previous studies. For readers' convenience, in this section, we summarize the content in each part of the thesis. Interested readers can refer to Chaps. 2 and 5 for an extended introduction to the first and second part of the thesis respectively.

1.3.1 Part I (Chapters 2 to 4): keV Sterile Neutrinos as a WDM Candidate

WDM particles have non-vanishing velocity dispersion thereby modifying the dynamics of gravitation collapse and structure formation. Their free streaming motion prevents density perturbations from growing at scales smaller than their free streaming length, leading to suppression on the matter power spectrum at small scales. This is the key reason for the WDM scenario to solve the small scale problems in the ΛCDM model. Since the free streaming length of WDM particles depends on their masses and distribution functions after decoupling, this dependence will modify the final matter power spectrum. Unlike the standard CDM particles, keV sterile neutrinos usually feature non-thermal distribution functions after decoupling, which strongly depend on the production mechanisms [113, 94, 259, 258, 256, 257, 200, 33, 49, 199, 237, 236]. Therefore, to investigate sterile neutrinos as a WDM candidate, we have to first understand their production in the early universe, which determines the distribution function of sterile neutrinos after decoupling, and then study how these distribution functions influence the matter power spectrum of the universe. These two important aspects are discussed individually in Chaps. 3 and 4.

In an extension of the SM invoked in Refs. [237, 236, 198, 258, 256, 257, 61, 32, 29, 31, 30, 81], sterile neutrinos can be produced via decay from a Higgs-like scalar beyond the SM [237, 236, 198]. Recent studies in Refs. [61, 65] have revealed that such a production mechanism yields a non-thermal (BD) distribution function that favors small momenta, remarkably different from the Dodelson-Widrow (DW) production mechanism, where sterile neutrinos are produced around 100 MeV via mixing with the active neutrinos in the SM [113]. Furthermore, the dependence of the matter power spectrum at small scales ($\sim 10^2$ kpc) on distribution function was analyzed in an analytical approach, where the power spectrum of BD sterile neutrinos is suppressed for scales smaller than 500 kpc when compared to that of the CDM case, and is substantial enhanced at small scales when compared to that of DW sterile neutrinos. This discovery on one hand justifies the expectation on WDM to smooth the small scale problems; on the other hand, it also helps to relax the tension between X-ray data and Lyman-α analysis.

Complimentary to the work in [61], we further realize that at such a high temperature of electroweak scale, SM vector bosons are thermalized with a large abundance, their decay also generates sterile neutrinos. Chap. 3 is devoted to study this new decay channel, understand its influence on the production rate and the mixing angle of sterile neutrinos. By combining this new decay channel with the decay via the Higgs-like scalar discussed above [61, 198, 199], we aim to systematically study sterile neutrinos produced at the electroweak scale.

By making use of the non-equilibrium finite temperature field theory developed in [63, 278, 59, 66, 67, 170], we obtain an effective Dirac equation for the sterile and active neutrinos doublet, whose self-energy corrections contain the medium effect from the thermalized vector bosons and the Higgs-like scalar. From the real and imaginary parts of these self-energy corrections, we extract information on the index of refraction in the medium and the production rate of sterile neutrinos respectively. We find that the production rate of sterile neutrinos via the decay of vector bosons is competitive with the production via scalar decay. By analyzing the mixing between the sterile and active neutrinos in the medium, we discover a new type of Mikheev-Smirnov-Wolfenstein (MSW) resonance in the absence of a lepton asymmetry besides the ordinary MSW resonance driven by the small lepton asymmetry. These MSW resonances correspond to the maximal mixing and enhance the production of sterile neutrinos. This new MSW resonance occurs in the low momentum region of $k/T \leq 1$ for temperature T above the electroweak scale and gradually disappears when the temperature drops below the electroweak scale. Moreover, at the resonance, the two massive neutrino states are degenerate, leading to a breakdown of the adiabaticity. Therefore, with the expanding universe rapidly crossing over these narrow resonances, we expect a highly non-thermal distribution function of sterile neutrinos after decoupling, which features an enhancement at small momenta because of the resonances.

After understanding the production of sterile neutrinos in the early universe, in Chap. 4, we investigate the influence of the distribution function on the structure growth and matter

power spectrum by carrying out a semi-analytical study on the linear structure growth of WDM candidates in a radiation-matter cosmology for arbitrary distribution function and mass in the keV scale.

Our work in Chap. 4 is a continuation of the previous study [65, 61], where the authors only consider density perturbations since matter-radiation equality. Instead, we evolve density perturbations including the Radiation Dominant (RD) phase, yielding a more self-consistent and complete analytical investigation on structure growth within the WDM scenario. To obtain the matter power spectrum for arbitrary WDM particles, the time evolution of initial density perturbations is divided into three stages: I) relativistic WDM particles in the RD era II) non-relativistic WDM particles in the RD era, and III) non-relativistic WDM particles in the Matter Dominant (MD) era. We solve the linearized collision-less Boltzmann equation governing the time evolution of density perturbations in each stage, and smoothly connect these solutions together in time, thus obtaining the density perturbations, transfer function and power spectrum today.

We find that the transfer function in the WDM scenario is related to two important length scales k_{eq} and k_{fs}. $k_{eq} \simeq 0.01(\mathrm{Mpc})^{-1}$ is the wave vector of perturbation modes that enter the Hubble radius at the matter-radiation equality. k_{fs}, called the free streaming wave vector, does not appear in the CDM paradigm. Its inverse describes the average distance traveled by free WDM particles from the matter-radiation equality to today, and plays a role analogous to the Jean's length in structure formation processes. k_{fs} also corresponds to the size of the co-moving horizon when WDM particles become non-relativistic. Heavier WDM particles with a colder distribution function features a bigger k_{fs} than lighter WDM particles with a warmer distribution (For CDM particles, $k_{fs} \to \infty$.), correspondingly, at small scales, the transfer function of colder species is closer to that of the CDM particles than the warmer species. Therefore, the transfer function of BD sterile neutrinos is less suppressed than that of the DW sterile neutrinos of the same mass. Our semi-analytical expression agrees nicely with the transfer function obtained from the Boltzmann codes in the fitting region ($\lambda \geq 1$ Mpc) available in the literature [165, 1, 274], reaching an error within a few percent.

Furthermore, we realize that the transfer function observed today contains information of the entire evolution history of the density perturbations of WDM particles. In stage I), an Integrated Sachs-Wolfe (ISW) effect, as a consequence of the time derivative of the gravitational potential produced by acoustic oscillations of the radiation fluid, enhances the transfer function for wave vectors smaller than k_{fs}. Moreover, at small scales roughly about $k \geq 2k_{fs}$, the transfer function oscillates due to the WDM acoustic oscillations and free streaming effect, which might suggest interesting observational signals on density perturbations with mass scales $10^8 M_\odot$ and $10^9 M_\odot$ for BD and DW sterile neutrinos respectively. We find a quasi-degeneracy between the mass and the distribution function of sterile neutrinos on the transfer function of WDM particles. This quasi-degeneracy implies an inherent ambiguity in the Lyman-α analysis to constrain masses of sterile neutrinos.

1.3.2 Part II (Chapters 5 to 7): Theory on Neutrino Oscillations

From Chap. 5 onwards, we switch to a different research topic to consider the theory of neutrino oscillations. After a brief introduction to the standard treatment on neutrino oscillations both in quantum mechanics and quantum field theory, we point out the entanglement issue recently discussed in the literature, which states that neutrinos produced from decay via charge current interactions are entangled with the corresponding charge lepton [92]. This entanglement may lead to some impact on the standard formulas of neutrino oscillations. In Chap. 6, we study dynamics of this entangled state directly as a function of time in a simplified theoretical model that describes the main features of neutrino oscillation experiments.

When this entangled state evolves, the charged lepton is usually detected by the near detector or stopped at a "beam dump" near the source, resulting in an disentangled neutrino state that travels to the far detector. By assuming the dis-entangling time to be t_S and that the dis-entangled neutrino state is measured at t_D in the far detector, the difference between t_D and t_S roughly corresponds to the baseline of the neutrino oscillation experiment. For long baseline neutrino oscillation experiments, this difference can be macroscopically

large [13, 9, 10]. Therefore the dynamics of the entangled state involves *two times*: the dis-entangling time t_S and the time t_D to measure the disentangled neutrino state at the far detector. To study this dynamics, conventional S-matrix calculation certainly cannot fulfill this requirement because it treats the production, propagation and detection processes of an neutrino oscillation experiment together as a single Feynman diagram, and only considers in and out states by taking the production and detection times asymptotically to infinities. In order to study the influence of entanglement and dis-entanglement on neutrino oscillations, we have to carry out the two-time measurement explicitly, by first evolving the entangled state to the dis-entangling moment t_S, and then evolving the dis-entangled neutrino state to the far detector.

To emphasize the importance of this *two-time* measurement idea and avoid unnecessary technical complications, we describe all particles by plane waves in this study, neglecting the wave packet treatment and focusing solely on the issues of entanglement, dis-entanglement and the *two-time* measurement. After understanding this dynamics, we will employ the wave packet idea in the future, thus investigate the issue of entanglement and dis-entanglement within a more consistent and complete theoretical picture of neutrino oscillations.

By carrying out this two-time measurement calculation, we obtain non-conventional expressions for the appearance and dis-appearance amplitudes and probabilities that depend on both time scales t_S and t_D. Under the long time limit and provided that $t_S \ll t_D$, the transition rate of long baseline neutrino oscillation experiments, defined as the time derivative of the transition probability, factorizes in terms of the usual quantum mechanical probability. When $t_S \sim t_D \sim L^{osc}$, where L^{osc} is the oscillation length scale, the oscillation amplitudes, the appearance and disappearance probabilities deviate significantly from the standard results, suggesting important corrections for short baseline oscillation experiments such as MiniBooNE [11] and LSND [35, 36, 37, 39, 38]. In these cases, the dynamics of dis-entanglement may introduce extra modulation with energy. Given the anomaly observed in the LSND and MiniBooNE neutrino oscillation experiments, it could be interesting to re-investigate these experiments by taking the dependence on the disentangling time into

account.

In Chap. 7, we consider the GSI anomaly, which refers to the unexpected time dependent modulation in the population of parent ions from the Electron Capture (EC) decays of $^{140}Pr^{58+}$ and $^{142}Pm^{62+}$. Based on the method developed in Chap. 6, we obtain directly the time evolution of the population of parent and daughter particles, taking into account that the quantum state arising from the decay of the parent particle is an entangled state of the neutrino and the daughter particle. In this way, we bypass the controversy of summing amplitudes or probabilities and exhibits directly the time evolution of the parent and daughter populations [175, 174, 173, 122, 145, 146, 86, 188, 235].

We show that both the decay rate of the parent particle and the production rate of the daughter particle do not feature oscillations arising from the interference of neutrino mass eigenstates, as a direct consequence of the orthogonality of the neutrino mass eigenstates. Therefore, our result, supplemented with an alternative explanation in terms of the imaginary part of the self-energy diagram of the parent particle, un-ambiguously shows that the GSI anomaly is not a consequence of neutrino oscillations [175, 174, 173, 122].

1.3.3 Chapter 8: Conclusion

Finally, Chap. 8 summarizes the main results of our work on sterile neutrinos in Chapters 3-4 and on the theory of neutrino oscillations in Chapters 6-7.

1.4 PUBLICATION LIST

The content of this thesis is based on four published articles. For readers' convenience, we give references to these articles in the following.

PART I: Sterile Neutrinos as a WDM Candidate

- "*Sterile neutrinos produced near the EW scale I: mixing angles, MSW resonances and production rates*",
  Jun Wu, Chiu-Man Ho and Daniel Boyanovsky,
  Phys. Rev. **D80**, 103511 (2009), arXiv:0902.4278.

- "*Small scale aspects of warm dark matter : power spectra and acoustic oscillations*",
  Daniel Boyanovsky and Jun Wu,
  Phys. Rev. **D83**, 043524 (2011), arXiv:1008.0992.

PART II: Theory of Neutrino Oscillations

- "*Dynamics of disentanglement, density matrix and coherence in neutrino oscillations*",
  Jun Wu, Jimmy A. Hutasoit, Daniel Boyanovsky and Richard Holman,
  Phys. Rev. **D82**, 013006 (2010), arXiv:1005.3260.

- "*Is the GSI anomaly due to neutrino oscillations? - A real time perspective -*",
  Jun Wu, Jimmy A. Hutasoit, Daniel Boyanovsky and Richard Holman,
  Phys. Rev. **D82**, 045027 (2010), arXiv:1006.5732.

Part I:

STERILE NEUTRINOS AS A WDM CANDIDATE

2.0 PART I: INTRODUCTION

2.1 CONCORDANCE ΛCDM COSMOLOGICAL MODEL

In the concordance ΛCDM standard cosmological model, the Universe today is composed approximately by 72.8% of a Dark Energy (DE) component, about 22.7% of dark matter (DM) and about 4.6% of ordinary matter (baryons) [176]. Such a composition is based on a series of revolutionary observations. The concept of DM was first proposed by Zwicky in 1933 by comparing the theoretical estimation and the observation of the rotational curves of the Coma cluster of galaxies [294, 295]. Unfortunately, people did not pay much attention to this idea until almost 30 years later. Since 1970, Rubin & Ford and other collaborators carried out a detailed study of the rotation velocity curves and mass distributions of individual galaxies, which suggests *significant mass located beyond the optical image* [250, 251]. In addition to this observational evidence of DM, various modern cosmological observations strongly support the existence of DM, including data from the Cosmic Microwave Background (CMB) [195], strong and weak lensing [269, 245], Bullet cluster [91], Big Bang Nucleosynthesis (BBN) [125], type Ia supernovae [248, 234], galaxy surveys [264], etc. The discovery of DE results from the revolutionary observations on far away type Ia supernovae in late 1990s [248, 234], which tried to trace the expansion history of the Universe through these standard candles. Subsequent observations have confirmed the early conclusion that the expansion of the Universe is accelerating [249, 177, 284, 187]. To explain the acceleration of the expansion rate, DE is required to work against the gravitational attraction of ordinary matter. Similar to DM, the existence of DE has to reconcile with other cosmological observations, e.g., CMB [176], BBN [125], gravitational lensing [269, 245], etc. All together along with inflation provide us with our current understanding of the Universe today.

Undeniably, physicists have gained tremendous useful information on DM and DE from these observations and analysis. However, all these observations are based on the gravitational property of DM and DE, providing little information on their nature from the particle physics point of view. Although DM particles are essential to the formation of cosmic structures observed today [112, 281], they exhibit very weak SM interactions, and pose great challenges to both direct and indirect detection of them [124]. DE is even more mysterious, obeying an equation of state with negative pressure [112, 281]. In order to understand what DM and DE are, we have to push our understanding to new physics beyond the SM. In fact, the incompleteness of SM was realized by physicists back to the mid-20th century, after the discovery of neutrino oscillations. The phenomenon of neutrino oscillation successfully explains the solar neutrino problem [283, 218, 166, 167, 168], and was confirmed by observation on atmospherical neutrinos [148, 169, 185, 34, 19] and terrestrial neutrino oscillation experiments [148, 18, 25, 26]. To enable the oscillation phenomena, neutrinos have to be massive and mix, directly contradicting the SM because in the SM, neutrinos are massless. Convincing experimental data on the existence of DM and neutrino oscillations are direct evidence of physics beyond the SM. In addition to that, the completeness and naturalness of the SM are also challenged by the gauge hierarchy problem, the SM flavor problem, the strong CP problem, etc. To have an overview of these problems, one can refer to Sec. II.B of [124] and references therein. Motivated by all the above problems, various theories have been proposed to address new physics beyond the SM. They usually predict new fundamental particles, providing many possible DM candidates. In Table I of [124], the author lists the most popular DM candidates motivated by different problems of the SM, and compares their basic properties and possible detection methods. We reproduce this table and show it here (also called Table. 1).

The puzzle of DM in cosmology, associated with the physics at the largest observational scales, and the problem of particle physics beyond the SM, of physics at the smallest observational scales, are tied together by the properties of DM. Progress on understanding one problem may shed light on the other. The interplay between cosmology and particle

	WIMPs	SuperWIMPs	Light $\tilde{G}$	Hidden DM	sterile ν	Axions
Motivation	GHP	GHP	GHP NPFP	GHP NPFP	ν mass	Strong CP
Naturally Correct Ω	Yes	Yes	No	Possible	No	No
Production Mechanism	Freeze Out	Decay	Thermal	Various	Various	Various
Mass Range	GeV-TeV	GeV-TeV	eV-keV	Gev-TeV	keV	μeV-meV
Temperature	Cold	Cold/Warm	Cold/Warm	Cold/Warm	Warm	Cold
Collisional				$\surd$		
Early Universe		$\surd\surd$		$\surd$		
Direct Detection	$\surd\surd$			$\surd$		$\surd\surd$
Indirect Detection	$\surd\surd$	$\surd$		$\surd$	$\surd\surd$	
Particle Colliders	$\surd\surd$	$\surd\surd$	$\surd\surd$	$\surd$		

Table 1: Summary of dark matter particle candidates, their properties, and their potential methods of detection. The particle physics motivations are discussed in Sec. II.B; GHP and NPFP are abbreviations for the gauge hierarchy problem and new physics flavor problem, respectively. In the last five rows, $\surd\surd$ denotes detection signals that are generic for this class of dark matter candidate and $\surd$ denotes signals that are possible, but not generic. "Early Universe" includes phenomena such as BBN and the CMB; "Direct Detection" implies signatures from dark matter scattering off normal matter in the laboratory; "Indirect Detection" implies signatures of late time dark matter annihilation or decay; and "Particle Colliders" implies signatures of dark matter or its progenitors produced at colliders, such as the Large Hadron Collider (LHC). See the text for details.

physics in theoretical, experimental and observational aspects suggests an opportunity to reveal the next layer of fundamental physics in the near future. This thesis only focuses on DM and its roles in structure formation. From Table 1, we see that being motivated by different problems of the SM, different DM candidates behave dramatically different in their mass ranges, production mechanisms, temperature and detection methods. Among all DM candidates, WIMPs represent the most popular and best studied DM particles. They have all the properties expected in the ΛCDM cosmological model. They are cold and collisionless, with negligible velocity dispersion that favors a hierarchical "bottom-up" structure formation. This CDM scenario works extremely successful on large scales, an example is shown in Figure 1, which compares the theoretical prediction on the power spectrum of cosmological density fluctuations based on the concordance ΛCDM model with different observational data. The theory and the observation agree nicely with each other on large scales.

Despite the great success of the concordance ΛCDM model, it features some "potential" problems at small scales, also indicated in Figure 1. At small scales, say $k \gtrsim 1\text{Mpc}^{-1}$, data from Lyman alpha Forest systematically deviates from the theoretical prediction, revealing a suppression on the power spectra. Moreover, other discrepancies from comparison between observations and N-body simulations on these small scales further challenge the validity of cold DM scenario. In the following section, we will review these small scale problems and motivate our work.

2.2 SMALL SCALE PROBLEMS OF ΛCDM MODEL

The small scale problems mainly come from the comparison between numerical N-body simulations based on the concordance ΛCDM cosmological model and observations on dwarf galaxy satellites of the Milky Way. Dwarf galaxies are unique objects in our universe to study properties of DM because these sub-galactic structures are DM dominant. However, it is really challenging to study these objects. From the simulation point of view, although the complicated baryonic physics is minimal for these objects, their influence on the astro-

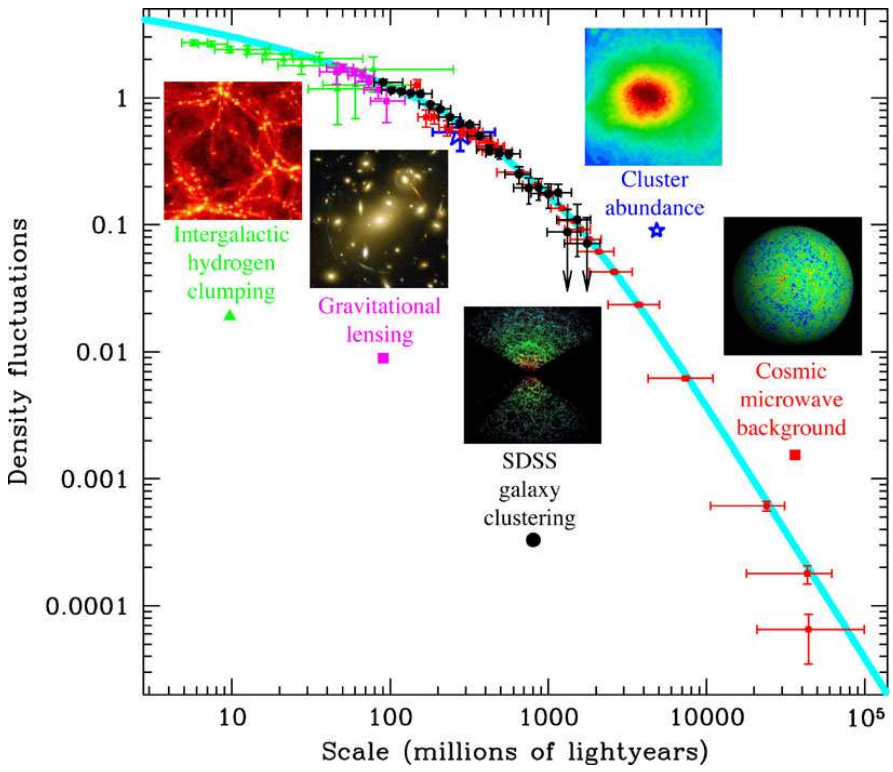

Figure 1: Comparison of theoretical predicted current density fluctuation power spectrum $P(k)$ with various observational data. The cyan solid line corresponds to the theoretical prediction based on the concordance ΛCDM cosmological model. Other observational data share the same cosmic matter budget parameters.

physical properties of dwarf galaxies is unclear and could be important. Not only we lack a certain understanding of the physics of galaxy formation, but also it is currently computationally formidable to include all baryonic processes. Until recently, high resolution N-body simulations start to include feedback procedures to model various baryonic physics [244]. From the observational point of view, because these objects are DM dominant, they emit very weak optical signals, making their detection really hard [244]. By comparing simulations with observations, several potentia problems of the CDM structure formation scenario are discovered, including the so-called "missing satellite problem" and the central cusps vs. cores problem, which are discussed in the following. Recently, more small scale problems are discussed in the literature, e.g., problem of the emptiness of the voids, which is another over-abundance problem in the ΛCDM model similar to the missing satellite problem, stating that high resolution simulations of the ΛCDM model predicts too many voids than observations of our Local Volume [266]. Moreover, Millennium-II and other hydrodynamical simulations of the formation of dwarf galaxies in the ΛCDM model over-predict the luminosity of the dwarf galaxies residing in halos with masses of order $10^{10} M_{\odot}$ [253].

2.2.1 Missing Satellite Problem

The "*missing satellite problem*" originally refers to the discrepancy between the predicted abundance of sub-halos based on numerical simulations within the CDM scenario and the number of observed low luminosity dwarf galaxies [191, 226, 179, 138, 109, 110, 197] around our Milky Way. However, such a direct comparison on the numbers of DM sub-halos and dwarf galaxies may not be completely accurate due to our current limitations on both simulations and observations, as discussed above. Therefore, the common strategy is to compare physical observables that mainly rely on DM properties, which can be estimated from both dissipationless N-body simulations and observations. Two quantities used in the literature are the circular velocity [226, 262, 196] and the mass of a sub-halo within a fixed physical radius, say $m_{0.6}$ for example, namely, mass within 0.6kpc of the sub-halo [196]. By comparing the cumulative number of sub-halos with that of dwarf galaxies as functions of circular velocity and $m_{0.6}$, the missing satellite problem is alleviated but does not disappear [244, 196],

N-body simulations still predicts about an order of magnitude more satellite galaxies than those observed around the Milky Way. According to Kravtsov [196], the missing satellite problem *can be stated as the discrepancy in the slopes of the circular velocity and $m_{0.6}$ mass functions inferred for observed satellites of the Milky Way and the slopes of these functions predicted for DM sub-halos in the MW-sized host halos formed in the concordance ΛCDM cosmology.* Meanwhile, detailed analysis on all the Milky Way dwarf galaxies also reveals all dwarf galaxies share a roughly same dynamical mass of about $10^7 M_\odot$ within radius about 0.3kpc despite that their luminosities range along several orders of magnitude [85, 244, 196].

2.2.2 Cusp Problems in Galaxy Centers

In addition to the missing satellite problem, N-body simulations also yield a density profile that increases monotonically towards the center [226, 126, 225, 120, 84, 292, 293, 111] as $\rho(r) \sim r^{-\gamma}$. In particular, $\gamma = 1$ corresponds to the Navarro-Frenk-White (NFW) profile [228, 229]. Steeper profiles with $\gamma \sim 1.2$ have been found recently in high resolution N-body simulations [111, 108]. These density profiles conflict with recent observational evidences that favor shallow cored profiles instead of cusps in dwarf spheroidal galaxies (dShps) [190, 95, 140, 141, 139, 288, 142, 135, 136, 137, 216, 44, 232, 100]. This core vs. cusp controversy is intensively studied in the literature. A sound understanding on the density profiles of dwarf galaxies is of great importance to DM indirect detection experiments. Future high resolution N-body simulations that include baryonic processes may solve the problem. Several mechanisms have been proposed to smooth such a discrepancy ([244] and references therein). However, this controversy between theoretical predictions and observations poses a challenge to the standard CDM scenario.

Warm dark matter particles (WDM) were invoked[227, 54, 40, 193, 192] as possible solutions to the small scale problems listed above. WDM particles feature a non-vanishing velocity dispersion with a range in between CDM and hot dark matter HDM, leading to a free streaming scale that cutoffs power at small scales thereby smoothing out small scale structure. If the free streaming scale of the WDM particles is smaller than the scale of galaxy clusters,

the large scale structure properties are indistinguishable from those of CDM, but may affect structure at small scales [58], thereby providing an explanation of the smoother inner profiles and the fewer satellites because particles escape away from the collapsing region. A small scale cutoff in the DM power spectrum may also explain the apparent smallness of galaxies at $z \sim 3$ found in Ref. [178]. Although these small scale problems, e.g., missing satellite problem and cusp vs. core problem, may be ultimately resolved by baryonic mechanisms such as complex "gastrophysics", there is an intrinsic interest in studying alternatives to the standard CDM paradigm from a theoretical point of view. Table. 1 has shown a wide possibility for potential DM particles, among which there are several WDM candidates. A systematical study on properties of WDM would complete our understanding on properties of DM and may have great implication in future direct and indirect DM detection experiments and observations. Among the listed WDM candidates in Table. 1, we will focus on sterile neutrinos as our subject of study. Sterile neutrinos are well motivated particles beyond the SM. Besides being suitable WDM candidates, they may also provide possible solutions to several astrophysical problems[200, 33, 49, 199] and have profound implications in particle physics [81, 124].

2.3 STERILE NEUTRINOS AND OBSERVATIONAL CONSTRAINTS

Sterile neutrinos, namely $SU(2)$ singlets, with masses in the $\sim$ keV range are the WDM candidate that we are interested in [113, 94, 259, 3, 4, 133, 2, 258, 256, 257, 200, 33, 49, 199, 237, 236, 64, 81]. The idea of sterile neutrinos was proposed by Pontecorvo to explain the neutrino oscillations [243]. They generate masses of active neutrinos in the SM through the see-saw mechanism [219, 223]. Due to their coupling and mixing with active neutrinos, sterile neutrinos could be generated in the early universe. Hence, their masses and mixing angles with active neutrinos are some of the most important properties of sterile neutrinos as DM particles. In principle, one can generate several generations of sterile neutrino, analogous to that of active neutrinos in the SM. Current theoretical models often consider only one generation for simplicity. To be proper DM particles, the masses and mixing angles of

sterile neutrinos have to be consistent with various cosmological observational constrains. In the following, we introduce these astrophysical observations and their constraints on sterile neutrino masses and mixing angles.

2.3.1 Upper Bound from X-ray Constraints

Because of their coupling with active neutrinos, sterile neutrinos would decay and generate X-ray signals through the process $\nu_h \to \nu_l \gamma$ [117], where ν_h and ν_l represent the heavy and light massive neutrinos which are mainly sterile and active respectively, and γ corresponds to the photon. The expected flux for such DM decay is given by [81]

$$F = \frac{M_{DM}^{fov}\Gamma}{4\pi D_L^2}\frac{E_\gamma}{M_S} \simeq 6.38 \left(\frac{M_{DM}^{fov}}{10^{10}M_\odot}\right)\left(\frac{\text{Mpc}}{D_L}\right)^2 \times \sin^2(2\theta)\left(\frac{M_S}{\text{keV}}\right)^2 \frac{\text{keV}}{\text{cm}^2 \cdot \text{sec}}. \tag{2.3.1}$$

M_{DM}^{fov} is the mass of DM within a telescope's field of view (FoV), Γ is the decay rate, D_L is the luminosity distance of the observed object, M_S is the sterile neutrinos mass and θ is the mixing angle between sterile and active neutrinos. Constraints on the observational flux can be translated into a constraining relation between the sterile neutrino M_S and the mixing angle θ through Eq. (2.3.1). Several X-ray observations try to search these X-ray signals using $XMN-Newton$ [75, 78, 69], $Chandra$ [5, 279, 80], $INTEGRAL$ [289, 74] and $Suzaku$ [209]. A recent analysis suggests a possible emission line of a 5 keV sterile neutrinos [208], however, further examination challenges this statement [70]. In summary, the fact that lack of X-ray photon emission lines sets an upper limit for the flux of sterile neutrino decay, which excludes a significant region of the sterile neutrino parameter space.

2.3.2 Lower Bond from Phase Space Density of Dwarf Galaxies

As the most DM dominated astrophysical objects in the universe, dwarf galaxies play an important role in studying DM properties. In particular, the phase space density of dwarf spheroidal galaxies (dSphs) sets the most robust lower bound on DM masses. According to Tremaine and Gunn [268, 64], the coarse grained phase space density either remains constant or diminishes under collisionless gravitational dynamical evolution. Therefore, the observed coarse grained phase space density of dSphs must be equal to or smaller than the primordial

phase space density. Detailed discussion on several DM candidates based on the generalized Tremaine-Gunn bound can be found in [64, 79, 154]. Since the phase space density depends on the distribution function of DM particles, sterile neutrino produced from different mechanisms yield different mass bounds. Unlike WIMPs and many other DM candidates, the production rate of sterile neutrinos is usually much smaller than the Hubble parameter [81], sterile neutrinos never become equilibrated with other particles in the early universe, leading to an non-thermal distribution function. In general, sterile neutrinos can be produced non-resonantly (NRP), namely through the Dodelson-Widrow (DW) mechanism [113], or resonantly (RP) through the lepton driven MSW resonance named after Mikheev, Smirnov and Wolfenstein [283, 218, 46]. Other production mechanism e.g., from scalar decay, is also possible in models beyond the SM [198, 237, 236]. The DW production mechanism gives a fairly tight lower mass bound $M_S > 1.7$ keV [79]. Combined with current X-ray observational constraints, it leaves a very limited allowed parameter space of sterile neutrinos for DW sterile neutrinos being the sole DM particles. The lower mass bound of RP mechanisms is much looser, sterile neutrinos with $M_S > 1$ keV can satisfy the requirement though further study is required [81]. Recent analysis [64, 61] reveals that combining the results for the distribution function of sterile neutrinos produced via scalar decay with dShps data yields a narrow window for the mass of sterile neutrinos: $0.56\ \text{keV} \leq M_S \leq 1.33\ \text{keV}$, whose robustness has been confirmed in Ref. [106].

2.3.3 Constraints From Lyman-α Forest

The Lyman-α analysis is potentially a powerful tool to study density perturbations at small scales, sensitive to perturbation scales $k \sim (0.1-5)h\ \text{Mpc}^{-1}$ and redshifts $2-4$ [81]. Lyman-α absorbtion lines in the spectra of far away quasars are produced by neutral hydrogen residing in the intergalactic medium along the line of sight. Neutral hydrogen is excited by Lyman-α photons from these distant quasars, leaving an absorption line in the quasar spectrum. As the universe expands with time, absorption lines produced at different redshifts form a trough in the spectrum, called the Lyman-α forest. The Lyman-α forest has complicated dependence on cosmological parameters. By fitting with other cosmological observations,

e.g., CMB and LSS data, one can extract information on total density fluctuations of DM particles at these small scales.

On top of the technical challenges of the Lyman-α analysis itself, there are further complications. For scales and redshifts probed by Lyman-α method, cosmological density perturbations start to become non-linear. Therefore, one has to carry out full hydrodynamical simulations to take into consideration these non-linear effects of both DM density perturbations and the dynamics of neutral hydrogen [72, 81]. Unfortunately, current hydrodynamical simulations cannot reach our desired accuracy, and various simple approximations have to be employed in these simulations [265, 153, 215, 273, 272, 246], yielding relatively big systematical errors in the Lyman-α analysis. Even so, Lyman-α forest is deemed able to constrain DM mass with a relative error of about 30% [72]. Future Lyman-α analysis may provide more accurate mass bounds for DM particles with the rapid improvement on hydrodynamical simulations and analyses on systematical errors. Finally, it is worth noting that being a probe of small scale density fluctuations, the Lyman-α method is also sensitive to different production mechanism of DM particles. The tension between the X-ray [75, 76, 78, 69, 279] and the Lyman-α forest data [254, 275, 271, 72] seems to exclude the possibility of NRP sterile neutrinos produced through DW mechanism being the dominant WDM component [233]. Recent Lyman-α analysis on RP sterile neutrinos substantially decreases the lower mass bound of sterile neutrinos, alleviates the tension with X-ray constraints, making sterile neutrinos still valid WDM candidates [73].

Combining all the constraints mentioned above, the allowed region of the parameter space of sterile neutrinos is shown in Figure 2 (Figure 4 of [81]). In addition to constraints from cosmological observations, sterile neutrinos also have interesting applications in astrophysics, e.g., to explain the pulsar kick [198, 50]. Constraints on sterile neutrino mass and mixing angle can also come from these phenomena. Interested readers can refer to [198] for details.

From all these discussion above, there is a clear motivation to study sterile neutrinos

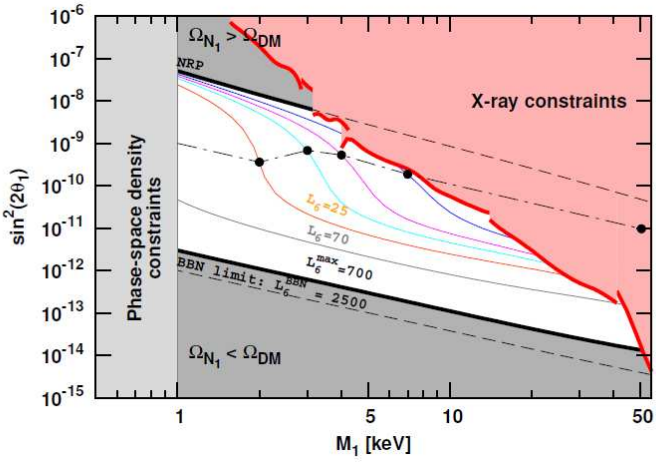

Figure 2: Figure from [81]. The allowed region of parameters for DM sterile neutrinos produced via mixing with the active neutrinos (unshaded region). The two thick black lines bounding this region represent production curves for NRP (upper line, $L_6 = 0$) and for RP (lower line, $L^max_6 = 700$) with the maximal lepton asymmetry, attainable in the theoretical model νMSM [257, 201]. L_6 corresponds to 10^6 times the lepton asymmetry. The thin colored curves between these lines represent production curves for (from top to bottom) $L_6 = 8, 12, 16, 25$, and 70. The red shaded region in the upper right corner represents X-ray constraints [78, 77, 209, 74] (rescaled by a factor of two to account for possible systematic uncertainties in the determination of DM content [80, 71]). The black dashed-dotted line approximately shows the RP models with the largest cold component. The black filled circles along this line are compatible with the Lyman-α bounds [73], and the points with $M_1 \leq 4$ keV are also compatible with X-ray bounds. The region below 1 keV is ruled out according to the phase-space density arguments [64, 79]. Abbreviation: BBN, big bang nucleosynthesis.

as a WDM candidate. In this part of study, we are going to investigate the properties of sterile neutrinos being WDM particles. In particular, we consider sterile neutrino parameters within the allowed region of its parameter space, as discussed here.

2.4 SUMMARY OF OUR WORK

In this section, we summarize our work on sterile neutrinos as a WDM candidate, which is divided into two major pieces. We begin this program by studying the sterile neutrino production at the electroweak scale and then develop a semi-analytical and simple derivation of matter power spectrum for arbitrary distribution functions.

2.4.1 Sterile Neutrinos Produced at the Electroweak Scale

As we have mentioned previously, sterile neutrinos are non-thermal DM particles, featuring non-trivial distribution functions depending on the production mechanism [113, 94, 259, 258, 256, 257, 200, 33, 49, 199, 237, 236]. Our first project, reported in Chapter 3, is to study the production of sterile neutrinos at the electroweak scale within a generalized version of the so called νMSM model [237, 236, 258, 256, 257, 32, 29, 31, 30, 81]. In addition to the conventional DW production mechanism which peaks around ~ 130 MeV [113], in this model, sterile neutrinos may be produced by the decay of a Higgs-like scalar beyond the SM with a mass of the order of the electroweak scale [200, 33, 49, 199, 237, 236, 198], as well as of SM gauge bosons W and Z. We focus on the sterile neutrino production via decays at a temperature of the electroweak scale because at this temperature region, vector bosons and the Higgs-like scalar are thermalized at a large abundance [237, 236, 61], which may significantly contribute to the production of sterile neutrinos.

Recent study in Ref. [61] revealed that the non-resonant production mechanism of sterile neutrinos by scalar decay leads to a non-thermal distribution function that favors small

momenta, remarkably different from sterile neutrinos produced by the DW mechanism [113], whose distribution function is that of a thermal relic decoupling relativistically multiplied by an overall factor of order 10^{-2}. Because it favors small momenta, the new sterile neutrino distribution function found in [61] could relax the tension between X-ray data and Lyman-α analysis, and also have important consequences for structure formation [61].

The Goals:

Our first project is a complement and generalization of the work presented in [61]. At the temperature of order of the electroweak scale, the charged and neutral vector bosons are present in the medium with large abundance, comparable to that of the Higgs-like scalar [237, 236, 198, 258, 256, 257, 61]. By their mixing with active neutrinos via a Yukawa coupling to the standard model Higgs [258, 256, 257], sterile neutrinos are produced by the decay of vector bosons, which could be an important contribution to sterile neutrino production at the temperature of the electroweak scale because of the large abundance of vector bosons.

Challenges and Strategy:

At such a high temperature, SM vector bosons and the Higgs-like scalar of electroweak scale are both in thermal equilibrium, leading to significant medium effects [283, 218, 189, 222, 132, 230, 171, 114, 115]; However, the production rate of sterile neutrinos never catches that of the Hubble expansion [81], demanding an out of equilibrium calculation. To meet these challenges, the main theoretical tool is the non-equilibrium formula of finite temperature quantum field theory, from which we derives an effective Dirac equation in the medium for the sterile and active neutrinos doublet following the method described in [63, 278, 59, 66, 67, 170]. Then, from the self-energy correction of the effective Dirac equation, we extract information on the index of refraction and the production rate of sterile neutrinos. The mixing angle between sterile and active neutrinos is also modified by the medium effect [283, 218, 189, 222, 132, 230, 171, 114, 115], making the maximal mixing, namely MSW resonance, possible. Resonantly produced sterile neutrinos usually features a much colder distribution function than that of non-resonantly produced sterile neutrinos, as shown in Figure 2 of [81], which may influence the structure formation [61, 65], therefore, we

hope to thoroughly understand the mixing between sterile and active neutrinos by obtaining the in-medium correction to the mixing angles.

Main Results:

Our main results are as follows:

- Sterile neutrinos are produced from decays of both SM vector bosons and of the beyond SM scalar. By comparing these two decay channels, we found that they contribute to the production rate and distribution function in similar forms, and sterile neutrino production rate via the decay of vector bosons in the medium is competitive with the production via scalar decay. The argument can be understood from simple dimensional analysis. For keV sterile neutrinos and the Higgs-like scalar of electroweak scale, the Yukawa coupling between the scalar and sterile neutrinos is about $Y \sim 10^{-8}$, corresponding to a production rate $\propto Y^2$. Whereas the contribution from vector boson decays is proportional to $\alpha_w \sin^2(\theta)$, with α_w and θ being the constant of weak interaction and the mixing angle between sterile and active neutrinos respectively. For $\theta \sim 10^{-5}$ [198, 209], the production rate of sterile-like neutrinos via vector boson decay can be of the same order of or larger than that from the decay of the Higgs-like scalar.

- By analyzing the mixing between active and sterile neutrinos, in addition to the usual lepton-driven MSW resonance occurring at $k/T \ll |\xi|$ with $|\xi|$ being the lepton asymmetry parameter consistent with the data from Wilkinson Microwave Anisotropy Probe (WMAP) and Big Bang Nucleosynthesis (BBN) [261], we find another MSW resonance even in the absence of a lepton asymmetry. For $1 \leq M_W/T \leq 3$, this resonance is in the low momentum region $0.2 \leq k/T \leq 1$ and well within the regime of validity of the perturbative expansion. These resonances are very narrow for $\theta \sim 10^{-5}$. At the resonances the propagating frequencies become exactly degenerate in striking contrast with the quantum mechanics of neutrino mixing wherein there is level repulsion at the resonance. This exact degeneracy at the resonance entails the breakdown of adiabaticity. It is a distinct consequence of the absorptive part of the self-energy and leads to a strong

damping regime.

- We argue that cosmological expansion leads to a rapid crossing of the narrow resonances resulting in both resonant and non-resonant sterile neutrino production. The distribution function after freeze-out is highly non-thermal with an enhancement at small momentum $k < T$. This low momentum enhancement of the non-thermal distribution function is expected [65, 61] to have important consequences: a shortening of the free-streaming length (smaller velocity dispersion) and an increase of the transfer function and power spectrum at small scales. We find a consistent range of parameters for which there is a resonance for nearly right-handed neutrinos at $T \sim M_W$. The general field theory framework allows a systematic study of the properties for both helicity states, including the helicity dependence of mixing angles and production rates.

2.4.2 Small Scale Aspects of WDM: Power Spectra and Acoustic Oscillations

After obtaining the production rate of sterile neutrinos in the early universe, in principle, one can solve the kinetic Boltzmann equation describing the production and decoupling of sterile neutrinos, and obtain the distribution function of sterile neutrinos after decoupling. In practice, it is much more complicated. Due to the mixing and non-adiabatic resonance during sterile neutrino production procedure, analytically solving the Boltzmann equation is technically challenging, we postpone the study to the future. Instead, we carry out a general semi-analytical study on structure formation of WDM, focusing on the dependence of power spectra on arbitrary DM distribution functions.

Analytical study on CDM structure formation at small scales has long been carried out [172, 112, 281], which helps to understand the physics and compliments the straightforward numerical calculations, e.g., CMBFAST [255]. Because most CDM particles are expected to be thermal relic that freeze out in the early universe and extremely non-relativistic, their power spectra of density fluctuations are insensitive to the distribution functions at the decoupling [172, 68], contrast to the case of WDM. In the recent analyses in [65, 61], the authors

have shown the dependence of small scale ($\sim 10^2$ kpc) density fluctuation power spectra on various distribution functions in an analytical approach, where non-thermal distribution of sterile neutrinos resulting from scalar decay indeed exhibit a suppression on power spectrum around 500 kpc compared with CDM case, and a substantial enhancement compared to DW produced sterile neutrinos. On one hand, such a discovery justifies the expected potential of WDM to smooth the small scale problems discussed previously; on the other hand, it also helps to relax the tension between X-ray data and Lyman-α analysis.

Our second project is a continuation of the previous study [65, 61], where the authors only consider density perturbations since matter-radiation equality. For the current study, we evolve density perturbations since primordial fluctuations right after inflation. Although density growth is generally believed to happen mainly in Matter Dominant (MD) era, keV sterile neutrinos have some special features such that their time evolution in Radiation Dominant (RD) era may suggest non-trivial contributions to the density perturbation power spectrum today, which will be discussed in detail in the following. Moreover, from a pure theoretical point of view, such a continuing study (following the work of [61, 65]) is necessary and sensible in order to obtain a self-consistent and complete analytical investigation on structure growth within the WDM scenario.

The Goals:

Our goals are actually twofold: i) to provide a semi-analytic understanding of the main physical processes that determine the transfer function of WDM candidates at small scales that entered the horizon well before matter-radiation equality for arbitrary distribution functions, ii) to provide a relatively simple formulation of the power spectrum that allows a straightforward numerical implementation, valid for arbitrary distribution functions. In order to achieve these goals we invoke several approximations: a) we neglect the contribution from baryons, b) we also neglect anisotropic stresses resulting from the free streaming of ultrarelativistic standard model active neutrinos. These approximations entail that the results of the transfer functions is trustworthy up to $10 - 15\%$ accuracy. However, the main purpose of this work is not to obtain the WDM transfer function to a few percent accuracy,

but to provide a semi-analytic tool, to study the main features of the transfer function at small scales for a particular WDM candidate given its distribution function determined by the microscopic process of production and decoupling. If the transfer function features important small scale properties that could potentially lead to substantial changes in structure formation, this would warrant more accurate study with the CMB codes and eventual inclusion into N-body simulations.

In this thesis we study the transfer function for WDM density and gravitational perturbations by solving the linearized collisionless Boltzmann equation in a radiation and matter dominated cosmology including the perturbations from the radiation fluid for arbitrary distribution function of the WDM particle, we expect the results (within the acknowledged possible errors) are valid for $z > 2$. In the following, we summarize the challenges we are facing and our strategy to achieve our goals.

Challenges and Strategy:

WDM particles with a mass in the keV range typically decouple from the primordial plasma when they are relativistic. For example, sterile neutrinos produced non-resonantly via the DW [113] mechanism or by the decay of scalar or vector bosons (BD) [198, 236, 61, 285] decouple at the QCD or Electroweak scale respectively. Therefore these species decouple when they are still relativistic in the RD era and become non-relativistic when $T \simeq m \simeq$ keV when the size of the comoving horizon is about Mpc.

Based on the above estimation, we anticipate that there are three stages of evolution for density perturbations: I) when the particle is still relativistic, this is a RD stage, II) when the particle is non-relativistic but still during the RD era, III) when matter perturbations dominate the gravitational potential, where the particle is already non-relativistic. During stages I) and II), the gravitational potential is completely determined by the radiation fluid, and serves as an external driving source for the linearized collision-less Boltzmann equation of WDM density perturbations. Otherwise, in stage III) when matter perturbations dominate, the gravitational potential is obtained from the well-known Poisson equation. As for

the initial conditions for the Boltzmann equation, we consider adiabatic initial conditions determined by the primordial perturbations seeded during inflation. Our main strategy is to smoothly connect piece-wise solutions of the linearized collision-less Boltzmann equation at different evolution stages listed above, using the solution in a previous stage as the initial condition for the next stage. Because the linearized collision-less Boltzmann equation is a first order differential equation in time, only the function at the end of a previous stage is needed as input of the next stage.

Main Results:

By carrying out the calculation following the strategy discussed above, we conclude our main results as:

- There are two relevant scales that determine the transfer function: i) $k_{eq} \simeq 0.01(\text{Mpc})^{-1}$ which is the wave vector of modes that enter the Hubble radius at matter-radiation equality, and ii) the dimensionless parameter κ which contains the free streaming wave vector

$$k_{fs} = \frac{\sqrt{3}k_{eq}}{2\langle V_{eq}^2\rangle^{1/2}}, \tag{2.4.1}$$

  where $\langle V_{eq}^2\rangle^{1/2}$ is the mean square root velocity dispersion of the WDM particle at matter-radiation equality. For a keV WDM candidate produced non-resonantly and decoupling at the electroweak or QCD scale, $k_{fs} \geq 10^3 k_{eq}$. The free streaming length scale $1/k_{fs}$ is proportional to the distance traveled by a non-relativistic particle with average velocity $\langle V_{eq}^2\rangle^{1/2}$ from matter-radiation equality until today, and it also determines the size of the comoving horizon η_{NR} when the WDM particles transit from relativistic to non-relativistic:

$$\eta_{NR} = \frac{\sqrt{3}}{\sqrt{2}k_{fs}}. \tag{2.4.2}$$

  This means that perturbations with $k > k_{fs}$ enter the horizon when the WDM particle is still relativistic and undergo suppression by relativistic free streaming between the time of horizon entry until η_{NR}.

- During stage I), the suppression of density fluctuations by free streaming is independent of the distribution function and the free streaming scale grows with the comoving horizon. However we find that perturbation modes that enter the horizon when the particle is relativistic with wavelengths up to the sound horizon are amplified via an early Integrated Sachs-Wolfe effect (ISW) as a consequence of the time derivative of the gravitational potential produced by acoustic oscillations of the radiation fluid. In stage II), the free streaming scale depends logarithmically on the comoving horizon, which suppresses the WDM density perturbations. In stage III), we turn the Boltzmann-Poisson equation into a self-consistent differential integral equation that admits a systematic Fredholm series solution. Its leading term is the Born approximation and lends itself to a simple and straightforward numerical analysis for arbitrary distribution functions. This approximation is equivalent to a fluid description but with an inhomogeneity and initial conditions completely determined by the past history during stages I) and II). The resulting fluid equation is a WDM generalization of the Meszaros equation [217, 161]. The solutions describe WDM acoustic oscillations, the suppression by free streaming is manifest in the inhomogeneity and initial conditions.

  In stage III) when WDM perturbations dominate the gravitational potential, density perturbations obey a self-consistent Boltzmann-Poisson integral equation which we analyze in a systematic expansion valid for small scales.

- Under the Born approximation, we obtain a semi-analytic expression for the transfer function and compare it to the CDM case. We analyze its numerical evaluation for arbitrary distribution functions, masses and decoupling temperatures. The transfer functions vary for different distributions with the same mass. We also provide an expression for the power spectra that interpolates between large and small scales and then compare with the results from the Boltzmann codes [165, 1, 274], which yields an excellent agreement. The ISW amplification of density perturbation enhances the transfer function for wavelengths larger than the free streaming length and is more pronounced for the colder species. WDM acoustic oscillations are manifest in transfer functions roughly for

$k \geq 2k_{fs}$. We analyze the main physical aspects of these oscillations and suggest that their amplification by non-linear gravitational collapse might lead to clumpiness on mass scales $10^8 M_\odot$ and $10^9 M_\odot$ for BD and DW sterile neutrinos respectively.

- Moreover, we confirm the quasi-degeneracy between sterile neutrino masses, distributions and decoupling temperatures: not only the value of the mass but also the detailed form of the distribution function along with the decoupling temperature determine the transfer function. Two particles of the same mass but very different distribution functions and decoupling temperatures, may feature very different power spectra. Conversely, two WDM particles of different masses and different distribution functions may feature similar power spectra on a wide range of scales. This result suggests that current constraints on the mass of the WDM particle from N-body simulations and the Lyman-α forest data need further understanding.

3.0 PART I: STERILE NEUTRINOS PRODUCED AT THE ELECTROWEAK SCALE

This chapter provides the technical details of sterile neutrino production at the electroweak scale as summarized in Sec. 2.4.1, and is based on results published in [285]. It is organized as follows: Sec. 3.1 is devoted to an introduction to the theoretical model. In Sec. 3.2, we obtain the effective Dirac equation in the medium for active and sterile neutrinos doublet, by employing non-equilibrium finite temperature field theory. In Sec. 3.3, we obtain the real part of self-energy corrections of sterile neutrinos, focusing on the mixing properties between active and sterile neutrinos. We also identify and discuss possible resonances. Correspondingly, Sec. 3.4 concentrates on the imaginary part of the self-energy corrections of sterile neutrinos, from which we obtain their production rate. Then, we apply our results to the expanding universe, sketching the dynamics of sterile neutrino production in the early universe in Sec. 3.5. Finally, we summarize and conclude this work in Sec. 3.6.

3.1 THE MODEL

The extension of the standard model presented in Refs. [237, 236, 198] generalizes the proposal of both the νMSM [258, 256, 257, 32, 29, 31, 30] and the model presented in [105, 103]. These models include three SU(2) singlet (sterile) neutrinos which couple to the active neutrinos via a see-saw mass matrix, in which the lightest sterile neutrino is a WDM candidate with mass of keV range. The generalized model in [237, 236, 198] gives a mass to this sterile neutrino via a Yukawa coupling to a Higgs-like scalar field which could be the neutral Higgs component, or another scalar whose expectation value is of the same order as that of the

SM Higgs boson, therefore this type of extension features only one scale.

We study a simplified version of these models by considering only one sterile and one active neutrino. In the usual see-saw mechanism, an off-diagonal Dirac mass matrix for the active species is considered along with a diagonal Majorana mass for the sterile neutrino [32, 29, 31, 30, 258, 256, 257, 189, 222, 132]. Instead of considering a Majorana sterile neutrino, we allow for Dirac mass terms for all species. This generalization allows us to study simultaneously the possibility of a lepton asymmetry in the active neutrino sector along with the possibility of a right-handed component leading to potentially relevant degrees of freedom within the same simple model. We hope to extract generic and robust features of the production rates and mixing angles of sterile neutrinos in the medium for various production mechanisms. Generalizing to three neutrino species can be done relatively straightforwardly but for the complications associated with larger mixing matrices, and the case of a Majorana neutrino is regained straightforwardly by projection.

Our model with one active (ν_a) and one sterile (ν_s) Dirac neutrinos is described by the Lagrangian density

$$\mathcal{L} = \mathcal{L}_{SM} + \overline{\nu}_s \, i \partial\!\!\!/ \, \nu_s - Y_1 \, \overline{\nu}_s \tilde{H}^\dagger l - Y_2 \, \overline{\nu}_s \Phi \nu_s + \mathcal{L}[\Phi] + \text{h.c.} \, , \tag{3.1.1}$$

where $\mathcal{L}_{SM}$ is the Lagrangian density of the SM and

$$l = \begin{pmatrix} \nu_a \\ f \end{pmatrix} , \quad \tilde{H} = \begin{pmatrix} H^0 \\ H^- \end{pmatrix} . \tag{3.1.2}$$

f is the charged lepton associated with ν_a and H^0, H^- are the components of the standard model Higgs doublet, and Φ is a real scalar singlet field whose expectation value gives a Dirac mass to the sterile neutrino. The Lagrangian density $\mathcal{L}[\Phi]$ describes the kinetic and potential terms of Φ. In the unitary gauge we write

$$H^0 = \langle H^0 \rangle + \sigma, \tag{3.1.3}$$

$$\Phi = \langle \Phi \rangle + \varphi, \tag{3.1.4}$$

and consistently with the single scale assumption in the νMSM: $\langle\Phi\rangle \sim \langle H^0\rangle$ are of the same order of magnitude, namely the electroweak scale and that their masses are also of the same scale. In fact our analysis is quite general, and this assumption will only be invoked for a quantitative assessment. The Lagrangian density (3.1.1) becomes

$$\mathcal{L} = \mathcal{L}_{SM} + \overline{\nu}_s \, i\partial\!\!\!/ \nu_s - \overline{\nu}_\alpha \; \mathbb{M}_{\alpha\beta} \; \nu_\beta - Y_1 \; \overline{\nu}_s \sigma \nu_a - Y_2 \; \overline{\nu}_s \varphi \nu_s + \mathcal{L}[\langle\Phi\rangle + \varphi] + \text{h.c}, \tag{3.1.5}$$

where $\{\alpha, \beta\} = \{a, s\}$ and

$$\mathbb{M} = \begin{pmatrix} 0 & m \\ m & M_s \end{pmatrix} \tag{3.1.6}$$

with

$$m = Y_1 \; \langle H^0 \rangle, \tag{3.1.7}$$

$$M_s = Y_2 \; \langle \Phi \rangle. \tag{3.1.8}$$

Introducing the "flavor" doublet (ν_a, ν_s), the diagonalization of the mass term $\mathbb{M}$ is achieved by a unitary transformation to the mass basis (ν_1, ν_2), namely

$$\begin{pmatrix} \nu_a \\ \nu_s \end{pmatrix} = U(\theta) \begin{pmatrix} \nu_1 \\ \nu_2 \end{pmatrix}, \qquad U(\theta) = \begin{pmatrix} \cos\theta & \sin\theta \\ -\sin\theta & \cos\theta \end{pmatrix} \; ; \tag{3.1.9}$$

where

$$\cos(2\theta) = \frac{M_s}{[M_s^2 + 4m^2]^{\frac{1}{2}}}, \qquad \sin(2\theta) = \frac{2m}{[M_s^2 + 4m^2]^{\frac{1}{2}}} \; . \tag{3.1.10}$$

In the mass basis

$$\mathbb{M}_m = U^{-1}(\theta) \mathbb{M} U(\theta) = \begin{pmatrix} M_1 & 0 \\ 0 & M_2 \end{pmatrix} \tag{3.1.11}$$

with

$$M_1 = \frac{1}{2}\left[M_s - \left[M_s^2 + 4m^2\right]^{\frac{1}{2}}\right],$$

$$M_2 = \frac{1}{2}\left[M_s + \left[M_s^2 + 4m^2\right]^{\frac{1}{2}}\right]. \tag{3.1.12}$$

We focus on a see-saw with $M_s \sim \text{keV} \gg m$, therefore

$$M_1 \simeq -\frac{m^2}{M_s}, \qquad M_2 \simeq M_s;$$
$$\sin(2\theta) \simeq \frac{2m}{M_s} \sim \left|\frac{M_1}{M_2}\right|^{\frac{1}{2}} \ll 1. \tag{3.1.13}$$

Taking $\langle H^0 \rangle \sim \langle \Phi \rangle$, the small mixing angle entails that $Y_1 \ll Y_2$ which results in self-energy corrections from the σ exchange are sub-leading as compared to those from the φ exchange. More specifically, and for a keV sterile neutrino, it follows that

$$Y_2 \sim 10^{-8} \gg Y_1; \qquad \sin(2\theta) \sim Y_1/Y_2\,. \tag{3.1.14}$$

Alternatively, we may consider a pre-determined see-saw mass matrix and set coupling constants $Y_1 = Y_2 = 0$, corresponding to a simpler extension of the SM that posits a mass matrix that originates beyond the SM.

Our goal is to obtain the dynamical aspects of sterile neutrinos in the medium, mixing angles, dispersion relations and damping rates, which determine the production rates. These are obtained directly from the solution of the equations of motion including the self-energy corrections in the medium. The one-loop self-energies require the massive neutrino propagators in the medium. For $\theta \ll 1$, the mass eigenstates $\nu_1 \sim \nu_a$ and $\nu_2 \sim \nu_s$; the active neutrino reaches equilibrium at $T \geq 1\,\text{MeV}$ via the weak interactions, whereas the sterile neutrinos are not expected to equilibrate. Therefore we assume that the mass eigenstate ν_1 is active-like, and features a Fermi-Dirac distribution function, whereas for ν_2 the propagators are the vacuum ones. Furthermore, it is possible to have a large lepton asymmetry storing in the neutrino sector, contrary to that of the charged leptons, which is forced to equal the negligible baryon asymmetry. Hence, the Fermi-Dirac distribution functions in the ν_1 propagator can include a chemical potential, which may drive MSW resonances in the medium. If there are MSW resonances, the roles of the medium eigenstates may be reversed. We will discuss these possibilities in details later. In our study we explicitly separate the fermionic and bosonic contributions to the self-energies to assess the consistency of the assumption that the eigenstate "1" is active-like.

3.2 EQUATION OF MOTION

The effective Dirac equation in the medium is derived with the methods of non-equilibrium quantum field theory described in [170, 67, 66, 59, 278, 63]. We follow the approach presented in Refs. [170, 67, 66, 59] and introduce an external Grassmann-valued source that couples linearly to the neutrino field via the Lagrangian density

$$\mathcal{L}_S = \overline{\nu}_\alpha \, \eta_\alpha + \overline{\eta}_\alpha \, \nu_\alpha \, , \tag{3.2.1}$$

whence the total lagrangian density is given by $\mathcal{L} + \mathcal{L}_S$. The external source induces an expectation value for the neutrino field which obeys the effective equation of motion with self-energy corrections from the medium [278, 63]. The equation of motion is derived by shifting the neutrino field $\nu^\pm_\alpha = \psi_\alpha + \Psi^\pm_\alpha$ with $\psi_\alpha = \langle \nu^\pm_\alpha \rangle$ and $\langle \Psi^\pm_\alpha \rangle = 0$, and obtained order by order in the perturbation theory [278, 63, 59, 170, 67, 66]. Since the self-energy corrections to the equations of motion contain the neutrino propagators, it turns out convenient to work in the mass basis, namely, $\alpha = (1, 2)$. Implementing this program up to one loop order, we find the following equation of motion for the doublet $\psi^T \equiv \big(\psi_1 \, , \, \psi_2\big)$:

$$\begin{aligned} -\eta(\vec{x}, t) \;\; &= \;\; \big(i \not{\partial} \mathbb{I} - \mathbb{M}_m \Sigma^{tad}_{sm} L\big) \, \psi(\vec{x}, t) \\ &\quad + \int d^3x' dt' \, \left[\Sigma^{ret}_{sm}(\vec{x} - \vec{x}', t - t') L + \Sigma^{ret}_{bsm}(\vec{x} - \vec{x}', t - t')\right] \psi(\vec{x}', t'), \end{aligned} \tag{3.2.2}$$

where $\mathbb{I}$ is the identity matrix, $\mathbb{M}_m = diag(M_1, M_2)$ is the mass matrix in the mass basis, $L = (1 - \gamma^5)/2$ is the left-handed chiral projection operator, Σ^{tad}_{sm} is the (local) tadpole contribution from the SM neutral current interaction as shown in Figure (3). $\Sigma^{ret}_{sm}(\vec{x} - \vec{x}', t - t')$ and $\Sigma^{ret}_{bsm}(\vec{x} - \vec{x}', t - t')$ are respectively the real-time retarded self-energies from both the SM higgs and the beyond SM scalar interactions. To simplify the notation, we will refer to beyond SM contribution by BSM thereafter. Explicit expressions of these corrections will be given in the following. Introducing the space-time Fourier transform in a spatial volume V

$$\psi(\vec{x}, t) = \frac{1}{\sqrt{V}} \sum_{\vec{k}} \int dk_0 e^{-ik_0 t i\vec{k}\cdot\vec{x}} \, \tilde{\psi}(k_0, \vec{k}), \tag{3.2.3}$$

and similarly for the self-energy kernels and the source term, the equation of motion in the mass basis becomes

$$\left[\left(\gamma_0 k_0 - \vec{\gamma}\cdot\vec{k}\right)\mathbb{I} - \mathbb{M}_m + \Sigma^{tad}_{sm}\, L + \Sigma_{sm}(k_0,\vec{k})\, L + \Sigma_{bsm}(k_0,\vec{k}\,)\right]\tilde{\psi}(k_0,\vec{k}) = -\tilde{\eta}(k_0,\vec{k})\ . \quad (3.2.4)$$

$\Sigma_{sm}(k_0,\vec{k})$ and $\Sigma_{bsm}(k_0,\vec{k})$ are the corresponding Fourier transform of the retarded self-energy corrections of $\Sigma^{ret}_{sm}(\vec{x}-\vec{x}',t-t')$ and $\Sigma^{ret}_{bsm}(\vec{x}-\vec{x}',t-t')$, respectively. Except for the tadpole term, they feature a dispersive representation

$$\Sigma(k_0,k) = \frac{1}{\pi}\int_{-\infty}^{\infty} d\omega\ \frac{\mathrm{Im}\Sigma(\omega,\vec{k}\,)}{\omega - k_0 - i\,0^+}. \quad (3.2.5)$$

3.2.1 One-Loop Self-Energy

We focus on the temperature region $M_{Z,\ W,\ \sigma,\ \varphi} \gtrsim T$, in which using the unperturbed thermal propagators for the scalar and vector bosons is valid [240, 238, 239, 83, 82, 128]. In subsection (3.4.4), we show that perturbation theory is valid for $k \gtrsim \alpha_w T$ and $M_{Z,\ W,\ \sigma,\ \varphi} \gtrsim T$; furthermore, for $k \ll M_W$ our results reproduce those found in the literature in the case of $T \ll M_W$ [230, 171] and the perturbative expansion is reliable for $M_W \gtrsim 2T$.

The SM charged and neutral current contributions to the self-energy in the mass basis are depicted in Figure 3. The Latin indices $\{i,j,k\} = \{1,2\}$ refer to the mass basis fields, and the label f in the intermediate fermion propagator of the charged current diagram in Figure 3 refers to the charged lepton associated with the active neutrino. The contributions from scalar exchange in the mass basis are depicted in Figure 4.

SM neutral currents: The tadpole contribution in the mass basis is given by

$$\Sigma^{tad}_{sm} = \Sigma^t\ \ U^{-1}(\theta)\begin{pmatrix} 1 & 0 \\ 0 & 0 \end{pmatrix} U(\theta)\ , \quad (3.2.6)$$

where[1]

$$\Sigma^t = -\gamma^0\frac{g^2}{4M_W^2}\int\frac{d^3q}{(2\pi)^3}\left(n_\nu - \overline{n}_\nu\right) = -\gamma^0\frac{g^2T^3}{24M_W^2}\,\xi\left[1+\frac{\xi^2}{\pi^2}\right], \qquad \xi = \frac{\mu}{T}\,. \quad (3.2.7)$$

[1] This expression corrects a typographic error in Refs. [170, 67, 66].

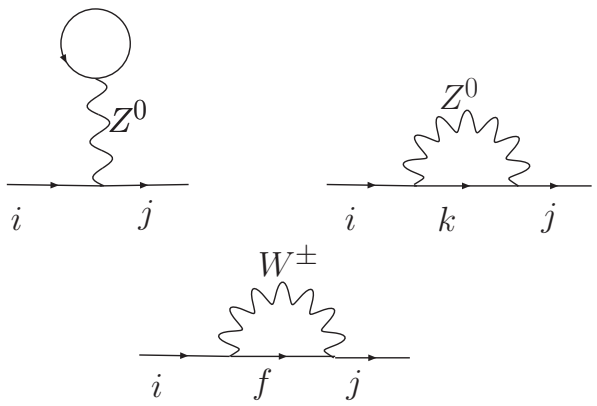

Figure 3: (sm) contributions to the self-energy Σ_{sm}. The indices $\{i, j, k\} = \{1, 2\}$ correspond to mass eigenstates, the index f for the intermediate fermion line in the charged current self-energy refers to the charged lepton associated with the active neutrino.

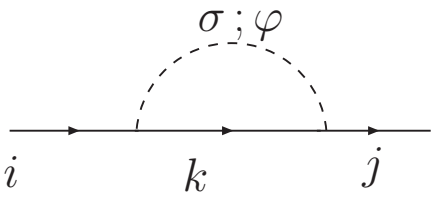

Figure 4: (bsm) contributions to the self-energy Σ_{bsm}. The indices $\{i, j, k\} = \{1, 2\}$ corresponding to mass eigenstates. The dashed line is a scalar propagator either for σ or φ

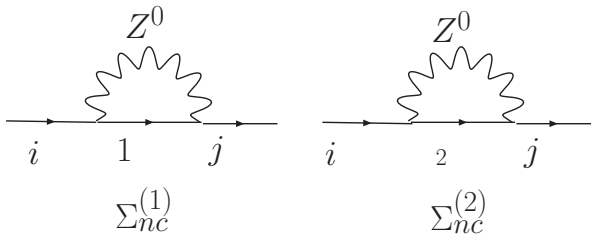

Figure 5: Neutral current contribution to the one-loop retarded self-energy Σ_{sm}. The indices $\{i, j\} = \{1, 2\}$ and the indices 1 and 2 denote the corresponding mass eigenstate in the intermediate state.

In this expression $n_\nu, \overline{n}_\nu$ are the Fermi-Dirac distribution functions for neutrinos and antineutrinos respectively. We have neglected the contribution from the asymmetry of the charged lepton and quark sectors since they are proportional to the negligible baryon asymmetry, but we allow for a lepton asymmetry stored in the neutrino sector. A recent analysis [261] from the latest WMAP and BBN data suggests that $|\xi| \lesssim 10^{-2}$. The neutral current diagrams that contribute to the one-loop self energy feature two different terms corresponding to the intermediate neutrino line being either ν_1 or ν_2. As argued above, for small mixing angles $\nu_1 \sim \nu_a$ and weak interactions equilibrate these mass eigenstates with the medium, therefore their finite temperature propagator features the Fermi-Dirac distribution function. However, $\nu_2 \sim \nu_s$ will not equilibrate with the medium since their coupling to the environmental degrees of freedom is suppressed by at least two powers of the small mixing angle, therefore ν_2 features a vacuum propagator. The one loop diagrams are shown in Figure 5, where the superscripts (1) and (2) are used to specify the intermediate neutrino propagator ν_1 and ν_2 respectively. In the mass basis we find for the neutral current contributions as

$$\Sigma_{nc}(k_0, \vec{k}) = \left[\cos^2\theta\, \Sigma_{nc}^{(1)}(k_0, \vec{k}) + \sin^2\theta\, \Sigma_{nc}^{(2)}(k_0, \vec{k})\right] U^{-1}(\theta) \begin{pmatrix} 1 & 0 \\ 0 & 0 \end{pmatrix} U(\theta)\ . \tag{3.2.8}$$

SM charged currents: the charged current one-loop self energy is shown in Figure 3, we find for its contribution in the mass basis

$$\Sigma_{cc}(k_0, \vec{k}) = \Sigma_{cc,sm}(k_0, \vec{k})\, U^{-1}(\theta) \begin{pmatrix} 1 & 0 \\ 0 & 0 \end{pmatrix} U(\theta)\ , \tag{3.2.9}$$

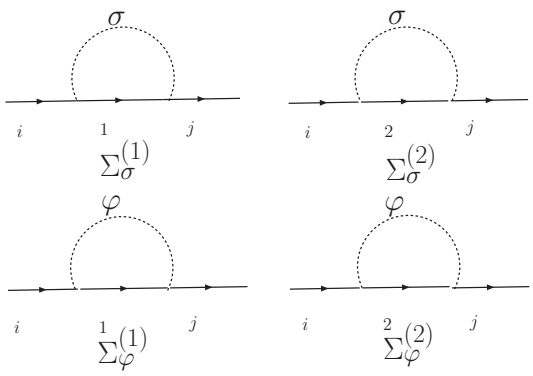

Figure 6: Scalar exchange contributions to the one-loop self-energy Σ_{bsm}. The indices $\{i, j\} = \{1, 2\}$ and the indices 1 and 2 denote the corresponding mass eigenstate in the intermediate state.

where $\Sigma_{cc,sm}(k_0, \vec{k})$ is the usual standard model one-loop self-energy in thermal equilibrium.

BSM scalar exchange: The scalar exchange contributions to the self-energy are shown in Figure 6. For $\sin^2\theta \ll 1$, we find

$$\begin{aligned}\Sigma_{bsm}(k_0,\vec{k}) &= \left[\cos^2\theta\,\Sigma_\sigma^{(1)}(k_0,\vec{k}) + \sin^2\theta\Sigma_\varphi^{(1)}(k_0,\vec{k}) + \cos^2\theta\Sigma_\varphi^{(2)}(k_0,\vec{k})\right] U^{-1}(\theta)\begin{pmatrix}0&0\\0&1\end{pmatrix}U(\theta)\\ &\quad + \cos^2\theta\,\Sigma_\sigma^{(2)}(k_0,\vec{k})\,U^{-1}(\theta)\begin{pmatrix}1&0\\0&0\end{pmatrix}U(\theta)\ . \end{aligned} \tag{3.2.10}$$

Summary of self-energies in the flavor basis: The structure of the self-energies to the leading order in $\sin^2\theta$ shown in (3.2.6-3.2.10) indicates that they are diagonal in the flavor basis, where the total self-energy is given by

$$\Sigma(k_0,\vec{k}) = \begin{pmatrix}\Sigma_{aa}(k_0,\vec{k}) & 0\\ 0 & \Sigma_{ss}(k_0,\vec{k})\end{pmatrix}\ , \tag{3.2.11}$$

where

$$\Sigma_{aa}(k_0,\vec{k}) = \left[\Sigma^t + \cos^2\theta\,\Sigma_{nc}^{(1)}(k_0,\vec{k}) + \sin^2\theta\,\Sigma_{nc}^{(2)}(k_0,\vec{k}) + \Sigma_{cc,sm}(k_0,\vec{k})\right] L + \cos^2\theta\,\Sigma_\sigma^{(2)}(k_0,\vec{k}), \tag{3.2.12}$$

$$\Sigma_{ss}(k_0,k) = \cos^2\theta\,\Sigma_\sigma^{(1)}(k_0,\vec{k}) + \sin^2\theta\Sigma_\varphi^{(1)}(k_0,\vec{k}) + \cos^2\theta\Sigma_\varphi^{(2)}(k_0,\vec{k})\ . \tag{3.2.13}$$

Since in the SM contributions we have explicitly factored out the left-handed projector L, the remaining contribution to Σ_{nc} and Σ_{cc} are those of a vector-like theory. The BSM contributions feature both chiralities for a Dirac mass term for the sterile neutrino, a left-handed Majorana mass term can be obtained by neglecting the right-handed contribution. We consider the regime $T \gg \{M_1, M_2, m_f\}$ and $\{k_0, k\} \gg \{M_1, M_2, m_f\}$, where m_f stands for the charged lepton mass, therefore we can safely neglect the mass terms and consider the propagators of massless fermionic fields. In this regime, the general form of the SM contributed self-energies with vector boson exchange, either charged or neutral currents is written in dispersive form as in Eq. (3.2.5) with [170, 67, 66, 59]

$$\begin{aligned} Im\Sigma_{sm}(\omega,\vec{k}) &= \pi g_{sm}^2 \int \frac{d^3q}{(2\pi)^3} \int dp_0\, dq_0 \delta(\omega - p_0 - q_0)\Big[1 - n_F(p_0) + N_B(q_0)\Big] \\ &\qquad \gamma^\mu \rho_F(p_0,\vec{p})\rho_B(q_0,\vec{q})\gamma^\nu\, P_{\mu\nu}(q_0,\vec{q}), \end{aligned} \tag{3.2.14}$$

where F stands for the fermionic species in the intermediate state. For ν_1 and charged lepton n_F is the Fermi-Dirac distribution function, whereas for ν_2 it is $n_F = 0$ since the "sterile" neutrino does not thermalize with the medium. For the BSM contributions, the general form for scalar exchange is

$$Im\Sigma_{bsm}(\omega,\vec{k}) = \pi Y^2 \int \frac{d^3q}{(2\pi)^3} \int dp_0\, dq_0 \delta(\omega - p_0 - q_0)\Big[1 - n_F(p_0) + N_B(q_0)\Big]\rho_F(p_0,\vec{p})\rho_B(q_0,\vec{q})\,. \tag{3.2.15}$$

where

$$g_{sm} = \begin{cases} \dfrac{g}{\sqrt{2}} & \text{Charge Current} \\ \dfrac{g}{2\cos(\theta_w)} & \text{Neutral Current} \end{cases} \tag{3.2.16}$$

and $Y = \{Y_1, Y_2\}$ for σ and φ exchange respectively. The spectral densities are respectively (for massless fermions):

$$\rho_F(p_0,\vec{p}) = \frac{1}{2}\left(\gamma^0 - \vec{\gamma}\cdot\frac{\vec{p}}{p}\right)\delta(p_0 - p) + \frac{1}{2}\left(\gamma^0 + \vec{\gamma}\cdot\frac{\vec{p}}{p}\right)\delta(p_0 + p)\,, \tag{3.2.17}$$

$$\rho_B(q_0,\vec{q}) = \frac{1}{2W_q}\big[\delta(q_0 - W_q) - \delta(q_0 + W_q)\big], \quad W_q = \sqrt{q^2 + M^2}. \tag{3.2.18}$$

The projection operator

$$P_{\mu\nu}(q_0,\vec{q}) = -\left[g_{\mu\nu} - \frac{q_\mu q_\nu}{M_{Z,W}^2}\right], \quad q^\mu = (q^0,\vec{q}) \tag{3.2.19}$$

and

$$\begin{aligned} n_F(p_0) &= \frac{1}{e^{(p_0-\mu)/T}+1}, \quad \overline{n}_F(p_0) = 1 - n_\nu(-p_0); \\ N_B(q_0) &= \frac{1}{e^{q_0/T}-1}. \end{aligned} \tag{3.2.20}$$

We have allowed a chemical potential only for $\nu_1 \sim \nu_a$ to include the possibility of a lepton asymmetry in the active neutrino sector.

In the expressions above, the masses for the scalars or vector bosons are $M_{\{\sigma,\ \varphi\}}$ and $M_{\{Z,\ W\}}$ as appropriate for each contribution. All the self-energies share the general form

$$\Sigma(k_0, \vec{k}) \equiv \gamma^0\, A(k_0, k) - \vec{\gamma}\cdot\widehat{\mathbf{k}}\; B(k_0, k)\,, \tag{3.2.21}$$

the detailed expressions for the imaginary parts of the SM and BSM contributions are given in the Appendices. In particular, for the neutral current tadpole $B(k_0, k) = 0$ and $A(k_0, k)$ can be recognized from Eq. (3.2.7). Combining (3.2.11) with this form we write the self-energy matrix in the flavor basis as

$$\begin{aligned} \Sigma^{tad}_{sm}\, L + \Sigma_{sm}(k_0, \vec{k})\, L + \Sigma_{bsm}(k_0, \vec{k}\,) &= \left[\gamma^0\ \mathbb{A}_L(k_0, k) - \vec{\gamma}\cdot\widehat{\mathbf{k}}\ \mathbb{B}_L(k_0, k)\right] L \\ &+ \left[\gamma^0\ \mathbb{A}_R(k_0, k) - \vec{\gamma}\cdot\widehat{\mathbf{k}}\ \mathbb{B}_R(k_0, k)\right] R\,. \end{aligned} \tag{3.2.22}$$

In the flavor basis the matrices $\mathbb{A}$ and $\mathbb{B}$ are of the form

$$\mathbb{A}(k_0, k) = \begin{pmatrix} A_{aa}(k_0, k) & 0 \\ 0 & A_{ss}(k_0, k) \end{pmatrix}, \quad \mathbb{B}(k_0, k) = \begin{pmatrix} B_{aa}(k_0, k) & 0 \\ 0 & B_{ss}(k_0, k) \end{pmatrix}, \tag{3.2.23}$$

where the matrix elements are obtained from the expressions (3.2.12) and (3.2.13). The equations of motion for the left (L) and right (R) handed components are obtained by multiplying the equation of motion (3.2.4) on the left by the projectors R and L respectively.

It proves convenient at this stage to separate the Dirac spinors into the left ψ_L and right ψ_R handed components and to expand them into helicity eigenstates [170, 67, 66], namely

$$\psi_L = \sum_{h=\pm 1} v^h \otimes \varphi^h, \qquad \varphi^h = \begin{pmatrix} \varphi_a^h \\ \varphi_s^h \end{pmatrix}, \tag{3.2.24}$$

and

$$\psi_R = \sum_{h=\pm 1} v^h \otimes \zeta^h, \qquad \zeta^h = \begin{pmatrix} \zeta_a^h \\ \zeta_s^h \end{pmatrix}, \tag{3.2.25}$$

where the left φ and right ζ handed doublets are written in the flavor basis, and v^h are eigenstates of the helicity operator

$$\widehat{h}(\widehat{\mathbf{k}}) = \gamma^0(\vec{\gamma}\cdot\widehat{\mathbf{k}})\,\gamma^5 = \vec{\sigma}\cdot\widehat{\mathbf{k}} \begin{pmatrix} \mathbb{1} & 0 \\ 0 & \mathbb{1} \end{pmatrix} \tag{3.2.26}$$

namely,

$$\vec{\sigma}\cdot\widehat{\mathbf{k}}\; v^h = h\; v^h, \tag{3.2.27}$$

with $h = \pm 1$. To leading order in weak and Yukawa couplings, and neglecting a commutator $[\mathbb{M}, \Sigma]$ because it is higher order in these couplings, we find in the flavor basis for both the left and right-handed component doublets

$$\big[(k_0^2 - k^2)\mathbb{I} + \big(k_0 - hk\big)\big(\mathbb{A}_L + h\mathbb{B}_L\big) + \big(k_0 + hk\big)\big(\mathbb{A}_R - h\mathbb{B}_R\big) - \mathbb{M}^2\big] \begin{pmatrix} \varphi^h \\ \zeta^h \end{pmatrix} = \begin{pmatrix} I_L^h \\ I_R^h \end{pmatrix}, \tag{3.2.28}$$

where $\mathbb{M}$ is the mass matrix in the flavor basis and the inhomogeneities in these equations are obtained by projection and using the corresponding equations, we need not specify them as they are no longer used in our study. In absence of interactions, for the left-handed component, a positive energy solution corresponds to $h = -1$ and a negative energy solution to $h = +1$ with the opposite assignment for the right-handed component. In the flavor basis

$$\mathbb{M}^2 = \overline{M}^2\mathbb{I} + \frac{\delta M^2}{2} \begin{pmatrix} -\cos(2\theta) & \sin(2\theta) \\ \sin(2\theta) & \cos(2\theta) \end{pmatrix}. \tag{3.2.29}$$

where

$$\overline{M}^2 \equiv \frac{1}{2}\big(M_1^2 + M_2^2\big) \;\; ; \;\; \delta M^2 \equiv M_2^2 - M_1^2\,, \tag{3.2.30}$$

and $M_{\{1,\,2\}}$ are given by Eq. (3.1.12). It proves convenient to define the combinations

$$\begin{aligned} S_h(k_0,k) &= (k_0+hk)\Big[\big(\mathbb{A}_R-h\mathbb{B}_R\big)_{aa}+\big(\mathbb{A}_R-h\mathbb{B}_R\big)_{ss}\Big] \\ &+ (k_0-hk)\Big[\big(\mathbb{A}_L+h\mathbb{B}_L\big)_{aa}+\big(\mathbb{A}_L+h\mathbb{B}_L\big)_{ss}\Big]\,, \end{aligned} \tag{3.2.31}$$

and

$$\begin{aligned} \Delta_h(k_0,k) &= \frac{(k_0+hk)}{\delta M^2}\Big[\big(\mathbb{A}_R-h\mathbb{B}_R\big)_{aa}-\big(\mathbb{A}_R-h\mathbb{B}_R\big)_{ss}\Big] \\ &+ \frac{(k_0-hk)}{\delta M^2}\Big[\big(\mathbb{A}_L+h\mathbb{B}_L\big)_{aa}-\big(\mathbb{A}_L+h\mathbb{B}_L\big)_{ss}\Big]\,, \end{aligned} \tag{3.2.32}$$

where we have suppressed the arguments. The equation of motion (3.2.28) can now be written as

$$\mathbb{G}_h^{-1}(k_0,k)\begin{pmatrix}\varphi^h\\ \zeta^h\end{pmatrix}=\begin{pmatrix}I_L^h\\ I_R^h\end{pmatrix}, \tag{3.2.33}$$

where the inverse propagator is given by

$$\mathbb{G}_h^{-1}(k_0,k)=\left(k_0^2-k^2+\frac{1}{2}S_h(k_0,k)-\overline{M}^{\,2}\right)\mathbb{I}-\frac{1}{2}\delta M^2\rho_h(k_0,k)\begin{pmatrix}-C_h(k_0,k) & D_h(k_0,k)\\ D_h(k_0,k) & C_h(k_0,k)\end{pmatrix}, \tag{3.2.34}$$

where

$$\rho_h(k_0,k)=\left[\Big(\cos(2\theta)+\Delta_h(k_0,k)\Big)^2+\sin^2(2\theta)\right]^{\frac{1}{2}} \tag{3.2.35}$$

and

$$C_h(k_0,k) = \frac{\Big(\cos(2\theta)+\Delta_h(k_0,k)\Big)}{\rho_h(k_0,k)}\,, \tag{3.2.36}$$

$$D_h(k_0,k) = \frac{\sin(2\theta)}{\rho_h(k_0,k)}\,. \tag{3.2.37}$$

We note that if $\Delta_h(k_0,k)$ were real, then $C_h(k_0,k)=\cos(2\theta_m^h(k_0,k))$ and $D_h(k_0,k)=\sin(2\theta_m^h(k_0,k))$ with $\theta_m^h(k_0,k)$ the mixing angle in the medium for the different helicity projections and as a function of frequency and momentum.

3.2.2 Propagator: complex poles and propagating modes in the medium

From (3.2.34) we read off the propagator projected onto helicity eigenstates

$$\mathbb{G}_h(k_0,k) = \frac{\mathbb{I}+\mathbb{T}_h(k_0,k)}{2\Big(\alpha_h(k_0,k)-\beta_h(k_0,k)\Big)} + \frac{\mathbb{I}-\mathbb{T}_h(k_0,k)}{2\Big(\alpha_h(k_0,k)+\beta_h(k_0,k)\Big)} \ , \tag{3.2.38}$$

where

$$\mathbb{T}_h(k_0,k) = \begin{pmatrix} -C_h(k_0,k) & D_h(k_0,k) \\ D_h(k_0,k) & C_h(k_0,k) \end{pmatrix} \ , \tag{3.2.39}$$

$$\alpha_h(k_0,k) = k_0^2 - k^2 + \frac{1}{2}S_h(k_0,k) - \overline{M}^2 \ , \tag{3.2.40}$$

$$\beta_h(k_0,k) = \frac{1}{2}\delta M^2 \rho_h(k_0,k) \ . \tag{3.2.41}$$

If $\Delta_h(k_0,k)$ given by Eq. (3.2.32) was real, the propagator (3.2.38) would be diagonalized by the unitary transformation

$$U_h(\theta_m^h(k_0,k)) = \begin{pmatrix} \cos(\theta_m^h(k_0,k)) & \sin(\theta_m^h(k_0,k)) \\ -\sin(\theta_m^h(k_0,k)) & \cos(\theta_m^h(k_0,k)) \end{pmatrix} \ , \tag{3.2.42}$$

leading to

$$U^{-1}(\theta_m)\,\mathbb{G}(k_0,k)U(\theta_m) = \begin{pmatrix} \dfrac{1}{\alpha(k_0,k)+\beta(k_0,k)} & 0 \\ 0 & \dfrac{1}{\alpha(k_0,k)-\beta(k_0,k)} \end{pmatrix} \ , \tag{3.2.43}$$

where we have suppressed the helicity argument for simplicity. However, because $\Delta_h(k_0,k)$ features an imaginary part determined by the absorptive part of the self-energies, there is no unitary transformation that diagonalizes the propagator. However, since the imaginary part is perturbatively small, the expression (3.2.43) clearly indicates that the pole for $\alpha=\beta$ corresponds to the mass eigenstate 2, namely a sterile-like neutrino state, and the pole for $\alpha=-\beta$ corresponds to the mass eigenstate 1, namely an active-like state.

We note that in absence of interactions, namely $S_h=0,\ \Delta_h=0$, it follows that

$$\alpha+\beta = k_0^2-k^2-M_1^2 \ , \tag{3.2.44}$$

$$\alpha-\beta = k_0^2-k^2-M_2^2 \ . \tag{3.2.45}$$

The propagating eigenstates in the medium are determined by the complex poles of the propagator (3.2.38), which again correspond to $\alpha_h(k_0,k) = \pm\beta_h(k_0,k)$. Before we analyze the complex poles, it proves convenient to separate the real and imaginary parts of α and β. For this purpose and to simplify notation, we suppress the label h and the arguments $\{k_0,\ k\}$ in these quantities, and we write

$$S = S_R + iS_I, \quad \Delta = \Delta_R + i\Delta_I \ , \tag{3.2.46}$$

where the subscripts $\{R,\ I\}$ stand for real and imaginary parts respectively. Furthermore, we define the mixing angles in the medium solely in terms of the real parts of the self-energy (index of refraction), namely

$$\cos(2\theta_m) = \frac{\cos(2\theta) + \Delta_R}{\rho_0}, \quad \sin(2\theta_m) = \frac{\sin(2\theta)}{\rho_0} \,, \tag{3.2.47}$$

where

$$\rho_0 = \left[\Big(\cos(2\theta) + \Delta_R \Big)^2 + \sin^2(2\theta) \right]^{\frac{1}{2}} . \tag{3.2.48}$$

An MSW resonance occurs whenever $\cos(2\theta_m) = 0$ [283, 218, 189, 222, 132], namely when

$$\Delta_R = -\cos(2\theta) \,. \tag{3.2.49}$$

We emphasize that both the mixing angle in the medium θ_m and ρ_0 depend on the helicity, k_0 and k. In terms of these quantities, we find

$$\beta = \frac{\delta M^2}{2} \rho_0 \, r \left[\cos(\phi) + i \sin(\phi) \right] \equiv \beta_R + i\beta_I \ , \tag{3.2.50}$$

where

$$r = \left[\big(1 - \tilde{\gamma}^2\big)^2 + \big(2\tilde{\gamma}\cos(2\theta_m)\big)^2 \right]^{\frac{1}{4}}, \quad \tilde{\gamma} = \frac{\Delta_I}{\rho_0} \ , \tag{3.2.51}$$

and

$$\begin{aligned} \phi \ = \ & \mathrm{sign}\big(\tilde{\gamma}\cos(2\theta_m)\big) \\ & \left\{ \frac{1}{2}\mathrm{arctg}\left| \frac{2\tilde{\gamma}\cos(2\theta_m)}{1-\tilde{\gamma}^2} \right| \Theta(1-\tilde{\gamma}^2) + \left(\frac{\pi}{2} - \frac{1}{2}\mathrm{arctg}\left| \frac{2\tilde{\gamma}\cos(2\theta_m)}{1-\tilde{\gamma}^2} \right| \right) \Theta(\tilde{\gamma}^2 - 1) \right\} . \end{aligned} \tag{3.2.52}$$

This form is similar to that obtained in a model of oscillations and damping with mixed neutrinos studied in Ref. [60], and suggests two distinct situations: a *weak damping* case for $|\tilde{\gamma}| < 1$ and a *strong damping* case for $|\tilde{\gamma}| > 1$. These cases will be analyzed below.

Zeroes of $\alpha+\beta$: We are concerned with the ultrarelativistic limit $k \gg M_2^2 \gg M_1^2$. Just as in the usual case [189, 222, 132], it is convenient to introduce the average or reference frequency

$$\overline{\omega}(k) = \sqrt{k^2 + \overline{M}^2}\,. \tag{3.2.53}$$

The poles are near $\overline{\omega}(k)$, therefore write

$$k_0 = \overline{\omega}(k) + \left(k_0 - \overline{\omega}(k)\right), \tag{3.2.54}$$

keeping only the linear term in $\left(k_0 - \overline{\omega}(k)\right)$, we find

$$\alpha + \beta \sim 2\overline{\omega}(k)\Big[k_0 - \Omega_1(k) + i\Gamma_1(k)\Big] \tag{3.2.55}$$

with

$$\Omega_1(k) = \overline{\omega}(k) - \frac{1}{4\overline{\omega}(k)}\Big[S_R + \delta M^2\rho_0 r\cos(\phi)\Big]_{k_0=\overline{\omega}(k)}\,, \tag{3.2.56}$$

$$\Gamma_1(k) = \frac{1}{4\overline{\omega}(k)}\Big[S_I + \delta M^2\rho_0 r\sin(\phi)\Big]_{k_0=\overline{\omega}(k)}\,. \tag{3.2.57}$$

Zeroes of $\alpha-\beta$: Proceeding in the same manner, we find

$$\alpha - \beta \sim 2\overline{\omega}(k)\Big[k_0 - \Omega_2(k) + i\Gamma_2(k)\Big] \tag{3.2.58}$$

with

$$\Omega_2(k) = \overline{\omega}(k) - \frac{1}{4\overline{\omega}(k)}\Big[S_R - \delta M^2\rho_0 r\cos(\phi)\Big]_{k_0=\overline{\omega}(k)}\,, \tag{3.2.59}$$

$$\Gamma_2(k) = \frac{1}{4\overline{\omega}(k)}\Big[S_I - \delta M^2\rho_0 r\sin(\phi)\Big]_{k_0=\overline{\omega}(k)}\,. \tag{3.2.60}$$

From (3.2.55) and (3.2.58), it is clear that the propagator in the medium features two Breit-Wigner complex poles corresponding to the two propagating modes in the medium. In the expressions above we have only focused on the positive energy modes. The expressions for the negative energy modes may be obtained from the following relations which are consequences

of the imaginary parts of the self-energies and the dispersive representation valid both for scalar and vector boson exchange (3.2.5),

$$\begin{aligned} \mathrm{Im}\mathbb{A}(-k_0,k;\mu) &= \mathrm{Im}\mathbb{A}(k_0,k;-\mu), \quad \mathrm{Re}\mathbb{A}(-k_0,k;\mu) = -\mathrm{Re}\mathbb{A}(k_0,k;-\mu)\ , \quad (3.2.61) \\ \mathrm{Im}\mathbb{B}(-k_0,k;\mu) &= -\mathrm{Im}\mathbb{B}(k_0,k;-\mu), \quad \mathrm{Re}\mathbb{B}(-k_0,k;\mu) = \mathrm{Re}\mathbb{B}(k_0,k;-\mu)\,. \quad (3.2.62) \end{aligned}$$

These properties can be read-off the explicit expressions for the imaginary parts of the self-energies given in the appendix equations (A.1.1-A.1.3) for the standard model contributions and equations (A.2.1-A.2.3) for the scalar exchange contributions. The matrices $\mathbb{A}$ are extracted from the coefficient of γ^0 and $\mathbb{B}$ from the coefficients of $\vec{\gamma}\cdot\hat{k}$ in the self-energies respectively. The relations for the real parts follow from the dispersive representation (3.2.5).

In what follows we use the ultrarelativistic approximation

$$\overline{\omega}(k) \simeq k + \frac{\overline{M}^2}{2k}\ . \tag{3.2.63}$$

In the limit of interest $k/T \lesssim 1$ with $M_1 \ll M_2 \sim M_s \sim \mathcal{O}(\mathrm{keV})$, the region $k < T \sim \mathcal{O}(100\ \mathrm{GeV})$ corresponds to a wide window in which the ultrarelativistic approximation is reliable. We note that the difference in the real part of the pole position in the ultrarelativistic limit becomes

$$\Omega_2(k) - \Omega_1(k) \simeq \frac{\delta M^2}{2k}\rho_0 r\cos(\phi)\,. \tag{3.2.64}$$

From the expression (3.2.52) for $|\tilde{\gamma}| > 1$, it follows that when an MSW resonance occurs, namely for $\theta_m = \pi/4$ resulting in $\cos(\phi) = 0$ and the real part of the poles become degenerate. This is in striking contrast with the quantum mechanical description of mixed neutrinos where no level crossing, or complete degeneracy, can occur. Indeed the degeneracy is a consequence of the fact that the self-energy is complex and only occurs when damping is strong in the sense that $|\tilde{\gamma}| > 1$. The degeneracy near an MSW resonance for strong damping will necessarily result in a breakdown of adiabaticity during cosmological evolution. We analyze below the conditions required for this phenomenon to occur.

Furthermore, as discussed in Refs. [237, 61], decoupling and freeze-out of sterile neutrinos of neutrinos produced via scalar decay occurs near the electroweak scale, and it will be seen

consistently that vector boson decay yields a production rate with a similar structure as for scalar decay therefore a similar range of temperatures in which sterile neutrino production by this mechanism is effective.

Perturbation theory is reliable when the change in the dispersion relations, namely positions of the poles in the propagators, is small. In the relativistic limit, the bare poles correspond to $k_0 = k$ for positive energy particles, therefore perturbation theory is valid for $k \gg \{(\Omega_{\{1,\,2\}} - k),\ \Gamma_{\{1,2\}}\}$, namely $k \gg \Sigma(k,k)$ where Σ is any of the self-energies. In the next section we obtain explicitly the self energies and in section (3.4.4) we assess the regime of validity of the perturbative expansion.

3.2.3 Helicity dependence: right-handed sterile neutrinos and standard model interactions

We have purposely kept the general form of the self-energies and propagators in terms of the helicity projections $h = \pm 1$. In the non-interacting massless case, positive energy left-handed particles correspond to $h = -1$ and negative energy left-handed correspond to $h = 1$, with the opposite assignment for right-handed particles. For the massive but ultrarelativistic case the mass term yields corrections to the handedness-helicity assignment of $\mathcal{O}(M^2/k^2)$.

$\underline{\mathbf{h = -1}}$: Neglecting sub-leading terms of $\mathcal{O}(\overline{M}^{\,2}/k^2)$ that multiply BSM right-handed contributions in the ultrarelativistic limit, we obtain

$$S(k) = 2k\Big[\big(\mathbb{A}_L - \mathbb{B}_L\big)_{aa} + \big(\mathbb{A}_L - \mathbb{B}_L\big)_{ss}\Big] , \tag{3.2.65}$$

$$\Delta(k) = \frac{2k}{\delta M^2}\Big[\big(\mathbb{A}_L - \mathbb{B}_L\big)_{aa} - \big(\mathbb{A}_L - \mathbb{B}_L\big)_{ss}\Big] . \tag{3.2.66}$$

$\underline{\mathbf{h = 1}}$: In this case the corrections of $\mathcal{O}(\overline{M}^{\,2}/k^2)$ multiply SM left-handed contributions, which may be of the same order of the BSM right-handed contributions. We find,

$$S(k) = 2k\Big[\big(\mathbb{A}_R - \mathbb{B}_R\big)_{aa} + \big(\mathbb{A}_R - \mathbb{B}_R\big)_{ss} + \frac{\overline{M}^{\,2}}{4k^2}\big(\mathbb{A}_L + \mathbb{B}_L\big)_{aa}\Big] , \tag{3.2.67}$$

$$\Delta(k) = \frac{2k}{\delta M^2}\Big[\big(\mathbb{A}_R - \mathbb{B}_R\big)_{aa} - \big(\mathbb{A}_R - \mathbb{B}_R\big)_{ss} + \frac{\overline{M}^{\,2}}{4k^2}\big(\mathbb{A}_L + \mathbb{B}_L\big)_{aa}\Big] . \tag{3.2.68}$$

The terms proportional to $\overline{M}^2/4k^2$ only receive contribution from the SM self-energies, whereas the right-handed components only originate in the contributions beyond the standard model which are suppressed by much smaller Yukawa couplings. However the last contribution in (3.2.68) from SM interactions may be of the same order as the BSM contributions for a relevant range of k. To see this, note that $\{\mathbb{A}_R, \mathbb{B}_R\} \sim Y_2^2 \sim 10^{-16}$, whereas $\{\mathbb{A}_L, \mathbb{B}_L\} \sim g^2 \sim 0.4$ therefore with $\overline{M} \sim$ keV and $k \lesssim 100\,\mathrm{GeV}$, it is clear that both BSM and SM contributions are of the same order. The point of maintaining the helicity dependence throughout is that for the case of sterile neutrinos, namely the propagating modes "2" in the medium, the exchange of standard model vector bosons yields a contribution to the positive helicity and positive energy components, namely the right-handed component, which could be of the same order of the BSM contributions for small k which is a region of interest for sterile neutrino production.

3.3 REAL PARTS: MIXING ANGLES AND MSW RESONANCES

The dispersion relations, namely the real parts of the poles, and the mixing angles in the medium are determined by the real parts of the self-energy, or the "index of refraction". Whereas the neutral current tadpole contribution (3.2.7) is real, the real part of the other contributions is obtained from the dispersive form (3.2.5), which is

$$\mathrm{Re}\Sigma(k_0,k) = \frac{1}{\pi}\int_{-\infty}^{\infty} d\omega\; \mathcal{P}\left(\frac{\mathrm{Im}\Sigma(\omega,\vec{k}\,)}{\omega - k_0}\right) . \tag{3.3.1}$$

In general, the real part must be obtained numerically and is a function of three parameters $k_0,\ k$ and μ, which makes its exploration a daunting numerical task. However, progress can be made by focusing on the "on-shell" contribution, namely setting $k_0 \simeq k$, and neglecting the dependence on μ, which is warranted in the whole region of $\{k,\ T\}$ of interest but for $\{\frac{k}{T}, \frac{|\mu|}{T}\} \ll M/T$, in which case we provide below an accurate approximate form. In obtaining the real parts we consider only the finite temperature contribution, because the zero temperature part is absorbed in the renormalization of the parameters in the Lagrangian.

BSM contributed scalars: For the real part of the scalar self-energy we find for $k_0 = k,\ \mu = 0$:

$$\mathrm{Re}\Sigma_{bsm} = \frac{Y^2 T}{16\pi^2}\left\{\gamma^0\left[Af\left(\frac{k}{T},\frac{M}{T}\right) + Ab\left(\frac{k}{T},\frac{M}{T}\right)\right] - \vec{\gamma}\cdot\widehat{\mathbf{k}}\left[Bf\left(\frac{k}{T},\frac{M}{T}\right) + Bb\left(\frac{k}{T},\frac{M}{T}\right)\right]\right\}, \tag{3.3.2}$$

where $Af,\ Bf$ and $Ab,\ Bb$ are the fermionic and bosonic contributions respectively and $Y = Y_{\{1,\ 2\}}$ for σ and φ exchange. Figure 7 shows $Af,\ Bf$ and $Ab,\ Bb$ for $M/T = \{1, 2, 3\}$ as a function of k/T.

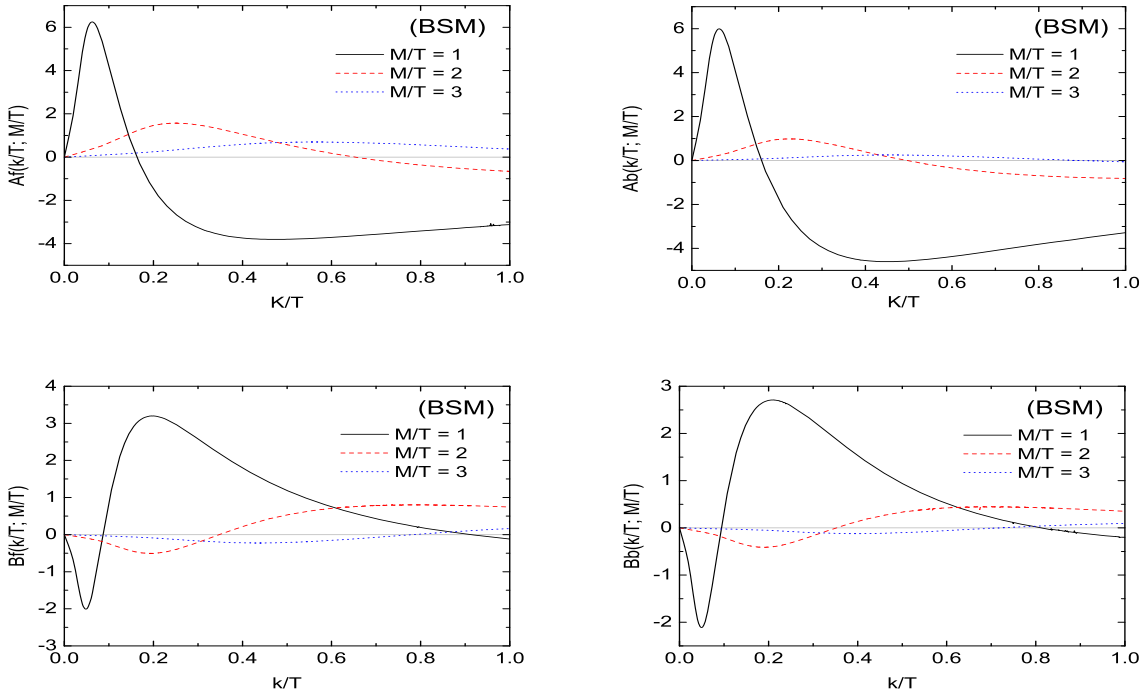

Figure 7: The functions $Af\left(\frac{k}{T},\ \frac{M}{T}\right)$, $Ab\left(\frac{k}{T},\frac{M}{T}\right)$, $Bf\left(\frac{k}{T},\frac{M}{T}\right)$ and $Bb\left(\frac{k}{T},\frac{M}{T}\right)$ with respect to k/T for $M/T = \{1, 2, 3\}$ in the expression of $\mathrm{Re}\Sigma_{bsm}$.

For $\Sigma^{(2)}_{\{\sigma,\ \varphi\}}$, the intermediate fermion line corresponds to a sterile-like neutrino, therefore for these contributions we must set $Af = 0, Bf = 0$, under the assumption that the sterile neutrino population can be neglected and the propagator for the internal line is the vacuum

one. For the mixing angle, the relevant contribution is $(A-B)$. Figure 8 displays $(Af-Bf)$ and $(Ab-Bb)$ for $M/T=\{1,2,3\}$ as functions of k/T.

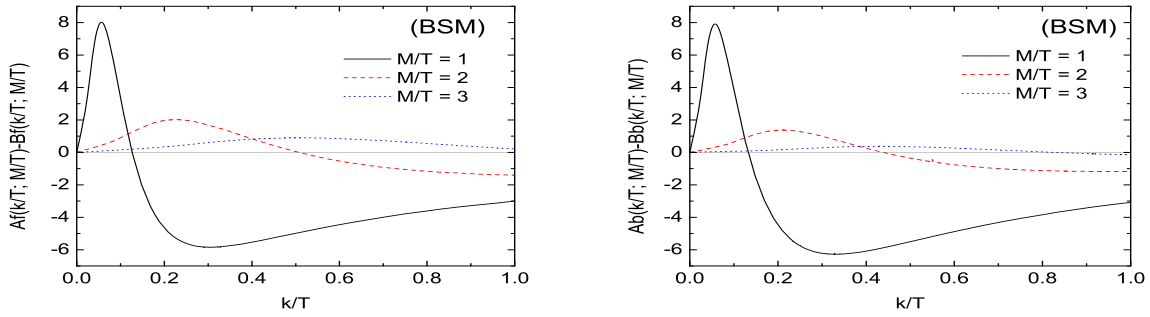

Figure 8: The functions $\left(Af(\frac{k}{T},\frac{M}{T})-Bf(\frac{k}{T},\frac{M}{T})\right)$, $\left(Ab(\frac{k}{T},\frac{M}{T})-Bb(\frac{k}{T},\frac{M}{T})\right)$ as functions of $\frac{k}{T}$ for $\frac{M}{T}=\{1,2,3\}$ for the case of scalars beyond the SM.

We note that the fermionic and bosonic contributions $\{Af,\ Ab\}$ are qualitatively very similar and the same property holds for $\{Bf,\ Bb\}$. Therefore neglecting the fermionic contributions both for $\Sigma^{(1)}$ does not affect the results and the conclusions in a substantial manner. This observation confirms that the general results presented below are robust even when the neutrinos "1" are not thermalized and their propagators are the vacuum ones.

Although an analytic form for the full range of $\{k_0,\ k,\ \mu\}$ is not available, we obtain an analytic expression for the relevant case $\{\frac{k_0}{T},\frac{k}{T},\frac{\mu}{T}\}\ll\frac{M}{T}\sim 1$. We find to leading order in the small ratios $\frac{k_0}{T}$, $\frac{k}{T}$ and $\xi=\frac{\mu}{T}$,

$$\mathrm{Re}\Sigma^{(1)}_{\sigma}(k_0,k) = \frac{Y_1^2T^2}{M_\sigma^2}\left\{\gamma^0\left[-\frac{T\,\xi}{12}\left(1+\frac{\xi^2}{\pi^2}\right)+\frac{7\pi^2}{120}\frac{k_0\,T^2}{M_\sigma^2}\left[1+F\left[M_\sigma/T\right]\right]\right]\right.$$
$$\left.-\vec{\gamma}\cdot\hat{k}\left[-\frac{7\pi^2}{360}\frac{k\,T^2}{M_\sigma^2}\left[1+J\left[M_\sigma/T\right]\right]\right]\right\}, \qquad (3.3.3)$$

$$\mathrm{Re}\Sigma^{(1)}_{\varphi}(k_0,k) = \frac{Y_2^2T^2}{M_\varphi^2}\left\{\gamma^0\left[-\frac{T\,\xi}{12}\left(1+\frac{\xi^2}{\pi^2}\right)+\frac{7\pi^2}{120}\frac{k_0\,T^2}{M_\varphi^2}\left[1+F[M_\varphi/T]\right]\right]\right.$$
$$\left.-\vec{\gamma}\cdot\hat{k}\left[-\frac{7\pi^2}{360}\frac{k\,T^2}{M_\varphi^2}\left[1+J[M_\varphi/T]\right]\right]\right\}, \qquad (3.3.4)$$

$$\mathrm{Re}\Sigma^{(2)}_{\sigma}(k_0,k)=\frac{Y_1^2T^2}{M_\sigma^2}\left\{\gamma^0\left[\frac{7\pi^2}{120}\frac{k_0\,T^2}{M_\sigma^2}F[M_\sigma/T]\right]-\vec{\gamma}\cdot\hat{k}\left[-\frac{7\pi^2}{360}\frac{k\,T^2}{M_\sigma^2}J[M_\sigma/T]\right]\right\}\,, \quad (3.3.5)$$

$$\mathrm{Re}\Sigma^{(2)}_{\varphi}(k_0,k)=\frac{Y_2^2T^2}{M_\varphi^2}\left\{\gamma^0\left[\frac{7\pi^2}{120}\frac{k_0\,T^2}{M_\varphi^2}F[M_\varphi/T]\right]-\vec{\gamma}\cdot\hat{k}\left[-\frac{7\pi^2}{360}\frac{k\,T^2}{M_\varphi^2}J[M_\varphi/T]\right]\right\}\,, \quad (3.3.6)$$

where

$$J(m) = \frac{120}{7\pi^4}\int_0^\infty dq\,\frac{q^2}{W_q}N_B(W_q)\Big[W_q^2+\frac{m^2}{2}\Big], \quad (3.3.7)$$

$$F(m) = \frac{120}{7\pi^4}\int_0^\infty dq\,\frac{q^2}{W_q}N_B(W_q)\Big[W_q^2-\frac{m^2}{2}\Big]. \quad (3.3.8)$$

These functions are displayed in Figure 11, they are $\mathcal{O}(1)$ in the region of interest $M_{\{\sigma,\,\varphi\}}\sim T$. A comprehensive numerical study of $\{Af,\ Ab,\ Bf,\ Bb\}$ confirms the validity of the above approximations for $k_0=k,\mu=0$ for $k/T\ll 1$.

SM vector bosons: Similarly, for the real part of the SM contributed self-energy, we find for $k_0=k$ and $\mu=0$

$$\mathrm{Re}\Sigma_{sm}(k,k)=\frac{g_{sm}^2T}{16\pi^2}\left\{\gamma^0\left[Af\left(\frac{k}{T},\frac{M}{T}\right)+Ab\left(\frac{k}{T},\frac{M}{T}\right)\right]-\vec{\gamma}\cdot\widehat{\mathbf{k}}\left[Bf\left(\frac{k}{T},\frac{M}{T}\right)+Bb\left(\frac{k}{T},\frac{M}{T}\right)\right]\right\}, \quad (3.3.9)$$

where we use the same definition, namely $\{Af,\ Bf\}$ and $\{Ab,\ Bb\}$ are the fermionic and bosonic contributions respectively. Figure 9 shows $\{Af,\ Bf\}$ and $\{Ab,\ Bb\}$ and Figure (10) shows $\left(Af(\frac{k}{T},\frac{M}{T})-Bf(\frac{k}{T},\frac{M}{T})\right)$ and $\left(Ab(\frac{k}{T},\frac{M}{T})-Bf(\frac{k}{T},\frac{M}{T})\right)$ for $\frac{M}{T}=\{1,2,3\}$ as functions of k/T.

Just as in the BSM case analyzed above, we note that the fermionic and bosonic contributions $\{Af,\ Ab\}$ are qualitatively similar and the same holds for $\{Bf,\ Bb\}$. Again this observation confirms that our results are robust, independently of whether any of the neutrino modes is thermalized.

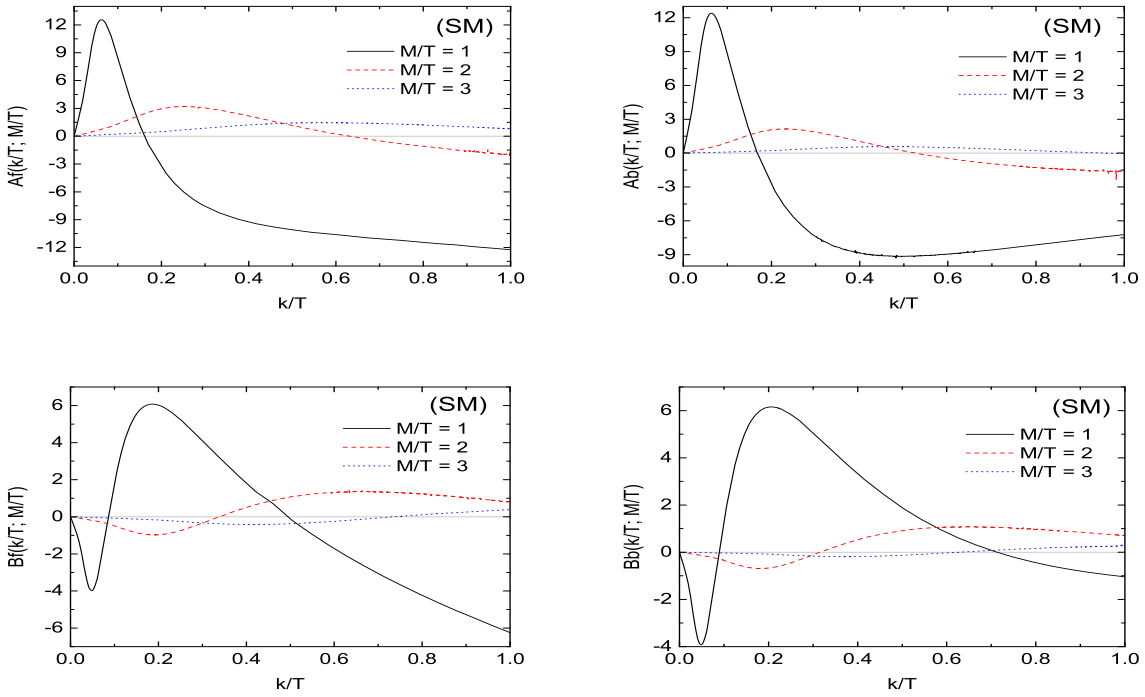

Figure 9: $Af(\frac{k}{T}, \frac{M}{T})$, $Ab(\frac{k}{T}, \frac{M}{T})$, $Bf(\frac{k}{T}, \frac{M}{T})$ and $Bb(\frac{k}{T}, \frac{M}{T})$ as functions of k/T for $\frac{M}{T} = \{1,\ 2,\ 3\}$ for the SM contributions with $\mu = 0$.

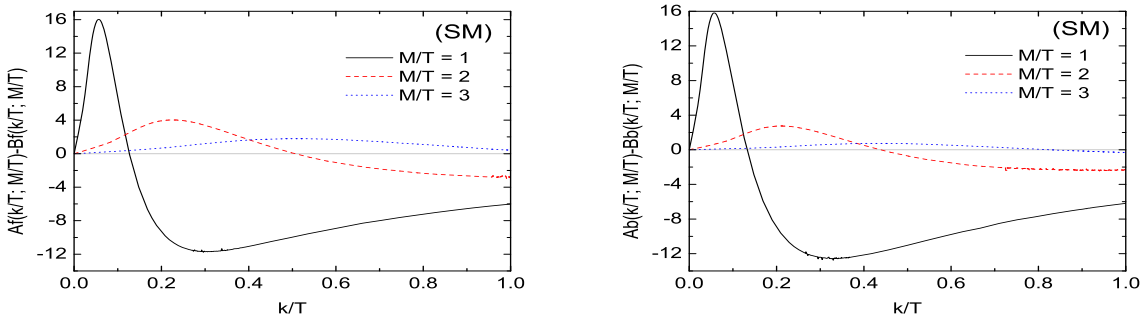

Figure 10: $\left(Af(\frac{k}{T},\frac{M}{T})-Bf(\frac{k}{T},\frac{M}{T})\right),\left(Ab(\frac{k}{T},\frac{M}{T})-Bb(\frac{k}{T},\frac{M}{T})\right)$ as functions of k/T for $\frac{M}{T}=\{1,2,3\}$ for the SM contributions with $\mu=0$.

We also obtain the analytic forms for $\mathrm{Re}\Sigma_{sm}(k_0,k)$ for $\left(\frac{k_0}{T},\ \frac{k}{T},\frac{\mu}{T}\right)\ll M_{\{W,\ Z\}}/T\sim 1$. To leading order in these small ratios we find

$$\mathrm{Re}\Sigma^{(1)}_{nc}(k_0,k) = \frac{g^2T^2}{4M_W^2}\left\{\gamma^0\left[-\frac{T\,\xi}{4}\left(1+\frac{\xi^2}{\pi^2}\right)+\frac{7\pi^2}{60}\frac{k_0\,T^2}{M_Z^2}\Big[1+G[M_Z/T]\Big]\right]\right.$$
$$\left.-\vec{\gamma}\cdot\hat{k}\left[-\frac{7\pi^2}{180}\frac{k\,T^2}{M_Z^2}\Big[1+G[M_Z/T]\Big]\right]\right\}, \qquad (3.3.10)$$

$$\mathrm{Re}\Sigma^{(2)}_{nc}(k_0,k)=\frac{g^2T^2}{4M_W^2}\left\{\gamma^0\left[\frac{7\pi^2}{60}\frac{k_0\,T^2}{M_Z^2}G[M_Z/T]\right]-\vec{\gamma}\cdot\hat{k}\left[-\frac{7\pi^2}{180}\frac{k\,T^2}{M_Z^2}G[M_Z/T]\right]\right\}, \qquad (3.3.11)$$

$$\mathrm{Re}\Sigma_{cc,sm}(k_0,k)=\frac{g^2T^2}{2M_W^2}\left\{\gamma^0\left[\frac{7\pi^2}{60}\frac{k_0\,T^2}{M_W^2}\Big[1+G[M_W/T]\Big]\right]-\vec{\gamma}\cdot\hat{k}\left[-\frac{7\pi^2}{180}\frac{k\,T^2}{M_W^2}\Big[1+G[M_W/T]\Big]\right]\right\}. \qquad (3.3.12)$$

In the charged current contribution we have neglected the asymmetry of the charged lepton because it is of the order of the baryon asymmetry. In the above expressions

$$G[m]=\frac{120}{7\pi^4}\int_0^\infty dq\ \frac{q^2}{W_q}N_B(W_q)\Big[W_q^2-\frac{m^2}{4}\Big],\quad N_B(W_q)=\frac{1}{e^{W_q}-1},\quad W_q=\sqrt{q^2+m^2}. \qquad (3.3.13)$$

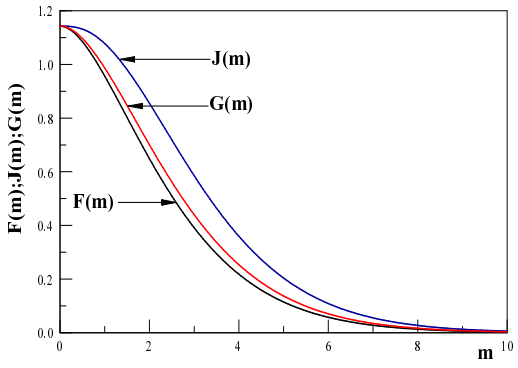

Figure 11: The functions $F(m),\ J(m)$ and $G(m)$ vs $m = M/T$.

This function is depicted in Figure 11, it is $\mathcal{O}(1)$ in the region of interest $T \sim M_{\{Z,W\}}$. The validity of these approximations for $k_0 = k,\ \mu = 0$ is confirmed by the numerical analysis of $Af,\ Ab,\ Bf$ and Bb for $k/T \ll 1$. It is remarkable that the leading order in $\{\frac{k_0}{T},\ \frac{k}{T}\}$ but for $M_{\{W,\ Z\}} \sim T$ reproduce the results of references [230, 171], which were obtained in the low energy limit $\{T, \mu\} \ll M_{\{W,\ Z\}}$. The numerical analysis carried out for $k_0 = k, \mu = 0$ confirms that for $M/T \gg 1$ the range of validity of the lowest order approximation in k/T increases and merges with the results given above in Eqs. (3.3.3-3.3.12) up to $k/T \sim 1$.

3.3.1 Mixing angles and MSW resonances:

As shown in detail in the previous sections, the mixing angle in the medium θ_m determined by the relations (3.2.47) depends on $\{k_0,\ k\}$ and the helicity h. On the mass shell of the propagating modes in the medium we can replace $k_0 \simeq k$ in the expressions for the real part of the matrices $\mathrm{Re}\mathbb{A},\ \mathrm{Re}\mathbb{B}$ for Δ_R, namely the real part of Eqs. (3.2.66) and (3.2.68) for $h = \mp 1$ respectively.

3.3.1.1 Case with vanishing lepton asymmetry For $\mu = 0,\ k_0 = k$ and general $\{k,\ M\}$, the fermionic and bosonic contributions to the real parts of the BSM contributed self-energies are given by Eq. (3.3.2), where the fermionic $(Af,\ Bf)$ and bosonic $(Ab,\ Bb)$

contributions are depicted in Figs. 7-8. The real parts of the SM contributed self-energies are given by Eq. (3.3.9) and the fermionic and bosonic contributions are depicted in Figs. 9-10.

These figures distinctly show that the contributions $\{Af,\ Ab\}$ and $\{Bf,\ Bb\}$ for BSM and SM contributed self-energies are qualitatively the same, with only a quantitative difference in the amplitudes. A remarkable result is that these functions change sign. In particular, the combinations $(Af - Bf)$ and $(Ab - Bb)$ which enter in Δ_R change sign at a value of k/T that depends on the ratio M/T. For $M/T \sim 1$ these differences vanish at $k/T \simeq 0.2$. A numerical exploration reveals that the sign change persists until $M/T \simeq 3$ but occurs at monotonically larger values of k/T. This behavior is shown in the figures above. We find that for $M/T \gtrsim 3$ the change in sign occurs for $k >> T$ or does not occur at all. On the mass shell $k_0 \sim k$ and for $\mu = 0$ this study reveals that Δ_R is negative in a wide region of momentum for $M/T \lesssim 1$. This fact entails that there are MSW resonances near the momentum regions where the coefficient functions change sign, even in *absence of a lepton asymmetry*. To understand this important point more clearly, let us study the case $h = \mp 1$ separately.

$\underline{\mathbf{h = -1}}$: In this case, Δ is given by Eq. (3.2.66); furthermore, from Eq. (3.2.13), it follows that $(\mathbb{A}_L - \mathbb{B}_L)_{ss}$ is determined by the BSM contributions which are suppressed by small Yukawa couplings $Y \lesssim 10^{-8}$ as compared to the SM contributions. Therefore the BSM contribution can be neglected and Δ_R is determined by the SM contributions given by Eq. (3.3.9). By approximating $\cos\theta \sim 1,\ \sin\theta \sim 0$ in Eq. (3.2.12) and letting $\delta M^2 \simeq M_s^2$, we find for $\mu = 0,\ h = -1$:

$$\Delta_R(k) \simeq \frac{g^2}{16\pi^2}\left(\frac{T}{M_s}\right)^2\left(\frac{k}{T}\right)\left\{f_W\left(\frac{k}{T},\frac{M_W}{T}\right) + \frac{1}{2\cos(\theta_w)} f_Z\left(\frac{k}{T},\frac{M_W}{T}\right)\right\}, \tag{3.3.14}$$

where

$$\begin{aligned} f_W &= Af\Big(\frac{k}{T},\frac{M_W}{T}\Big) + Ab\Big(\frac{k}{T},\frac{M_W}{T}\Big) - Bf\Big(\frac{k}{T},\frac{M_W}{T}\Big) - Bb\Big(\frac{k}{T},\frac{M_W}{T}\Big) \\ f_Z &= Af\Big(\frac{k}{T},\frac{M_Z}{T}\Big) + Ab\Big(\frac{k}{T},\frac{M_Z}{T}\Big) - Bf\Big(\frac{k}{T},\frac{M_Z}{T}\Big) - Bb\Big(\frac{k}{T},\frac{M_Z}{T}\Big). \end{aligned} \tag{3.3.15}$$

Taking as representative $T \sim 100\,\mathrm{GeV}$ and $M_s \sim \mathrm{keV}$, it follows that

$$\frac{g^2}{16\pi^2}\left(\frac{T}{M_s}\right)^2 \simeq 2.7 \times 10^{13}\,. \tag{3.3.16}$$

Figure 10 shows that for $M_{\{W,\,Z\}}/T \lesssim 3$ there is a region of k/T in which the bracket in (3.3.15) is negative and there is a value $(k/T)_c$ that increases with M/T at which the bracket vanishes, for example, from the Figure 10, we find $(k/T)_c \sim \{0.2,\ 0.45,\ 1\}$ for $M/T \sim \{1,\ 2,\ 3\}$ respectively. For $k/T < (k/T)_c$ the bracket is positive (for $\mu = 0$) whereas for $k/T > (k/T)_c$ it is negative, therefore there is a value of k/T at which the resonance condition (3.2.49) is fulfilled. Since the coefficient of the bracket is $\approx 10^{13}$ (See Eq. (3.3.16).) and the terms inside the bracket are of $\mathcal{O}(1)$ for $k/T \lesssim 1$, plus $\cos\theta \sim 1$, it follows that the MSW resonance occurs for a value of k/T such that the bracket $\sim 10^{-13}$ namely for $k/T \sim (k/T)_c$. The large coefficient (3.3.16) results in a very narrow MSW resonance as can be seen as follows, expanding Δ_R near $(k/T)_c$ as

$$\Delta_R(k) \simeq -\kappa \left(\left(\frac{k}{T}\right) - \left(\frac{k}{T}\right)_c \right) + \cdots , \quad \kappa > 0 , \tag{3.3.17}$$

where $\kappa \gtrsim 10^{13}$ for $M_{\{W,\,Z\}}/T \lesssim 3$ shown in Figure 10, and by approximating $\cos(2\theta) \sim 1$ we find

$$\sin^2(2\theta_m) \simeq \frac{\epsilon^2}{\left[\left(\left(\frac{k}{T}\right) - \left(\frac{k}{T}\right)_c - \frac{1}{\kappa} \right)^2 + \epsilon^2 \right]} , \tag{3.3.18}$$

where $\epsilon = \sin(2\theta)/\kappa$. If taking $\sin(2\theta) \sim 10^{-5}$ [209], it follows that $\epsilon \lesssim 10^{-18}$ which makes the resonance very narrow. During cosmological expansion the ratio $\frac{M}{T}(t)$ increases with the scale factor, while the ratio k/T (with k the physical momentum) is fixed. Therefore, for a fixed value of $k/T < 1$ as M/T increases the resonance is crossed very sharply.

$\underline{\mathbf{h = 1}}$: To assess the possibility of MSW resonances for $h = 1$ we need the real part of (3.2.68). From (3.2.12) and (3.3.2), it follows that $\{(\mathbb{A}_R - \mathbb{B}_R)_{aa} \propto Y_1^2,\ (\mathbb{A}_R - \mathbb{B}_R)_{ss}\} \propto Y_2^2$, since $Y_2 \gg Y_1$ we can neglect the first term which corresponds to σ-exchange. Similarly, in the term $(\mathbb{A}_R - \mathbb{B}_R)_{ss}$ we also neglect the contribution from σ-exchange and approximate $\cos\theta \sim 1$, $\sin\theta \sim 0$ in (3.2.13), hence only $\Sigma_\varphi^{(2)}$ contributes to Σ_{ss}. Furthermore, by approximating $\delta M^2 \sim \overline{M}^2 \sim M_s^2$, we finally find for $h = 1,\ \mu = 0$:

$$\begin{aligned} \Delta_R(k) \ \simeq \ & -\left(\frac{Y_2 T}{\sqrt{8}\pi M_s}\right)^2 \left(\frac{k}{T}\right) \left[Ab\Big(\frac{k}{T}, \frac{M_\varphi}{T}\Big) - Bb\Big(\frac{k}{T}, \frac{M_\varphi}{T}\Big) \right] \\ & + \frac{g^2}{128\pi^2}\left(\frac{T}{k}\right) \left\{ g_W\left(\frac{k}{T}, \frac{M_W}{T}\right) + \frac{1}{2\cos(\theta_w)} g_Z\left(\frac{k}{T}, \frac{M_W}{T}\right) \right\} , \end{aligned} \tag{3.3.19}$$

where

$$
\begin{aligned}
g_W &= Af\Big(\frac{k}{T},\frac{M_W}{T}\Big)+Ab\Big(\frac{k}{T},\frac{M_W}{T}\Big)+Bf\Big(\frac{k}{T},\frac{M_W}{T}\Big)+Bb\Big(\frac{k}{T},\frac{M_W}{T}\Big),\\
g_Z &= Af\Big(\frac{k}{T},\frac{M_Z}{T}\Big)+Ab\Big(\frac{k}{T},\frac{M_Z}{T}\Big)+Bf\Big(\frac{k}{T},\frac{M_Z}{T}\Big)+Bb\Big(\frac{k}{T},\frac{M_Z}{T}\Big)\,. \qquad (3.3.20)
\end{aligned}
$$

Ab and Bb in the first line of Eq. (3.3.19) are displayed in Figure 7. We note that with $T\sim 100\text{GeV}, M_s\sim \text{keV}$, the value of the Y_2 (See Eq. (3.1.14).) is such that $\frac{Y_2 T}{M_s}\sim\mathcal{O}(1)$, therefore, the right panel of Figure 8 suggests that the BSM contribution may yield an MSW resonance in the region $\{k/T\lesssim 0.15,\ M_\varphi\sim T\}$, where the BSM contribution $Ab-Bb$ is positive and large. Since $\frac{g^2}{128\pi^2}\sim 3.4\times10^{-4}$ and $\{Af+Bf,\ Ab+Bb\}\sim\mathcal{O}(1)$ for $k/T\lesssim 1$, it follows that the SM contribution to Δ_R is sub-leading for $k/T\lesssim 1$ and the BSM contribution may lead to an MSW resonance in this region depending on the parameters of the extension beyond the SM.

3.3.1.2 Case With non-vanishing lepton asymmetry $(\mu\neq 0,\ \frac{\mathbf{k}}{\mathbf{T}}\ll\frac{\mathbf{M}}{\mathbf{T}}\sim\mathbf{1})$

All above discussions are valid only for $\mu=0$; for $\mu\neq 0$, a full numerical evaluation of the real parts of the kernel is not available. However, the bounds on the lepton asymmetry from Ref. [261] suggest that $|\mu/T|\lesssim 0.02\ll 1$, and we can obtain a reliable understanding of the influence of the lepton asymmetry in the neutrino sector by focusing on the region of $k/T\ll 1$, where we can use the results (3.3.3) to (3.3.6) for BSM contributions, and (3.2.7) along with (3.3.10) to (3.3.12) for SM contributions. Moreover, we can further simplify the calculation by approximating $\cos\theta\sim 1,\ \sin\theta\sim 0$ in (3.2.12) and (3.2.13), and letting $\delta M^2\sim M_s^2$.

For $h=-1$, again we neglect the BSM contributions to $\Delta_R(k)$ in (3.2.66), and for $\{\mu/T,\ k/T\}\ll 1$, we obtain,

$$
\Delta_R(k)\simeq\frac{g^2T^3k}{M_W^2M_s^2}\Big\{-\frac{5\,\xi}{24}+\frac{7\pi^2}{90}\Big(\frac{k}{T}\Big)h(\frac{M_Z}{T})\Big\}, \qquad (3.3.21)
$$

where

$$h(\frac{M_Z}{T}) = \left[\Big(\frac{T}{M_Z}\Big)^2\left(1+G\Big(\frac{M_Z}{T}\Big)\right)+2\Big(\frac{T}{M_W}\Big)^2\left(1+G\Big(\frac{M_W}{T}\Big)\right)\right], \tag{3.3.22}$$

and the function G follows the expression in Eq. (3.3.13). We note that for $T \sim M_W$ and $M_s \sim$ keV the prefactor

$$\frac{g^2T^3k}{M_W^2M_s^2} \sim 10^{16}\Big(\frac{k}{T}\Big), \tag{3.3.23}$$

the resonance condition (3.2.49) can be fulfilled for $\xi > 0$ when the bracket in (3.3.21) approximately vanishes, that is

$$\Big(\frac{k}{T}\Big) \sim \frac{25\ \xi}{56\pi^2} \Rightarrow k \sim 0.05\ \mu\ , \tag{3.3.24}$$

where we have used $G(M_{W,Z}/T) \sim 1$ at $T \sim M_W$, a result that can be gleaned from Figure 11. For $\xi > 0$ this MSW resonance occurs for antineutrinos, namely $k_0 = -k$, following from the relations (3.2.61) and (3.2.62).

Similarly, for $h = 1$ and $\{\frac{\mu}{T},\ \frac{k}{T}\} \ll 1$, we obtain

$$\begin{aligned}\Delta_R(k) \ \simeq\ & -\left(\frac{Y_2T}{M_s}\right)^2\Big(\frac{T}{M_\varphi}\Big)^4\Big(\frac{k}{T}\Big)^2\frac{7\pi^2}{180}\left[J(\frac{M_\varphi}{T})+3F(\frac{M_\varphi}{T})\right]\\ &+\left(\frac{gT}{M_W}\right)^2\Big(\frac{T}{k}\Big)\left\{-\frac{5\xi}{192}+\frac{7\pi^2}{1440}\Big(\frac{k}{T}\Big)h(\frac{T}{M_Z})\right\}.\end{aligned} \tag{3.3.25}$$

Obviously, there is a competition between SM and BSM contributions in Eq. (3.3.25). When $T \sim M_{\{W,\ Z,\ \varphi\}}$, $\{J(1), F(1), G(1)\} \sim 1$ and $(Y_2T)/M_s \sim 1$, the BSM contribution to $\Delta_R(k)$ is

$$\Delta_R^{(bsm)} \sim -\frac{7\pi^2}{45}\Big(\frac{k}{T}\Big)^2 = -1.54\Big(\frac{k}{T}\Big)^2, \tag{3.3.26}$$

and the SM contribution to $\Delta_R(k)$ is

$$\Delta_R^{(sm)} \sim 0.1\Big(\frac{T}{k}\Big)\left[-\frac{5\xi}{192}+\Big(\frac{k}{T}\Big)\frac{7\pi^2}{240}\right] \sim 0.029 - 3\times10^{-3}\Big(\frac{T}{k}\Big)\ \xi. \tag{3.3.27}$$

The resonance happens for $\Delta_R(k) \sim -1$, namely

$$3\times10^{-3}\Big(\frac{T}{k}\Big)\ \xi \sim 1.029. \tag{3.3.28}$$

Obviously, one is always able to find a value of k/T to satisfy Eq. (3.3.28) for any given positive lepton asymmetry ξ. For $|\xi| \sim 10^{-2}$ consistent with the WMAP and BBN data [261], we obtain

$$\frac{k}{T} \sim 3 \times 10^{-3}\, \xi \sim 3 \times 10^{-5}\,. \tag{3.3.29}$$

Note that the asymmetry term from SM contribution dominates over the BSM contribution, which is different from $\mu = 0$ case where BSM contribution would dominate as shown in (3.3.19). This analysis leads us to conclude that for a lepton asymmetry hidden in the neutrino sector compatible with the bounds from Ref. [261], it is possible to have two MSW resonances.

3.4 IMAGINARY PARTS: WIDTHS FROM VECTOR AND SCALAR BOSON DECAY

The quasiparticle widths $\Gamma_{\{1,\,2\}}(k)$ are given by Eqs. (3.2.57) and (3.2.60). Analyzing the explicit expressions for the imaginary parts of the SM and BSM contributions given in the appendix, Eqs. (A.1.1)-(A.1.3), and (A.2.1)-(A.2.3) respectively, the "on-shell" contributions are obtained from those whose δ function constraints can be satisfied for $\omega \sim k$. It is straightforward to find that only the terms with $\delta(\omega + p - W_{\vec{p}+\vec{k}})$ have non-vanishing support for $\omega \simeq k$. These terms are given in the last lines of (A.1.2) and (A.1.3) for the SM contributions and the last lines of (A.2.2) and (A.2.3) for the BSM contributions.

These contributions to the quasiparticle widths in the medium arise from the decay of the intermediate boson, either the vector bosons in the SM contributions or the scalars in the BSM contributions. This is depicted in Figure 12, the Cutkosky cut through the intermediate boson (vector or scalar) yields the imaginary part. The process that contributes on shell $\omega \simeq k$ is the decay of the boson into the fermions (neutrinos and/or charged leptons) depicted in this figure. The fact that the decay of a heavy intermediate state leads to a width was recognized in Ref. [62].

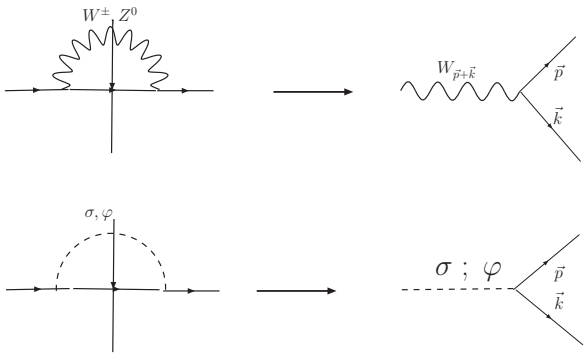

Figure 12: The Cutkosky cut for the imaginary part of the SM and BSM contributions, and the contribution on the mass shell $\omega \simeq k$.

The analysis of different cases is simplified by introducing

$$\Gamma_{aa}(k_0,k) = \quad \mathrm{Im}\left[\frac{(k_0+hk)}{2k}\big(\mathbb{A}_R - h\mathbb{B}_R\big)_{aa} + \frac{(k_0-hk)}{2k}\big(\mathbb{A}_L + h\mathbb{B}_L\big)_{aa}\right], \quad (3.4.1)$$

$$\Gamma_{ss}(k_0,k) = \quad \mathrm{Im}\left[\frac{(k_0+hk)}{2k}\big(\mathbb{A}_R - h\mathbb{B}_R\big)_{ss} + \frac{(k_0-hk)}{2k}\big(\mathbb{A}_L + h\mathbb{B}_L\big)_{ss}\right], \quad (3.4.2)$$

in terms of which (See Eq. (3.2.32).),

$$\begin{aligned} S_I &= 2k\Big[\Gamma_{aa}(k_0,k) + \Gamma_{ss}(k_0,k)\Big], \\ \Delta_I(k_0,k) &= \frac{2k}{\delta M^2}\Big[\Gamma_{aa}(k_0,k) - \Gamma_{ss}(k_0,k)\Big]. \end{aligned} \quad (3.4.3)$$

We need these quantities evaluated on the "mass shell", namely for positive energy $k_0 = \overline{\omega}(k) \sim k + \overline{M}^2/2k$. We find:

$\underline{\mathbf{h=-1}}$:

$$\Gamma_{aa}(k) \simeq \mathrm{Im}\big(\mathbb{A}_L - \mathbb{B}_L\big)_{aa},\ \Gamma_{ss}(k) \simeq \mathrm{Im}\big(\mathbb{A}_L - \mathbb{B}_L\big)_{ss}. \quad (3.4.4)$$

$\underline{\mathbf{h=1}}$:

$$\Gamma_{aa}(k) \simeq \mathrm{Im}\left[\big(\mathbb{A}_R - \mathbb{B}_R\big)_{aa} + \frac{\overline{M}^2}{4k^2}\ \big(\mathbb{A}_L + \mathbb{B}_L\big)_{aa}\right],\ \Gamma_{ss}(k) \simeq \mathrm{Im}\big(\mathbb{A}_R - \mathbb{B}_R\big)_{ss}. \quad (3.4.5)$$

In the above expressions, we have used $Y_{\{1,\,2\}} \ll g$ and $\overline{M}^2/4k^2 \ll 1$ and neglected terms accordingly, we have suppressed the arguments on $\mathbb{A}$ and $\mathbb{B}$. However, these matrix elements depend on k. The term with $\mathbb{A}_L + \mathbb{B}_L$ in (3.4.5) is noteworthy: the leading contribution to this term is from SM interactions, even setting the Yukawa couplings in the BSM sector to zero, *a nearly right-handed sterile neutrino is produced via the decay of the vector bosons.* The expression for the imaginary parts (3.2.57) and (3.2.60) simplify in two relevant limits [60]:

a) weak damping $|\tilde{\gamma}| \ll 1$: in this limit we find

$$r\sin(\phi) \simeq \tilde{\gamma}\cos 2\theta_m \tag{3.4.6}$$

leading to the following results for the poles with positive energy

$$\Gamma_1(k) = \Gamma_{aa}(k)\cos^2\theta_m + \sin^2\theta_m\Gamma_{ss}(k)\ , \tag{3.4.7}$$

$$\Gamma_2(k) = \Gamma_{aa}(k)\sin^2\theta_m + \cos^2\theta_m\Gamma_{ss}(k)\,. \tag{3.4.8}$$

Furthermore, the difference in the dispersion relations becomes

$$\Delta\Omega_{wd} \equiv \Omega_2(k) - \Omega_1(k) \simeq \frac{\delta M^2}{2k}\rho_0\,, \tag{3.4.9}$$

which is the usual result for neutrino mixing.

b) strong damping $|\tilde{\gamma}| \gg 1$: in this limit we find

$$r\sin(\phi) \simeq \tilde{\gamma}\ \mathrm{sign}(\cos(2\theta_m))\left[1 - \frac{\sin^2(2\theta_m)}{2\tilde{\gamma}^2}\right] \tag{3.4.10}$$

leading to the following results

$$\Gamma_1(k) = \frac{1}{2}\big[\,\Gamma_{aa}(k)+\Gamma_{ss}(k)\,\big] + \frac{1}{2}\big[\,\Gamma_{aa}(k)-\Gamma_{ss}(k)\,\big]\left(\mathrm{sign}(\cos(2\theta_m)) - \frac{\sin^2(2\theta_m)}{2\tilde{\gamma}^2}\right)\ , \tag{3.4.11}$$

$$\Gamma_2(k) = \frac{1}{2}\big[\,\Gamma_{aa}(k)+\Gamma_{ss}(k)\,\big] - \frac{1}{2}\big[\,\Gamma_{aa}(k)-\Gamma_{ss}(k)\,\big]\left(\mathrm{sign}(\cos(2\theta_m)) - \frac{\sin^2(2\theta_m)}{2\tilde{\gamma}^2}\right)\ . \tag{3.4.12}$$

In this case the frequency difference between the propagating states becomes

$$\Delta\Omega_{sd} \equiv \Omega_2(k) - \Omega_1(k) \simeq \frac{\delta M^2}{2k}\rho_0 |\cos(2\theta_m)| = \frac{\delta M^2}{2k}|\cos(2\theta) + \Delta_R(k)| \,. \tag{3.4.13}$$

This is a remarkable result, the frequency difference vanishes at a MSW resonance in striking contrast with the usual quantum mechanics description of neutrino mixing and oscillations wherein there is a "level repulsion" at an MSW resonance that prevents level crossing. In all the expressions above $\Gamma_{aa}(k)$ and $\Gamma_{ss}(k)$ are given by (3.4.4) and (3.4.5) in the respective cases $h = \mp 1$, and the mixing angle θ_m is obtained from Eq. (3.2.47) evaluating Δ_R at $k_0 = k$.

The widths for negative energy and $h = \mp 1$ are obtained from the expressions above by the replacement $\mu \to -\mu$, this is a consequence of the relations (3.2.61), (3.2.62) and the fact that the chemical potential is CP-odd, therefore the particle and antiparticle widths only differ because of the chemical potential.

We emphasize that the results (3.4.7), (3.4.8) and (3.4.11), (3.4.12) are general, and hold to all orders in perturbation theory as they follow from the general form of the self-energies. In particular these relations are valid beyond the one-loop order studied here and hold for any processes that contributes to the absorptive parts of the self-energy at one-loop or higher order.

3.4.1 Widths from scalar and vector boson decay:

As discussed above, the imaginary parts of the self-energy are given in the appendix, both for SM and BSM contributions. Inspection of the different delta functions shows that the only contribution "on-shell", namely $\omega \simeq k$, arises from the terms with $\delta(\omega + p - W_{\vec{p}+\vec{k}})$ in the expressions for the imaginary parts (A.2.2) and (A.2.3). This delta function corresponds to a Cutkosky cut that describes the process of a scalar (in BSM contributions) or a vector boson (in SM contributions) decay into a neutrino and another lepton, displayed in Figure 12.

BSM Scalars: For scalars, the (R) and (L) components are the same. We find for σ and φ exchange that

$$\mathrm{Im}(\mathbb{A}_R - \mathbb{B}_R) = \mathrm{Im}(\mathbb{A}_L - \mathbb{B}_L) = \frac{Y^2}{32\pi}\frac{T}{k}\frac{M^2}{k^2}\ln\left[\frac{1 + C_1\, e^{-x^*-\xi}}{1 - e^{-x^*-y}}\right], \tag{3.4.14}$$

where

$$x^* = \frac{M^2}{4kT}, \quad \xi = \frac{\mu}{T}, \quad y = \frac{k}{T}, \tag{3.4.15}$$

and

$$C_1 = \begin{cases} 1 & \text{for } \Sigma^{(1)}_{\{\sigma,\,\varphi\}}\,, \\ 0 & \text{for } \Sigma^{(2)}_{\{\sigma,\,\varphi\}}\,. \end{cases} \tag{3.4.16}$$

In the relevant region $k < M_{\{\sigma,\,\varphi\}} \sim T$, we can safely neglect the contribution from the leptonic chemical potential in (3.4.14) and set $\xi = 0$ since the bounds from Ref. [261] suggest that $|\xi| \lesssim 0.02$. The result (3.4.14) agrees with that found in Ref. [61] for the decay of the scalar boson into sterile neutrinos (2) ($C_1 = 0$) for vanishing chemical potential. For $k/T \ll M/T \sim 1$ we can approximate

$$\mathrm{Im}(\mathbb{A}_R - \mathbb{B}_R) = \mathrm{Im}(\mathbb{A}_L - \mathbb{B}_L) = \frac{Y^2}{32\pi}\frac{T}{k}\frac{M^2}{k^2}\; e^{-x^*}\Big(C_1 + e^{-y}\Big)\,. \tag{3.4.17}$$

SM Vector bosons: For SM vector boson exchange which only contains (L) component, the imaginary parts "on-shell" are obtained from the terms with $\delta(\omega + p - W_{\vec{p}+\vec{k}})$ in the imaginary parts of (A.1.2) and (A.1.3). By setting $\omega \simeq k$, we find

$$\mathrm{Im}(\mathbb{A}_L - \mathbb{B}_L) = \frac{g_{sm}^2 T}{16\pi}\frac{M^2}{k^2}\ln\left[\frac{1 + C_2\, e^{-x^*-\xi}}{1 - e^{-x^*-y}}\right], \tag{3.4.18}$$

where g_{sm} is given by Eq. (3.2.16), $M = M_{\{Z,\,W\}}$ for neutral and charged current contributions respectively, and

$$C_2 = \begin{cases} 1 & \text{for } \Sigma^{(1)}_{nc}, \Sigma_{cc}\,, \\ 0 & \text{for } \Sigma^{(2)}_{nc}\,. \end{cases} \tag{3.4.19}$$

For positive energy and positive helicity, namely right-handed, we also need (See Eq. (3.4.5).):

$$\mathrm{Im}(\mathbb{A}_L + \mathbb{B}_L) = \frac{g_{sm}^2 T}{8\pi}\left\{\ln\left[\frac{1 + C_2\, e^{-x^*}}{1 - e^{-x^*-y}}\right] + \frac{2T}{k}\left[Li_2\big(e^{-x^*-y}\big) - C_2\, Li_2\big(-e^{-x^*}\big)\right]\right\}, \tag{3.4.20}$$

where Li_2 is the dilogarithm or Spence's function and we have set $\mu = 0$. This expression is greatly simplified in the limit $k/T \ll M/T \sim 1$, with the result

$$\mathrm{Im}(\mathbb{A}_L + \mathbb{B}_L) \simeq \frac{g_{sm}^2 T^2}{4\pi k}\; e^{-x^*}\Big(C_2 + e^{-y}\Big)\;. \tag{3.4.21}$$

In the above results for vector bosons, $M = M_{\{W,\,Z\}}$ respectively. We can now gather all the results needed for $\Gamma_{aa}(k)$, $\Gamma_{ss}(k)$ in (3.4.4) and (3.4.5), obtaining the quasiparticle widths $\Gamma_{\{1,\,2\}}(k)$ from them. Approximating $\cos\theta \sim 1, \sin\theta \sim 0$, we find,

$$\mathrm{Im}\big(\mathbb{A}_R - \mathbb{B}_R\big)_{aa} = \frac{Y_1^2 T}{32\pi}\left(\frac{M_\sigma^2}{k^2}\right)\ln\left[\frac{1}{1-e^{-x_\sigma^*}\;e^{-y}}\right], \tag{3.4.22}$$

$$\begin{aligned}\mathrm{Im}\big(\mathbb{A}_R - \mathbb{B}_R\big)_{ss} &= \mathrm{Im}\big(\mathbb{A}_L - \mathbb{B}_L\big)_{ss} \\ &= \frac{Y_1^2 T}{32\pi}\left(\frac{M_\sigma^2}{k^2}\right)\ln\left[\frac{1+e^{-x_\sigma^*}}{1-e^{-x_\sigma^*}\;e^{-y}}\right] + \frac{Y_2^2 T}{32\pi}\left(\frac{M_\varphi^2}{k^2}\right)\ln\left[\frac{1}{1-e^{-x_\varphi^*}\;e^{-y}}\right],\end{aligned} \tag{3.4.23}$$

$$\begin{aligned}\mathrm{Im}\big(\mathbb{A}_L - \mathbb{B}_L\big)_{aa} &= \frac{g^2 T}{32\pi}\left\{\frac{1}{2\cos^2(\theta_w)}\left(\frac{M_Z^2}{k^2}\right)\ln\left[\frac{1+e^{-x_Z^*}}{1-e^{-x_Z^*}\;e^{-y}}\right] + \left(\frac{M_W^2}{k^2}\right)\ln\left[\frac{1+e^{-x_W^*}}{1-e^{-x_W^*}\;e^{-y}}\right]\right\} \\ &+ \frac{Y_1^2 T}{32\pi}\left(\frac{M_\sigma^2}{k^2}\right)\ln\left[\frac{1}{1-e^{-x_\sigma^*}\;e^{-y}}\right],\end{aligned} \tag{3.4.24}$$

$$\begin{aligned}\mathrm{Im}\big(\mathbb{A}_L + \mathbb{B}_L\big)_{aa} &= \frac{g^2 T}{16\pi}\left\{\frac{1}{2\cos^2(\theta_w)}\left[\ln\left(\frac{1+e^{-x_Z^*}}{1-e^{-x_Z^*}\;e^{-y}}\right) + \frac{2T}{k}\Big[Li_2\big(e^{-x_Z^*}\;e^{-y}\big) - Li_2\big(-e^{-x_Z^*}\big)\Big]\right]\right. \\ &\left. + \ln\left(\frac{1+e^{-x_W^*}}{1-e^{-x_W^*}\;e^{-y}}\right) + \frac{2T}{k}\Big[Li_2\big(e^{-x_W^*}\;e^{-y}\big) - Li_2\big(-e^{-x_W^*}\big)\Big]\right\} \\ &+ \frac{Y_1^2 T}{16\pi}\left(\frac{2T}{k}\right)Li_2\big(e^{-x_\sigma^*}\;e^{-y}\big).\end{aligned} \tag{3.4.25}$$

In the expressions above, we have defined

$$x_\alpha^* = \frac{M_\alpha^2}{4kT}, \tag{3.4.26}$$

with $\alpha = \{\sigma,\ \varphi,\ Z,\ W\}$. For small values of the arguments $Li_2(z) \sim z$, which may be used appropriately whenever $x_\alpha^* > 1$, a situation describing the relevant range $\{M_\alpha \sim T, k < T\}$. Eqs. (3.4.22-3.4.25), combined with (3.4.4) and (3.4.5), yield the complete expressions for the quasiparticle widths $\Gamma_{\{1,\,2\}}$ in all cases, and as per the discussion below, the production rates.

3.4.2 Imaginary parts: from the width to the production rates.

The connection between the quasiparticle widths corresponding to the imaginary part of the self-energy "on-shell" and the production rate is established via the Boltzmann equation for the production of a given species, in this case that of a "sterile" neutrino. Consider the scalar vertex $Y_1\overline{\nu}_s\,\sigma\nu_a$ as an example, the analysis is similar for the other, including vertices from SM contributions. According to the Boltzmann equation, the production rate of sterile neutrinos is of the form (gain)− (loss) (See for example the appendix in Ref. [61]).). The gain term corresponds to the decay process $\sigma \to \overline{\nu}_a + \nu_s$ and is given by [61]

$$\left.\frac{dn_s(k)}{dt}\right|_{gain} = \int \frac{d^3p}{(2\pi)^3}\Big|\mathcal{M}_{fi}\Big|^2\,\delta\big(W_{\vec{p}+\vec{k}}-p-k\big)N_B\big(W_{\vec{p}+\vec{k}}\big)(1-\overline{n}_F(p))(1-n_s(k))\;, \quad (3.4.27)$$

where N_B, n_F are the bosonic and fermionic distribution functions respectively. The loss term describes the inverse process, namely, the recombination $\overline{\nu}_a + \nu_s \to \varphi$ with

$$\left.\frac{dn_s(k)}{dt}\right|_{loss} = \int \frac{d^3p}{(2\pi)^3}\Big|\mathcal{M}_{fi}\Big|^2\,\delta\big(W_{\vec{p}+\vec{k}}-p-k\big)\Big[1+N_B\big(W_{\vec{p}+\vec{k}}\big)\Big]\overline{n}_F(p)n_s(k)\,. \quad (3.4.28)$$

Therefore, when putting together, the Boltzmann equation is of the form

$$\begin{aligned}\frac{dn_s(k)}{dt} \;=\; & \int \frac{d^3p}{(2\pi)^3}\Big|\mathcal{M}_{fi}\Big|^2\,\delta\big(W_{\vec{p}+\vec{k}}-p-k\big) \\ & \left\{N_B\big(W_{\vec{p}+\vec{k}}\big)(1-\overline{n}_F(p))(1-n_s(k)) - \Big[1+N_B\big(W_{\vec{p}+\vec{k}}\big)\Big]\overline{n}_F(p)n_s(k)\right\}\,.\end{aligned} \quad (3.4.29)$$

If the distribution function of the particle in question is slightly perturbed off equilibrium, the relaxation rate of the distribution function towards equilibrium is obtained by writing $n_s(k) = n_s^{eq}(k) + \delta n_s(k)$ and linearizing the Boltzmann equation in $\delta n_s(k)$ [278, 63]. The linearized Boltzmann equation reads

$$\frac{d\delta n_s(k)}{dt} = -\Gamma_{rel}\;\delta n_s(k)\;, \quad (3.4.30)$$

where

$$\Gamma_{rel} = \int \frac{d^3p}{(2\pi)^3}\Big|\mathcal{M}_{fi}\Big|^2\,\delta\big(W_{\vec{p}+\vec{k}}-p-k\big)\Big[\overline{n}_F(p)+N_B\big(W_{\vec{p}+\vec{k}}\big)\Big]\;. \quad (3.4.31)$$

As discussed in Refs. [278, 63], the relaxation rate Γ_{rel} is twice the quasiparticle width since the distribution function is bilinear in the fields. The relation between Γ_{rel} and the on-shell width becomes evident comparing the expression (3.4.31) with the "on-shell" imaginary parts, namely the last lines in Eqs. (A.1.2), (A.1.3), (A.2.2) and (A.2.3) with $\omega \simeq k$. The production rate of the sterile species is obtained by neglecting the inverse process and neglecting the sterile population buildup in the Boltzmann equation (3.4.29), namely,

$$\left.\frac{dn_s(k)}{dt}\right|_{prod} = \int \frac{d^3p}{(2\pi)^3}\left|\mathcal{M}_{fi}\right|^2 \delta\big(W_{\vec{p}+\vec{k}} - p - k\big) N_B\big(W_{\vec{p}+\vec{k}}\big)(1-\overline{n}_F(p)) \ . \tag{3.4.32}$$

Therefore by obtaining the bosonic and fermionic contributions to the quasiparticle widths as in the previous section, we can obtain the production rate. Although the term with the product $N_B\overline{n}_F$ is not included in the width, such a term is smaller than the term with N_B only, because under the limit $\mu/T \ll 1$, $p^2\overline{n}_F(p)$ features a maximum at $p/T \sim 2.3$ where $\overline{n}_F(p) \sim 0.09$. Therefore, for the important region in the integral $p \gtrsim T$, the production and relaxation rates only differ by a few percent, and the results for the relaxation rates yield a reliable approximation to the production rate. An important bonus of obtaining the production rate from the quasiparticle decay width is the correct dependence on the mixing angle in the medium, which would be missed by a naive perturbative calculation. Therefore, we conclude that the quasiparticle width yields an very good approximation to the production rate, in particular it describes correctly the dependence on the mixing angles in the medium, both on its magnitude and k-dependence. In particular, the result (3.4.23) confirms the result of Ref. [61] for $Y_1 = 0$. For the scalar contribution, the right and left-handed components yield the same result, multiplying (3.4.23) by a factor 2 in the total rate, and as discussed above the production rate is twice the width, which restores the factor 4 between (3.4.23) and the result in Ref. [61] which corresponds to the case $Y_1 = 0$.

Finally, we conclude that the results of Eqs. (3.4.4), (3.4.5), (3.4.7), (3.4.8), (3.4.11) and (3.4.12) along with the explicit forms (3.4.22-3.4.25) provide a complete and reliable assessment of the production rates ready to be input in the kinetic equations with the cosmological expansion [61].

3.4.3 Weak or strong damping?

We now have all the ingredients to assess under which circumstances the weak ($|\tilde{\gamma}| \ll 1$) or strong ($|\tilde{\gamma}| \gg 1$) damping conditions are fulfilled. In terms of the widths and the real parts, it follows that

$$\tilde{\gamma} \simeq \frac{2k}{M_s^2} \frac{\Big[\Gamma_{aa}(k) - \Gamma_{ss}(k)\Big]}{\left[\Big(\cos(2\theta) + \Delta_R(k)\Big)^2 + \sin^2(2\theta)\right]^{\frac{1}{2}}} \; . \tag{3.4.33}$$

For $h = -1$, $(\Gamma_{aa} - \Gamma_{ss})$ and Δ_R are dominated by the SM contributions, therefore from Eqs. (3.3.15) and (3.4.24), we find

$$\Delta_R(k) \sim \frac{g^2}{16\pi^2}\frac{kT}{M_s^2}\,\mathcal{A}(k) \; , \tag{3.4.34}$$

$$\Delta_I(k) \sim \frac{g^2}{32\pi}\frac{kT}{M_s^2}\left(\frac{M_Z}{k}\right)^2 \mathcal{B}(k) \, , \tag{3.4.35}$$

where $\mathcal{A}(k), \mathcal{B}(k)$ can be read off (3.3.15) and (3.4.24). In the region of parameters where $\Delta_R(k) \gg \cos(2\theta) \sim 1$, it follows that $\tilde{\gamma} \simeq \Delta_I(k)/\Delta_R(k)$, furthermore, for $k < T \sim M_{\{Z,W\}}$ the function $\mathcal{B}(k) \sim e^{-x_Z^*} \ll 1$, leading to $\Delta_I/\Delta_R \ll 1$ corresponding to the weak damping case in which the widths, or the production rates, are given by (3.4.7) and (3.4.8). On the other hand, when far away from the MSW resonances but in the region where $\cos(2\theta) \sim 1 \gg \Delta_R(k)$, it also follows that $\Delta_I/\Delta_R \ll 1$, corresponding again to the weak damping regime. Therefore the parameter region far away from MSW resonances, either above or below, corresponds to the weak damping regime.

When close to the MSW resonances $\cos(2\theta) + \Delta_R \sim 0$ and $\tilde{\gamma} \sim \Delta_I/|\sin(2\theta)|$, in the region of relevance for our analysis $T \sim M_{\{Z,\,W\}}$ with $M_s \sim$ keV, it follows that

$$\frac{\Delta_I(k)}{|\sin(2\theta)|} \sim \frac{4\times 10^{13}}{|\sin(2\theta)|}\left(\frac{k}{T}\right)\left(\frac{M_Z}{k}\right)^2 \mathcal{B}(k) \; . \tag{3.4.36}$$

Since the resonance occurs at $k/T < 1$ for $M_{\{Z,\,W\}} \sim T$, we conclude that the strong damping condition $\tilde{\gamma} \gg 1$ is fulfilled *near MSW resonances*. Because the MSW resonance(s) are very narrow for $T \simeq M_{\{Z,\,W\}}$ as discussed above (See the discussion leading to Eq. (3.3.18).), we conclude that in most of the regime of temperatures and momenta, the weak damping results

(3.4.7) and (3.4.8) are valid; and only in a very narrow region near the MSW resonances, the strong damping results (3.4.11) and (3.4.12) are needed. An identical analysis confirms a similar conclusion for the case $h = 1$, namely, the weak damping condition holds in most of the relevant range of $\{M/T,\ k/T\}$ but for a narrow region near the MSW resonances in which the strong damping condition holds.

An alternative interpretation of the weak and strong damping regime is obtained using Eq. (3.4.9) to write

$$\tilde{\gamma} \simeq \frac{\Gamma_{aa} - \Gamma_{ss}}{\Delta\Omega_{wd}} \ . \tag{3.4.37}$$

Since $\Delta\Omega_{sd} \leq \Delta\Omega_{wd}$ the denominator gives an upper bound to the oscillation frequency between the active and sterile neutrinos. The weak damping regime $|\tilde{\gamma}| \ll 1$ describes the case in which there are many oscillations before the overlap amplitude is suppressed, whereas the strong damping regime describes the case in which damping occurs before oscillations take place. For a similar discussion see the references in [66, 67, 170].

3.4.4 Regime of validity of perturbation theory.

In the relativistic approximation, the validity of the perturbative expansion requires that $k \gg \{\Sigma_{bsm},\ \Sigma_{sm}\}$. Since the weak interaction coupling constant g_{sm} is much larger than $Y_{\{1,\ 2\}}$, we focus on the SM contributions only. From the expression (3.3.9) and the results displayed in Figure 9, we see that for $M_W/T \gtrsim 1$, $\mathrm{Re}\Sigma_{sm} \propto \alpha_w T$ since the coefficient functions $\{A,\ B\} \lesssim 12$. Therefore, perturbation theory is valid for $k \gg T/30$, hence for $M_W/T \gtrsim 1$ the resonances in absence of lepton asymmetry at $0.2 \lesssim k/T \lesssim 1$ for $1 \lesssim M_W/T \lesssim 3$ are comfortably within the regime of validity of the perturbative expansion. The lepton-asymmetry induced resonance for $k/T \ll M_W/T$ is the usual resonance and for $T \ll M_W$ the expressions (3.3.10) to (3.3.12) reduce to the results available in the literature [230, 171]. In the regime $k \ll T < M_W$, the on-shell self-energies are linear in k. We see that, for $g^2 \sim 0.4$, the terms proportional to k are $\ll 1$ for $M_W \gtrsim 2T$, hence perturbation theory is reliable within the regime of interest in this article. The imaginary parts are always perturbatively small because of the exponential suppression factors $e^{-M^2/kT}$.

3.5 NEUTRINO PRODUCTION IN AN EXPANDING UNIVERSE

In this study, we aim to study the production of sterile neutrinos in cosmology near the electroweak scale when the universe is radiation dominated. To include the effects of cosmological expansion in the production rates and mixing angles, one must first replace the momentum $k \to k_p(t) = k/a(t)$ and temperature $T \to T(t) = T_i \, \frac{a_i}{a(t)}$, where k is the comoving momentum, $a(t)$ the scale factor and $\{T_i,\ a_i\}$ correspond to the initial temperature and scale factor at which the kinetic equations are initialized. Whereas the ratio $k_p(t)/T(t) = k/(T_i\ a_i)$ is constant, and $M/T(t) = Ma(t)/(T_i\ a_i)$ grows during the expansion. Consider setting initial conditions at $T_i \lesssim M_W$, so that $M/T_i \sim 1$, the analysis in Sec. 3.3 shows that there exists at least one very narrow MSW resonance even for nearly right-handed sterile neutrinos (two if a lepton asymmetry in the neutrino sector is included) at a value $\left(\frac{k_p(t)}{T(t)}\right)_c < 1$.

For $\frac{k_p(t)}{T(t)} < \left(\frac{k_p(t)}{T(t)}\right)_c$, the analysis shows that $\Delta_R \gg 1$ and

$$\theta_m \sim \frac{\theta}{\Delta_R} \ll \theta \,, \tag{3.5.1}$$

correspondingly, we find

$$\begin{aligned} \Gamma_1 &\sim \Gamma_{aa} \,, \\ \Gamma_2 &\sim \Gamma_{ss} + \left(\frac{\theta}{\Delta_R}\right)^2 \Gamma_{aa} \,. \end{aligned} \tag{3.5.2}$$

In this case, the mode "1" is active-like and it is produced with a weak interaction rate, whereas the mode "2" is sterile like and is produced with the rate similar to that in Ref. [61] plus small corrections from SM interaction suppressed by the mixing angle in the medium $\sim \theta/\Delta_R$. On the other hand, if $\frac{k_p(t)}{T(t)} > \left(\frac{k_p(t)}{T(t)}\right)_c$, we found that $\Delta_R \ll -1$ leading to $\theta_m \sim \pi/2$, namely, the mode "1" becomes sterile-like and the mode "2" is active like, with the production rates

$$\begin{aligned} \Gamma_1 &\sim \left(\frac{\theta}{2\Delta_R}\right)^2 \Gamma_{aa} + \Gamma_{ss} \,, \\ \Gamma_2 &\sim \Gamma_{aa} \,. \end{aligned} \tag{3.5.3}$$

As the cosmological expansion proceeds, eventually $M/T(t) \gg 1$ and the resonances disappear, for example, in absence of a lepton asymmetry, the MSW resonances for $k_p(t)/T(t) < 1$ disappear around $M/T(t) \gtrsim 3$. Δ_R remains large but positive, the mixing angle in the medium is given by (3.5.1), and the production rates are given by (3.5.2) for all values of $k_p(t)/T(t)$, namely the mode "1" remains the active-like and the mode "2" the sterile-like.

In Sec. 3.4.1, we note that

$$\{\Gamma_{ss},\ \Gamma_{aa}\} \propto \left(\frac{M^2}{k^2}\right) \ln\left[\frac{1}{1-e^{-x^*}e^{-y}}\right], \tag{3.5.4}$$

this is precisely the form of the production rate that leads to a freeze-out distribution function enhanced at small momentum, a feature that leads to a larger free streaming length and transfer function at small scales [61].

During the time when $M/T(t) \sim 1$, the MSW resonance leads to a non-thermal population of neutrinos: for $\frac{k_p(t)}{T(t)} < \left(\frac{k_p(t)}{T(t)}\right)_c$, there is a bigger production rate, leading to large populations, of mode "1", and a smaller production rate, leading to small populations, of "2" (sterile like); whereas for $\frac{k_p(t)}{T(t)} > \left(\frac{k_p(t)}{T(t)}\right)_c$, there is a "population inversion" in the sense that mode "1" is slightly populated whereas mode "2" will be substantially populated, however, without the small momentum enhancement. Consider a fixed value of $k_p(t)/T(t) < 1$ during the cosmological expansion, the ratio $M/T(t) \propto a(t)$ increases, sweeping through the MSW resonance. When it happens, the mixing angle in the medium vanishes very rapidly because of the narrow resonance and the mode "2" becomes sterile-like. As the expansion continues, the MSW resonances in absence of a lepton asymmetry disappear altogether, and the mixing angles and production rates are given by (3.5.1) and (3.5.2) respectively for all values of $k_p(t)/T(t)$. The population of the active-like neutrino, namely mode "1", continues to build up via weak interaction processes, including those that become dominant at $T \ll M_W$ and eventually thermalizes, whereas the population of the sterile-like neutrino will be frozen-out as the production rate Γ_2 shuts-off since Γ_{ss} vanishes rapidly for $M/T(t) \ll 1$ (See Ref. [61].)

and $\theta_m \to 0$ as $M/T(t) \gg 1$ even when Γ_{aa} remains large down to the decoupling temperature of weak interactions ~ 1 MeV.

This analysis indicates that sterile neutrino production via the decay of scalar or vector bosons will be effective only around the region of $M_W/T(t) \sim 1$, and the distribution function at freeze-out will be *strongly non-thermal* with very small population but an enhancement at small momentum as found in Ref. [61]. However, the weak interaction contribution will freeze out much later, depending on the temperature dependence of the mixing angle in the medium and will eventually merge with the non-resonant (DW) production mechanism [113] at $T \sim 130$MeV. Even though, the non-thermal distribution built up during the time when scalar and vector boson decays dominate the production will remain.

Finally, it is important to understand the self-consistency of the analysis. In obtaining the self-energies we had assumed that the eigenstate "1" is active-like with a thermal distribution function. We have learned, however, that there are resonances and whether the eigenstates "1" and "2" are active-like or sterile-like depending on k, namely on which side of the MSW resonance the wave vector lies. This finding calls into question the thermal nature of the neutrino propagator in the intermediate state. (Of course there is no such ambiguity in the charged lepton propagator that enters in the charged current self-energy.) Notwithstanding this issue, we have found that the fermionic and bosonic contributions to the real parts of the self-energies are qualitatively the same with a rather small quantitative difference, both for SM and BSM contributions. Therefore, replacing the thermal fermion propagator for a vacuum one leads to a minor quantitative modification of our arguments. Because of the enormous pre-factors, the conclusions about the sharpness of the resonance and the resonance positions do not change and the general analysis remains the same. Therefore, we conclude that the results obtained above are robust, not depending on whether the intermediate fermion line features a thermal or vacuum propagator or non-thermal propagator interpolating between these two cases.

3.6 CONCLUSION

A comprehensive program to assess the viability of any potential DM candidate begins with the microphysics of the production and freeze-out process of the particle physics candidate. This initial step determines the distribution function at freeze-out which in turn determines, along with the mass, its abundance, free streaming length, phase space density at decoupling and the transfer function and power spectrum in the linear regime. Our objective is to carry out this program for sterile neutrinos with mass in the keV range which seems to be the range favored not only as a DM candidate [49, 81] but also provide potential solutions to a host of astrophysical problems [200, 33, 49, 199].

In this chapter, we focus on the first step, to study the production of sterile neutrinos in a temperature regime near the electroweak scale in an extension beyond the standard model, in which the see-saw mass matrix emerges from expectation values of Higgs-like scalars with masses of the order of the electroweak scale. This simple and compelling extension of the SM features only one scale yet yields rich phenomenology [200, 33, 49, 199, 258, 256, 257, 237]. The main observation in this study is that in this temperature range, sterile neutrinos are produced by the decay not only of the Higgs-like scalar as explored in Refs. [237, 61] but also of the charged and neutral vector bosons of the SM. We consider active and sterile species to be Dirac fermions to allow a lepton asymmetry hidden in the active neutrino sector consistent with recent bounds from WMAP and BBN [261].

The assessment of the contribution from the SM vertices to sterile neutrino production requires an analysis of the mixing angles in the medium and production rates. We extract these information from the full equation of motion of the active and sterile neutrinos, which contains the self-energies corrections in the medium. The real part of the self-energy determines the dispersion relations and mixing angles in the medium, and the imaginary part determines the production rates. We analyze and compare the contributions from "beyond the standard model" and standard model interactions to the mixing angles, dispersion relations and production rates, thereby facilitating the analysis of different situations.

By including a small lepton asymmetry in the neutrino sector with a value compatible with the bounds from WMAP and BBN [261], we found the usual MSW resonances at $k < \mu \ll T$, where μ is the chemical potential for the active species that determines the lepton asymmetry. Moreover, *even in the absence of a lepton asymmetry*, we identify another kind of MSW resonances in the temperature regime $T \gtrsim M_W$ for $k/T \lesssim 1$. Both resonances are very narrow. For the vanishing lepton asymmetry case, the resonance occurs at a value $(k/T)_c$ that depends on the ratio M_W/T with $0.15 \lesssim (k/T)_c \lesssim 1$ for $1 \lesssim (M_W/T) \lesssim 3$. The position of the resonance $(k/T)_c$ increases with M_W/T, the resonance eventually disappear for $M_W \gg T$ recovering the result valid in the Fermi limit of the weak interactions [230, 171]. Near these resonances, the contribution of the imaginary part of the self-energies leads to a strong damping regime, and the difference in the propagating frequencies vanishes exactly at the position of the resonance, with a concomitant breakdown of the adiabaticity. Furthermore, we have found that it is quite possible that the region of parameters of the extension beyond the SM allows for MSW resonances for positive energy, positive helicity, namely nearly right-handed states both with and without lepton asymmetry. We also find that the decay of the $\{Z^0,\ W^{\pm}\}$ vector bosons leads to the production of nearly right-handed sterile-like neutrinos. Because the resonances are very narrow, we obtain simple expressions for the production rates of active and sterile neutrinos in Sec. **??**, which are valid in a wide range of temperatures and clearly displays the contribution from SM and BSM interactions.

Finally, we apply our results and observations to an expanding universe. We have argued that in the early universe the cosmological expansion leads to a highly non-thermal distribution function for sterile neutrinos with an enhancement at the low momentum region $k < T$ both as a consequence of the narrow MSW resonances and the vanishing of the mixing angle and production rates below the electroweak scale. The form of the production rates via scalar and vector boson decay are similar to that found in Ref. [61], thus we expect that due to small momentum enhancement, sterile neutrinos would feature a smaller free streaming length and larger power spectrum at small scales as compared to the DW mechanism [113, 61]. These observations may yield interesting applications in cosmological

density fluctuations, which is the main topic of the following chapter.

4.0 PART I: LINEAR STRUCTURE GROWTH IN THE WDM SCENARIO

In this chapter, we consider the dynamics of linear structure formation in the WDM scenario. In particular, we focus on small scale aspects, where WDM particles behave very different from CDM particles and may yield interesting applications in cosmology, e.g., to solve the small scale problems [244, 196] in the standard ΛCDM scenario. This study was published in [68], based on which, this chapter is re-organized as follows. In Sec. 4.1, the basic expansion history of the universe is introduced, defining useful parameters convenient for later discussions. Then, in Sec. 4.2, we focus on density perturbations of the universe, and discuss the general aspects of the history of structure formation, valid for both CDM and WDM. Sec. 4.3 compares the CDM and the WDM scenarios in a qualitative way, where we also present our strategy of analytically studying the WDM case. Secs. 4.4 and 4.5 are devoted to detailed studies of the CDM and WDM cases respectively. Although density fluctuations have been thoroughly studied for the CDM case in the literature, we provide an alternative point of view in Sec. 4.4, which helps to understand the connection between the CDM and the WDM scenarios. It provides a benchmark for later discussions on the WDM case. In Sec. 4.6, from the study in Sec. 4.5, we obtain the transfer function and the power spectrum for arbitrary WDM mass and distribution function. Then we consider two specific cases and discuss several interesting features of the WDM transfer function and power spectrum. Furthermore, we compare our semi-analytical results with those from Boltzmann codes [165, 1, 274] in some known cases, and comment on the possible application in current analysis of cosmological data. Finally, we conclude this chapter and summarize our results in Sec. 4.7.

4.1 COSMOLOGY PRELIMINARIES: FRIEDMAN EQUATION

In this chapter, we adopt the geometric units $G = c = \hbar = 1$ and only consider a radiation and matter dominated cosmology. Primordial density fluctuations grow since the RD era and become significant in the MD era, forming all the structures we observe today. Only very recently, our universe has become dominated by dark energy (ΛD) [260, 87]. In a matter-radiation cosmology, the Friedman equation that governs the Hubble expansion is given by

$$H^2 = \frac{\dot{a}^2}{a^2} = H_0^2 \left(\frac{\Omega_r}{a^4} + \frac{\Omega_m}{a^3} \right) = \frac{H_0^2 \Omega_m}{a^4}(a + a_{eq}), \tag{4.1.1}$$

where the dot stands for derivative with respect to conformal time η instead of cosmological time t, the scale factor is normalized to $a_0 = 1$ today, and

$$a_{eq} = \frac{\Omega_r}{\Omega_m} \simeq \frac{1}{3229}. \tag{4.1.2}$$

By introducing

$$\tilde{a} = \frac{a}{a_{eq}}, \tag{4.1.3}$$

it follows that in conformal time η,

$$\frac{d\tilde{a}}{d\eta} = H_0 \left(\frac{\Omega_m}{a_{eq}} \right)^{1/2} \sqrt{1 + \tilde{a}}. \tag{4.1.4}$$

Solving the above equation, we find the conformal time

$$\eta = 2 \left(\frac{a_{eq}}{H_0^2 \ \Omega_m} \right)^{1/2} \left[\sqrt{1 + \tilde{a}} - 1 \right] = 288.46 \left[\sqrt{1 + \tilde{a}} - 1 \right] \text{ Mpc}, \tag{4.1.5}$$

where we have used $\Omega_m h^2 = 0.134$ [202, 195]. At matter-radiation equality, we define

$$k_{eq} = H_{eq} a_{eq} = \left(\frac{H_0^2 \Omega_m}{a_{eq}} \right)^{1/2} \sqrt{2} \simeq 9.8 \times 10^{-3} (\text{Mpc})^{-1}, \tag{4.1.6}$$

which is the co-moving wave vector of perturbation mode that enters the Hubble radius at matter-radiation equality. Correspondingly, from Eq. (4.1.5), the co-moving horizon at matter-radiation equality is

$$\eta_{eq} = \frac{2\sqrt{2}}{H_{eq} a_{eq}} (\sqrt{2} - 1) \simeq 120 \text{ Mpc}. \tag{4.1.7}$$

Combining the above information and solving (4.1.5), we find

$$\tilde{a} = \frac{\eta}{\eta_*}\left(\frac{\eta}{4\eta_*} + 1\right), \tag{4.1.8}$$

where

$$\eta_* = \frac{\sqrt{2}}{k_{eq}} = \frac{\eta_{eq}}{2(\sqrt{2}-1)}. \tag{4.1.9}$$

In the RD era where $\eta/\eta_* \ll 1$, it yields

$$\eta \simeq \tilde{a}\eta_* \simeq 144.23\ \tilde{a}\ \text{Mpc}; \tag{4.1.10}$$

On the other hand, in the MD era where $\eta/\eta_* \gg 1$, it yields

$$\tilde{a} \simeq \frac{\eta^2}{4\eta_*^2}. \tag{4.1.11}$$

4.2 DENSITY PERTURBATION OF DMS: GENERAL ASPECTS

Structure formation is an important topic in cosmology because it explains the formation of all galaxies and clusters that we observe today in our universe. Observations on large scales and the near isotropy of the CMB suggest that our universe is isotropic and homogeneous, consistent with the Friedman-Robertson-Walker (FRW) metric [112, 281]. However, the local universe is highly anisotropic and inhomogeneous. It is generally believed that all these inhomogeneous structures began with tiny quantum fluctuations during inflation, these fluctuations grow under gravitational collapse during the evolution history of the universe and become what we observe today. Following this logic, to study density fluctuations, we have to perturb the homogenous universe and track the time evolution of these perturbations. A complete and self-consistent study of density and gravitational perturbations should be done within the framework of GR, which describes the gravitational interaction that are essential for structure formation of the universe. Equations governing these cosmic fluctuations in the framework of GR were first derived by Ma and Bertschinger [212]. Since perturbations of all components in the universe are coupled together through gravitational interactions, it is difficult to analytically solve the coupled system. For our purposes, we focus on density

perturbations of the DM component because they are directly related to structure formation of the universe. Most DM candidates decouple from the thermal plasma in the early universe, after freeze-out the time evolution of DM distribution functions is governed by the collision-less Boltzmann equation. Density and gravitational perturbations are studied by linearizing the perturbed collision-less Boltzmann equation.

4.2.1 Collision-less Boltzmann Equation

The collision-less Boltzmann equation [112, 281, 212] is:

$$\frac{d}{d\eta} f(\vec{x}, \vec{p}, \eta) = 0. \tag{4.2.1}$$

η is the conformal time (also the co-moving horizon in the geometric unit). This equation is valid for any DM particle after decoupling from the Local Thermal Equilibrium (LTE). By expanding Eq. (4.2.1) out, we find

$$\frac{d}{d\eta} f(\vec{x}, \vec{p}, \eta) = \left(\frac{\partial}{\partial \eta} + \vec{v} \cdot \vec{\nabla}_{\vec{x}} + \frac{d\vec{p}}{d\eta} \cdot \vec{\nabla}_{\vec{p}} \right) f(\vec{x}, \vec{p}, \eta) = 0, \tag{4.2.2}$$

where $\vec{\nabla}_{\vec{x}}$ and $\vec{\nabla}_{\vec{p}}$ correspond to the gradient with respect to the coordinate $\vec{x}$ and the momentum $\vec{p}$ respectively. The co-moving velocity $\vec{v}$ is defined as

$$\vec{v} := \frac{d\vec{x}}{d\eta}, \tag{4.2.3}$$

and $d\vec{p}/d\eta$ is determined by the geodesic equation of the DM particle. If we choose to work in the conformal Newtonian (longitudinal) gauge, which is convenient to extract the physical insight, perturbations of the metric are given by,

$$g_{00} = -a^2(\eta) \left[1 + 2\psi(\vec{x}, \eta)\right], \tag{4.2.4}$$

$$g_{ij} = a^2(\eta) \left[1 - 2\phi(\vec{x}, \eta)\right]. \tag{4.2.5}$$

By neglecting the stress anisotropy, not important for DM density perturbations, $\psi(\vec{x}, \eta) = \phi(\vec{x}, \eta)$. Hence, spacetime perturbations are characterized by the single quantity ϕ, corresponding to gravitational potential in the Newtonian limit.

4.2.1.1 Unperturbed Collision-less Boltzmann Equation

To study density perturbations of DM, we write

$$f(\vec{x},\vec{p},\eta) = f_0(\vec{x},\vec{p},\eta) + f_1(\vec{x},\vec{p},\eta) + f_2(\vec{x},\vec{p},\eta) + ..., \tag{4.2.6}$$

where f_0 is the unperturbed distribution function, f_1 is the first order perturbation of the distribution function, and f_2 is the second order perturbation, etc. We only consider the linear perturbation f_1 in this chapter. The isotropy and homogeneity of the unperturbed universe described by the FRW metric suggest that f_0 is isotropic and homogeneous, therefore a function of $p = |\vec{p}|$ and η only, yielding $f_0 = f_0(p,\eta)$. It turns out convenient to work with the time independent co-moving momentum $\vec{p}_c$, which satisfies

$$\frac{dp_c}{d\eta} = 0. \tag{4.2.7}$$

Correspondingly, from Eq. (4.2.2), the collision-less Boltzmann equation yields

$$\frac{\partial}{\partial\eta} f_0(p_c,\eta) = 0, \tag{4.2.8}$$

Hence, f_0 only depends on the magnitude of the co-moving momentum p_c, namely, $f_0 = f_0(p_c)$, reflecting the fact that f_0 is static with respect to conformal time η.

As discussed in Refs. [64, 61, 65], in general, f_0 is a function of $y = p_c/T_{0,d}$ and $x = m/T_d$, where m is the mass of DM particles, T_d the decoupling temperature and $T_{0,d}$ the decoupling temperature today. From conservation of the total entropy, it is easy to find

$$T_{0,d} = T_{CMB}\left(\frac{2}{g_d}\right)^{1/3}, \tag{4.2.9}$$

where T_{CMB} is the temperature of the CMB photons today and g_d is the number of ultra-relativistic degrees of freedom at decoupling. The specific expression of f_0 depends on the properties of DM particles and the physics of decoupling. We are interested in keV sterile neutrinos as a WDM candidate. According to Chap. 3, sterile neutrinos can be produced in

various mechanisms, among which Dodelson-Widrow (DW) mechanism [113, 81] and Higgs-like scalar decay (BD) [198, 237, 236, 65, 61, 285] mechanism are of particular interest [1]. Both production mechanisms lead to non-thermal distribution functions of f_0. For the DW mechanism,

$$f_0(y) = \frac{\beta}{e^y + 1}, \tag{4.2.10}$$

where $\beta \simeq 10^{-2}$ [113, 61]. As for the sterile neutrinos produced through decay of a Higgs-like scalar beyond the SM,

$$f_0(y) = \lambda \frac{g_{5/2}(y)}{\sqrt{y}}, \tag{4.2.11}$$

where

$$g_{5/2}(y) = \sum_{n=1}^{\infty} \frac{e^{-ny}}{n^{5/2}}, \tag{4.2.12}$$

and $\lambda \simeq 10^{-2}$ for keV sterile neutrinos [61]. As a comparison, we also consider the most popular CDM candidate, WIMPs, with masses of 100GeV and decoupling temperature $T_d \simeq$ 10MeV, which freeze-out with a Maxwell-Boltzmann (MB) distribution, hence

$$f_0(y) = \mathcal{N} e^{-\frac{y^2}{2x}}. \tag{4.2.13}$$

Here $\mathcal{N}$ is just a normalization constant, and recall that $x = m/T_d$. For later convenience, we define

$$\overline{y^2} = \frac{\int_0^\infty dy y^4 f_0(y)}{\int_0^\infty dy y^2 f_0(y)} := \frac{1}{N} \int_0^\infty dy y^4 f_0(y), \tag{4.2.14}$$

where

$$N = \int_0^\infty dy y^2 f_0(y). \tag{4.2.15}$$

Direct calculation shows that for the three unperturbed distributions discussed above, we have

$$\overline{y^2} = \begin{cases} 15\dfrac{\zeta(5)}{\zeta(3)} = 12.939 & DW \\ \dfrac{35\zeta(7)}{4\zeta(5)} = 8.509 & BD \\ 3x = \dfrac{3m}{T_d} & MB \end{cases} \tag{4.2.16}$$

[1] In Chap. 3, we also discuss sterile neutrinos produced by decay of SM vector bosons. Due to the complications associated with MSW resonances, we could not obtain an explicit distribution function for such production mechanism; however, we have argued that it is expected to produce a similar distribution function to that of BD. (See the conclusion section in Sec. 3.6.)

4.2.1.2 Linearly Perturbed Collision-less Boltzmann Equation

The first order perturbation of the collision-less Boltzmann equation yields the time evolution of the first order perturbed distribution function f_1. Defining

$$F_1(\vec{x}, \vec{p}_c, \eta) = \frac{1}{N} f_1(\vec{x}, \vec{p}_c, \eta), \tag{4.2.17}$$

where N is defined in Eq. (4.2.15), then, $F_1(\vec{x}, \vec{p}_c, \eta)$ obeys the following equation:

$$\frac{\partial}{\partial \eta} F_1(\vec{x}, \vec{p}_c, \eta) + \vec{v} \cdot \vec{\nabla}_{\vec{x}} F_1(\vec{x}, p_c, \hat{n}, \eta) + \frac{d\tilde{f}_0}{dp_c} \left(\frac{dp_c}{d\eta}\right) = 0, \tag{4.2.18}$$

where

$$\tilde{f}_0 = \frac{f_0}{N} \tag{4.2.19}$$

and $\vec{p}_c = p_c \hat{n}$ with $\hat{n}$ being a unit vector. To obtain Eq. (4.2.18), we have made use of the fact of $\tilde{f}_0 = \tilde{f}_0(p_c)$. Note that $\tilde{f}_0$ instead of F_1 appears in the last term of Eq. (4.2.18). The reason is simple, because $\frac{dp_c}{d\eta} = 0$ for the unperturbed distribution function. In the linearly perturbed collision-less Boltzmann equation, it becomes perturbatively non-vanishing under the gravitational interactions. Recall the geodesic equation in the conformal Newtonian gauge:

$$\frac{dp_c}{d\eta} = p_c \dot{\phi} - \epsilon(p_c, \eta) \hat{n} \cdot \vec{\nabla} \phi, \tag{4.2.20}$$

where $\epsilon(p_c, \eta)$ is the co-moving energy defined as

$$\epsilon(p_c, \eta) = \sqrt{p_c^2 + m^2 a^2}. \tag{4.2.21}$$

m is the mass of the DM particles, and $\vec{v} = d\vec{x}/d\eta = \vec{p}_c/\epsilon$. Inserting Eq. (4.2.20) into (4.2.18) and Fourier expanding the linearly perturbed collision-less Boltzmann equation in the k-space, we find for F_1 that

$$\frac{\partial}{\partial \eta} F_1(\vec{x}, p_c, \hat{n}, \eta) + i \frac{p_c}{\epsilon} (\hat{n} \cdot \vec{k}) F_1(\vec{k}, p_c, \hat{n}, \eta) + \frac{d\tilde{f}_0}{dp_c} \left[p_c \dot{\phi} - i(\hat{n} \cdot \vec{k}) \epsilon \phi\right] = 0. \tag{4.2.22}$$

By solving Eq. (4.2.22), we obtain the time evolution of F_1, and calculate physical quantities such as the perturbed number density and the perturbed energy density defined as

$$\delta = \int dy y^2 F_1(y, \eta), \tag{4.2.23}$$

$$\frac{\delta\rho}{\rho_0} = \frac{\int dy y^2 F_1(y, \eta) \epsilon(y, \eta)}{\int dy y^2 \tilde{f}_0(y) \epsilon(y, \eta)}. \tag{4.2.24}$$

To simplify the notation, we replace p_c by q. Correspondingly the linearly perturbed collisionless Boltzmann equation becomes

$$\frac{\partial}{\partial\eta}\ F_1(\vec{k},q,\hat{n},\eta)+i\frac{q}{\epsilon}(\hat{n}\cdot\vec{k})\ F_1(\vec{k},q,\hat{n},\eta)+\frac{d\tilde{f}_0}{dq}\ \left[q\dot{\phi}-i(\hat{n}\cdot\vec{k})\epsilon\phi\right]=0. \tag{4.2.25}$$

4.2.2 Formal Solution Of The Linearly Perturbed Collision-less Boltzmann Equation

As pointed out previously, we need to solve Eq. (4.2.25) to find the time evolution of F_1. Formally, we can get the solution very easily. We combine the first two terms in Eq. (4.2.25) as a total derivative by multiplying Eq. (4.2.25) by $e^{i\vec{k}\cdot\int_{\eta_0}^{\eta}\vec{v}(\eta')d\eta'}$, where $\vec{v}$ is given in (4.2.3) and $\vec{l}$ is defined as

$$\vec{l}=\int_{\eta_0}^{\eta}\vec{v}(\eta')d\eta'. \tag{4.2.26}$$

$\vec{l}$ corresponds to the free steaming distance of DM particles with momentum $\vec{q}$, namely the distance traveled by these DM particles freely from time η_0 to η. Let $\mu=\hat{n}\cdot\hat{k}$. In terms of l and μ, we obtain the formal solution

$$\begin{aligned}&F_1(k,q,\mu,\eta)\\ =\ & e^{-ik\mu(l-l_0)}F_1(k,q,\mu,\eta_0)-q\frac{d\tilde{f}_0}{dq}\int_{\eta_0}^{\eta}d\eta'\ e^{-ik\mu(l-l')}\left(\dot{\phi}(k,\mu,\eta')-ik\mu\frac{\epsilon}{q}\phi(k,\mu,\eta')\right),\end{aligned} \tag{4.2.27}$$

where l, l', l_0 correspond to Eq. (4.2.26) with upper limits η, η' and η_0 respectively. Eq. (4.2.27) gives the formal solution of the perturbed distribution function. To actually get an expression of F_1, we need to know the gravitational potential ϕ and carry out the integral explicitly. From the linearly perturbed Einstein equation, time evolution of ϕ in the conformal Newtonian gauge is governed by [112, 281]

$$\phi(\vec{k},\eta)+3\frac{\mathcal{H}}{k}\left(\frac{\dot{\phi}(\vec{k},\eta)}{k}+\frac{\mathcal{H}}{k}\phi(\vec{k},\eta)\right)=-\frac{3}{4}\frac{k_{eq}^2}{k^2\tilde{a}^2}\left[\tilde{a}\left(\frac{\delta\rho}{\rho}\right)_m+\left(\frac{\delta\rho}{\rho}\right)_r\right], \tag{4.2.28}$$

where $\mathcal{H}$ is defined as:

$$\mathcal{H}=\frac{\dot{\tilde{a}}}{\tilde{a}}. \tag{4.2.29}$$

Again, the dot stands for derivative with respect to the conformal time η, and $\tilde{a}$ is the scale factor divided by a_{eq} (See Eq. (4.1.3)). When the universe is RD, $\tilde{a} \ll 1$, $(\delta\rho/\rho)_r$ dominates the density perturbation while when the universe is MD, $\tilde{a} \gg 1$, $(\delta\rho/\rho)_m$ becomes dominant. [2]

Recall that $\delta\rho_{\{r,m\}}$ are related to F_1 as indicated in Eqs. (4.2.23) and (4.2.24), making (4.2.27) a self-consistent equation. According to GR, the gravitational potential ϕ and F_1 form a coupled system and need to be solved together. When the universe is in the RD era, contribution from $(\delta\rho/\rho)_m$ is totally negligible. In such a case, ϕ is analytically solvable [112, 281], it is determined by acoustic oscillations of the photon fluid and given by

$$\phi(k,\eta) = -3\phi_i \frac{\frac{z}{\sqrt{3}}\cos(\frac{z}{\sqrt{3}}) - \sin(\frac{z}{\sqrt{3}})}{\left(\frac{z}{\sqrt{3}}\right)^3}, \tag{4.2.30}$$

where ϕ_i is the initial value and $z = k\eta$ with k being the co-moving wave vector. The $1/\sqrt{3}$ represents the sound speed in the photon fluid. z is a useful quantity because $2\pi/k = \lambda$ corresponds to the size of the perturbation modes. When $z < 2\pi$, $\lambda > \eta$, these modes are outside of the co-moving horizon; for $z > 2\pi$, the corresponding modes are within the horizon. The behavior of ϕ in the RD era is illustrated in Figure 13, from which we see that, for any given k, the perturbed gravitational potential drops dramatically (cubic power law, see z^{-3} in Eq. (13)) after the corresponding perturbation mode enters the horizon.

Similarly, when the universe enters in the MD era, Eq. (4.2.28) can also be simplified because now matter density perturbations dominate, and radiation density perturbations can be safely neglected [112, 281]. Moreover, all the perturbation scales responsible for the structures observed today have been well into the co-moving horizon before matter-radiation equality, therefore, the corresponding equation for ϕ reduces to the familiar Newtonian Poisson equation, namely

$$\phi(\vec{k},\eta) = -\frac{3}{4}\frac{k_{eq}^2}{k^2\tilde{a}}\left(\frac{\delta\rho}{\rho}\right)_m. \tag{4.2.31}$$

[2] In the CDM case, $(\delta\rho/\rho)_m$ dominates over $(\delta\rho/\rho)_r$ in the RD era soon after perturbation modes enter the horizon. This phenomenon is called radiation cross-over, which will be discussed in the following.

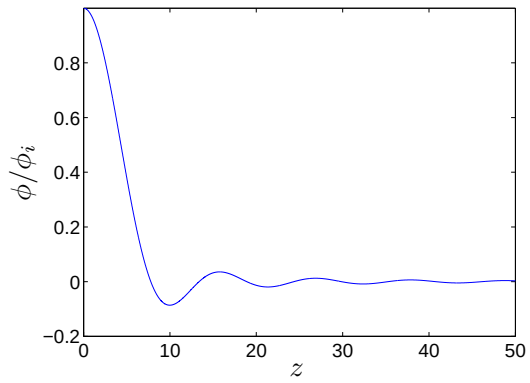

Figure 13: Perturbed gravitational potential ϕ in the RD era.

4.2.3 Initial Condition

From the physical point of view, initial conditions are determined by inflation. At such early time, all the perturbation modes that we are interested in are outside of the horizon, therefore, we only need to consider super-horizon modes, corresponding to taking $k \to 0$. According to Eq. (4.2.27), F_1 becomes

$$\begin{aligned} F_1(k,q,\mu,\eta) &= F_1(k,q,\mu,\eta_0) - q\frac{d\tilde{f}_0}{dq}\int_{\eta_0}^{\eta} d\eta'\dot{\phi} \\ &= F_1(k,q,\mu,\eta_0) - q\frac{d\tilde{f}_0}{dq}\Big(\phi(k,\eta) - \phi_i(k)\Big), \end{aligned} \tag{4.2.32}$$

where $\phi_i(k)$ is the initial value of the gravitational potential generated during inflation. For the radiation components,it is useful to write F_1 as

$$F_1(k,q,\mu,\eta) = -\Theta_r(k,\mu,\eta)q\frac{d\tilde{f}_0}{dq}, \tag{4.2.33}$$

where the subscript r represents the radiation component. Combining Eqs. (4.2.32) and (4.2.33), we have, for the super-horizon modes of radiation components,

$$\Theta_r(k,\mu,\eta) - \phi(k,\eta) = \Theta_{ri}(k) - \phi_i(k) = \text{const.}; \tag{4.2.34}$$

For matter density perturbations, it is helpful to calculate the number density perturbation δ, where

$$\delta = \int d\vec{q} F_1(k, q, \mu, \eta) = 3\phi(k, \eta) + \delta_i - 3\phi_i(k), \tag{4.2.35}$$

thus, for the super-horizon modes of matter components,

$$\delta - 3\phi(k, \eta) = \delta_i - 3\phi_i = \text{const.}. \tag{4.2.36}$$

Now, let us consider the gravitational potential in Eq. (4.2.28). Because i) $k \to 0$ and ii) the early universe is completely RD, Eq. (4.2.28) reduces to

$$\mathcal{H}\dot{\phi}(\vec{k}, \eta) + \mathcal{H}^2\phi(\vec{k}, \eta) = -\frac{\mathcal{H}^2}{2}\left(\frac{\delta\rho}{\rho}\right)_r. \tag{4.2.37}$$

In the RD era,

$$\mathcal{H} = \frac{1}{\eta}, \tag{4.2.38}$$

and

$$\delta_r := \left(\frac{\delta\rho}{\rho}\right)_r = 4\Theta_{r0}. \tag{4.2.39}$$

Here Θ_{r0} is the monopole of Θ_r, which is defined as

$$\Theta_{r0}(k, \eta) := \int_{-1}^{1} d\mu \ \Theta_r(k, \mu, \eta) P_0(\mu). \tag{4.2.40}$$

$P_0(\mu)$ is the 0th-order Legendre polynomial. Similarly, the lth-order multipole is just

$$\Theta_{rl}(k, \eta) = \int_{-1}^{1} d\mu \ \Theta_r(k, \mu, \eta) P_l(\mu), \tag{4.2.41}$$

where P_l is the lth-order Legendre polynomial. Since all physically interesting perturbation modes are outside of the horizon at such early time (equivalent to setting $k \to 0$), a hypothetical observer would see a homogeneous and isotropic universe. All higher order multipoles Θ_{rl} are negligible compared with Θ_{r0}, thus

$$\Theta_{r0} \simeq \Theta_r. \tag{4.2.42}$$

Plugging Eqs. (4.2.38), (4.2.39) and (4.2.42) into (4.2.37), we obtain

$$\eta\dot{\phi}(\vec{k}, \eta) + \phi(\vec{k}, \eta) = -2\Theta_{r0}. \tag{4.2.43}$$

Recall that $\Theta_r - \Phi = \text{const.}$. Differentiating Eq. (4.2.43), we get

$$\ddot{\phi} + \frac{4}{\eta}\dot{\phi} = 0. \tag{4.2.44}$$

There are two independent solutions for ϕ: $\phi \propto$ const. and $\phi \propto \eta^{-3}$. The second solution decays fast, quickly becomes sub-leading, yielding a physically irrelevant solution. Therefore, ϕ is a constant at the beginning. This constant, called ϕ_i, is determined by the details of inflation. By making use of Eq. (4.2.43) again, we find

$$\phi_i = -2\Theta_{r0} \Rightarrow \Theta_{r0} = -\frac{1}{2}\phi_i. \tag{4.2.45}$$

Correspondingly, according to Eq. (4.2.34), for super-horizon perturbation modes,

$$\phi - \Theta_r = \frac{3}{2}\phi_i. \tag{4.2.46}$$

Now, let us focus on the matter component, which satisfies $\delta - 3\phi = \text{const.}$. Plus the condition $\Theta_r - \phi = \text{const.}$, we have

$$\delta - 3\Theta_r = \text{const.} \tag{4.2.47}$$

If the constant in 4.2.47 equals zero, it is called the *adiabatic* initial condition; if the constant is non-vanishing, it is called the *isocurvature* initial condition. In this paper, we adopt the adiabatic initial condition which is consistent with the CMB data [195, 202], therefore,

$$\delta_i = 3\Theta_{r0} = -\frac{3}{2}\phi_i; \qquad \delta - 3\phi = -\frac{9}{2}\phi_i \tag{4.2.48}$$

4.2.4 Transfer Function and Super-horizon Mode

After choosing the initial condition, we can derive the time evolution of density perturbations. In this section, we first study the super-horizon modes, which are used to scale the transfer function, one of the most important physical observables in cosmology. From the previous section, we known that for super-horizon perturbation modes,

$$\Theta_{r0} - \phi = -\frac{3}{2}\phi_i, \quad \delta - 3\phi = -\frac{9}{2}\phi_i. \tag{4.2.49}$$

As long as we know the time evolution of ϕ, we also know that of Θ_{r0} and δ. To study ϕ, we again consider the Einstein equation (4.2.28). With Eq. (4.2.49) and the condition $k \to 0$ for super-horizon modes, we rewrite (4.2.28) as

$$\tilde{a}\dot{\tilde{a}}\dot{\phi}(\vec{k},\eta) + \dot{\tilde{a}}^2\phi(\vec{k},\eta) = -\frac{3}{4}k_{eq}^2\left[(4+3\tilde{a})\phi - (6+\frac{9}{2}\tilde{a})\phi_i\right]. \tag{4.2.50}$$

Changing variable $\frac{d}{d\eta} \to \frac{d}{d\tilde{a}}$, we obtain

$$\tilde{\phi}' + \frac{5\tilde{a}+6}{2\tilde{a}(1+\tilde{a})}\tilde{\phi} = \frac{3(4+3\tilde{a})}{4\tilde{a}(1+\tilde{a})}, \tag{4.2.51}$$

where $\tilde{\phi} = \phi/\phi_i$ and $\tilde{\phi}' = d\tilde{\phi}/d\tilde{a}$. Introduce a function

$$f(\tilde{a}) = \frac{\tilde{a}^3}{\sqrt{1+\tilde{a}}}, \tag{4.2.52}$$

then

$$\frac{1}{f(\tilde{a})}\frac{d}{d\tilde{a}}\left[f(a)\tilde{\phi}\right] = \frac{3(4+3\tilde{a})}{4\tilde{a}(1+\tilde{a})}. \tag{4.2.53}$$

With the initial condition $\tilde{\phi} = 1$ at $\tilde{a} = 0$, we can solve for ϕ, which gives

$$\phi = \frac{\phi_i}{10\tilde{a}^3}\left(9\tilde{a}^3 + 2\tilde{a}^2 - 8\tilde{a} - 16 + 16\sqrt{1+\tilde{a}}\right). \tag{4.2.54}$$

In Figure 14, we plot the behavior of $\tilde{\phi}$ as a function of $\tilde{a}$.

During most of the evolution, ϕ remains nearly constant. It varies smoothly around matter-radiation equality, before which it maintains the initial value ϕ_i. While at late time, as $\tilde{a} \to \infty$,

$$\phi \simeq \frac{9}{10}\phi_i. \tag{4.2.55}$$

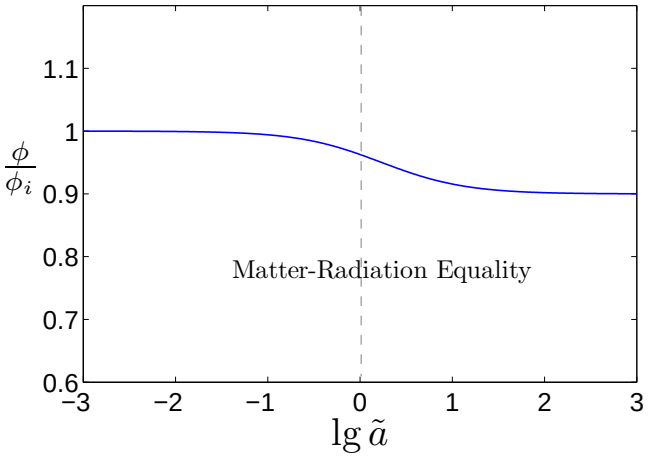

Figure 14: Time evolution of gravitational potential ϕ for super-horizon modes. The dashed line corresponds to the Matter-Radiation equality.

With the relation (4.2.49) in mind, we conclude that for super-horizon modes, both radiation and matter density perturbations remain nearly constant. The transfer function $T(k)$, which plays a significant role in structure formation in the linear region, is defined as

$$T(k) := \frac{\phi(k, a \to \infty)}{\phi_{\text{super-horizon}}(k, a \to \infty)} = \frac{10}{9\phi_i}\phi(k, a \to \infty). \tag{4.2.56}$$

In the following, we obtain the transfer functions for various DM particles.

4.3 CDM AND WDM: DIFFERENT EVOLUTION HISTORIES

We are ready to discuss the physically relevant scales of density perturbation, which are responsible for the structures observed today. The time evolution of these perturbations depends on the properties of DM particles, and lead to very different transfer functions. According to their free-streaming properties, different DM particles are classified into three categories, CDM, WDM and HDM. CDM features small velocity dispersion and has the

shortest free-streaming distance, it is usually described by a heavy particle. 100 GeV WIMPs, e.g., neutralinos predicted in super-symmetric theories beyond the SM, are the most popular CDM candidate. They decouple from LTE around the temperature $T = 10$ MeV. On the other hand, HDM has the longest free streaming distance that leads to top-down structure formation. Standard model neutrinos are well-known HDM candidates. However, current cosmological observations have excluded the possibility of HDM being the major DM component [194, 112]. Therefore, we consider CDM and WDM only.

WDM has free streaming distance in between CDM and HDM. Since current cosmological observations on large scales agree excellently with theoretical predictions based on the CDM scenario, the free-streaming distance of WDM must not conflict with these observations. To meet these requirements, keV sterile neutrinos with free steaming length of about Mpc scale are a proper WDM candidate as discussed in Sec. 2.3. They yield the same results for large scale perturbations but are expected to give different results for small scale perturbations, thus potentially solving the small scale problems in cosmology [244, 191, 226, 179, 138, 81, 93, 282]. As mentioned previously, sterile neutrinos can be produced through different mechanisms in the early universe. In this chapter, we consider two mechanisms, yielding the distribution functions f_0 given by Eqs. (4.2.10) and (4.2.11).

The time evolution of CDM has been thoroughly studied both analytically and computationally at small scales. We consider CDM here as a comparison with WDM as well as using it as a benchmark for the calculation of the WDM case. The time evolution of CDM is determined by two scales: the co-moving horizon, which separates the super-horizon and the sub-horizon perturbation modes, and matter-radiation equality, separating the RD universe from the MD universe. These two scales are illustrated in panel (a) of Figure 15. These two scales divide the entire region into four sub-regions. Each sub-region is well understood analytically. An exact connection of these sub-regions requires numerical fitting, but a very good approximation (with less than 10% error) can be achieved analytically [113]. As for keV sterile neutrinos, we follow the same strategy. However, they involve one more scale than WIMPs since they decouple at the temperature of electroweak scale, much higher than

the mass of sterile neutrinos. At that time, sterile neutrinos are produced fully relativistic, behaving as a radiation component. As the universe evolves, the temperature goes down, gradually becoming lower than the mass of sterile neutrinos. When this happens, sterile neutrinos transform from relativistic state to non-relativistic state and their clustering properties change dramatically. For keV sterile neutrinos, the transition temperature is roughly the same as the mass scale, and the universe is still in deep RD era. Therefore, different from the WIMPs case, there are three scales involved in time evolution of sterile neutrinos: i) a_{NR}, the value of the scale factor when sterile neutrinos transform from relativistic to non-relativistic states; ii) a_{eq}, separating RD and MD universe; iii) finally, η, the co-moving horizon, separating sup-horizon and sub-horizon perturbation modes. The last two scales are the same as WIMPs while the first one is unique for sterile neutrinos, as indicated in panel (b) of Figure 15. We can estimate the value of a_{NR} by noting that according to Eq. (4.2.21), sterile neutrinos are relativistic if $q \gg ma$ and are non-relativistic if $q \ll ma$. The transition is defined to satisfy $ma_{NR} = \sqrt{\langle q^2 \rangle}$ such that

$$\tilde{a}_{NR} = \frac{\sqrt{\langle q^2 \rangle}}{ma_{eq}} := \sqrt{\langle V_{eq}^2 \rangle}, \tag{4.3.1}$$

where the bracket $\langle \cdots \rangle$ refers to the statistical average. Correspondingly, $\langle q^2 \rangle$ is the average squared co-moving momentum of the WDM particles, and $\langle V_{eq}^2 \rangle$ is the average squared velocity at matter-radiation equality. Since $y = q/T_{0,d}$ with $T_{0,d}$ being the decoupling temperature today, we find,

$$\tilde{a}_{NR} = \sqrt{\langle V_{eq}^2 \rangle} = \frac{T_{0,d}}{ma_{eq}} \sqrt{\overline{y^2}} \simeq 7.59 \times 10^{-4} \sqrt{\overline{y^2}} \left(\frac{\text{keV}}{m} \right) \left(\frac{2}{g_d} \right)^{1/3}. \tag{4.3.2}$$

The values of $\overline{y^2}$ for the distributions under our consideration are given in Eq. (4.2.16), from which we find $\sqrt{\overline{y^2}} \sim \mathcal{O}(1)$ for both DW and BD sterile neutrinos. Correspondingly, $\tilde{a}_{NR} \ll 1$ for keV sterile neutrinos, meaning that indeed the universe is still deep in the RD era. Therefore, according to Eq. (4.1.10), $\tilde{a}_{NR} \simeq \eta_{NR}/\eta_*$, yielding

$$\eta_{NR} \simeq \eta_* \sqrt{\langle V_{eq}^2 \rangle}. \tag{4.3.3}$$

$\eta_{NR} \simeq 0.2\ (\text{Mpc})^{-1}$ if taking $m \sim$ keV and $\sqrt{\overline{y^2}} \sim \mathcal{O}(1)$, which corresponds to the co-moving horizon at the transition time. For perturbation modes larger than η_{NR}, they enter

the co-moving horizon when sterile neutrinos become non-relativistic, thus follow the similar evolution history as WIMPs. However, for perturbation modes smaller than η_{NR}, they enter the co-moving horizon when sterile neutrinos are still relativistic, thus experience a different evolution history. In this chapter, we focus on these small scales and study their time evolution and compare with that of WMIPs.

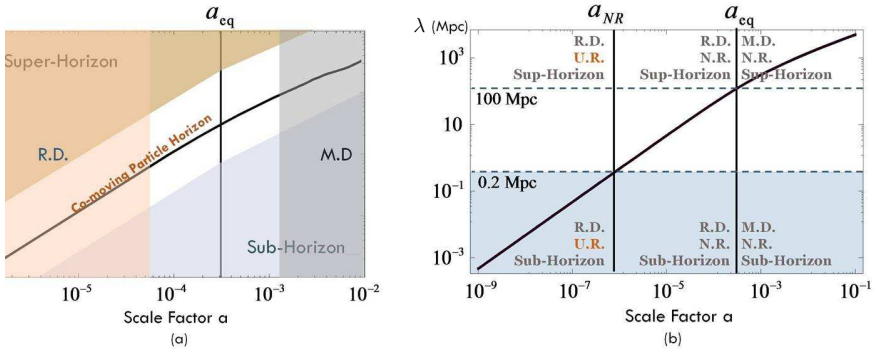

Figure 15: Summary of time evolution of various perturbations modes of WIMPs and sterile neutrinos. Panel (a) is for WIMPs and panel (b) is for sterile neutrinos. Each λ-value corresponds to one perturbation mode. The scale factor also labels the time arrow. For each case, we demonstrate the important scales involved in the time evolution, as discussed in detail in the context. The shaded regions of panel (a) show the analytically solvable regions, which has been thoroughly studied in [112]. The shaded area in panel (b) emphasizes the perturbation modes experienced different evolution history from that of WIMPs.

4.3.1 Our Strategy

Our strategy of solving the problem is as follows: as pointed out previously, small scale perturbations of sterile neutrinos experience three evolution stages. When they first enter the horizon, namely stage one, sterile neutrinos are fully relativistic. Later, during stage two, when the temperature of the universe drops below the mass of sterile neutrinos ($\sim$ keV), they become non-relativistic while the universe is still in the RD era. Finally, in stage three, the universe becomes MD and sterile neutrinos are non-relativistic. We make use of the formal solution (4.2.27) to solve for each stage individually, and then connect them

together because the collision-less Boltzmann equation is a first order differential equation in time, the solution at the end of the previous stage is the initial condition for the next stage. In practice, sterile neutrinos transform smoothly from relativistic to non-relativistic status. However, we neglect the details of the transition in the calculation and connect the relativistic and non-relativistic solutions directly together. Despite the error introduced in such an approximation, the main physical conclusions are not affected, as demonstrated by a numerical analysis.

4.3.2 Free Streaming Distance of CDMs and WDMs

For later convenience, let us compare the free streaming distance of CDM and WDM in this section. In particular, we only consider the three distributions discussed in Sec. 4.2.1.1, namely the distribution functions of WIMPs, DW and BD sterile neutrinos. In addition to the scales that separate the three stages of the time evolution of DM density perturbations, free streaming length is another important quantity that determines the growth of structures. It describes the motion of the DM particles that works against the gravitational attraction. According to Eq. (4.2.26),

$$l - l_i = \int_{\eta_i}^{\eta} v(\eta')d\eta' = \int_{\eta_i}^{\eta} d\eta' \frac{q}{\epsilon}. \tag{4.3.4}$$

For relativistic particles, $\epsilon \simeq q$,

$$l - l_i = \eta - \eta_i. \tag{4.3.5}$$

The free streaming distance is of the same order as the co-moving horizon size, therefore, all perturbation modes within the horizon are suppressed and no structure can grow. While in the non-relativistic limit, $\epsilon \simeq ma$, thus

$$l - l_i \simeq \frac{q}{m} \int_{\eta_i}^{\eta} \frac{d\eta'}{a(\eta')}. \tag{4.3.6}$$

Recall that, in a universe with only radiation and matter components,

$$\tilde{a} = \frac{\eta}{\eta_*} \left(1 + \frac{\eta}{4\eta_*}\right). \tag{4.3.7}$$

With the above relation, we obtain

$$
\begin{aligned}
k(l-l_i) &= \frac{\alpha y}{2}\ln\left|\frac{z+\sqrt{z^2+\alpha^2\bar{y}^2/4}}{z_i+\sqrt{{z_i}^2+\alpha^2\bar{y}^2/4}}\right| \\
&\simeq \begin{cases} \dfrac{\alpha y}{2}\ln\left|\dfrac{\eta}{\eta_i}\right| & \text{the RD era } (\tilde{a}\ll 1) \\ \alpha y\ 2\eta_*\left(\dfrac{1}{\eta_i}-\dfrac{1}{\eta}\right) & \text{the MD eta } (\tilde{a}\gg 1) \end{cases}
\end{aligned}
\tag{4.3.8}
$$

where $z=k\eta$ and $y=q/T_{0,d}$ as before. The new variable α is defined as

$$
\alpha := 2\sqrt{2}k\frac{T_{0,d}}{m\ a_{eq}k_{eq}} \simeq 0.22\ k\left(\frac{2}{g_d}\right)^{1/3}\left(\frac{\text{keV}}{m}\right)\text{Mpc}, \tag{4.3.9}
$$

Here $T_{0,d}$ is the decoupling temperature today and g_d is the relativistic degrees of freedom at decoupling of the DM component. The free streaming distance in the MD era is much smaller than that in the RD era, which means structure growth mainly happens during the MD era. It is worthwhile to point out that l depends on f_0 only in the non-relativistic limit, as shown explicitly in (4.3.5) and (4.3.8). Since all physical observables correspond to statistical average over y, the average value of the free streaming distance is proportional to $\sqrt{\overline{y^2}}$ for any given distribution f_0. For the distributions of our interest, y is strongly peaked around $\sqrt{\overline{y^2}}$ as given by Eq. (4.2.16). Therefore, from (4.3.8), the quantity $\alpha\sqrt{\overline{y^2}}$ scales the free streaming distances of non-relativistic DM particles, becoming a convenient quantity to compare for different distribution functions. For later convenience, let us define

$$
\kappa := \alpha\sqrt{\overline{y^2}} = 0.22\ k\sqrt{\overline{y^2}}\left(\frac{2}{g_d}\right)^{1/3}\left(\frac{\text{keV}}{m}\right). \tag{4.3.10}
$$

Thus, from (4.2.16), we obtain

$$
\kappa=\alpha\sqrt{\overline{y^2}}=\begin{cases} 0.7914\ k\ \text{Mpc}\left(\dfrac{2}{g_d}\right)^{1/3}\left(\dfrac{\text{keV}}{m}\right) & \text{DW}, \\ 0.6417\ k\ \text{Mpc}\left(\dfrac{2}{g_d}\right)^{1/3}\left(\dfrac{\text{keV}}{m}\right) & \text{BD}, \\ 0.3811\times 10^{-6}\ k\ \text{Mpc}\left(\dfrac{2}{g_d}\right)^{1/3}\left(\dfrac{100\text{GeV}}{m}\right)^{1/2}\left(\dfrac{10\text{MeV}}{T_d}\right)^{1/2} & \text{WIMPs}. \end{cases}
\tag{4.3.11}
$$

From (4.3.11), the free steaming distance of sterile neutrinos is of about the order of 1Mpc (cluster scale), but that of WIMPs is much smaller, only a few tenths of a pc. Hence, the free

streaming effect of WIMPs is totally negligible because its free streaming distance is much smaller than the scale of any cosmological structure of interest, leading to the approximation $l_{\rm WIMPs} \simeq 0$ throughout the entire history of structure growth. Under such an approximation, density perturbations of WIMPs are greatly simplified. In the following discussion we will show that the power spectrum and the transfer function of WIMPs are independent of f_0. From the numerical point of view, the most popular codes to calculate the power spectrum in the linear region, e.g., CMBFAST [255, 291, 290] and CAMB [203], are dealing with CDM. Therefore, no information of f_0 is included in these codes. To obtain an accurate power spectrum (transfer function) for sterile neutrinos (or other WDM candidates), one needs to modify these programs and include the information of the unperturbed distribution function. This is a computationally intensive task.

To get a deeper physical insight, in analogy with the Jean's wave vector in the fluid perturbations, we introduce $k_{fs}(t)$ such that

$$k_{fs}(t) = \frac{\sqrt{4\pi G \rho_m(t)}}{a(t)\sqrt{\langle V^2(t)\rangle}}, \tag{4.3.12}$$

where

$$\rho_m(t) = \frac{\rho_{m0}}{a(t)^3}, \tag{4.3.13}$$

$$\langle V^2(t)\rangle = \frac{\langle V_0^2\rangle}{a^2(t)}. \tag{4.3.14}$$

ρ_{m0} and $\langle V_0^2\rangle$ are the values of ρ_m and $\langle V^2\rangle$ today. Direct evaluation gives

$$\langle V_0^2\rangle = \overline{y^2}\left(\frac{T_{d,0}}{m}\right)^2. \tag{4.3.15}$$

Because density perturbations grow significantly since matter-radiation equality, $k_{fs}(t_{eq})$, defined as the free streaming wave vector, is of special interest, which gives

$$k_{fs} = k_{fs}(t_{eq}) = \frac{2\pi}{\lambda_{fs}} = \frac{\sqrt{3}}{2}\frac{k_{eq}}{\sqrt{\langle V^2(t_{eq})\rangle}}. \tag{4.3.16}$$

Correspondingly, λ_{fs} is called the free streaming length. Recall the expression of η_{NR} in Eq. (4.3.3), we find

$$\eta_{NR} = \frac{4\pi}{\sqrt{6}}\lambda_{fs} = \frac{\sqrt{3}}{\sqrt{2}}\frac{1}{k_{fs}}. \tag{4.3.17}$$

Therefore, the free streaming length and η_{NR} are of the same order. For any mass and distribution function of DM particles, we can calculate the free streaming wave vector directly. For 1 keV DW and BD sterile neutrinos, we get

$$k_{fs}^{(DW)} \simeq 7.7\ (\text{Mpc})^{-1}, \tag{4.3.18}$$

$$k_{fs}^{(BD)} \simeq 14.12\ (\text{Mpc})^{-1}. \tag{4.3.19}$$

Since η_{NR} describes the transition of sterile neutrinos from relativistic stage to non-relativistic stage, perturbation scales smaller (larger) than η_{NR} enter the horizon when the WDM particles are relativistic (non-relativistic); on the other hand, as an analogy to the Jean's length, $k_{fs} = 2\pi/\lambda_{fs}$ separates the perturbation scales that undergo substantial growth from those suppressed by free streaming effect. Since η_{NR} and λ_{fs} are of the same order, it means that density perturbations of WDM mainly grow when the particles become non-relativistic. Based on the above observation, the dimension-less quantity κ turns out useful, corresponding to

$$\frac{\kappa}{2} = \alpha\sqrt{\overline{y^2}} = k\eta_{NR} = \frac{\sqrt{3}}{\sqrt{2}}\frac{k}{k_{fs}}. \tag{4.3.20}$$

It implies that $\kappa \gtrsim 2$ corresponds to perturbation modes entering the horizon when the particles are relativistic while $\kappa \lesssim 2$ corresponds to the modes entering the horizon non-relativistically.

Finally, we would like to point out that it is the heavy mass of WIMP particles that leads to a rather small velocity dispersion and dramatically reduces their free streaming distance. $l = 0$ actually corresponds to the limit $m \to \infty$, namely $\alpha \simeq 0$. In the following, we will first discuss the time evolution of WIMPs and then that of sterile neutrinos. As we take the limit $\alpha \to 0$, our results for sterile neutrinos are expected to recover those of WIMPs. In this sense, CDM serves as a special case for the general studies on the time evolution of WDM and as a benchmark for our WDM calculation.

4.4 CDM CASE: TIME EVOLUTION AND THE TRANSFER FUNCTION

For WIMPs, they are non-relativistic since the end of inflation, where the seeds of structure formation are generated. Therefore, we only need to consider the non-relativistic limit of the formal solution (4.2.27), corresponding to $\epsilon \simeq ma$. The formal solution becomes

$$F_1(k,q,\mu,\eta) = e^{-ik\mu(l-l_i)}F_1(k,\mu,\eta_i) - q\frac{d\tilde{f}_0}{dq}\int_{\eta_i}^{\eta} d\eta'\, e^{-ik\mu(l-l')}\left[\dot{\phi}(k,\mu,\eta') - ik\mu\frac{m}{q}\phi(k,\mu,\eta')\right]. \tag{4.4.1}$$

The subscript i labels the initial condition. It turns out convenient to work directly with the perturbed number density δ instead of F_1 because δ is equivalent to the perturbed energy density in the non-relativistic limit. By introducing a new variable

$$ds := d\eta/a(\eta) \tag{4.4.2}$$

and recalling that $l = 0$ for WIMPs, we obtain

$$\begin{aligned}\delta(k,\mu,s) &= \int d\vec{q}\, F_1(k,q,\mu,s) \\ &= \delta_i - 3\phi_i + 3\phi(k,s) - k^2\int_{s_i}^{s} ds' a(s')^2(s-s')\phi(k,s').\end{aligned} \tag{4.4.3}$$

As $k \to 0$, Eq. (4.4.3) becomes $\delta(k,\mu,s) - 3\phi(k,s) = \delta_i - 3\phi_i$, recovering our previous result of super-horizon modes. Using the initial condition $\delta_i = -3\phi_i/2$, we have

$$\delta(k,s) = -\frac{9}{2}\phi_i + 3\phi(k,s) - k^2\int_{s_i}^{s} ds' a(s')^2(s-s')\phi(k,s'). \tag{4.4.4}$$

The gravitational potential ϕ behaves differently in the RD and MD era (See Eqs. (4.2.30) and (4.2.31).), thus we need to consider these two cases separately. To do that, let us first consider the new variable s. According to its definition in (4.4.2), straightforward calculation shows

$$s = \frac{\eta_*}{a_{eq}}\ln\left|\frac{\sqrt{1+\tilde{a}}-1}{\sqrt{1+\tilde{a}}+1}\right| = \frac{2\eta_*}{a_{eq}}u, \tag{4.4.5}$$

where $\tilde{a}$ is given by (4.1.3), and u is defined as

$$u := \frac{1}{2}\ln\left|\frac{\sqrt{1+\tilde{a}}-1}{\sqrt{1+\tilde{a}}+1}\right|. \tag{4.4.6}$$

It is a useful variable for our later discussion.

4.4.1 Density Perturbations of WIMPs in the RD Era

When the universe is RD, ϕ is given by Eq. (4.2.30). Plugging it into (4.4.4) and carrying out the integration, we obtain

$$\delta(k,\eta) = 9\phi_i \left\{ -\frac{1}{2} + \frac{\sin x - x\cos x}{x^3} - \ln\left(\frac{x}{x_i}\right)\frac{\sin x_i}{x_i} + \frac{\sin x_i}{x_i} - \frac{\sin x}{x} + \mathcal{C}_i(x) - \mathcal{C}_i(x_i) \right\}, \tag{4.4.7}$$

where

$$x := \frac{z}{\sqrt{3}} = \frac{k\eta}{\sqrt{3}} \tag{4.4.8}$$

and $\mathcal{C}_i$ is the cosine integral function [8] defined as

$$\mathcal{C}_i(x) = \int dx \frac{\cos(x)}{x}. \tag{4.4.9}$$

The initial value $x_i = 0$, leading to

$$\mathcal{C}_1(x_i)|_{x_i\to 0} \simeq \gamma_E + \ln(x_i) + \mathcal{O}(x_i^2), \tag{4.4.10}$$

$$\left.\frac{\sin x_i}{x_i}\right|_{x_i\to 0} \simeq 1. \tag{4.4.11}$$

$\gamma_E = 0.577216$ is the Euler Gamma constant. Consequently,

$$\delta(k,x) = 6\delta_i \left\{ \gamma_E - \frac{1}{2} + \ln x + \frac{x\cos x - \sin(x)}{x^3} + \frac{\sin(x)}{x} - \mathcal{C}_i(x) \right\}. \tag{4.4.12}$$

Again, we have made use of the initial condition $\delta_i = -3\phi_i/2$. Obviously, when $x = 0$, $\delta(k,0) = \delta_i$. In Figure 16, we have shown the behavior of δ in terms of x. Obviously, density perturbations start to grow since they enter the horizon ($k\eta \simeq 1$). They grow rapidly at the beginning and slow down after $x \simeq 5$. In particular, at very large x,

$$\delta(k,x) \simeq 6\delta_i \left(\gamma_E - \frac{1}{2} + \ln x \right). \tag{4.4.13}$$

The density perturbations experience a logarithmic growth, as is well-known from a simple Newtonian study. Based on the discussion above, we conclude that DM density perturbations can grow in a RD universe even though the gravitational potential ϕ itself decays cubically (See Eq. (4.2.30)). On the other hand, in the RD era, photons are undergoing acoustic oscillations, the magnitude of whose perturbations does not grow at all [112]. To verify this statement, let us consider the radiation component.

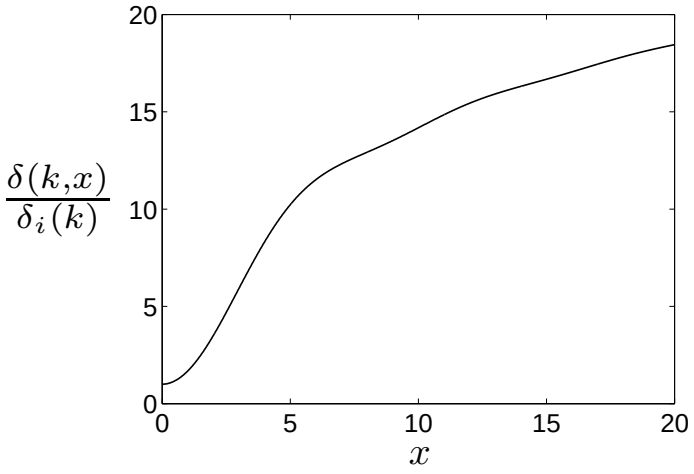

Figure 16: Time evolution of density perturbations of WIMPs in the RD era with respect to its initial value. $x = k\eta/\sqrt{3}$. When $x \simeq 1/\sqrt{3}$, the perturbation mode enters the horizon and start to grow. At late times, the density perturbations grow logarithmically, as shown in Eq. (4.4.13)

4.4.1.1 Density Perturbations of Photons in The RD Era The density perturbation of photons is very easy to obtain because i) the gravitational potential ϕ is already known in the RD era; ii) in this period, ϕ is mainly determined by the radiation component, contribution from the DM is negligible. Therefore, according to Eq. (4.2.28) and by neglecting the matter perturbation, we get

$$\left(\frac{\delta\rho}{\rho}\right)_r = -\frac{4}{3}\frac{k^2\tilde{a}^2}{k_{eq}^2}\left[\phi(\vec{k},\eta) + 3\frac{\mathcal{H}}{k}\left(\frac{\dot{\phi}(\vec{k},\eta)}{k} + \frac{\mathcal{H}}{k}\phi(\vec{k},\eta)\right)\right]. \tag{4.4.14}$$

With the expression of the gravitational potential in (4.2.30), we find

$$\begin{aligned}\left(\frac{\delta\rho}{\rho}\right)_r &= 6\phi_i\left(\cos x + \frac{2\cos x}{x^2} - \frac{2\sin x}{x^3}\right) \\ &\simeq 6\phi_i\cos x \quad \text{for } x \gg 1.\end{aligned} \tag{4.4.15}$$

Indeed, photons oscillate acoustically as we expect.

4.4.1.2 Radiation Cross-over Perturbations of the radiation component oscillate in the RD era with a constant magnitude; and DM density perturbations grow logarithmically simultaneously. Eventually perturbations of DM will exceed that of the radiation component, and become the dominant contribution to the gravitational potential even though the universe is still in the RD era. This process is called the radiation cross-over. According to our previous result, for perturbation modes deep inside the horizon,

$$\begin{aligned} \delta_r &:= \left(\frac{\delta\rho}{\rho}\right)_r \simeq 6\phi_i \cos x, \\ \delta &\simeq 9\phi_i \ln x. \end{aligned}$$

As shown in Eq. (4.2.28), when $\tilde{a}\delta \geq \delta_r$, the DM density perturbations become dominant for the gravitational potential. The cross-over corresponds to the critical value that

$$\tilde{a}\delta = \delta_r \Rightarrow \frac{3}{2}\tilde{a} \ln x = \cos x. \tag{4.4.16}$$

Since the left hand side of (4.4.16) is monotonically increasing with respect to $\tilde{a}$ and $\cos x \leq 1$, the cross-over occurs approximately when

$$\tilde{a}_c \ln x_c = \frac{2}{3}. \tag{4.4.17}$$

In Figure 17, we show the value of x_c for several perturbation modes. It is clear to see that for the small scale perturbations of our interest, the radiation cross-over happens around

$$\frac{x_c}{x_*} \simeq \mathcal{O}(10^{-1}) \Rightarrow \frac{\eta_c}{\eta_*} \simeq \mathcal{O}(10^{-1}). \tag{4.4.18}$$

The result is consistent with our previous assumption that the cross-over happens deep in the RD era. As long as the cross-over happens, DM density perturbations become the dominant contribution to the gravitational potential ϕ even though the universe is still RD. From the perturbation point of view, for simplicity, we call the universe since the radiation cross-over to be MD. However, its precise meaning is just what is stated here.

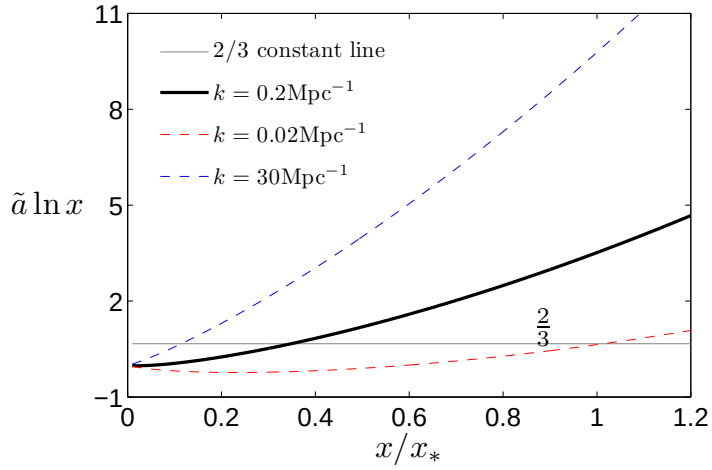

Figure 17: Radiation cross-over for difference perturbation modes. $x_* = k\eta_*/\sqrt{3} = 83.32\ k$. $x_c/x_* \ll 1$ means that the cross-over happens deep in the RD era, which is true for the small scale perturbation modes we are interested in, namely $k \geq 0.2\text{Mpc}^{-1}$. Moreover, for perturbations larger than 30 Kpc, $x \geq 0.1x_* \simeq 8$, the expressions of δ_r and δ under large x limit are well justified.

4.4.2 Density Perturbations of WIMPs in the MD Era

After radiation cross-over, density perturbations enter the MD era, where ϕ is described by Eq. (4.2.31) instead of (4.2.30). Making use of the formal solution in (4.4.4), we divide the time integral into two parts,

$$\begin{aligned}\delta(k,s) &= -\frac{9}{2}\phi_i - \frac{9k_{eq}^2}{4\tilde{a}k^2}\delta(k,s) \\ &\quad -k^2\int_{s_i}^{s_c} ds' a(s')^2(s-s')\phi(k,s') + \frac{3}{4}k_{eq}^2 a_{eq}^2\int_{s_c}^{s} ds'\tilde{a}(s')(s-s')\delta(k,s').\end{aligned} \tag{4.4.19}$$

In the first and second time integrals, the gradational potential ϕ is given by Eqs. (4.2.30) and (4.2.31) in the RD and MD eras respectively. Note that for the small scale perturbation modes under our consideration, $\frac{k_{eq}^2}{k^2\tilde{a}} \ll 1$, thus the second term in Eq. (4.4.19) can be safely neglected. Differentiate Eq. (4.4.19) with respect to s twice, the first integral vanishes

because it is only first order in s, thus, we obtain

$$\frac{d^2\delta}{ds^2} - \frac{3}{4}k_{eq}^2 a_{eq}^2 \tilde{a}(s)\delta(k,s) = 0. \tag{4.4.20}$$

4.4.2.1 2nd-order Legendre Equation According to the expression of s in (4.4.5), s is a function of $\sqrt{\tilde{a}+1}$ only, thus we introduce $\zeta = \sqrt{\tilde{a}+1}$ and write

$$s = \frac{\eta_*}{a_{eq}} \ln\left(\frac{\zeta-1}{\zeta+1}\right). \tag{4.4.21}$$

Correspondingly,

$$u = \frac{1}{2}\ln\left(\frac{\zeta-1}{\zeta+1}\right). \tag{4.4.22}$$

In terms of ζ, Eq. (4.4.20) becomes

$$(\zeta^2-1)\frac{d^2}{d\zeta^2}\delta + 2\zeta\frac{d}{d\zeta}\delta(k,\zeta) - 6\delta(k,\zeta) = 0, \tag{4.4.23}$$

corresponding to a 2nd-order Legendre equation. Therefore, density perturbations of WIMPs in the MD era are governed by a 2nd-order Legendre equation, whose two independent solutions are the Legendre polynomials $P_2(\zeta)$ and $Q_2(\zeta)$:

$$P_2(\zeta) = \frac{1}{2}(3\zeta^2-1), \tag{4.4.24}$$

$$Q_2(\zeta) = \frac{1}{2}P_2(\zeta)\ln\left(\frac{\zeta+1}{\zeta-1}\right) - \frac{3}{2}\zeta. \tag{4.4.25}$$

The general solution of δ is a superposition of P_2 and Q_2, namely

$$\begin{aligned}\delta(k,\zeta) &= AP_2(\zeta) + BQ_2(\zeta) \\ &= \frac{A}{2}(3\zeta^2-1) + \frac{B}{4}(3\zeta^2-1)\ln\left(\frac{\zeta+1}{\zeta-1}\right) - \frac{3B}{2}\zeta.\end{aligned} \tag{4.4.26}$$

The coefficients A and B are determined by smoothly connecting density perturbations in the MD era with those in the RD era. Thus,

$$\delta_{MD}(k,\eta_c) = \delta_{RD}(k,\eta_c), \tag{4.4.27}$$

$$\frac{d}{d\eta_c}\delta_{MD}(k,\eta) = \frac{d}{d\eta_c}\delta_{RD}(k,\eta), \tag{4.4.28}$$

where δ_{MD} is the density perturbation in the MD era, given by (4.4.26); δ_{RD} is the density perturbation in the RD era as shown in (4.4.12); η_c is the time for the radiation cross-over. From previous discussion, we show that it is reasonable to assume the large x limit for the radiation cross-over, thus,

$$\delta_{RD}(k,\eta_c) \simeq -9\phi_i \left(\ln x_c + \gamma_E - \frac{1}{2}\right) = -9\phi_i \left[\ln \tilde{a}_c + \ln\left(x_* e^{\gamma_E - 1/2}\right)\right], \tag{4.4.29}$$

where $x_* = k\eta_*/\sqrt{3}$. Here we have made use of the relation between $\tilde{a}$ and η in Eq. (4.1.3). For $d\delta/d\eta_c$, we obtain

$$\frac{d\delta}{d\eta_c} = -9\phi_p \left(\frac{d\tilde{a}_c}{d\eta_c}\right)\frac{1}{\eta_c}. \tag{4.4.30}$$

On the other hand, at the radiation cross-over

$$\frac{\eta_c}{\eta_*} \sim \mathcal{O}(10^{-1}) \Rightarrow \tilde{a}_c \sim \mathcal{O}(10^{-1}). \tag{4.4.31}$$

As $\tilde{a}_c$ is a small quantity, we can Taylor expand Eq. (4.4.26) in terms of $\tilde{a}_c$ to obtain the expressions of δ_{MD} and $d\delta_{MD}/d\eta_c$, which yields

$$\delta_{MD}(k,\eta_c) = -\frac{B}{2}\ln\tilde{a}_c + A + (\ln 2 - \frac{3}{2})B, \tag{4.4.32}$$

$$\frac{d}{d\eta_c}\delta(k,\eta_c) = -\frac{B}{2}\left(\frac{d\tilde{a}_c}{d\eta_c}\right)\frac{1}{\eta_c}. \tag{4.4.33}$$

Plugging δ_{MD}, δ_{RD} and their derivatives into the initial conditions (4.4.27) and (4.4.28), we find

$$A = -9\phi_i \ln\left(4x_* e^{\gamma_E - 7/2}\right), \tag{4.4.34}$$

$$B = 18\phi_i. \tag{4.4.35}$$

Finally, the density perturbations of WIMPs in the MD era is given by

$$\delta(k,\eta) = -\frac{9\phi_i}{2}\left\{(3\tilde{a}+2)\left[\ln\left(\frac{\sqrt{\tilde{a}+1}-1}{\sqrt{\tilde{a}+1}-1}\right) + \ln(4x_*) + \gamma_E - \frac{7}{2}\right] + 6\sqrt{\tilde{a}+1}\right\}. \tag{4.4.36}$$

In Figure 18, we demonstrate the transition of δ from the RD region to the MD region.

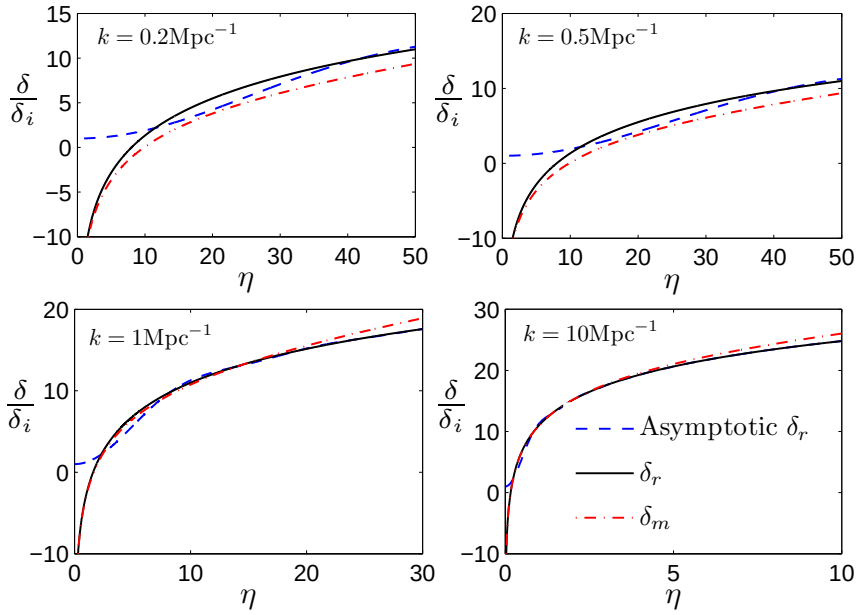

Figure 18: Transition of δ from the RD region to the MD region for various perturbation modes. The transition gets better for small scale modes $k < 0.5\text{Mpc}^{-1}$.

4.4.2.2 Transfer Function of WIMPs For structure formation in cosmology, one of the most interesting quantities is the transfer function $T(k)$ because it is directly related to observations. In Eq. (4.2.56), we have defined the transfer function $T(k)$ as

$$T(k) = \frac{10}{9\phi_i}\phi(k, a \to \infty). \tag{4.4.37}$$

Since the universe is MD as $a \to \infty$, ϕ is related to δ through the Poisson equation (4.2.31) at small scales when $k \ll k_{eq}$. Correspondingly, the transfer function becomes

$$T(k) = -\frac{1}{\phi_i}\frac{5k_{eq}^2}{6k^2}\left.\frac{\delta}{\tilde{a}}\right|_{\tilde{a}\to\infty}. \tag{4.4.38}$$

As $\tilde{a} \to \infty$, the density perturbation of WIMPs δ given in Eq. (4.4.36) is asymptotically equal to

$$\delta(k, \eta) = -\frac{9\phi_i}{2}\tilde{a}\left(\ln 4x_* + \gamma_E - \frac{7}{2}\right). \tag{4.4.39}$$

Therefore, direct calculation shows that the transfer function of WIMPs is given by

$$T_{\rm WIMPs}(k) = \frac{45k_{eq}^2}{4k^2}\left[\ln\left(\frac{4k\eta_*}{\sqrt{3}}\right) + \gamma_E - \frac{7}{2}\right]. \tag{4.4.40}$$

Eq. (4.4.40) agrees with the results of [280] and [172]. Moreover, comparison between the analytical result (Eq. (4.4.40)) and the numerical fitting has been discussed by Weinberg in [280], which shows very good agreement within a few percent error. Also, we want to emphasize that, as pointed out previously, the transfer function of WIMPs is independent of the distribution function f_0, very different from the WDM case discussed in the next section.

4.4.2.3 An Alternative Method: To Compare with the WDM Case In addition to the method introduced in the previous section, we consider an alternative way of solving density perturbations of WIMPs in the MD era by making use of the variable u. The main reason to do so is that it is easier to compare the CDM and WDM cases in this way. First of all, let us rewrite Eq. (4.4.23) in terms of u, which gives

$$\frac{d^2}{du^2}\delta(k,u) - 6\tilde{a}(u)\delta(k,u) = 0. \tag{4.4.41}$$

It is straightforward to show that

$$\zeta = -\coth u. \tag{4.4.42}$$

Moreover, define $\Delta(k,u)$ such that

$$\delta(k,u) = \Delta(k,u) + I[k,u], \tag{4.4.43}$$

where $I[k,u]$ is the density perturbation induced by radiation components given by Eq. (4.4.4):

$$I[k,u] = -\frac{9}{2}\phi_i + 3\phi_r(k,u) - \frac{8k^2}{k_{eq}^2}\int_{u_i}^{u_c} du'\tilde{a}(u')^2(u-u')\phi_r(k,u'). \tag{4.4.44}$$

ϕ_r is the gravitational potential in the RD era in Eq. (4.2.30). Also, we have applied the relation between s and u in Eq. (4.4.5). Before the radiation cross-over, $\delta(k,u) = I[k,u]$. Recall that

$$u = \frac{1}{2}\ln\left(\frac{\sqrt{\tilde{a}+1}-1}{\sqrt{\tilde{a}+1}+1}\right), \tag{4.4.45}$$

it is always negative. Eq. (4.4.41) is valid for $\tilde{a} \in (\tilde{a}_*, \infty)$, correspondingly, the value of u lies in $(u_c, 0)$, where u_c is just

$$u_c = \frac{1}{2} \ln \left(\frac{\sqrt{a_c + 1} - 1}{\sqrt{a_c + 1} + 1} \right). \tag{4.4.46}$$

In terms of $\Delta(k, u)$, Eq. (4.4.41) becomes,

$$\frac{d^2}{du^2} \Delta(k, u) - 6\tilde{a}(u) \Delta(k, u) = 6\tilde{a}(u) I[k, u], \tag{4.4.47}$$

With the initial conditions

$$\Delta(k, u_c) = \left. \frac{d}{du} \Delta(k, u) \right|_{u=u_c} = 0. \tag{4.4.48}$$

We make use of the Green's function technique to solve Eq. (4.4.47), which gives

$$\Delta(k, u) = 6 \int_{u_c}^{u} du' \mathcal{G}(u - u') \tilde{a}(u') I[k, u']. \tag{4.4.49}$$

$\mathcal{G}(u - u')$ is the Green's function of Eq. (4.4.47) defined as

$$\mathcal{G}(u - u') = \frac{P_2(u) Q_2(u') - P_2(u') Q_2(u)}{W[P_2(u), Q_2(u)]}. \tag{4.4.50}$$

Because Δ and δ obey the same homogeneous equation, P_2 and Q_2 are just the 2nd-order Legendre polynomials obtained previously in Eqs. (4.4.24) and (4.4.25). $W[P_2(u), Q_2(u)]$ is the Wronskian of the two solutions, which equals one. Since the transfer function corresponds to the limit $\tilde{a} \to \infty$, equivalent to $u \to 0$. Asymptotically, we find,

$$P_2(u) \simeq \frac{3}{2} \frac{1}{u^2} \simeq \frac{3}{2} \tilde{a}, \tag{4.4.51}$$

$$Q_2(u) \simeq \frac{2}{15} u^3 \simeq \frac{2}{15} \tilde{a}^{-3/2}. \tag{4.4.52}$$

P_2 is the linear growing mode and Q_2 is the decaying mode. At late time, the growing mode becomes dominant, thus, the Green's function becomes

$$\mathcal{G}(u - u')|_{u \to 0} \simeq P_2(u) Q_2(u') \simeq \frac{3}{2} \tilde{a}\ Q_2(u'). \tag{4.4.53}$$

Plugging (4.4.53) into Eq. (4.4.49) [3], we obtain

$$\Delta(k, u \to 0) \simeq 9\tilde{a} \int_{u_c}^{0} du' Q_2(u') \tilde{a}(u') I[k, u']. \tag{4.4.54}$$

Correspondingly,

$$\delta(k, u \to 0) = I[k, 0] + 9\tilde{a} \int_{u_c}^{0} du' Q_2(u') \tilde{a}(u') I[k, u']. \tag{4.4.55}$$

Based on our previous discussion in the RD era, density perturbations induced by the radiation component mostly increases logarithmically, $I[k, 0]$ can be safely neglected. Finally, we have

$$\delta(k, u \to 0) \simeq 9\tilde{a} \int_{u_c}^{0} du' Q_2(u') \tilde{a}(u') I[k, u']. \tag{4.4.56}$$

The transfer function thus becomes

$$T(k) = -\frac{1}{\phi_i} \frac{15 k_{eq}^2}{2k^2} \int_{u_c}^{0} du' Q_2(u') \tilde{a}(u') I[k, u']. \tag{4.4.57}$$

It is straightforward to show that this result is consistent with Eq. (4.4.40). In the following, we will compare this result with the WDM result.

4.5 WDM CASE: TIME EVOLUTION OF STERILE NEUTRINO DENSITY PERTURBATIONS

In this section, we discuss the time evolution of density perturbations of sterile neutrinos with the focus of small scale aspects. For perturbation modes smaller than 0.2 Mpc, sterile neutrinos are still fully relativistic when these perturbations enter the horizon, then they become non-relativistic in the RD era and finally enter the MD dominant era. We study each stage individually and finally obtain the transfer function.

[3] To justify our result, we have made use of another fact that $I(k, u)$ decays fast as $u \to 0$. Only u' around u_c actually contribute mostly to the integral. Thus for the decaying mode $Q_2(0) \int_{u_c}^{0} du' P_2(u') \tilde{a}(u') I[k, u']$, although P_2 increases as $u \to 0$, $I[k, u']$ actually decays faster, thus leaving the integral still negligible compared to the growth mode.

4.5.1 Stage I: Relativistic Sterile Neutrinos in the RD Era

When sterile neutrinos are relativistic, $\epsilon = \sqrt{q^2 + m^2 a^2} \simeq q$ and the free streaming distance $l - l_i = \eta - \eta_i$ according to Eq. (4.3.5). By setting $\eta_i = 0$, the formal solution (4.2.27) becomes

$$F_1(k, q, \mu, \eta) = e^{-ik\mu\eta} F_{1i}(k, q, \mu) - q\frac{d\tilde{f}_0}{dq} \int_0^\eta d\eta' \; e^{-ik\mu(\eta-\eta')} \left(\dot{\phi}(k, \mu, \eta') - ik\mu\phi(k, \mu, \eta') \right). \tag{4.5.1}$$

Relativistic sterile neutrinos behave like a radiation component, thus we expand F_1 as

$$F_1(k, q, \mu, \eta) = -\Theta_s(k, \mu, \eta) q \frac{df_0}{dq}, \tag{4.5.2}$$

where the subscript s represents sterile neutrinos. According to (4.5.1), for Θ_s, we have

$$\Theta_s(k, \mu, \eta) = e^{-ik\mu\eta} \Theta_{si}(k, \mu) + \int_0^\eta d\eta' \; e^{-ik\mu(\eta-\eta')} \left[\dot{\phi}(k, \mu, \eta') - ik\mu\phi(k, \mu, \eta') \right]. \tag{4.5.3}$$

Integrating by parts, we obtain

$$\Theta_s(k, \mu, \eta) = -\phi(k, \mu, \eta) + e^{-ik\mu\eta} \left[\Theta_{si}(k, \mu) + \phi_i \right] + 2 \int_0^\eta d\eta' \; e^{-ik\mu(\eta-\eta')} \frac{d\phi}{d\eta'}. \tag{4.5.4}$$

Expanding the angle dependence on μ into Legendre polynomials,

$$\Theta_s(k, \mu, \eta) = \sum_{l=0}^{\infty} (-i)^l (2l + 1) P_l(\mu) \Theta_{sl}(k, \eta), \tag{4.5.5}$$

$$e^{-ik\mu(\eta-\eta')} = \sum_{l=0}^{\infty} (-i)^l (2l + 1) P_l(\mu) j_l(k(\eta - \eta')), \tag{4.5.6}$$

where j_l is the l-th order spherical Bessel function. Applying these expressions to (4.5.4) and making use of the relation $\Theta_{si} = -\phi_i/2$, we find

$$\Theta_{sl}(z) = -\phi(z)\delta_{l,0} + \frac{\phi_i}{2} j_l(z) + 2 \int_0^z dz' \left(\frac{d\phi}{dz'} \right) j_l(z - z'), \tag{4.5.7}$$

where $z = k\eta$ and $z' = k\eta'$ as before. The gravitational potential ϕ in the RD era is given by Eq. (4.2.30). Therefore, Eq. (4.5.7) shows the dynamics of density perturbations

of relativistic sterile neutrinos in the RD universe. In particular, for sup-horizon modes, $z = k\eta \sim 0$, and $\phi = \text{const.}$, yielding

$$\Theta_{sl}(z) = -\frac{\phi_i}{2}\delta_{l,0}, \tag{4.5.8}$$

recovering our previous result. Also it is interesting to compute the perturbed number density of sterile neutrinos, where

$$\delta = \int d\vec{q} F_1(q, \mu, \eta) = 3\Theta_{s0}. \tag{4.5.9}$$

Let us focus on Θ_{s0}. According to (4.5.7),

$$\Theta_{s0} = -\phi(z) + \frac{\phi_i}{2} j_0(z) + 2\int_0^z dz' \left(\frac{d\phi}{dz'}\right) j_0(z - z'), \tag{4.5.10}$$

whose behavior is illustrated in Figure 19. The last term of (4.5.10) describes an ISW con-

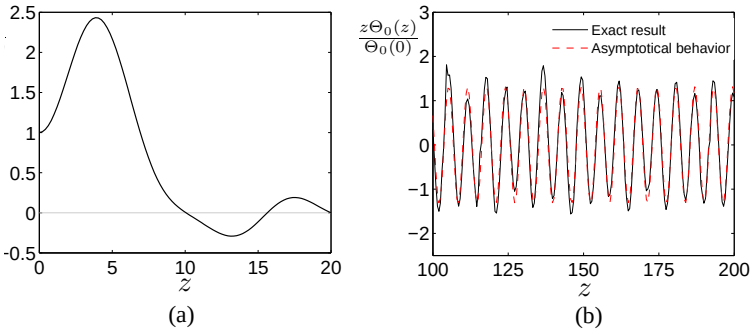

Figure 19: Time evolution of Θ_0 of relativistic sterile neutrinos in the RD universe. Panel (a) shows the early time evolution, where perturbation modes just enter the horizon. The initial growth of the perturbation is due to the ISW effect, reaching maximum around the sound horizon. Eventually these perturbations damp out because of the strong free-streaming suppression of relativistic sterile neutrinos. Panel (b) shows the late time evolution, which is compared with the asymptotic behavior of Eq. (4.5.12).

tribution akin to that in the temperature fluctuations of photons [112, 281]. Due to such an ISW effect, the density perturbations of sterile neutrinos experience an initial kick right after entering the horizon, leading to a growth of density perturbations up to the sound horizon, as shown in the figure. Mathematically, we see that derivative of the gravitational potential ϕ is

negative when the perturbation modes enter the horizon, and its modulus increases, reaching a maximum approximately at the sound horizon $\frac{k\eta}{\sqrt{3}} \simeq \pi$ as shown in Figure 20; meanwhile the free streaming function $j_0(z - z')$ is approximately constant for $z \simeq z'$, therefore the integrand receives the largest contribution near the upper limit. Combining together, the total integral peaks near the sound horizon. However, at late time, free streaming effect becomes dominant. Eventually, these perturbations damp out due to the strong suppression from free streaming. As $z \gg 1$,

$$j_l(z)|_{z\gg 1} \simeq \frac{1}{z}\sin\left(z - \frac{l\pi}{2}\right) + \mathcal{O}(\frac{1}{z^3}). \tag{4.5.11}$$

Making use of the asymptotic behavior in (4.5.11) as well as noting that ϕ decays fast at large z, we obtain for Θ_{sl},

$$\Theta_{sl}(z)|_{z\gg 1} \simeq 3\phi_i \frac{\sin\left(z - \frac{l\pi}{2}\right)}{z}\left[\frac{5}{2} - \sqrt{3}\ln\left(\frac{\sqrt{3}+1}{\sqrt{3}-1}\right)\right] + \mathcal{O}(\frac{1}{z^2}). \tag{4.5.12}$$

At late time, density perturbations of sterile neutrinos oscillate with the period $z = 2n\pi$ and their magnitude is proportional to z^{-1}. Such an oscillatory behavior makes sterile neutrinos, as DM particles, distinct from relativistic photons which experience acoustic oscillation with a different period $z/\sqrt{3} = 2n\pi$, similar to the gravitational potential ϕ (4.2.30).

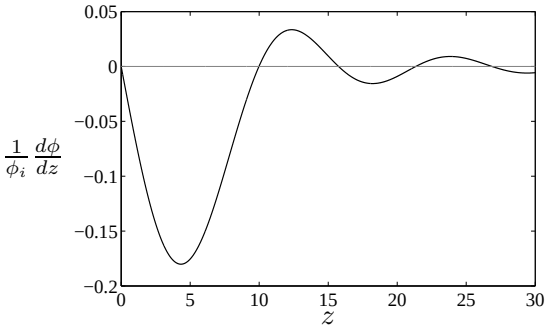

Figure 20: Derivative of the gravitational potential ϕ in the RD era with respect to z, which leads to the ISW kick when perturbation modes of relativistic DM particles enter the horizon in the RD universe.

Eq. (4.5.12) is valid for $z \gg 1$ until sterile neutrinos become non-relativistic. As mentioned previously, sterile neutrinos become non-relativistic roughly when the temperature of the universe drops below their masses, namely $T \leq m$, from which we estimate the transition scale η_{NR} to be

$$\eta_{NR} \simeq \eta_* \left(\frac{T_0}{m a_{eq}}\right) = 0.112 \left(\frac{\text{keV}}{m}\right) \text{Mpc}. \tag{4.5.13}$$

For perturbation modes smaller than 0.2 Mpc, $z_{NR} = k\eta_{NR} > 1$, thus, Eq. (4.5.12) describes the perturbations of sterile neutrinos reasonably well when they become non-relativistic.

4.5.2 Stage II and III: Non-relativistic Sterile Neutrinos

After η_{NR}, sterile neutrinos are non-relativistic; meanwhile, the universe is still deep into the RD era. As we emphasized in our strategy, we are going to neglect details of the transition from relativistic to non-relativistic states of sterile neutrinos. Therefore, the sterile neutrinos are assumed to be fully non-relativistic since η_{NR}. Again, let us start from the formal solution (4.2.27). At non-relativistic limit, $\epsilon \simeq ma$, the formal solution becomes

$$\begin{aligned} F_1(k,q,\mu,\eta) &= e^{-ik\mu(l-l_{NR})} F_1(k,\mu,\eta_{NR}) \\ &\quad -q\frac{d\tilde{f}_0}{dq}\int_{\eta_{NR}}^{\eta} d\eta'\; e^{-ik\mu(l-l')}\left[\dot{\phi}(k,\mu,\eta') - ik\mu\frac{m}{q}\phi(k,\mu,\eta')\right]. \end{aligned} \tag{4.5.14}$$

η_{NR} and l_{NR} respectively label the time and free streaming distance when sterile neutrinos become non-relativistic. By integrating over F_1 and introducing $ds = d\eta/a$ as defined in (4.4.2), we obtain the perturbed number density

$$\begin{aligned} \delta(k,\mu,s) &= 3\phi(k,s) + \int d\vec{q} e^{-i\frac{kq\mu}{m}(s-s_{NR})} F_1(k,\mu,s_{NR}) + \int d\vec{q}\; q\frac{d\tilde{f}_0}{dq} e^{-i\frac{kq\mu}{m}(s-s_{NR})}\phi(s_{NR}) \\ &\quad + \int_{s_{NR}}^{s} ds'\phi(k,s')\left[\frac{d}{ds'}\Pi_2(k,s-s') - a^2k^2(s-s')\Pi_1(k,s-s')\right], \end{aligned} \tag{4.5.15}$$

where

$$\Pi_1(k,s-s') := \int d\vec{q}\tilde{f}_0 e^{-i\frac{kq\mu}{m}(s-s')}, \tag{4.5.16}$$

$$\Pi_2(k,s-s') := \int d\vec{q}q\frac{d\tilde{f}_0}{dq} e^{-i\frac{kq\mu}{m}(s-s')} = -\left[3 + (s-s')\frac{\partial}{\partial s}\right]\Pi_1(k,s-s'). \tag{4.5.17}$$

Unlike WIMPs, the free streaming distance of sterile neutrinos cannot be neglected and plays an important role in the time evolution of density perturbations. It turns out convenient to write $F_1(k,\mu,s_{NR}) = -q\frac{d\tilde{f}_0}{dq}\Theta_s(k,\mu,\eta_{NR})$ and

$$\Theta_s(k,\mu,s_{NR}) = \sum_{l=0}^{\infty}(-i)^l(2l+1)P_l(\mu)\Theta_{sl}(k,s_{NR}), \tag{4.5.18}$$

where Θ_{sl} is given by (4.5.7). Furthermore, by expanding all terms in (4.5.15) with the Legendre polynomials and integrating over the angular dependence μ making use of the orthogonality condition of $P_l(\mu)$, we get

$$\begin{aligned}\delta(k,s) &= 3\phi(k,s) - k^2\int_{s_{NR}}^{s} ds'\phi(k,s')a^2(s')(s-s')\int d\vec{q}q^2\tilde{f}_0 j_0\left(\frac{kq}{m}(s-s')\right)\\ &+\frac{3\phi_i}{2}\int d\vec{q}q\frac{d\tilde{f}_0}{dq}j_0\left(z_{NR}+\frac{kq}{m}(s-s_{NR})\right)\\ &+2\int d\vec{q}q\frac{d\tilde{f}_0}{dq}\int_0^{z_{NR}}dz\phi_z j_1\left(z_{NR}-z+\frac{kq}{m}(s-s_{NR})\right).\end{aligned} \tag{4.5.19}$$

As pointed out previously in the CDM case, u is a convenient variable for WDM density perturbations. Reorganizing Eq. (4.5.19) in terms of u and separating the time evolution between the RD and the MD eras, we obtain

$$\delta(k,u) - 3\phi_m(k,u) - \frac{6}{\alpha}\int_{u_c}^{u}du'\tilde{a}(u')\delta(k,u')\Pi(\alpha,u-u') = I(k,u) \tag{4.5.20}$$

where

$$\begin{aligned}I(k,u) &= 3\phi_r(k,u) - \frac{8k^2}{\alpha k_{eq}^2}\int_{u_{NR}}^{u_c}\tilde{a}^2(u')\phi_r(k,u')\Pi\left(\alpha,u-u'\right)du'\\ &+\int dyy^3\frac{d\tilde{f}_0(y)}{dy}\left\{\frac{3\phi_i(k)}{2}j_0\left[\alpha y(u-u_{NR})+\frac{\kappa}{2}\right]\right.\\ &\left.+2\int_0^{\frac{\kappa}{2}}dz'\phi_r(z')j_1\left[\alpha y(u-u_{NR})+\frac{\kappa}{2}-z'\right]\right\},\\ \Pi(\alpha,u-u') &= \int dyy\tilde{f}_0\sin\left(\alpha y(u-u')\right).\end{aligned} \tag{4.5.21}$$

To obtain Eq. (4.5.20), we have used the facts that $y = q/T_{0,d}$, $\kappa = \alpha\sqrt{\overline{y^2}}$, and $kq(s-s')/m = \alpha y(u-u')$ where α is defined in (4.3.9). $I(k,u)$, called the inhomogeneous term, describes density perturbations up to the radiation cross-over, after which density perturbations evolve

in the MD era[4]. Also, we specify the gravitational potential in the RD era (ϕ_r) and in the MD era (ϕ_m). From the Poisson equation (4.2.31), for $u > u_c$ in the MD era,

$$\phi_m(k,u) = -\frac{3}{4}\frac{k_{eq}^2}{k^2\tilde{a}}\delta(k,u), \tag{4.5.22}$$

For perturbation modes smaller than 0.2 Mpc, $\frac{k_{eq}^2}{k^2} \ll 1$, leading to $\phi_m(k,u) \ll \delta(k,u)$. We thus neglect it from Eq. (4.5.20). Finally, we obtain

$$\delta(k,u) - \frac{6}{\alpha}\int_{u_c}^{u} du'\tilde{a}(u')\delta(k,u')\Pi(\alpha,u-u') = I(k,u). \tag{4.5.23}$$

4.5.2.1 Inhomogeneous Equation for Sterile Neutrino Density Perturbations

Similar to the CDM case, to solve Eq. (4.5.23), we first transform the integral equation into a differential one by differentiating Eq. (4.5.23) twice with respect to u, it yields

$$\frac{d^2}{du^2}\delta - 6\tilde{a}(u)\delta + \kappa^2\delta = \frac{d^2}{du^2}I(k,u) + \kappa^2 I(k,u) - 6\alpha\int_{u_c}^{u} du'\tilde{a}(u')\delta(k,u')\tilde{\Pi}(\alpha,u-u'), \tag{4.5.24}$$

where $\tilde{\Pi}$ is the kernel equal to

$$\tilde{\Pi}(\alpha,u-u') = \frac{1}{N}\int dy\ y f_0(y)(\overline{y^2} - y^2)\sin\left[\alpha y(u-u')\right]. \tag{4.5.25}$$

Again, introduce the quantity $\Delta(k,u) = \delta(k,u) - I(k,u)$, correspondingly, Eq. (4.5.24) becomes

$$\frac{d^2}{du^2}\Delta(k,u) - 6\tilde{a}(u)\Delta(k,u) + \kappa^2\Delta(k,u) = 6\tilde{a}I(k,u) + \mathcal{I}(k,u), \tag{4.5.26}$$

where

$$\mathcal{I}(k,u) := -6\alpha\int_{u_c}^{u} du'\tilde{a}(u')\delta(k,u')\tilde{\Pi}(\alpha,u-u'). \tag{4.5.27}$$

It becomes clear now why $I(k,u)$ is called the inhomogeneous term. In particular, note that the CDM case corresponds to taking $\alpha \to 0$ (See Eqs. (4.3.8) and (4.3.9).), which leads to $\kappa \to 0$ as well. Under these limits, Eq. (4.5.26) indeed reduces to the CDM equation in

[4]We have assumed that $u_c \geq u_{NR}$, which is justified from the following simple arguments: when sterile neutrinos are relativistic, small density perturbations are highly suppressed as shown in Eq. (4.5.12), these perturbations grow only for non-relativistic sterile neutrinos, namely after η_{NR}. Only when perturbation modes start to grow, radiation cross-over is possible to happen. Therefore, $\eta_c > \eta_{NR}$, leading to $u_c > u_{NR}$.

Eq. (4.4.41). Therefore, the CDM case actually corresponds to a special limit of WDM case as $\alpha \to 0$.

To solve Eq. (4.5.26), again we apply the Green's function technique. We first solve the homogeneous equation, making use of the two independent homogeneous solutions to construct the Green's function, then write down the full solution of Eq. (4.5.26) with the initial conditions:

$$\Delta(k, u_c) = \frac{d}{du}\Delta(k, u)\bigg|_{u=u_c} = 0. \tag{4.5.28}$$

4.5.2.2 Asymptotic Behavior Before solving the homogeneous equation, it is helpful to consider the asymptotic behavior first. Recall that $u < 0$ and goes to zero as $\tilde{a} \to \infty$ given by (4.4.6). Thus, as $u \to 0$ ($\tilde{a} \to \infty$)

$$\tilde{a}(u) \simeq \frac{1}{u^2}\bigg|_{\lim u\to 0}. \tag{4.5.29}$$

Consequently, the homogeneous equation becomes

$$\frac{d^2}{du^2}\Delta(k, u) - \frac{6}{u^2}\Delta(k, u) = 0, \tag{4.5.30}$$

which has two independent solutions $g_g = u^{-2}$ and $g_d = u^3$, corresponding to the growing and decaying modes respectively. At late time, the growing mode becomes dominant because it exhibits a linear growth proportional to the scale factor $\tilde{a}$. This is similar to the CDM case in the MD era. Then, let us examine the effect of the inhomogeneous terms. In Eq. (4.5.26), there are two inhomogeneous contributions: i) the inhomogeneous term $I(k, u)$ and ii) the kernel $\mathcal{I}(\delta, u)$. Both $I(k, u)$ and $\mathcal{I}(k, u)$ are finite as $u \to 0$ due to the exponential decay of the distribution function, making them sub-leading to $6\tilde{a}\delta$. Therefore, the asymptotic linear growth of g_d accurately describes the behaviors of WDM particles at late times.

4.5.2.3 Homogeneous Equation: 2nd-order Associated Legendre Equation

We are ready to discuss the homogeneous equation

$$\frac{d^2}{du^2}\Delta(k,u) - 6\tilde{a}(u)\Delta(k,u) + \kappa^2\Delta(k,u) = 0. \tag{4.5.31}$$

In terms of u, the Wronskian of Eq. (4.5.31) is a constant, which can be obtained from the asymptotic behavior. However, to solve the homogeneous equation (4.5.31), it turns out more convenient to work with $\zeta = \sqrt{\tilde{a}+1}$ instead of u. In terms of ζ, the homogeneous equation (4.5.31) becomes

$$\frac{d}{d\zeta}\left[(1-\zeta^2)\frac{d\Delta}{d\zeta}\right] + \left(6 + \frac{\kappa^2}{1-\zeta^2}\right)\ \Delta = 0. \tag{4.5.32}$$

Remarkably, Eq. (4.5.32) corresponds to a 2nd-order associated Legendre equation of ζ. As $\alpha \to 0$, it reduces to the CDM case, an ordinary 2nd-order Legendre Equation (4.4.23), as expected. Introduce $m = i\kappa$, then the two independent solutions of the 2nd-order Legendre equation, $P_2^m(\zeta)$ and $Q_2^m(\zeta)$, are respectively equal to:

$$P_2^m(k,\zeta) = \frac{1}{\Gamma(1-m)}\left(\frac{1+\zeta}{1-\zeta}\right)^{m/2} F(-2,3;1-m;\frac{1-\zeta}{2}), \tag{4.5.33}$$

$$Q_2^m(k,\zeta) = \frac{\sqrt{\pi}}{2^3}\frac{\Gamma(m+3)}{\Gamma(2+3/2)}\frac{(1-\zeta^2)^{m/2}}{\zeta^{m+3}}\ F(\frac{m+4}{2},\frac{m+3}{2};3.5;\frac{1}{\zeta^2}). \tag{4.5.34}$$

Here F represents the hyper-geometric function [8]. Since m is purely imaginary, both $P_2^{\pm m}$ and $Q_2^{\pm m}$ are solutions of Eq. (4.5.32) and they are complex in general. For the physical reason, only real parts are needed. Furthermore, to recover results for the CDM case under the limit $\alpha \to 0$, $P_2^m(k,\zeta)$ and $Q_2^m(k,\zeta)$ are reorganized to give two new homogeneous solutions of Eq. (4.5.32). First of all, define

$$g_g(k,\zeta) := \mathrm{Re}\left[\Gamma(1-m)(-1)^{-m/2}P_2^m(k,\zeta)\right]. \tag{4.5.35}$$

Expanding (4.5.35), we obtain,

$$\begin{aligned} g_g(k,\zeta) = {} & \cos(\kappa u(\zeta))\left[\frac{3(2-\kappa^2)}{(\kappa^2+1)(\kappa^2+4)}(\zeta-1)^2 + \frac{3}{\kappa^2+1}(\zeta-1)+1\right] \\ & + \sin(\kappa u(\zeta))\left[\frac{9\kappa}{(\kappa^2+1)(\kappa^2+4)}(\zeta-1)^2 + \frac{3\kappa}{\kappa^2+1}(\zeta-1)\right]. \end{aligned} \tag{4.5.36}$$

As $u \to 0$, ζ goes to infinity and,

$$g_g(k,\zeta) \simeq \frac{3(2-\kappa^2)}{(\kappa^2+1)(\kappa^2+4)}\zeta^2 \simeq \frac{3(2-\kappa^2)}{(\kappa^2+1)(\kappa^2+4)}\tilde{a}. \tag{4.5.37}$$

Indeed, as indicated by the name, $g_g(k,\zeta)$ corresponds to the growing mode of density perturbations. To simplify the notation, introduce an angle θ such that

$$\cos\theta = \frac{2-\kappa^2}{\sqrt{(\kappa^2+1)(\kappa^2+4)}}, \qquad \sin\theta = \frac{3\kappa}{\sqrt{(\kappa^2+1)(\kappa^2+4)}}. \tag{4.5.38}$$

Consequently,

$$g_g(\zeta) = \sin\theta\ \cos(\kappa u-\theta)\ \frac{1}{\kappa}\left(\zeta^2 - \frac{\kappa^2+1}{3}\right) - \sin\theta\ \sin(\kappa u-\theta)\,\zeta. \tag{4.5.39}$$

Similarly, the other independent solution, defined as the decaying mode, is given by

$$g_d(\zeta) := \mathrm{Re}\left[e^{\kappa\pi}\frac{\Gamma(3-m)}{\Gamma(3)}\frac{\sinh(\kappa\pi)}{\kappa\pi}Q_2^m(\zeta)\right]. \tag{4.5.40}$$

By expanding g_d, we obtain

$$g_d(\zeta) = \frac{\sin(\kappa u)}{2\kappa}\left(\kappa^2+1-3\zeta^2\right) - \frac{3\zeta}{2}\cos(\kappa u). \tag{4.5.41}$$

Asymptotically, as $u \to 0$,

$$g_d(\zeta) \simeq \frac{(\kappa^2+4)(\kappa^2+1)}{30}\zeta^{-3} \simeq \frac{(\kappa^2+4)(\kappa^2+1)}{30}\tilde{a}^{-\frac{3}{2}}. \tag{4.5.42}$$

As expected, g_d is indeed decaying at late time. Write g_g and g_d in terms of u by using the relation $\zeta = -\coth(u)$, thus

$$g_g(k,u) = \sin\theta\ \cos(\kappa u-\theta)\ \frac{1}{\kappa}\left(\coth(u)^2 - \frac{\kappa^2+1}{3}\right) + \sin\theta\ \sin(\kappa u-\theta)\coth(u). \tag{4.5.43}$$

$$g_d(k,u) = \frac{\sin(\kappa u)}{2\kappa}\left[\kappa^2+1-3\coth(u)^2\right] + \frac{3}{2}\cos(\kappa u)\coth(u). \tag{4.5.44}$$

In particular, as $u \to 0$, $\zeta \simeq -1/u$, the asymptotic behavior of (4.5.43) and (4.5.44) becomes

$$g_g(k,u) \simeq \frac{3(2-\kappa^2)}{(\kappa^2+1)(\kappa^2+4)}\ \frac{1}{u^2} \simeq \frac{3(2-\kappa^2)}{(\kappa^2+1)(\kappa^2+4)}\ \tilde{a}, \tag{4.5.45}$$

$$g_d(k,u) \simeq -\frac{(\kappa^2+4)(\kappa^2+1)}{30}\ u^3 \simeq -\frac{(\kappa^2+4)(\kappa^2+1)}{30}\ \tilde{a}^{-3/2}. \tag{4.5.46}$$

As a result, it is straightforward to calculate the Wronskian, which is

$$W[g_g,g_d] = \frac{dg_g(u)}{du}g_d(u) - \frac{dg_d(u)}{du}g_g(u) = 1 - \frac{\kappa^2}{2}. \tag{4.5.47}$$

Note that in the CDM limit, $\kappa \to 0$, the Wronskian equals one, recovering the WIMPs' result. The two homogeneous solutions are shown in Figure 21.

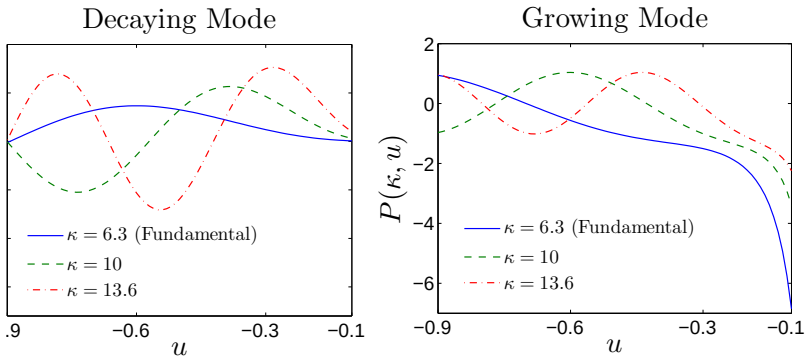

Figure 21: Homogeneous solutions $g_g(k,u)$ and $g_d(k,u)$ of the homogeneous equation (4.5.31) vs. u for various perturbation modes. The left panel corresponds to the growing mode and the right panel the decaying mode.

4.5.2.4 Green's Function And the Full Solution With the homogeneous solutions, it is straightforward to write down the Green's function for Eq. (4.5.24), which is

$$\mathcal{G}(k, u-u') \;=\; \frac{2}{2-\kappa^2}\left[g_g(k,u)g_d(k,u') - g_d(k,u)g_g(k,u')\right]. \tag{4.5.48}$$

Thus, the complete solution for the inhomogeneous equation (4.5.24) is obtained from the Green's function:

$$\Delta(k,u) = \int_{u_c}^{u} du'\mathcal{G}(k,u-u')\left[6\tilde{a}(u')I(k,u') + \mathcal{I}(k,u')\right], \tag{4.5.49}$$

which is subject to the initial condition (4.5.28). Correspondingly, the density perturbation $\delta(k,u)$ becomes

$$\delta(k,u) = I(k,u) + \int_{u_c}^{u} du'\mathcal{G}(k,u-u')\left[6\tilde{a}(u')I(k,u') + \mathcal{I}(k,u')\right]. \tag{4.5.50}$$

We obtain the solution for the WDM density perturbations except for one caveat. Recall the definition of the kernel in Eq. (4.5.27), $\mathcal{I}(k,u)$ itself is an integral function of $\delta(k,u)$. Therefore, the exact expression of $\delta(k,u)$ requires to solve the highly non-trivial integral

equation (4.5.50). Fortunately, $\mathcal{I}(k,u)$ is a small quantity, enabling Eq. (4.5.50) to be solved iteratively. By inserting the expression of $\mathcal{I}(k,u)$ in Eq. (4.5.50),

$$\delta(k,u) \;=\; \delta^{(0)}(k,u) - 6\alpha \int_{u_c}^{u} du' \mathcal{G}(k,u-u') \int_{u_c}^{u'} du'' \tilde{a}(u'') \tilde{\Pi}(\alpha, u'-u'') \delta(k,u''), \tag{4.5.51}$$

where

$$\delta^{(0)}(k,u) = I(k,u) + \int_{u_c}^{u} du' \mathcal{G}(k,u-u')\ 6\tilde{a}(u') I(k,u') \tag{4.5.52}$$

is the leading term without the kernel $\mathcal{I}(k,u)$. Eq. (4.5.51) is similar to the iterative solution in the quantum scattering theory, $\delta^{(0)}$ corresponds to the Born approximation, under which

$$\delta_B(k,u) = \delta^{(0)}(k,u) = I(k,u) + \int_{u_c}^{u} du' \mathcal{G}(k,u-u')\ 6\tilde{a}(u') I(k,u'). \tag{4.5.53}$$

Here the subscript "B" emphasizes the Born approximation.

To justify the Born approximation, let us focus on the kernel $\mathcal{I}(k,u)$ in (4.5.27). As long as $\mathcal{I}(k,u)$ is small and sub-leading compared to the other inhomogeneous term $6\tilde{a}I(k,u)$, it is safe to expect δ_B a pretty good approximation of $\delta(k,u)$. Recall

$$\tilde{\Pi}(\alpha, u-u') = \frac{1}{N} \int dy f_0(y) y \left(\overline{y^2} - y^2\right) \sin\left[\alpha y (u-u')\right], \tag{4.5.54}$$

which depends on the distribution function. For the MB distribution (the WIMPs case), direct evaluation gives

$$\tilde{\Pi}(\alpha, u-u') = e^{-\frac{\kappa^2}{6}(u-u')^2} \left(\frac{m}{T_d}\right)^2 \alpha^3 (u-u')^3. \tag{4.5.55}$$

Obviously, under the CDM limit $\alpha \to 0$, $\tilde{\Pi}$ vanishes, yielding $\mathcal{I}(k,u) = 0$ as expected. As for the WDM case, let us consider DW sterile neutrinos first, namely $f_0 = \frac{\beta}{e^y+1}$, which gives

$$\tilde{\Pi}(\alpha, u-u') = \frac{4Q}{3\zeta(3)} \sum_{n=1}^{\infty} (-1)^{n+1} \frac{n}{\tau^2} \left[\overline{y^2} - \frac{12(n^2-Q^2)}{\tau^4}\right], \tag{4.5.56}$$

where $Q := \alpha(u-u')$ and $\tau := \sqrt{n^2+Q^2}$. Finally, for BD sterile neutrinos, $f_0 = \lambda\frac{g_{5/2}(y)}{\sqrt{y}}$, leading to

$$\tilde{\Pi}(\alpha, u-u') = \frac{\sqrt{2}Q}{3\zeta(5)}\sum_{n=1}^{\infty}\frac{1}{(n\tau)^{\frac{5}{2}}}\sqrt{1+\frac{n}{\tau}}\,\frac{2n+\tau}{n+\tau}\left\{\overline{y^2} - \frac{15}{4}\left[\frac{4n+\tau}{2n+\tau}\frac{(n^2-Q^2)}{\tau^4} + \frac{2n^2}{(2n+\tau)\tau^3}\right]\right\}. \tag{4.5.57}$$

Combining Eqs. (4.5.54), (4.5.56) and (4.5.57), we find that for larger $Q \gg 1$, $\tilde{\Pi}$ decreases with increasing value of Q. On the other hand, when $Q \to 0$, Taylor expansion shows that $\tilde{\Pi}(\alpha, u-u')$ is proportional to Q^3, which is also indicated directly by Eq. (4.5.54).

After analyzing the asymptotic behavior of $\tilde{\Pi}$, let us compare $\mathcal{I}(k,u)$ with $I(k,u)$ to justify the Born approximation. At early time when $u \sim u_c$, $I(k,u) \simeq I(k,u_c)$ and $\delta(k,u_c) \simeq \delta_B(k,u_c)$. On the other hand, $\tilde{\Pi}$ approaches zero as $Q^3 \propto (u-u')^3$ for both DW and BD sterile neutrinos. Correspondingly, $\mathcal{I}(k,u)$ in (4.5.27) is proportional to $(u-u_c)^4$ and much smaller than $6\tilde{a}I(k,u)$. At late time as $u \to 0$, $I(k, u\to 0)$ is finite and $6\tilde{a}I(k,u\to 0) \propto \tilde{a}$. Meanwhile $\tilde{a} \simeq u^{-2}$ and $\delta \propto \tilde{a}$. Applying these asymptotic behaviors to Eq. (4.5.27), we find that $u' \sim 0$ contributes most to $\mathcal{I}(k,u)$, leading to $\mathcal{I}(k,u) \propto \ln(\tilde{a})$ also much smaller than $6\tilde{a}I(k,u)$. Therefore, in the entire region of u, it is reasonable to assume $\mathcal{I}(k,u)$ is sub-leading and can be treated as a perturbation. The Born approximation result δ_B thus indeed is a good approximation of density perturbations of non-relativistic sterile neutrinos.

4.5.2.5 The Born Approximation Of Density Perturbations

Under the Born approximation,

$$\delta(k,u) \simeq \delta(k,u)_B = I(k,u) + 6\int_{u_c}^{u} du'\mathcal{G}(k,u-u')\;\tilde{a}(u')I(k,u'), \tag{4.5.58}$$

where $I(k,u)$ is given by Eq. (4.5.21). At this stage, we can numerically evaluate the above equation to obtain the density perturbations of sterile neutrinos. However, to illustrate the physics behind, we identify three contributions to the inhomogeneity $I(k,u)$ and discuss them separately. According to (4.5.21), $I(k,u)$ is reorganized as

$$I(k,u) = I_1(k,u) + I_2(k,u) + I_{ISW}(k,u), \tag{4.5.59}$$

where

$$I_1(k,u) = -\frac{8k^2}{\alpha k_{eq}^2}\int_{u_{NR}}^{u_c} du'\ \tilde{a}^2(u')\phi_r(k,u')\Pi\left(\alpha, u-u'\right), \tag{4.5.60}$$

$$I_2(k,u) = \frac{3\phi_i(k)}{2}\int dy\ y^3\frac{d\tilde{f}_0(y)}{dy}j_0\left[\alpha y(u-u_{NR})+\frac{\kappa}{2}\right], \tag{4.5.61}$$

$$I_{ISW}(k,u) = 2\int dy\ y^3\frac{d\tilde{f}_0(y)}{dy}\int_0^{\frac{\kappa}{2}} dz'\phi_r(z')j_1\left[\alpha y(u-u_{NR})+\frac{\kappa}{2}-z'\right]. \tag{4.5.62}$$

We have neglected the term $3\phi_r$ in the expression of $I(k,u)$ because it decays quadratically ($\propto 1/(k\eta)^2$) and is absolutely negligible in the MD era. As indicated by the name, I_{ISW} is attributed to the ISW effect in the relativistic stage of sterile neutrinos. As $\alpha, \kappa \to 0$, we reach the CDM limit

$$I_1(k,u) \simeq -\frac{8k^2}{k_{eq}^2}\int dy\ y^2\tilde{f}_0\int_{u_{NR}}^{u_c} du'\ \tilde{a}^2(u')\phi_r(k,u')(u-u'), \tag{4.5.63}$$

$$I_2(k,u) \simeq -\frac{9}{2}\phi_i, \tag{4.5.64}$$

$$I_{ISW}(k,u) \simeq 0. \tag{4.5.65}$$

To compare with Eq. (4.4.44), once again, we confirm that $\alpha \to 0$ corresponds to the CDM case. Moreover, it is worth emphasizing that the ISW term vanishes for the CDM limit as we expected, indicating that indeed it is a unique feature of WDM when sterile neutrinos are relativistic. In Figure 22, we compare the contributions of the three inhomogeneous terms to the transfer function up to a scaling factor $\frac{4}{(\kappa^2+1)(\kappa^2+4)}$ (See Eq. (4.6.6).) for sterile neutrinos and WIMPs. Figure 22 clearly indicates a suppression of the transfer function for sterile neutrinos at small scales compared with that of the WIMPs.

4.6 WDM CASE: TRANSFER FUNCTION AND POWER SPECTRUM

With the semi-analytical scheme discussed previously to compute density perturbations of sterile neutrinos, we are ready to investigate various physical quantities, e.g., the transfer function and the power spectrum, and discuss their application to current understanding on structure formation of our universe.

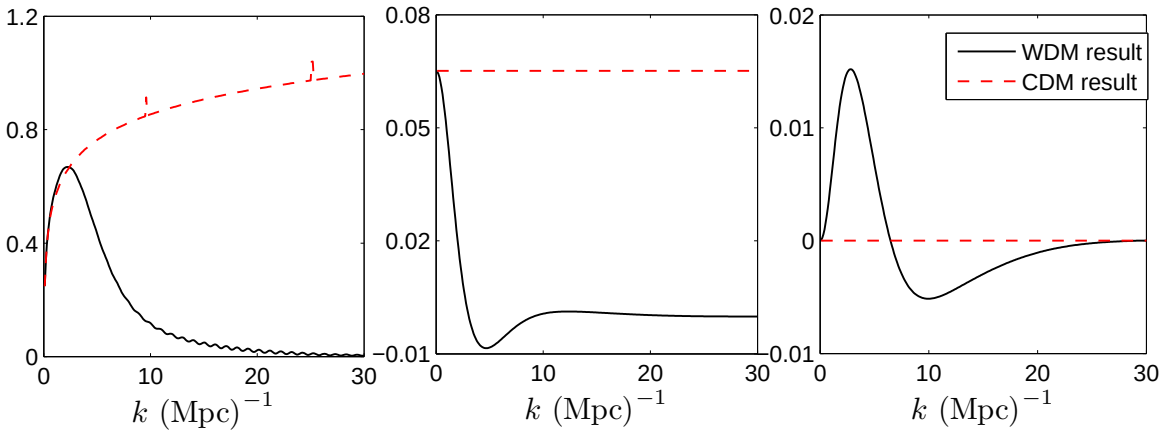

Figure 22: Contribution of the three inhomogeneous terms $I_1(k,u)$, $I_2(k,u)$ and $I_3(k,u)$ to the transfer function defined in Sec. 4.6, up to an overall scaling factor. In this figure, we compare the results of the 1keV DW sterile neutrino (black solid line) and WIMPs for the CDM case (red dashed line). Panel (a) corresponds to the contribution from $I_1(k,u)$, panel (b) to $I_2(k,u)$ and panel (c) to $I_{ISW}(k,u)$.

4.6.1 Transfer Function of Sterile Neutrinos

Similar to the CDM case, at late time, the growing mode dominates over the decaying mode in the Green's function $\mathcal{G}(k,u-u')$, yielding

$$\mathcal{G}(k,u-u') \simeq \frac{2}{2-\kappa^2} g_g(k,u) g_d(k,u'). \tag{4.6.1}$$

Furthermore, taking the asymptotic behavior of the growing mode as $u \to 0$, we obtain

$$\mathcal{G}(k,u-u') \simeq \frac{6\tilde{a}}{(\kappa^2+1)(\kappa^2+4)}\ g_d(k,u'). \tag{4.6.2}$$

Plugging Eq. (4.6.2) into the Born approximation result (4.5.58). At late time, we find,

$$\delta(k,0) \simeq I(k,0) + \frac{36\ \tilde{a}}{(\kappa^2+1)(\kappa^2+4)} \int_{u_c}^{0} du' g_d(k,u')\ \tilde{a}(u') I(k,u'). \tag{4.6.3}$$

The second term, proportional to the scale factor $\tilde{a}$, goes to infinity, while the first term stays constant; therefore, we can neglect the first term in the late time limit. Finally, the density perturbation δ at late time becomes

$$\delta(k) \simeq \frac{36\ \tilde{a}}{(\kappa^2+1)(\kappa^2+4)} \int_{u_c}^{0} du' g_d(k,u')\ \tilde{a}(u') I(k,u'). \tag{4.6.4}$$

Correspondingly, according to its definition in (4.4.38), the transfer function of sterile neutrinos is

$$T_{B(\mathrm{SNs})}(k) = -\frac{30k_{eq}^2}{\phi_i k^2} \frac{1}{(\kappa^2+1)(\kappa^2+4)} \int_{u_c}^{0} du' g_d(k,u')\ \tilde{a}(u') I(k,u'). \tag{4.6.5}$$

Here the subscript "B" and "SNs" are used to emphasize the Born approximation and sterile neutrinos separately. It turns out convenient to compare the transfer functions of WIMPs and sterile neutrinos by defining their ratio,

$$\begin{aligned} \overline{T}_{B(\mathrm{SNs})}(k) &:= \frac{T_{B(\mathrm{SNs})}(k)}{T_{\mathrm{WIMPs}}(k)} = \frac{T_{B(\mathrm{SNs})}(k)}{T_{B(\mathrm{SNs})}(k;\alpha\to 0)} \\ &= \frac{4}{(\kappa^2+1)(\kappa^2+4)} \left[\frac{\int_{u_c}^{0} du' g_d(k,u')\ \tilde{a}(u') I(k,u')}{\int_{u_c}^{0} du' Q_2(u')\ \tilde{a}(u') I(k,u';\alpha\to 0)} \right]. \end{aligned} \tag{4.6.6}$$

Here we have made use of the fact that the CDM case corresponds to a special limit ($\alpha \to 0$) of the WDM result. In Figure 23, we demonstrate the ratio for 1keV DW sterile neutrinos. In particular, panels (b) and (c) show the behaviors of the transfer function $\overline{T}_{B(\mathrm{DW})}$ for small and large wave vectors k respectively. For very large scale perturbations as $k \to 0$, the transfer function of DW sterile neutrinos is similar to that of WIMPs. However, for small scale perturbation modes, the transfer function of sterile neutrinos is suppressed with respect to that of the WIMPs. More interestingly, at even smaller perturbation scale, say $k \geq 10\ (\mathrm{Mpc})^{-1}$, the transfer function demonstrates some peculiar oscillation feature, which has never been found before. To investigate the dependence of $\overline{T}_{B(\mathrm{DW})}$ on the masses and distributions of sterile neutrinos, also to investigate how general this new oscillation feature is, we need to compare the transfer function of sterile neutrinos for different masses and production mechanisms. These results will be discussed below.

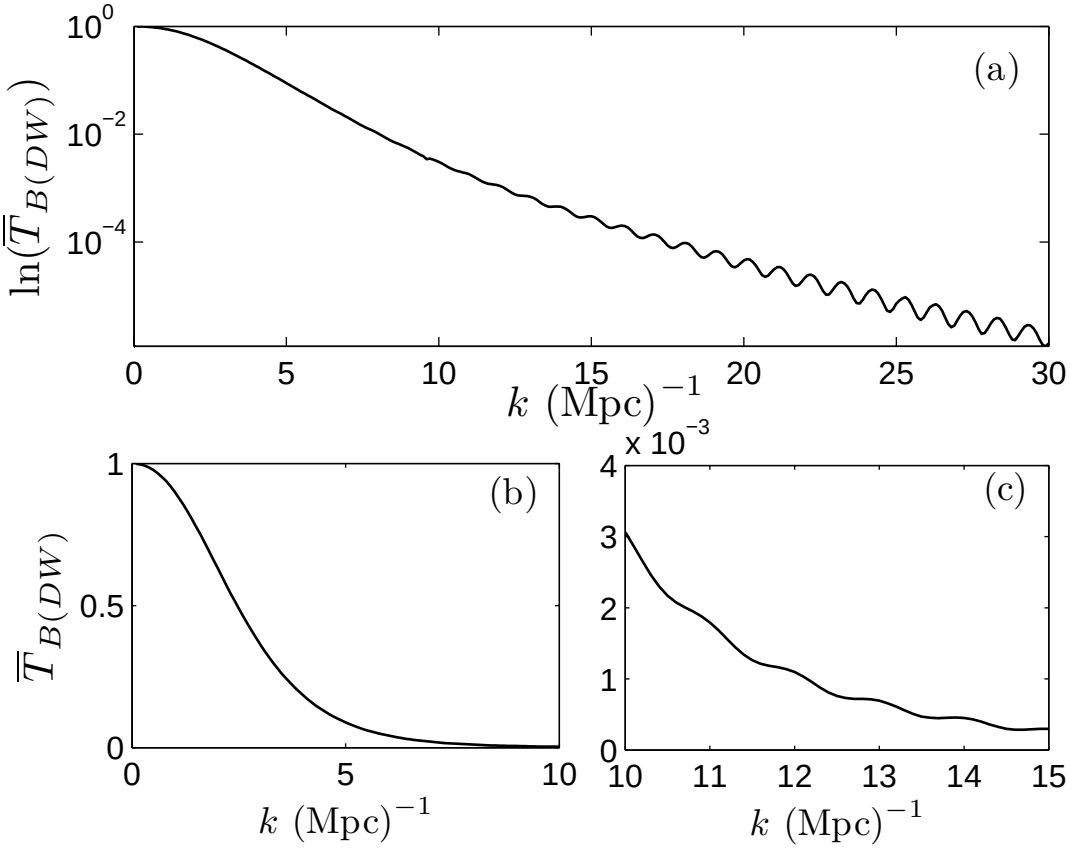

Figure 23: $\overline{T}_{B(\mathrm{DW})}(k)$ for DW sterile neutrinos with $m = 1$keV. Panel (a) shows the logarithmic of $T_{B(\mathrm{DW})}$ for a wide range of $k \in (0, 30)$. As $k \to 0$, the WDM and CDM transfer functions coincide with each other for super-horizon modes, consistent with the physical expectation. Panel (b) shows the values of $\overline{T}_{B(\mathrm{DW})}(k)$ for relatively small k from 0 to 10, corresponding to perturbation scales larger than 100Kpc. The WDM transfer function drops quickly with respect to the CDM transfer function as k increases. Panel (c) shows the ratio of the transfer functions for even smaller perturbation modes. The WDM transfer function starts to oscillate with a period about 1Mpc, a new unique feature of WDM density perturbations, which may hint interesting observational signatures.

4.6.1.1 Numerical Evaluation In principle, for any given sterile neutrino mass and distribution function, one can numerically evaluate all integrals involved in Eq. (4.6.6) and obtain the transfer function. We try to simplify these integrals as much as possible for an efficient numerical implementation.

First of all, note that the upper limit in $I_1(k,u)$ is u_c, corresponding to the radiation cross-over, namely the transition from when the gravitational potential is dominated by the radiation fluid to when it is dominated by DM perturbations. In the CDM analysis, we have found that this scale is a few tenth of the scale of matter-radiation equality for perturbation modes we are interested in (See Eq. (4.4.18)). Furthermore, density perturbations in the CDM case depend only logarithmically on the scale factor around radiation cross-over, making the exact value of u_c insensitive to small errors. In the WDM scenario, we expect the stronger free-streaming effect to further suppress the growth of matter density perturbations in the RD era, and delay the time of radiation cross-over. With the information obtained from the CDM case, it is sensible to approximate $u_c \simeq u_{eq}$, namely,

$$u_c \simeq u_{eq} = \frac{1}{2}\ln\left[\frac{\sqrt{2}-1}{\sqrt{2}+1}\right] \simeq -0.881. \tag{4.6.7}$$

We will confirm this approximation in the following numerical evaluation.

By replacing u_c by $u_{eq} = -0.881$, $I_1(k,u)$ becomes

$$I_1(k,u) = -\frac{8k^2}{\alpha k_{eq}^2}\int_{u_{NR}}^{u_{eq}} du'\tilde{a}^2(k,u')\phi_r(k,u')\int dyy\tilde{f}_0(y)\sin\left[\alpha y(u-u')\right]. \tag{4.6.8}$$

By manipulating this equation to optimize its behavior under the numerical evaluation, we finally obtain

$$\begin{aligned}
\tilde{I}_1(k,u) &= -\frac{I_1(k,u)}{3\phi_i} \\
&\simeq \left(-\frac{6}{\alpha}\right)\int dyy\tilde{f}_0(y)\Bigg\{\frac{\alpha y}{2}\int_{x_{NR}}^{x_{eq}} dx'\ \left(\frac{\sin x'}{x'^2}-\frac{1}{x'}\right)\cos\left[\alpha y\left(u+\frac{1}{2}\ln(1+\frac{4x_*}{x'})\right)\right] \\
&\quad +\left(1+\frac{x_{eq}}{4x_*}\right)\frac{\sin(x_{eq})}{x_{eq}}\sin\left[\alpha y\left(u+\frac{1}{2}\ln(1+\frac{4x_*}{x_{eq}})\right)\right] \\
&\quad -\frac{\sin(x_{NR})}{x_{NR}}\sin\left[\alpha y\left(u+\frac{1}{2}\ln(1+\frac{4x_*}{x_{NR}})\right)\right] \\
&\quad +\sin\left[\alpha y\left(u+\frac{1}{2}\ln(\frac{4x_*}{x_{NR}})\right)\right]-\sin\left[\alpha y\left(u+\frac{1}{2}\ln(\frac{4x_*}{x_{eq}})\right)\right]\Bigg\},
\end{aligned} \tag{4.6.9}$$

where x is related to u by

$$x = 4x_* \frac{e^{2u}}{1 - e^{2u}}. \tag{4.6.10}$$

In practice, we will use Eq. (4.6.9) for numerical calculations. Details to derive $I_1(k, u)$ from Eq. (4.6.8) to Eq. (4.6.9) can be found in App. B. The integrals associated with $I_2(k, u)$ and $I_3(k, u)$ can be numerically calculated directly.

4.6.1.2 Transfer Function of Sterile Neutrinos With Different Masses And Distributions

With the simplification mentioned in the previous section, we carry out all the numerical integrations in Eq. (4.6.6) and compare the transfer functions of sterile neutrinos for different masses and production mechanisms. In Figure 24, we plot the transfer function in Eq. (4.6.6) for both DW and BD sterile neutrinos with masses of 1 keV and 2 keV respectively in both linear and log scales. Since the BD distribution is colder than the DW distribution, the transfer function of BD sterile neutrinos is less suppressed than that of DW sterile neutrinos with the same mass. On the other hand, under the same production mechanism, sterile neutrinos with heavier masses are colder than those with lighter masses, again leading to less suppression on their transfer functions. Moreover, it is interesting to note from Figure 24 that despite the different masses as well as different distributions, the transfer function of 2 keV DW sterile neutrinos is very close to that of 1 keV BD sterile neutrinos for perturbation modes $k \leq 10\ \mathrm{Mpc}^{-1}$. This observation may suggest profound applications on current cosmological data analysis, which will be discussed in detail in the following. Finally, from Figure 24, the oscillatory feature at small scales of the transfer functions of DW sterile neutrinos is obvious, but for the BD case, the oscillations seem not clear in the figure. However, by extending the transfer function to even smaller scales, one can identify these oscillations more easily. In the following discussions, we will investigate the oscillation feature of the transfer function explicitly.

4.6.1.3 ISW Enhancement

As discussed previously in Eqs. (4.5.60) to (4.5.62) and their CDM limits Eqs. (4.5.63) to (4.5.65), the contribution I_{ISW}, corresponding to the so called ISW effect [112], comes from the evolution of density perturbations during stage I, and vanishes in the CDM limit. Therefore it is a distinct contribution to the WDM transfer

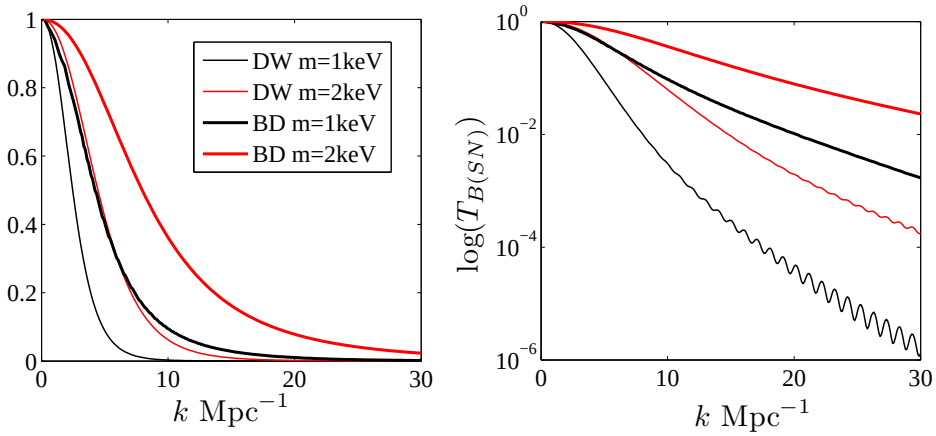

Figure 24: Transfer functions of DW and BD sterile neutrinos with $m = 1$keV and $m = 2$keV respectively in linear (left panel) and log (right panel) scales. The thin (thick) solid lines correspond to DW (BD) sterile neutrinos and the black lines are for the case of $m = 1$keV while the red lines for $m = 2$keV.

function and arises from the time derivative of the gravitational potential in the RD era which is driven by the acoustic oscillations of the radiation fluid. Although this ISW effect, yielding perturbation growth in the early stage, cannot be the dominant contribution to the final transfer function as directly shown in Figure 22, it is still interesting to investigate its origin and dependence on different physical parameters. Figure 19 has shown the influence of the ISW effect on density perturbations of WDM particles, where we learn that it features a peak when the perturbation mode is approximately of the same size as the sound horizon at η_{NR}. Following the similar argument, the presence of a peak can also be gleaned from the expression of I_{ISW} directly, which locates around the first maximum of the spherical Bessel function j_1. Let us call this value p_*. Hence, according to the expression of I_{ISW} in Eq. (4.5.62), the peak value of the ISW effect corresponds to

$$\alpha y(u - u_{NR}) + \frac{\kappa}{2} - z' \simeq p_*. \tag{4.6.11}$$

Note that $\kappa = \alpha\sqrt{\overline{y^2}}$ and $z' \in (0, \kappa/2)$ and $\alpha \propto k/m$ as defined in (4.3.9). The ISW peak value corresponds to a wave vector k that is proportional to $m/\sqrt{\overline{y^2}}$. Therefore the hotter

species, with smaller mass m and larger $\sqrt{\overline{y^2}}$, must feature a peak at a smaller value of k while the colder species feature the peak at a larger value k. This expectation is borne out by Figure 25, which displays the ISW contribution to the Born ratio $\overline{T}_{B(\mathrm{SNs})}(k)$ in (4.6.6). The ISW enhancement extends to larger values of k for the colder species. For small k, the contributions I_2 and I_{ISW} feature opposite signs as shown in Figure 22, therefore, the ISW enhancement competes with and is partially canceled by I_2, yielding an overall suppression of the transfer function with respect to CDM. Nevertheless, the ISW enhancement could prolong the region in k where the transfer function is closer to that of CDM.

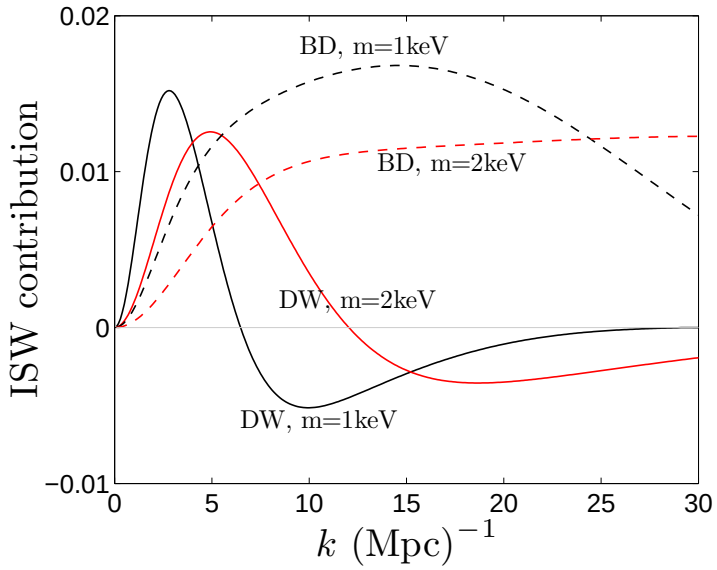

Figure 25: ISW contribution to the Born approximated transfer function $\overline{T}_{B(\mathrm{SNs})}(k)$ in Eq. (4.6.6). For simplicity, We only plot the ISW contribution to the integral in the numerator of (4.6.6) for sterile neutrinos with different masses and distribution functions. Solid(dashed) lines correspond to DW(BD) sterile neutrinos. Black ones refer to sterile neutrinos with masses $m = 1$ keV and red ones are for $m = 2$ keV.

4.6.1.4 "Acoustic Oscillations" of WDM In addition to the unique ISW effect, there is another special feature of the WDM transfer function: as pointed out previously, at small scale perturbation modes, namely large wave vector k, we find that the transfer function of sterile neutrinos oscillates. This is analogous to the acoustic oscillations found in the power

spectrum of CDM, we therefore call this oscillation behavior as "acoustic oscillations" of WDM. For different sterile neutrinos with different masses and production mechanisms, it turns out a common behavior. In general, the oscillation feature is more obvious for WDM particles with warmer production mechanisms and smaller masses, as shown in Figure 24. When extending the transfer function of BD sterile neutrinos in Figure 24 to even smaller scales, we can identify the oscillations clearly as shown in Figure 26. Given the generality of the WDM acoustic oscillations, we try to identify sources of these oscillation features in this section.

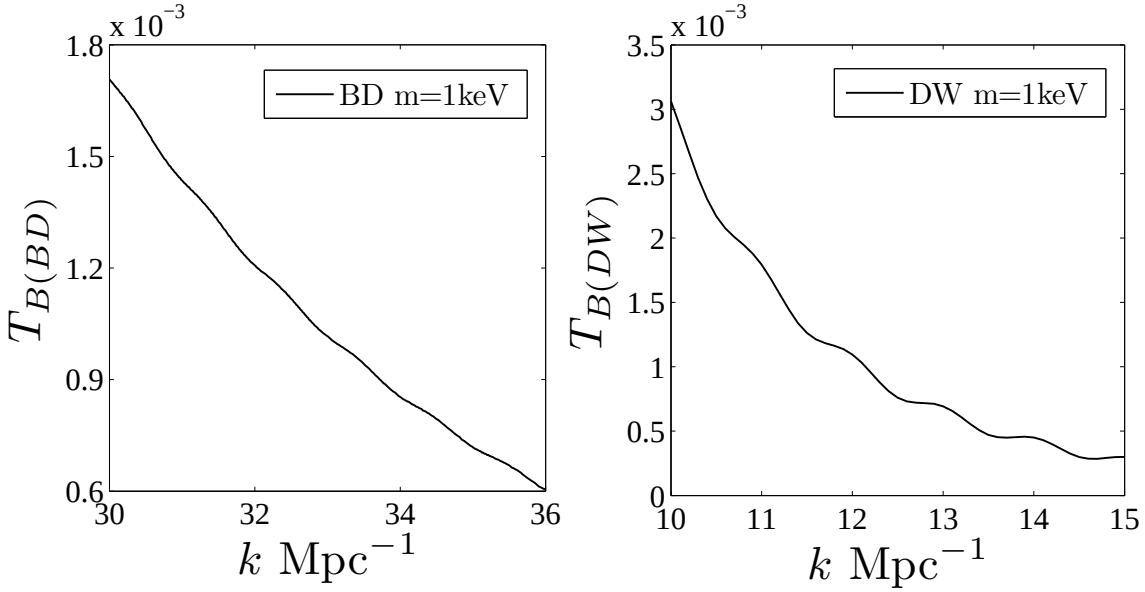

Figure 26: The oscillation feature on the transfer function in Eq. (4.6.6) for $m = 1$keV sterile neutrinos with BD distribution in the left panel and DW distribution in the right panel. Note that oscillations start from different values of ks.

In Figure 22, we have compared the three inhomogeneous contributions to the WDM transfer function, where we found $I_1(k, u)$ is the dominant term. Furthermore, it features the similar oscillation behavior to $\overline{T}_{B(\mathrm{SNs})}(k)$ at small scales. Hence, we recognize this should be the origin for the acoustic oscillations, and focus on this term in the following discussion. According to the expression of $I_1(k, u)$ in Eq. (4.5.60) and $\overline{T}_{B(\mathrm{SNs})}(k)$ defined in (4.6.6),

$I_1(k,u)$ contributes to the transfer function by integrated with the decaying mode $g_d(k,u')$ times the scale factor given by Eq. (4.5.58). $g_d(k,u)$ is in general an oscillatory function vanishing at u = 0, and there is a particular fundamental mode corresponding to $\kappa \simeq 6.3$ that features only one other node at matter-radiation equality as shown in Figure 21. For perturbation modes with $\kappa < 6.3$, $g_d(k,u)$ does not oscillate; while for perturbation modes with $\kappa > 6.3$, $g_d(k,u)$ oscillates with respect to u. On the other hand, the explicit form of I_1 given in Eq. (4.6.8) reveals at least two contributions that lead to oscillations: the gravitational potential ϕ_r features an acoustic oscillation and $\sin[\alpha y(u-u')]$ corresponds to the free streaming effect. Unfortunately, the oscillation feature from the free streaming term is washed away after integrating over the distribution function $\tilde{f}_0(y)$. By comparing the remaining two contributions from g_d and ϕ_r, we note that ϕ_r decreases in power law with respect to increasing wave vector k, thus, the oscillation behavior resulting from ϕ_r manifests for larger scale perturbation modes(corresponding to smaller ks). However, for WDM cases, we observe the "acoustic oscillations" at small scales. Therefore, we conclude that the "acoustic oscillations" of WDM transfer functions mainly result from the free streaming effect embedded in the decaying mode g_d, in contrast to the oscillation feature of transfer function discovered in [207]. Since g_d starts to oscillate from $\kappa \simeq 6.3$, we estimate the "acoustic oscillations" manifest for $\kappa \geq 6.3$, leading to

$$k \geq 6.3\frac{\sqrt{2}}{2\sqrt{3}}k_{fs} \sim 2.6k_{fs}. \tag{4.6.12}$$

This approximated estimation seems supported by numerical evaluations: for 1 keV DW sterile neutrinos, $k_{fs} \simeq 7.7$ Mpc^{-1} where the oscillations in transfer function start from $k \sim 11$ Mpc^{-1}; for 1 keV BD sterile neutrinos with $k_{fs} \simeq 14.12$ Mpc^{-1}, oscillations start from $k \sim 30$ Mpc^{-1}. These behaviors are shown in Figure 26. At the CDM limit, $k_{fs} \to \infty$, thus the oscillations disappear.

These oscillation features suggest interesting observation signals; however, at the scale where WDM acoustic oscillations emerge, the transfer function is strongly suppressed by free-streaming. And as a result of this suppression in the power spectrum, the relevance of these WDM acoustic oscillations for structure formation is not clear. Moreover, at such

small scales, density perturbations become highly non-linear. Whether the non-linear effect would wash out or amplify the oscillation features of density perturbation power spectrum needs further investigation. If these oscillations indeed appear as observational signals, we expect to observe clumpiness in the mass distribution with mass scales $M_{DW} \sim 3 \times 10^9 M_\odot$ and $M_{BD} \sim 1.8 \times 10^8 M_\odot$ for DW and BD sterile neutrino respectively.

4.6.2 Power Spectrum Of Sterile Neutrinos

The power spectrum normalized to CDM is given by

$$\overline{P}_{B(\mathrm{SNs})}(k) = \left[\overline{T}_{B(\mathrm{SNs})}(k)\right]^2 . \tag{4.6.13}$$

Correspondingly, the power spectrum of sterile neutrinos is

$$P_{B(\mathrm{SNs})} = P_{CDM}(k)\left[\overline{T}_{B(\mathrm{SNs})}(k)\right]^2 . \tag{4.6.14}$$

To estimate $P_{CDM}(k)$, we note that the transfer function for WDM particles is indistinguishable from that of the CDM for small k, and our CDM transfer function (4.4.40) is consistent with that of Weinberg in [280] for small scale perturbations, which agrees nicely with the BBKS numerically fitted transfer function [43]. Therefore, we use the numerical fit provided by Bardeen *et al.* [43] for the CDM transfer function (without baryons) to extrapolate $P_{CDM}(k)$ to large scales:

$$P_{CDM}(k) = A k^{n_s}\left[T_{BBKS}(k)\right]^2 , \tag{4.6.15}$$

where A is the overall amplitude and is determined by the power spectrum of scalar fluctuations during inflation [112] and $n_s \simeq 0.96$ is the index of scalar perturbations during inflation [202, 195]. Without baryons and with three relativistic (standard model) neutrinos [43]:

$$T_{BBKS}(k) \simeq \frac{\ln(1+2.34K)}{2.34K}\left[1+3.89K+(16.1K)^2+(5.46K)^3+(6.71K)^4\right]^{-1/4} , \tag{4.6.16}$$

where

$$K = \frac{k}{\Omega_m h^2}\ \mathrm{Mpc}^{-1}. \tag{4.6.17}$$

Plugging Eqs. (4.6.16) and (4.6.15) into (4.6.14), and making use of the expression of $\overline{T}_{B(\mathrm{SNs})}(k)$ in Eq. (4.6.6), we obtain the power spectrum of sterile neutrinos as

$$P_{B(\mathrm{SNs})}(k) = Ak^{n_s}\left[\frac{4T_{BBKS}}{(\kappa^2+1)(\kappa^2+4)}\frac{\int_{u_c}^{0} du' g_d(k,u')\ \tilde{a}(u')I(k,u')}{\int_{u_c}^{0} du' Q_2(u')\ \tilde{a}(u')I(k,u';\alpha\to 0)}\right]^2 . \tag{4.6.18}$$

This compact expression provides an interpolation between large and small scales that describes accurately the CDM limit for long-wavelengths and captures the free streaming suppression at small scales encoded in the Born approximation. Its numerical implementation is fairly straightforward for arbitrary distribution functions, masses and decoupling temperatures.

4.6.3 Comparison to Numerical Results From Boltzmann Codes

The WDM power spectrum for non-thermal sterile neutrinos produced via the DW mechanism has been studied in Refs. [94, 259, 165, 3, 4, 133, 1, 274]. The most recent studies using the Boltzmann codes CMBFAST [255, 291, 290] and/or CAMB [203] have been reported in [165, 1, 274]. The results in [274] coincide with those in [165] and are summarized by the fit given by Eqs. (6) and (7) in [274]. In both studies, the distribution function for sterile neutrinos is the DW type as shown in (4.2.10). Nevertheless, the fitting function provided in Ref. [274] fits the results of the Boltzmann code in the range $k < 5h$ Mpc^{-1} [274].

Compared with [274] and [165], in Ref. [2], the kinetic equation for the production of DW sterile neutrinos was solved numerically and the solution was input in the numerical Boltzmann codes. In this study, the explicit form of the distribution function is not provided but instead a fitting formula for the transfer function normalized to CDM is given, corresponding to Eqs. (11) and (12) in [2]. Whereas the fitting function in Ref. [274] is of the same form as that in [2], they differ in the powers of momenta: at large ks, the fitting formula in Ref. [2] falls off with a power $\simeq k^{-6.93}$ whereas the fit given by Ref. [274] falls off with a power $\simeq k^{-10}$. Consequently, these two fits yield a large difference at small scales even though they agree with each other substantially at large scales (See Figure 4 in Ref. [2]). Since the distribution function in [2] has been obtained directly from the numerical integration of the

kinetic equation, it is not clear whether the main differences in the transfer function are a result of this effect, that the distribution function obtained from numerically solving the kinetic equation is different from the form (4.2.10) as used in [274] and [165].

For our purpose, it turns out convenient to directly compare our results with those in [274] because both studies use the same distribution function (4.2.10) and neglects baryons. However, in [274], it includes dark energy $\Omega_\Lambda = 0.7$ while our study does not. We compare our results for the transfer function T(k) (normalized to CDM) given by Eq. (4.6.6) with those obtained from the fitting functions in Ref. [274] and [2]. According to the discussion in [274], we are aware that its fitting function may not be correct for $k > 5h$ Mpc^{-1}. Also, a direct comparison of our results with those in Ref. [2] may not be fair because our assumed distribution function in (4.2.10) could be different from the effective distribution function in [2], and the difference cannot be quantified in the absence of a functional form. Furthermore, we use the "standard" value $g_d = 10.75$ for these comparisons, whereas in Ref. [2], the actual value of g_d may differ because this species of sterile neutrinos is produced very near the QCD phase transition where the effective number of relativistic degrees of freedom varies rapidly. Recognizing all these caveats, we compare the normalized transfer functions calculated from the three methods in Figure 27.

We find a remarkable agreement, to less than 5% with the fit given by the non-thermal case in Eqs. (6) and (7) in Ref. [274] in a wide range where their fit is valid. In Figure 27, the comparison is in a range similar to [2] to highlight agreements and discrepancies. In all cases reported in the literature, the range studied or displayed are for wave vectors k far smaller than the range in which the acoustic oscillations become manifest. The approximate estimate for the threshold suggests that for $m = 0.5, 1.0, 1, 7$ keV, oscillations should be manifest for $k \geq 7.5, 15.0, 25.6\ h$ (Mpc)$^{-1}$ respectively. Figure 28 displays the transfer function in (4.6.6) in a linear-linear scale for $k \geq 2k_{fs}$ and $m = 1.0, 1.7$ keV. These figures are the continuation of the solid lines displayed in Figure 27 up to the smaller scales. This comparison, despite all the caveats mentioned above, suggests that the semi-analytic formulation along with the Born approximation summarized by (4.6.6) captures the essential physical processes and

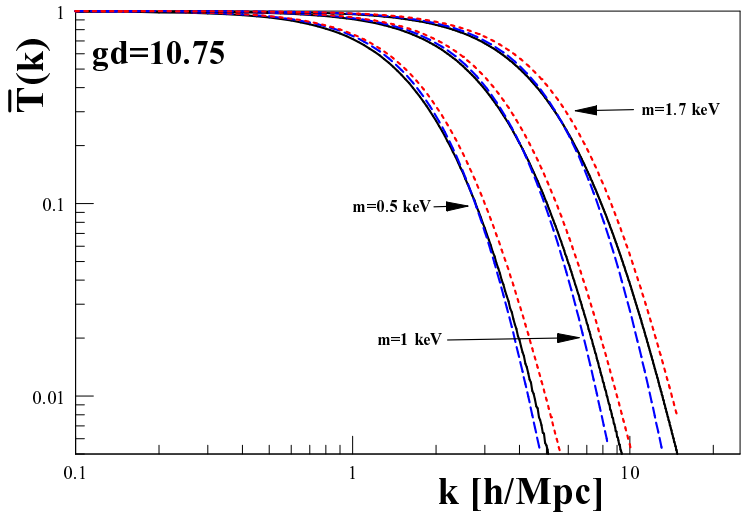

Figure 27: Comparison of the normalized transfer function for DW with the results from Boltzmann codes. The solid line is the semi-analytical result from Eq. (4.6.6), the (blue) dashed line is the result from the interpolation of non-thermal case in Ref. [274], the (red) dotted line is the result from the interpolating fit in Ref. [165]. For all cases $h = 0.72$, $\Omega_{DM}h^2 = 0.133$ and $g_d = 10.75$.

provide a reliable tool to study the transfer function and the power spectrum for arbitrary distribution functions.

4.6.4 Impact On N-body Simulation And Lyman-α Constraints

N-body simulations of galaxy formation and high resolution Layman-α spectra analysis are the two most powerful techniques currently available to constrain the mass of WDM particles [81]. The most recent large scale N-body simulations [267, 213] incorporate WDM by considering a power spectrum that is cutoff at small scales, however, initial velocity dispersion is not yet included in the simulations. Extracting constraints from the Lyman-α forest involves also large scale numerical simulations, and the most recent constraints [271, 73, 72] on the mass of WDM particles rely on specific distribution functions, usually using either a thermal or DW distribution functions. The DW distribution function is proportional to a thermal distribution function with the proportionality constant to determine the abundance but irrelevant for the free streaming length or indeed the transfer function. Only in [73], the authors

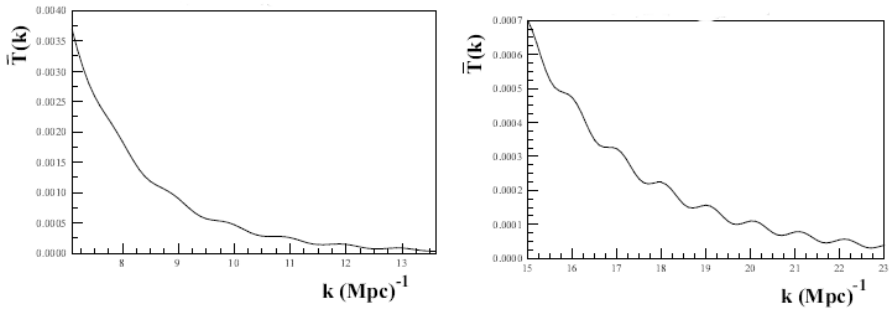

Figure 28: $\overline{T}_{B(DW)}(k)$ from the semi-analytical approximation (4.6.6) displaying the acoustic oscillations at small scales $k \geq 2k_{fs} \simeq 10.8, 18.5$ $(\text{Mpc})^{-1}$ for $m = 1.0, 1.7$ keV respectively. Note that the horizontal scale is in $(\text{Mpc})^{-1}$ and that vertical scales differ by a factor 5 between the two figures.

consider a more realistic case allowing Resonantly Produced (RP) sterile neutrinos. Current Lyman-α constraints combined with X-ray seem to exclude the DW production mechanism as the sole producing method for sterile neutrinos [81]. The sensitivity of N-body simulations and Lyman-α analysis on WDM distribution functions has been realized and discussed in the literature [73, 72, 81]. The mass and the distribution function of WDM particles form a quasi-degenerate parameter space to influence the simulated or observed power spectrum of density fluctuations because both of them can affect the coldness of the WDM particles. Our study confirms this quasi-degeneracy feature in that more massive sterile neutrinos with a DW distribution function feature a similar power spectrum as less massive sterile neutrinos with a colder BD distribution function in a wide range of scales. To make this more explicit, Figure 29 displays the normalized power spectrum defined in (4.6.13).

From this figure it is clear that $\overline{P}_{B(DW)}(k)$ with $m = 2$ keV is almost indistinguishable from $\overline{P}_{B(BD)}(k)$ with $m = 1$ keV for $k \leq 10$ $(\text{Mpc})^{-1}$, well within the sensitive region of Lyman-α forest analysis. Therefore, we emphasize that the mass is not the only relevant indicator for the power spectrum of the WDM particle, but also other two important aspects must enter in the assessment: the decoupling temperature (higher for the colder particles)

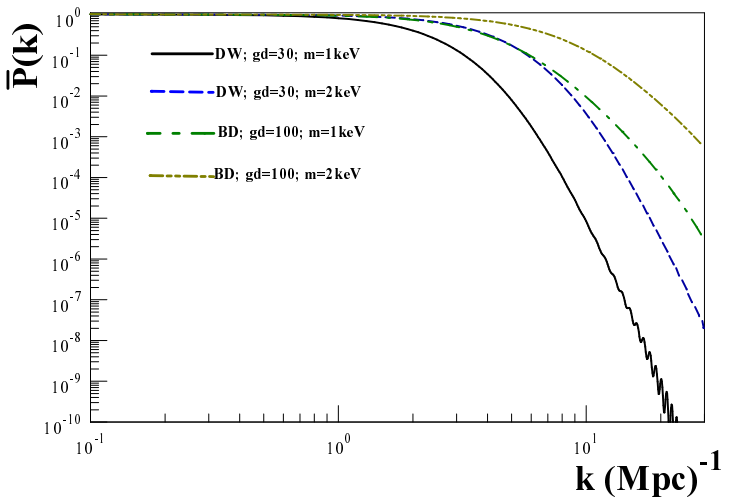

Figure 29: Normalized power spectrum (4.6.13) for DW and BD sterile neutrinos with $m = 1, 2$ keV.

and the details of the distribution function at small momenta: enhanced small momentum behavior leads to a colder species and a less suppressed power spectrum, for a given mass. Because of this quasi-degeneracy, current constraints on the mass of the WDM particle, either from WDM simulations, or from Lyman-α forest analysis based on thermal or DW distribution functions do not directly apply to non-thermal WDM particles. In Ref. [73], the authors consider a more realistic distribution function of sterile neutrinos, on which the mass constraints do not contradict with current cosmological observations. To further highlight this point, we plot in Figure 30 the full power spectrum defined in (4.6.18) for the different species under our consideration. Again, the cases of BD sterile neutrinos with $m = 1$ keV and DW sterile neutrinos with $m = 2$ keV are nearly indistinguishable for $k \leq 10$ (Mpc)$^{-1}$.

4.7 SUMMARY AND CONCLUSION

In this chapter, we provide a semi-analytical study of small scale aspects of the power spectrum of WDM candidates in a radiation-matter cosmology for arbitrary mass and distribution

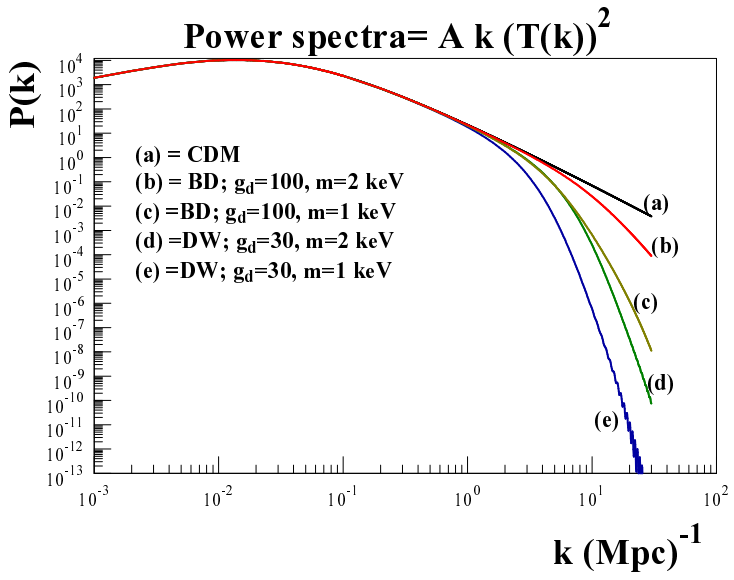

Figure 30: The matter power spectrum

function of the decoupled WDM particle. There are three stages in the evolution of density perturbations of WDM candidates that decouple while they are relativistic: stages I) and II) describe the evolution during the RD era when the particles change from relativistic and non-relativistic form, while the gravitational potential is dominated by the radiation fluid. During stage III, the particle is non-relativistic and matter density perturbations dominate the gravitational potential. We consider adiabatic initial conditions determined when all the cosmologically relevant modes are outside the horizon, consistent with inflation and CMB data from WMAP [195, 202]. The linearized collisionless Boltzmann equation is solved for the three stages, with the solution of the previous stage acting as the initial condition for the next stage. By connecting these piece-wise solutions, we obtain the transfer function and power spectrum of WDM particles. We find the transfer function is characterized by two widely separated scales: $k_{eq} \sim 0.01$ (Mpc)$^{-1}$ the wave vector of perturbation modes that enter the horizon at matter-radiation equality, and the free streaming wave vector k_{fs} in κ.

According to our definition,

$$k_{fs} = \frac{\sqrt{3}k_{eq}}{2\langle V_{eq}^2\rangle^{1/2}} = \frac{\sqrt{2}}{\sqrt{3}}\eta_{NR}, \tag{4.7.1}$$

where $\langle V_{eq}^2\rangle^{1/2}$ is the mean square root velocity dispersion of the WDM particle at matter-radiation equality. Meanwhile, k_{fs} is also of the same scale as η_{NR}, namely the size of the comoving horizon when the WDM particle becomes non-relativistic.

During stages I) and II), the acoustic oscillations in the radiation fluid dominate the gravitational potential, leading to an ISW effect that amplifies WDM density perturbations on scales larger than the sound horizon at η_{NR}. This amplification translates in a prolonged plateau in the transfer function for $k < k_{fs}$, which is more pronounced for colder species since these feature a smaller k_{fs}.

In stage III) when the particle is non-relativistic and WDM perturbations dominate the gravitational potential, the evolution is described by the Boltzmann-Poisson equation which yields an integral equation for density perturbations and is equivalent to integro-differential equation with an inhomogeneity and initial conditions determined by the past history during stages I) and II). This equation is amenable to a systematic Fredholm expansion valid at small scales, whose leading order is the Born approximation that establishes a direct relation with a fluid description of WDM perturbations. The resulting fluid equation is the generalization of Meszaros equation for CDM but with an inhomogeneity and initial conditions that incorporate suppression by free streaming during the first two stages. The Born approximation lends itself to a simple numerical implementation for arbitrary distribution functions and mass of the decoupled WDM particle. The transfer functions and power spectra resulting from the fluid equation feature WDM acoustic oscillations at small scales roughly of $k \geq 2k_{fs}$, as a consequence of free-streaming effect with non-vanishing velocity dispersions.

With the expression of transfer function under the Born approximation, we study two non-resonant sterile neutrino distributions with various masses about keV range in detail, from which we investigate the mass and distribution dependence of the transfer function. In

addition, we also discuss the influence of these parameters on ISW enhancement and WDM acoustic oscillations. Although the power spectrum is strongly suppressed by free streaming at the scales at which WDM acoustic oscillations emerge, we conjecture that non-linear gravitational collapse might amplify these oscillations into peaks and troughs in the matter distribution at small scales, leading to clumpiness on mass scales of $10^9 M_\odot$ for DW and of $10^8 M_\odot$ for BD sterile neutrinos. Perhaps coincidentally this latter scale is of the order of the mass contained within a half-light radius in the (DM) halos of spiral, low surface brightness and dwarf spheroidal galaxies [276, 277].

To compare our semi-analytical transfer function and power spectrum with the results from Boltzmann codes [165, 1, 274], we obtain an approximate form of power spectrum that interpolates between large and small scales for arbitrary distribution functions based on [43]. In spite of several caveats in the comparison, we find an excellent agreement within 5% error between these results in the region of scales where the fit is valid.

Finally, our study reveals a quasi-degeneracy between the mass, properties of the distribution function and decoupling temperature of the WDM candidate: particles with the same mass but that decoupled at different temperature with very different distribution functions may yield similar power spectrum in a wide range of scales. For example, the power spectrum of DW sterile neutrinos with $m \sim 2$ keV is similar to that of BD sterile neutrinos with $m \sim 1$ keV for $k \leq 10$ $(\mathrm{Mpc})^{-1}$. This result suggests caveats on the constraints on the mass of sterile neutrinos from current WDM N-body simulations and Lyman- forest data that typically input the distribution functions of thermal or DW species.

Part II:

THEORY OF NEUTRINO OSCILLATIONS

5.0 PART II: INTRODUCTION

In the second part of the thesis, we consider a different research topic, focusing on some subtle aspects of the theory of neutrino oscillation phenomena.

Since their discovery in 1930, neutrinos have attracted a lot of attention [189, 132, 148]. In particular, their masses, mixing and oscillations are some of the most fascinating aspects of neutrino physics because they directly lead to physics beyond the standard model [189, 222, 132], and offer an excellent example of macroscopic quantum coherence, for example, in long baseline oscillation experiments this coherence is maintained over hundreds of kilometers [25, 27, 13, 14, 9, 10]. Phenomenologically, they provide an explanation of the solar neutrino problem [283, 218, 148, 166, 167] and other interesting applications in astrophysics and cosmology [189, 222, 132, 148, 41, 156, 182, 183, 220, 221, 101, 102, 104, 168, 114, 115].

In 1957, by proposing the concept of sterile neutrinos, Pontecorvo first studied the oscillation between active and sterile neutrinos by analogy with $K^0 - \bar{K}^0$ oscillations [241]. Soon after, with the discovery of muon neutrinos in Brookhaven National Laboratory in 1962 [96], physicists found more than one flavor active neutrinos in nature, and realized that neutrino oscillations between different flavors are possible as long as neutrinos are massive and lepton number is not conserved. The mixing and oscillation between different flavor neutrinos were first studied by Maki, Nakagawa and Sakata in 1962 [214]. Moreover, Pontecorvo and Gribov [242, 155] predicted the solar neutrino problem and discussed its relation with the electron-muon neutrino oscillations in the sun in the late 1960s. Nowadays, it is widely accepted that there are at least three generations of flavor neutrinos ν_e, ν_μ and ν_τ, correspondingly there are three neutrino mass eigenstates ν_1, ν_2 and ν_3. Each flavor neutrino state is a linear

superposition of all mass eigenstates. Neutrino oscillations provide unique opportunities to determine fundamental properties of these neutrinos, e.g., their mixing angles and their mass differences. The oscillation probability $P_{\nu_\alpha \to \nu_\beta}$ derived from quantum mechanics is given by

$$\begin{aligned} P_{\nu_\alpha \to \nu_\beta} &= \delta_{\alpha\beta} - 4 \sum_{i>j} \Re[U^*_{\alpha i} U_{\beta i} U_{\alpha j} U^*_{\beta j}] \sin^2 \left[1.27 \left(\frac{\Delta m^2_{ij}}{\mathrm{eV}^2} \right) \left(\frac{L}{\mathrm{km}} \right) \left(\frac{\mathrm{GeV}}{E} \right) \right] \\ &\quad + 2 \sum_{i>j} \Im[U^*_{\alpha i} U_{\beta i} U_{\alpha j} U^*_{\beta j}] \sin \left[2.54 \left(\frac{\Delta m^2_{ij}}{\mathrm{eV}^2} \right) \left(\frac{L}{\mathrm{km}} \right) \left(\frac{\mathrm{GeV}}{E} \right) \right], \end{aligned} \tag{5.0.1}$$

where $P_{\nu_\alpha \to \nu_\beta}$ corresponds to the appearance and disappearance transition probabilities for $\beta \neq \alpha$ and $\beta = \alpha$ respectively, $\Delta m^2_{ij} = m^2_i - m^2_j$ is the square mass difference between the i-th and j-th massive neutrinos, and U is the mixing matrix depending on the mixing angles between different massive neutrinos. Eq. (5.0.1) is equivalent to (5.1.10) whose derivation is briefly reviewed in the next section. In the standard 3ν oscillation paradigm, observations on neutrino oscillations can testify and measure neutrino parameters Δm^2_{21}, Δm^2_{32}, $\sin^2\theta_{12}$, $\sin^2\theta_{23}$ and $\sin^2\theta_{13}$, where θ_{ij} ($\{i,j\} = \{1,2,3\}$) is the mixing angle between the i-th and j-th neutrino mass eigenstates. Furthermore, the square mass difference Δm^2_{31} can be derived from the relation

$$\Delta m^2_{12} + \Delta m^2_{23} + \Delta m^2_{31} = 0. \tag{5.0.2}$$

Despite early theoretical discussions on neutrino oscillations, experimental observations on neutrino oscillations were developed relatively late, partially because of the technical difficulties due to the small masses and extremely weak interactions of neutrinos. However, there is a noteworthy exception of pioneering solar neutrino experiment in the Homestake Mine led by Davis [97, 99, 98, 90], which started in 1970. The Homestake experiment detected solar neutrinos through the inverse β-decay Cl-Ar reaction, which observed a deficit in solar neutrino flux compared with the theoretical prediction from the standard solar model [42]. This deficit was confirmed by later solar neutrino experiments from SAGE [6], GALLEX/GNO [164, 20], SNO [12], Kamiokande, Super-Kamiokande (SK) [263]. This deficit is referred to as the so called solar neutrino problem, which is explained by MSW resonances between the first and the second neutrino mass eigenstates in the solar medium. Solar neutrino experiments are sensitive to the mass gap between ν_1 and ν_2. A global fit

of the data based on solar neutrino experiments plus the long baseline reactor experiment KamLAND [26, 134] gives the mass difference and mixing angle between ν_1 and ν_2 as [127]

$$\Delta m^2_{12} = (7.58^{+0.6}_{-0.59}) \times 10^{-5}\ \text{eV}^2, \quad \sin^2\theta_{12} = 0.312^{+0.052}_{-0.047}. \tag{5.0.3}$$

In addition to solar neutrino experiments, atmospheric neutrinos provide another excellent opportunity to study neutrino oscillations. Atmospheric neutrinos are created through interactions of cosmic rays, whose energy spectra range from 0.1 GeV to 10^{20} GeV, with the nuclei in the atmosphere of the Earth. These cosmic rays interact with the atmosphere and generate a lot of pion particles that decay mainly into muons and muon neutrinos. Again, these muons decay into electrons and electron neutrinos, leading to an expected ratio of about 2 : 1 for muon and electron neutrinos. Neutrinos produced through these processes are called atmospheric neutrinos [148]. Atmospheric neutrinos with energy from 100 MeV to 10^4 GeV can be captured by underground detectors through scattering on nuclei. The first indication of atmospheric neutrino oscillations came from the measurement at Kamiokande in 1988 [169], which detected only 60% of the expected sub-GeV and multi-GeV μ-neutrino events predicted by Monte Carlo calculation, while the measurement of e-neutrinos is consistent with the Monte Carlo result. Hence, the observation suggested an ratio of 1 : 1 instead of 2 : 1 for muon and electron neutrinos. The anomaly observed by the Kamiokande was confirmed by other atmospheric neutrino experiments, e.g., Irvine-Michigan-Brookhaven (IMB) experiment [89, 45, 185], SK [131, 130, 34], Soudan-2 [252, 19] and MACRO [21, 22]. Besides the deficit in total μ-neutrino events, SK and Soudan-2 [131, 130, 34, 252, 19] also measured an asymmetry between up-coming and down-going μ-neutrino events as well as their zenith angle dependence. These observations suggested that part of the up-coming μ-neutrino flux disappears, leading to a natural explanation of μ-neutrino oscillations because the up-coming and down-going μ-neutrinos travel to the detector from quite different distances. Atmospheric neutrino oscillations are sensitive to the mass gap between the second and the third massive neutrinos. Combined data of atmospheric neutrino experiments with those from Long Baseline (LBL) neutrino oscillation experiments and reactor neutrino

oscillation experiments [127, 23, 24, 25, 56, 55, 57, 18], it was found that $\nu_\mu \to \nu_\tau$ oscillations with $\Delta m^2_{23} \simeq (2.35^{+0.32}_{-0.29}) \times 10^{-3}$ $(\text{eV})^2$ and $\sin^2\theta_{23} = 0.42^{+0.22}_{-0.08}$ gave the best fit [127]. The positive sign of Δm^2_{23} corresponds to the normal mass hierarchy of neutrinos.

Based on the study of solar and atmospheric neutrino experiments, phenomena of neutrino oscillations have been confirmed and widely accepted as a common behavior of neutrinos, from which one can extract important information on the fundamental properties of neutrinos. Moreover, there is another class of neutrino oscillation experiments, called terrestrial neutrino oscillation experiments, that help to improve our accessibility to the parameter space of neutrinos. Depending on their neutrino sources, they are classified into reactor and accelerator experiments. According to Eq. (5.0.1), neutrino oscillation experiments can detect either the appearance or the disappearance probability based on their detection channels, corresponding to appearance or disappearance neutrino oscillation experiments. Again, from Eq. (5.0.1), it is clear that neutrino oscillation experiments designed with different baselines (ranging from a few tens of meters to hundreds of kilometers) and energy scales (a few MeV to GeV) are sensitive to different square mass gaps of neutrinos, based on which, neutrino oscillation experiments are divided into Short Baseline (SBL) experiments which are sensitive to neutrino square mass gaps above 0.1 eV^2 and Long Baseline (LBL) experiments sensitive to neutrino square mass gaps below 0.1 eV^2. Most SBL experiments, which started in the 80's, did not find any neutrino oscillation signal, and they usually provide an exclusion curve on the parameter space of neutrinos. There is one exception, LSND experiment found a signal in the $\bar{\nu}_\mu \to \bar{\nu}_e$ channel [35, 36, 37] and a even weaker signal in the $\nu_\mu \to \nu_e$ channel [39, 38]. Recent experimental data from MiniBooNE running in antineutrino mode seems to support the LSND result [11]. The LBL accelerator experiments, for example, K2K experiment [18], confirm the observation on atmospheric neutrino experiments. Moreover, KamLAND [26] can push the constraint on neutrino mass difference down to 10^{-5} eV, and set the most stringent constraint on the mass difference Δm^2_{21} when combined with the solar neutrino data. Measuring θ_{13} is the current focus of many terrestrial neutrino oscillation experiments. A most up-to-date global data analysis of neutrino oscillation experiments strongly favors a non-zero θ_{13} [127], which is consistent with the recent data from the T2K

experiment [7, 107]. Daya Bay [162] and Double CHOOZ [28] are about to take data in the near future, which will push the sensitivity in $\sin^2(2\theta_{13})$ better than 0.01. Furthermore, current and future experimental efforts keep revealing details of neutrino mixing and oscillations between the three generations and beyond, e.g., determining the mass hierarchy of the three neutrinos, and finding the CP violation phase of the neutrino mixing matrix, etc [148].

5.1 THEORY OF NEUTRINO OSCILLATION IN PLANE WAVE LIMIT

Given the importance of neutrino oscillations, it is reasonable to request a rock-solid theory on it. The simplest theoretical approach is analogous to Rabi-oscillations in a two-state system (see for example, [129, 121, 51, 52, 53, 189, 222, 132, 41] and references therein) and treats neutrinos as plane waves. The physical origin of neutrino oscillations is that "flavor" and massive neutrino eigenstates are different. Neutrinos interact only through weak interactions, in particular, in charge current interactions, each neutrino interacts with a charged lepton by exchanging a W-boson. There are three charged lepton flavors in nature, namely e, μ and τ. Corresponding to each charged lepton flavor, there is a neutrino with the same flavor. Therefore, we have e-, μ- and τ-neutrinos, which are called "flavor" neutrinos. On the other hand, massive neutrinos correspond to the eigenstates that diagonalize the mass matrix of neutrinos, which is determined by the specific model. Each massive neutrino has a fixed mass. For any given momentum, the massive neutrino has a fix energy and can propagate freely. Mass eigenstates are in general different from the "flavor" states, more precisely, each "flavor" state is a linear superposition of all massive eigenstates, or vice versa. Consequently, the simplest picture of neutrino oscillation can be summarized as follows: when a "flavor" neutrino is created initially, it is a linear superposition of all massive neutrino states. As time evolves, each massive neutrino component evolves independently according to e^{-iEt}, making the corresponding coefficient of its contribution to the flavor state a function of time. Therefore, if one tries to measure the initial flavor state at some later time, one will find that the original flavor can change and oscillate into other neutrino flavors.

The same idea can also be described mathematically. Let us assume an α-flavor neutrino is created initially:

$$|\nu_\alpha(\vec{k})\rangle = \sum_i U_{\alpha i}|\nu_i(\vec{k})\rangle, \tag{5.1.1}$$

where $U_{\alpha i}$ is the coefficient of the i-th massive neutrino $|\nu_i\rangle$ when decomposing $|\nu_\alpha\rangle$ into the mass space. Both $|\nu_\alpha\rangle$ and $|\nu_i\rangle$ are normalized to one, thus, it is straightforward to prove the unitarity of the matrix $U_{\alpha i}$, namely

$$\sum_i U^*_{\alpha i}U_{\beta i} = \delta_{\alpha,\beta}. \tag{5.1.2}$$

As time evolves, each massive eigenstate evolves independently according to $e^{-i\hat{H}t}$, thus

$$|\nu_\alpha(\vec{k},t)\rangle = e^{-i\hat{H}t}|\nu_\alpha(\vec{k})\rangle = \sum_i U_{\alpha i}\ e^{-i\hat{H}t}|\nu_i(\vec{k})\rangle = \sum_i e^{-i\omega_i t}\ U_{\alpha i}|\nu_i(\vec{k})\rangle, \tag{5.1.3}$$

where $\omega_i = \sqrt{|\vec{k}|^2 + m_i^2}$ and m_i is the mass of the i-th massive neutrino. Consequently, at a later time, if one goes to measure this neutrino state, one will find that

$$P_{\alpha\to\beta}(\vec{k},t) = \left|\langle\nu_\beta(\vec{k})|\nu_\alpha(\vec{k},t)\rangle\right|^2 = \sum_{i,j} U_{\alpha i}U^*_{\beta i}U^*_{\alpha j}U_{\beta j}\ e^{-i\frac{\Delta m^2_{ij}t}{2k}}. \tag{5.1.4}$$

When $\beta \neq \alpha$, $P_{\alpha\to\beta}(\vec{k},t)$ is the probability to observe a β-flavor neutrino state with momentum $\vec{k}$ at time t. Since in general $P_{\alpha\to\beta}(\vec{k},t) \neq 0$, it means an initial α-flavor neutrino can change its flavor into a β neutrino in the time evolution. Therefore, $P_{\alpha\to\beta}(\vec{k},t)$ is called the transition probability, or appearance probability. To obtain the above expression, we have assumed that all neutrinos are ultra-relativistic, an excellent approximation for most cases of neutrino oscillations due to the small masses of neutrinos (Current bounds of neutrino masses are below one eV.). Under ultra-relativistic limit,

$$\omega_i(\vec{k}) \simeq k + \frac{m_i^2}{2k}. \tag{5.1.5}$$

Here, k is the magnitude of the momentum $\vec{k}$, referring to the energy scale E associated with the oscillation. Correspondingly, Δm^2_{ij} is the mass difference between the i-th and j-th massive neutrinos, namely

$$\Delta m^2_{ij} = m_i^2 - m_j^2. \tag{5.1.6}$$

Moreover, in the ultra-relativistic limit, the velocity of each massive neutrinos is close to that of photos, therefore,

$$L \simeq t, \tag{5.1.7}$$

where L and t are the distance and time traveled by the neutrino state (We take the speed of light $c = 1$.). In terms of E and L, we find

$$P_{\alpha\to\beta}(E, L) = \sum_{i,j} U_{\alpha i} U^*_{\beta i} U^*_{\alpha j} U_{\beta j}\ e^{-i\frac{\Delta m^2_{ij} L}{2E}}. \tag{5.1.8}$$

It turns out convenient to define another length scale

$$L^{osc}_{ij} = \frac{4\pi E}{\Delta m^2_{ij}}, \tag{5.1.9}$$

which is called the oscillation length. It defines the characteristic length scale of oscillation for the given neutrino energy scale and mass difference between any two massive neutrino states. Finally, by reorganizing the transition probability, we obtain

$$\begin{aligned} P_{\alpha\to\beta}(E, L) &= \sum_{i,j} U_{\alpha i} U^*_{\beta i} U^*_{\alpha j} U_{\beta j}\ e^{-2\pi i \frac{L}{L^{osc}_{ij}}} \\ &= \sum_i |U_{\alpha i}|^2 |U_{\beta i}|^2 + 2\sum_{i>j} U_{\alpha i} U^*_{\beta i} U^*_{\alpha j} U_{\beta j} \cos\left(2\pi \frac{L}{L^{osc}_{ij}}\right). \end{aligned} \tag{5.1.10}$$

In addition to the coefficients of mixing matrix determined by the intrinsic properties of neutrinos, the oscillation pattern of the transition probability $P_{\alpha\to\beta}$ depends on the ratio of L and L^{osc}_{ij}. In neutrino oscillations experiment, L is also called the baseline.

On the other hand, when $\beta = \alpha$, $P_{\alpha\to\alpha}(\vec{k}, t)$ becomes the disappearance probability, describing the probability to measure the original α-flavor neutrino state. Straightforward calculation shows that

$$P_{\alpha\to\alpha}(E, L) = 1 - \sum_{\beta\neq\alpha} P_{\alpha\to\beta}(E, L) < 1. \tag{5.1.11}$$

Together, the appearance and disappearance probabilities give a conserved total probability. In real neutrino oscillation experiments, one can measure either appearance or disappearance probability and extract information on mass differences and mixing angles between different

massive neutrinos. In spite of the simple derivation, it grabs the most essential ingredients of the neutrino oscillation phenomenon, that is, the mixing of neutrino mass eigenstates and their coherent quantum interference (See Eq. (5.1.4).) make a flavor neutrino state change its flavor during the time evolution.

Though simple and intuitive, such a theory is not self-consistent because the requirement of energy-momentum conservation forbids two neutrinos with definite energy and momenta to interfere and oscillate. To solve this controversy, the wave packet nature of these neutrino states was pointed out and studied by Nussinov [231] and Kasyer [180]. In practice, each neutrino state is not created as a plane wave, instead, is a wave packet with some energy-momentum uncertainties determined by the production mechanism. It is these energy-momentum uncertainties that enable different massive neutrinos to interfere coherently, and generate the oscillation between different flavor states. The wave packet idea is an serious improvement to the theory of neutrino oscillations; yet, it is still not complete and satisfactory. Giunti, Kim and Lee found that it is impossible to construct a Fock space in general for the weak-interacting flavor neutrino states [151]; the wave forms and size of the wave packets of neutrinos depend on both the production and detection mechanism, which are missing in the calculation. To solve these problems, detailed wave packet models of neutrino oscillations including its production and detection processes are developed in both the framework of quantum mechanics [247, 150, 147, 144] and the framework of Quantum Field Theory (QFT) [149, 143, 159, 160, 158, 156, 119, 116]. For reviews of these work, one can refer to [48, 181, 16, 15].

5.2 NEUTRINO OSCILLATION UNDER WAVE PACKET TREATMENT

As mentioned above, neutrino oscillation under wave packet treatment can be done both within the framework of quantum mechanics and QFT; however QFT is a more natural framework to include the production and detection processes, and determine the wave packet

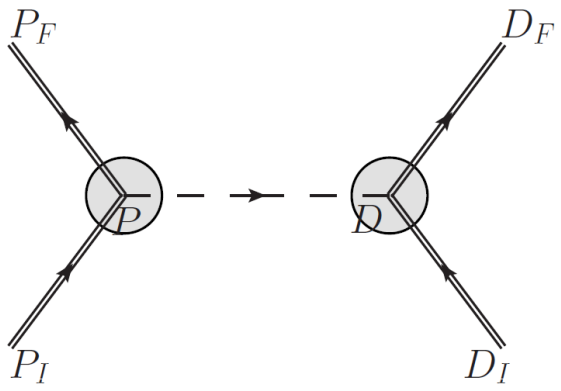

Figure 31: An schematic representation of neutrino oscillation experiments in QFT framework.

form of the neutrino states. Therefore, in this section, we will summarize the theory of neutrino oscillation under wave packet treatment in QFT description by following the work of [149, 152, 159, 160, 157].

In QFT, the three stages of an neutrino oscillation experiment, namely the production, propagation and detection, are combined together to be described by a single "Feynman" diagram as shown in Figure 31, where neutrinos act as intermediate states. Each external particle except neutrino in the production and detection processes is described by a localized wave packet, thus this method is also called the external wave packet model [48]. Standard field theoretical S-matrix calculation is applied to this "Feynman" diagram, where the transition amplitude is defined as

$$\mathcal{A} = \langle P_F, D_F | \hat{T} \left(e^{-i \int d^4x \hat{H}_I(x)} \right) | P_I, D_I \rangle, \tag{5.2.1}$$

where P_I, P_F and D_I, D_F correspond to the initial and final states of the production and detection processes respectively, and $\hat{H}_I$ is the interaction Hamiltonian in the interaction picture. $P_{I(F)}$ and $D_{I(F)}$ are all described by wave packets, whose expressions depend on the specific production and detection mechanisms. For example, in many cases, neutrinos are produced and detected through charge current weak interactions [143]. The calculation is

straightforward but tedious, which we choose not to present it here. Instead, we summarize the main results of these calculations and their physical interpretations. In order to simplify the discussion, some parameters or notations may not be explained in detail, interested reader can refer to [149, 152, 159, 160, 157, 47, 16, 15] for their explicit expressions and calculation details. Following the convention used in Ref. [15], the general expression of the transition amplitude, resulting from the Feynman diagram in Figure 31, can be written as

$$\mathcal{A}_{\alpha\to\beta} = \sum_j U^*_{\beta j} U_{\alpha j} \int \frac{d^4p}{(2\pi)^4} \Phi_{jP}(p^0,\vec{p})\ \Phi_{jD}(p^0,\vec{p})\ \frac{2p_0 e^{-ip^0T+i\vec{p}\cdot\vec{L}}}{p^2-m_j^2+i\epsilon}, \tag{5.2.2}$$

where Φ_{jP} and Φ_{jD} are called the overlap functions, respectively corresponding to the interactions associated with the j-th massive neutrino of energy-momentum $(p^0,\vec{p})$ at the production and detection areas. The last factor in Eq. (5.2.2) is the propagator of the j-th massive neutrino with T and $\vec{L}$ representing the time and distance traveled by this neutrino from production to detection. It is noteworthy pointing out that the oscillation feature of $\mathcal{A}_{\alpha\to\beta}$ results from the coherent interference of the phase $e^{-ip_0T+i\vec{p}\cdot\vec{L}}$ of different massive neutrinos. By expanding all wave packets into plane wave basis, Φ_{jP} and Φ_{jD} become (See Eq. (25) in [15])

$$\begin{aligned}
\Phi_{jP}(p^0,\vec{p}) &= \int d^4x_1 e^{ip\cdot x_1} \int [d\vec{q}] \int [d\vec{k}] f_{P_I}(\vec{q},\vec{P}_{P0}) f^*_{P_F}(\vec{k},\vec{K}_{P0}) e^{-i(q-k)\cdot x_1} M_{jP}(q,k),\\
\Phi_{jD}(p^0,\vec{p}) &= \int d^4x_2 e^{ip\cdot x_2} \int [d\vec{q}] \int [d\vec{k}] f_{D_I}(\vec{q},\vec{P}_{D0}) f^*_{D_F}(\vec{k},\vec{K}_{D0}) e^{-i(q-k)\cdot x_2} M_{jD}(q,k).
\end{aligned} \tag{5.2.3}$$

Here $\{p,q,k\}$ and $\{x_1,x_2\}$ are momentum and coordinate 4-vectors, and the dot, as in $p\cdot x_1$, means product of 4-vectors. $[d\vec{q}]$ and $[d\vec{k}]$ are covariant differential displacements over three momenta $\vec{q}$ and $\vec{k}$, whose explicit expressions are not important for our purpose and can be found in [15]. M_{jP} and M_{jD} are the matrix element of the interactions at production and detection areas. Most importantly, $f_{P_I}(\vec{p},\vec{P}_{P0})$, $f_{P_F}(\vec{p},\vec{K}_{P0})$, $f_{D_I}(\vec{p},\vec{P}_{D0})$ and $f_{D_F}(\vec{p},\vec{K}_{D0})$ are the momentum distribution functions of the initial and final particle wave packets entering the interactions, with momentum centers $\vec{P}_{P0}$, $\vec{K}_{P0}$, $\vec{P}_{D0}$ and $\vec{K}_{D0}$ respectively. They are usually chosen to be Gaussian distributions because in this case, all the integrations in

(5.2.3) and (5.2.2) are analytically doable, resulting in analytical expressions for the transition amplitudes and probabilities.

By taking Gaussian wave forms and carrying out all the integrations in (5.2.3) and (5.2.2), according to [149, 152, 143, 47], up to a normalization constant, the transition amplitude has the following structure,

$$\mathcal{A}_{\alpha\to\beta}(\vec{L},T) \propto \sum_j U^*_{\beta j}U_{\alpha j}\ M_j(\vec{q},\omega_j)\ e^{-S_j(\vec{q},\omega_j)}\ e^{-i\omega_j T+iqL-\frac{(L-v_jT)^2}{4\Sigma_j}}, \tag{5.2.4}$$

where q and $\omega_j=\sqrt{q^2+m_j^2}$ are respectively the momentum and energy of the j-th neutrino, and $v_j=q/\omega_j$ is the corresponding group velocity of the j-th neutrino wave packet. $M_j(\vec{q},\omega_j)$ contains the details of the interactions irrelevant to oscillation phenomena at the production and detection areas, e.g., the spin and helicity information, etc. $S_j(\vec{q},\omega_j)$ results from the Gaussian integration, describing the approximate energy-momentum conservation under the wave packet treatment. Due to the wave packet feature of all the interacting particles, the energy-momentum conservation cannot be exact, instead, the conservation requirement is relaxed by the wave packet uncertainties at both production and detection areas. If the neutrino momentum $\vec{q}$ is such that it deviates from the exact energy-momentum conservation by an amount well within the total uncertainty of the production and detection processes, $S_j(\vec{q},\omega_j)\sim 0$, $e^{-S_j(\vec{q},\omega_j)}$ is of order one; on the other hand, if $\vec{q}$ deviates from the exact conservation by an amount significantly beyond the allowed total uncertainty, $e^{-S_j(\vec{q},\omega_j)}\gg 1$, thus the transition amplitude is exponentially suppressed due to the breakdown of the approximate energy-momentum conservation. Finally, Σ_j is interpreted as an effective uncertainty associated with both the production and the detection processes, whose explicit expression is given by Eq. (15) in [152]. Strictly speaking, both $M_j(\vec{q},\omega_j)$ and $S_j(\vec{q},\omega_j)$ are functions of neutrino mass m_j, but since neutrinos are so light that they are always ultra-relativistic in neutrino oscillation experiments under most considerations, the dependence of M_j and S_j on m_j is very weak [149, 152, 143, 159, 47, 16, 15]. By neglecting their neutrino mass dependence, we obtain

$$\mathcal{A}_{\alpha\to\beta}(\vec{L},T) \propto M(\vec{q})e^{-S(\vec{q})}\sum_j U^*_{\beta j}U_{\alpha j}\ e^{-i\omega_j T+iqL-\frac{(L-v_jT)^2}{4\Sigma_j}}. \tag{5.2.5}$$

The transition probability $P_{\alpha\to\beta}(T,\vec{L})$ is simply the square of Eq. (5.2.5). Under the ultra-relativistic limit of the neutrinos and by integrating it over the time T [1], straightforward calculation yields [152, 143]

$$P_{\alpha\to\beta}(\vec{L}) = \sum_i |U_{\alpha i}|^2|U_{\beta i}|^2 + 2Re\sum_{i>j} U_{\alpha i}U^*_{\beta i}U^*_{\alpha j}U_{\beta j}e^{-2\pi i\frac{L}{L^{osc}_{ij}}-\left(\frac{L}{L^{coh}_{ij}}\right)^2-2\pi^2\rho^2\left(\frac{\sigma_{x,eff}}{L^{osc}_{ij}}\right)^2}, \quad (5.2.6)$$

where ρ is a dimensionless number of order one and $\sigma_{x,eff}$ is the effective width in the coordinate space (namely total spatial uncertainty) depending on both the production and the detection processes. Their explicit expressions are given in Eqs. (16) and (17) in [47]. The transition probability (5.2.6) under the wave packet treatment is similar to the plane wave result in Eq. (5.1.10), both of them contain the oscillation phase determined by the ratio of L/L^{osc}_{ij}. However, in addition to the oscillation phase, the wave packet treatment introduces two more exponential terms. First of all, it introduces a coherence length scale, called L^{coh}_{ij}, which is defined as

$$L^{coh}_{ij} = \frac{4\sqrt{2}E^2}{\Delta m^2_{ij}}\sigma_{x,eff}. \quad (5.2.7)$$

The coherence length L^{coh}_{ij} describes the distance within which the wave packets of i-th and j-th massive neutrinos remain coherent with each other. Due to their mass difference, i-th and j-th massive neutrino wave packets have different group velocities. With respect to the time evolution, the two wave packets gradually become separated although they were originally created at the same place. Eventually, they have no overlap and lose the coherence between each other, leading to the disappearance of neutrino flavor oscillations when $L \gg L^{coh}_{ij}$. Secondly, according to Eq. (5.2.6), the transition probability becomes significant only when $\sigma_{x,eff} \ll L^{osc}_{ij}$, meaning that in order to manifest the neutrino oscillation phenomenon, the total effective width of the wave packets at production and detection areas, namely the total uncertainty in the coordinate space, must be much smaller than the oscillation length. Otherwise, the neutrino wave packets do not have enough sensitivity to discriminate small neutrino mass differences, again leading to the disappearance of neutrino flavor oscillations.

[1] The reason to integrate over T is that the propagation time is usually not measured in neutrino oscillation experiments [159, 152, 15].

In summary, the appearance of L_{ij}^{coh} and $\sigma_{x,eff}$ tells us that the neutrino oscillation pattern may disappear as a result of the de-coherence of different massive neutrino wave packets, or it disappears because the effective spatial spread of the interacting wave packets is too wide to distinguish the small neutrino mass differences. These arguments are consistent with the physical intuitions. Compared with the plane wave calculation, apparently, the wave packet treatment exhibits a more realistic and complete picture for neutrino oscillations.

Despite the great improvement of the wave packet treatment in QFT, the conventional S-matrix calculation is a "black-box" calculation, for given initial (in) states to produce neutrinos and final (out) states resulting from detection of neutrinos, physics associated with neutrinos is solely governed by the interaction Lagrangian. However, neutrino oscillations turn out more complicated than such a "black-box" treatment. For example, discussion on coherence aspects of neutrinos [143, 159, 160, 158, 92, 118, 116, 119, 211, 210, 163] has recognized that the neutrino state produced by the decay of a parent particle via charged current interactions is in fact *entangled* with that of the charged lepton. Whether this entanglement will influence the neutrino oscillation formula or not remains to be discussed in the literature [92, 211, 210, 163]. In the following section, we are going to discuss several subtle aspects of the neutrino oscillation phenomenon, and try to motivate our research.

5.3 SUBTLE ISSUES OF THE THEORY OF NEUTRINO OSCILLATIONS

As mentioned above, the previous quantum field theory treatment of neutrino mixing and oscillations is S-matrix theoretic in nature, making use of in-out wave-packets spatially localized at the source, or the "near" detector, and the far detector. However, the S-matrix calculation takes the interaction time to infinity, even with some case of setting the initial and final wave packets at infinite source and detector times [88, 119, 116, 118, 186]. On the other hand, a neutrino oscillation experiment usually keeps a finite baseline, with wave packets defined at some initial time at the source and final time at the far detector.

This apparent incongruity is often justified with the statement that time is not measured in appearance or disappearance experiments. While this is true, it is a practical, but not a fundamental reason for taking the infinite time limit. In principle, one can still measure the time in an neutrino oscillation experiment. For example, one can consider a gedanken experiment in which clocks at the source (near detector) and far detector are synchronized via global positioning satellites and register the detection of the charged leptons at the source and far detector at the time t_S and t_D, respectively. Obviously, the time difference registered by these clocks $t_D - t_S \simeq L$, with L being the baseline. This time measurement bares uncertainties of the order of the size of the source and detector for the interaction vertices from which the charged leptons emerge are localized within these regions, although current resolution of the interaction vertices is much more accurate than this scale.

Furthermore, taking the infinite time limit as in the S-matrix calculation enforces total energy conservation via an overall delta function in the transition amplitude. The transition probability treats the square of this delta function as overall energy conservation multiplied by the total time of the interaction, from which an interaction rate is extracted by dividing by this time (in the long time limit). However, oscillations arising from quantum mechanical interference have nothing to do with a transition rate and in principle do not feature a secular evolution in time. By recognizing this problem of the conventional theoretical approach, we hope to develop a real time calculation of neutrino oscillations, namely keeping the finite time limit in neutrino oscillation calculations.

On the other hand, the issue of entanglement in neutrino oscillations was pointed out by Cohen *et al.* [92]. They argued that neutrinos produced from decay via the charge current interaction are actually entangled with the charge leptons, being the other decay products. When this entangled state evolves, there are two possibilities. If we measure the charged lepton before neutrinos are detected, it disentangles the quantum state at a time determined either by the detection process of the charged lepton at the source or by stopping at a "beam dump" near the source. This disentangled neutrino state then evolves further in time and is detected at the "far detector" via another charged lepton. Therefore the production,

disentanglement and detection involve *two times*: the time at which the charged lepton is observed at the source (if observed at all) or stopped at a beam dump near the source, which is when the neutrino/charged lepton state is disentangled, and the time when the neutrino is observed via a charged lepton in the far detector. We note that for long-baseline experiments these two time scales are widely separated [13, 9, 10]. On the other hand, if the charged lepton is not observed before neutrino detection, neutrinos are thus described by a reduced *density matrix*, obtained by tracing out the charged lepton. In this case, we can track the behavior of the off-diagonal elements, *i.e.*, the coherence which contain information on the interference between the different neutrino mass eigenstates.

We are particularly interested in the first case. As pointed above, it involves two measurement times. S-matrix calculation certainly cannot fulfill this requirement because it considers in and out states only and takes the production and detection times asymptotically to infinity. In order to study the influence of entanglement and disentanglement on neutrino oscillations, we have to study the detailed dynamics of the entangled state explicitly to the disentangling moment, then evolve the dis-entangled neutrino state to the far detector. This is consistent with our previous argument that neutrino oscillations should be considered under the finite time limit. To emphasize the importance of this *two-time* measurement idea, we divide the study into two steps. In the first step, we neglect the wave packet nature of all particles, describing them by plane waves. In this way, we avoid all the technical complications associated with wave packet treatment, and focus solely on the issues of entanglement, dis-entanglement and the *two-time* measurement. Then, in the second step, we apply the wave packet idea to our study, thus investigate the issue of entanglement and dis-entanglement within a more consistent and complete theoretical picture of neutrino oscillations. In this thesis, however, we only report our study of the first step, which has been published in research journals. The second part of study is still under developing, therefore, we choose not to present it here. Even so, we still comment on the general expectations on the wave packet treatment following our ideas.

5.4 SUMMARY OF OUR WORK

Based on the above discussion, we hope to provide a clear motivation for our study in this part. Then, in the following, let us summarize our work.

5.4.1 Dynamics of Disentanglement And Coherence In Neutrino Oscillations

As advertised in the introduction, in this study, we focus on the entanglement and disentanglement issue of neutrino oscillations within the plane wave limit and QFT framework. This study has been reported in [286], where we worked under the finite time limit and explicitly study the time evolution from production to detection processes. By carrying out the two-time measurement study, we found that oscillation amplitudes and probabilities depend on both time scales, namely, the two times when the neutrino-lepton state is disentangled (t_S) and when the dis-entangled neutrino is measured (t_D). We obtain a non-standard transition probability, whose time derivative, namely transition rate, reduces to the standard results in the long time limit for long baseline neutrino oscillation experiments. (See Eq. (2.49) in [286] to obtain the standard oscillation probability.) However, when $t_S \sim t_D \sim L^{osc}$, where L^{osc} is the oscillation length scale, the oscillation amplitudes and probabilities deviates significantly from the standard results. Although this condition cannot be true for long-baseline oscillation experiments, it could be the case for short-baseline oscillation experiments. Hence, this could give rise to a re-interpretation of their results by taking the dependence on the disentangling time into account.

5.4.2 Application of the Plane Wave Result to the GSI Anomaly

As an application of our plane wave calculations, we consider the GSI anomaly, investigating the interpretation of GSI anomaly as a result of neutrino oscillations. Following the method developed in the previous study, we obtain the time evolution of the population of parent and daughter particles directly in real time, considering explicitly the quantum entanglement between the daughter particle and neutrino mass eigenstates in the two-body decay. We confirm that the decay rate of the parent particle and the growth rate of the daughter

particle do *not* feature a time modulation from interference of neutrino mass eigenstates. The lack of interference is a consequence of the orthogonality of the mass eigenstates. This result also follows from the density matrix obtained by tracing out the unobserved neutrino states. We confirm this result by providing a complementary explanation based on Cutkosky rules applied to the Feynman diagram of the self-energy of the parent particle.

6.0 PART II: DYNAMICS OF DISENTANGLEMENT AND COHERENCE IN NEUTRINO OSCILLATIONS

This chapter is based on our published article [286], where we re-investigate the theory of neutrino oscillations by focusing on the dynamics of disentanglement, density matrix and coherence of this phenomenon. To simplify the calculation and emphasize on our main points, we consider the neutrino oscillation in the plane wave limit in this study. This chapter is organized as follows: in Sec. 6.1, we introduce a simple theoretical model containing all necessary ingredients for the phenomenon of neutrino oscillations, but neglecting all irrelevant and technically complicated aspects. Then, based on this simple model, we consider the interaction at the source (near detector) and far detector in Secs. 6.2 and 6.3 respectively. In particular, in Sec. 6.2, we study the case when the entangled state of neutrino and lepton is dis-entangled by the measurement of the lepton, and compare to the case when the lepton is not measured. In Sec. 6.3, we obtain the transition amplitude and probability of neutrino oscillations, investigating the influence of the dis-entanglement on these experimental observables. Sec. 6.4 discusses the possible application of our results to short baseline neutrino oscillation experiments and comments on the modifications under the wave packet treatment. Finally, we briefly conclude our work in Sec. 6.5.

6.1 A MODEL OF "NEUTRINO" OSCILLATIONS

The goal of this work is to study the dynamics of mixing and oscillation of neutrinos in quantum field theory with a finite time interval. In order to exhibit the main results in a clear and simpler manner, we introduce a bosonic model that describes mixing, oscillations

and charged current weak interactions reliably without the complications associated with fermionic and gauge fields. We can do so because the technical complications associated with spinors and gauge fields are irrelevant to the physics of mixing and oscillations, as is obviously manifest in meson mixing. Our model is defined by the following Lagrangian density

$$\mathcal{L} = \mathcal{L}_0[W, l_\alpha] + \mathcal{L}_0[\nu_\alpha] + \mathcal{L}_{\rm int}[W, l_\alpha, \nu_\alpha], \tag{6.1.1}$$

with $\alpha = e$ or μ and

$$\mathcal{L}_0[\nu] = \frac{1}{2}\left[\partial_\mu \Psi^T \partial^\mu \Psi - \Psi^T \mathbb{M} \Psi\right] , \tag{6.1.2}$$

where Ψ is a flavor doublet representing the neutrinos

$$\Psi = \begin{pmatrix} \nu_e \\ \nu_\mu \end{pmatrix}, \tag{6.1.3}$$

and $\mathbb{M}$ is the mass matrix

$$\mathbb{M} = \begin{pmatrix} m_{ee} & m_{e\mu} \\ m_{e\mu} & m_{\mu\mu} \end{pmatrix} . \tag{6.1.4}$$

The interaction Lagrangian is similar to the charged current interaction of the standard model, namely

$$\mathcal{L}_{\rm int}(\vec{x}, t) = g\, W(\vec{x}, t)\Big[l_e(\vec{x}, t)\, \nu_e(\vec{x}, t) + l_\mu(\vec{x}, t)\, \nu_\mu(\vec{x}, t)\Big], \tag{6.1.5}$$

where g is the coupling constant. $W(x)$ represents the vector boson, or alternatively the pion field, and l_α with $\alpha = \{e, \mu\}$ the two charged leptons. The mass matrix is diagonalized by a unitary transformation

$$U^{-1}(\theta)\, \mathbb{M}\, U(\theta) = \begin{pmatrix} m_1 & 0 \\ 0 & m_2 \end{pmatrix}, \tag{6.1.6}$$

where

$$U(\theta) = \begin{pmatrix} \cos\theta & \sin\theta \\ -\sin\theta & \cos\theta \end{pmatrix} . \tag{6.1.7}$$

In terms of the doublet of mass eigenstates, the flavor doublet can be expressed as

$$\begin{pmatrix} \nu_e \\ \nu_\mu \end{pmatrix} = U(\theta) \begin{pmatrix} \nu_1 \\ \nu_2 \end{pmatrix} . \tag{6.1.8}$$

This bosonic model clearly describes charged current weak interactions reliably as it includes all the relevant aspects of mixing and oscillations.

We consider "neutrino" oscillation experiments following the interaction processes illustrated in Figure 32, that is

$$W \to l_\alpha + \nu_\alpha \rightsquigarrow \begin{cases} W + l_\beta \quad , \beta \neq \alpha & \text{appearance;} \\ W + l_\alpha & \text{disappearance.} \end{cases} \tag{6.1.9}$$

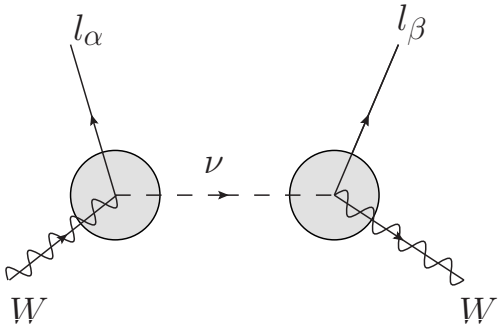

Figure 32: Typical experiment in which the charged leptons are measured at a near and far detector and the neutrino is an intermediate state.

Throughout this work, we will use plane wave states for simplicity of exposition, though we discuss some of the modifications that the use of wave packets would require later in this chapter. In order to study aspects of coherence we consider a simplified interaction Lagrangian density

$$\mathcal{L}_I = g\, W\, e\, \nu_e = g\, W\, e(\cos\theta\, \nu_1 + \sin\theta\, \nu_2), \tag{6.1.10}$$

focusing only on one lepton, which we refer to as the "electron". The full coupling as in Eq. (7.2.5) can be treated similarly without modifying the main conclusions. Although W may be interpreted as a charged vector boson, the analysis is obviously the same if it describes a pion field.

6.2 INTERACTION NEAR THE SOURCE

We can study aspects of coherence by focusing on the Fock state obtained upon evolution of the decaying initial state. We consider a plane-wave Fock initial state $\big|W(\vec{k})\big\rangle$ at $t_i = 0$. The time evolution operator is

$$e^{-iH(t-t_i)} = e^{-iH_0 t}\; U(t,t_i)\; e^{iH_0 t_i}, \tag{6.2.1}$$

where

$$U(t,t_i) = T\; e^{i\int_{t_i}^{t}\; d^3x\, dt\, \mathcal{L}_{\rm int}(\vec{x},t)} \tag{6.2.2}$$

is the time evolution operator in the interaction picture and H_0 is the non-interacting Hamiltonian. By time t, the initial state has evolved into $\big|W(\vec{k})\big\rangle\; e^{-iE^W_{\vec{k}}\, t} + \big|\Psi_e(t)\big\rangle$. To lowest order in the interaction, we find the second term to be

$$\big|\Psi_e(t)\big\rangle = ig\; e^{-iH_0 t}\; \int_0^t dt' \int d^3x\; \Big[W(\vec{x},t')\, e(\vec{x},t')(\cos\theta\, \nu_1(\vec{x},t') + \sin\theta\, \nu_2(\vec{x},t'))\Big]\; \big|W(\vec{k})\big\rangle, \tag{6.2.3}$$

where all the fields are in the interaction picture. Though the field operator W can either annihilate the initial state or create another W particle, the state with two W particles features faster oscillations that will average out. In what follows, we consider only the Fock state resulting from the annihilation of the initial particle, leading to the state

$$\begin{aligned}\big|\Psi_e(t)\big\rangle \;\simeq\; & \frac{g}{2\sqrt{2VE^W_{\vec{k}}}}\; e^{-iE^W_{\vec{k}}\, t}\; \sum_{\vec{q}} \Bigg\{ \frac{\sin\theta}{\sqrt{\Omega_{2,\vec{p}}\; E^e_{\vec{q}}}}\; \big|\nu_{2,\vec{p}}\big\rangle \big|e_{\vec{q}}\big\rangle \left[\frac{e^{i(E^W_{\vec{k}} - E^e_{\vec{q}} - \Omega_{2,\vec{p}})t} - 1}{(E^W_{\vec{k}} - E^e_{\vec{q}} - \Omega_{2,\vec{p}})}\right] \\ & + \frac{\cos\theta}{\sqrt{\Omega_{1,\vec{p}}\; E^e_{\vec{q}}}}\; \big|\nu_{1,\vec{p}}\big\rangle \big|e_{\vec{q}}\big\rangle \left[\frac{e^{i(E^W_{\vec{k}} - E^e_{\vec{q}} - \Omega_{1,\vec{p}})t} - 1}{(E^W_{\vec{k}} - E^e_{\vec{q}} - \Omega_{1,\vec{p}})}\right] \Bigg\},\end{aligned} \tag{6.2.4}$$

where $\vec{p} = \vec{k} - \vec{q}$ and Ω_1, Ω_2 refer to the energies of the first and second massive neutrinos. The electron and the neutrinos are *entangled*[1]. The neutrino state that is entangled with the muon is obtained from (7.3.7) by replacing $\cos\theta \to -\sin\theta$; $\sin\theta \to \cos\theta$.

[1]The result for the wavefunction in Ref. [**?**] may be understood using a (non-perturbative) Wigner-Weisskopf approximation for the decaying parent particle, replacing $E_W \to E_W - i\Gamma_W$. Taking $t \gg 1/\Gamma_W$ in the integral replaces the brackets in (7.3.7) by $1/(E_W - E^e - \Omega_j - i\Gamma_W)$ whose absolute value is proportional to $\delta(E_W - E^e - \Omega_j)/\Gamma_W$.

In what follows, we consider ultrarelativistic neutrinos and write

$$\Omega_1 = \overline{\Omega} - \Delta, \qquad \Omega_2 = \overline{\Omega} + \Delta, \tag{6.2.5}$$

where

$$\overline{\Omega} = \left[p^2 + \frac{m_1^2 + m_2^2}{2}\right]^{\frac{1}{2}}, \quad \Delta = \frac{\delta m^2}{4\overline{\Omega}}, \quad \delta m^2 = m_2^2 - m_1^2, \tag{6.2.6}$$

taking $\Delta \ll \overline{\Omega}$ as is the case for ultrarelativistic nearly degenerate neutrinos.

6.2.1 Unobserved daughter particles: time evolution of the density matrix

If the electrons (or daughter particle in Ref. [92]) are not observed, they can be traced out of the density matrix $\big|\Psi_e(t)\big\rangle\big\langle\Psi_e(t)\big|$. This gives the reduced density matrix

$$\begin{aligned}
\rho_r(t) &= \mathrm{Tr}_e\big|\Psi_e(t)\big\rangle\big\langle\Psi_e(t)\big| \\
&= \frac{g^2}{8VE_{\vec{k}}^W}\sum_{\vec{q}}\Bigg\{\frac{\sin^2\theta}{\Omega_{2,\vec{p}}\;E_{\vec{q}}^e}\Big|\nu_{2,\vec{p}}\Big\rangle\big\langle\nu_{2,\vec{p}}\big|\left[\frac{\sin\left(\left(E_{\vec{k}}^W - E_{\vec{q}}^e - \Omega_{2,\vec{p}}\right)\frac{t}{2}\right)}{\left(E_{\vec{k}}^W - E_{\vec{q}}^e - \Omega_{2,\vec{p}}\right)/2}\right]^2 \\
&\quad + \frac{\cos^2\theta}{\Omega_{1,\vec{p}}\;E_{\vec{q}}^e}\Big|\nu_{1,\vec{p}}\Big\rangle\big\langle\nu_{1,\vec{p}}\big|\left[\frac{\sin\left(\left(E_{\vec{k}}^W - E_{\vec{q}}^e - \Omega_{1,\vec{p}}\right)\frac{t}{2}\right)}{\left(E_{\vec{k}}^W - E_{\vec{q}}^e - \Omega_{1,\vec{p}}\right)/2}\right]^2 \\
&\quad + \frac{\sin 2\theta}{2E_{\vec{q}}^e\sqrt{\Omega_{2,\vec{p}}\;\Omega_{1,\vec{p}}}}\left[\frac{\sin\left(\left(E_{\vec{k}}^W - E_{\vec{q}}^e - \Omega_{2,\vec{p}}\right)\frac{t}{2}\right)}{\left(E_{\vec{k}}^W - E_{\vec{q}}^e - \Omega_{2,\vec{p}}\right)/2}\right]\left[\frac{\sin\left(\left(E_{\vec{k}}^W - E_{\vec{q}}^e - \Omega_{1,\vec{p}}\right)\frac{t}{2}\right)}{\left(E_{\vec{k}}^W - E_{\vec{q}}^e - \Omega_{1,\vec{p}}\right)/2}\right] \\
&\quad \times\left[e^{-i\frac{\delta m^2}{4\overline{\Omega}}t}\Big|\nu_{2,\vec{p}}\Big\rangle\big\langle\nu_{1,\vec{p}}\big| + e^{i\frac{\delta m^2}{4\overline{\Omega}}t}\Big|\nu_{1,\vec{p}}\Big\rangle\big\langle\nu_{2,\vec{p}}\big|\right]\Bigg\}, \quad \vec{p} = \vec{k} - \vec{q}\,.
\end{aligned} \tag{6.2.7}$$

This expression contains remarkable information. The function $\sin^2(xt)/x^2$ is the usual "diffraction" function of Fermi's Golden rule. In the formal long time limit, $\sin^2(xt)/x^2 \to \pi\, t\, \delta(x)$, the first two terms of the density matrix, which are the diagonal entries in the mass basis, describe the production process of the mass eigenstates. As will be seen below, in the long time limit, the time derivative of these two terms yields the production rate for the mass eigenstates. In the formal $t \to \infty$ limit, these are the diagonal terms obtained in Ref. [92], where in that reference, the product of delta functions is again understood as the total time elapsed times an energy conserving delta function.

The off-diagonal terms in the last line of (6.2.7) describe the "coherences" and display the oscillatory phases from the interference of the mass eigenstates. The time dependent factors of the off-diagonal density matrix elements determine the *coherence* between the mass eigenstates and will be a ubiquitous contribution in the real time description of oscillations that follows below. The functions

$$f_{\pm}(x,t;\Delta) = \frac{2\sin\left[(x\pm\Delta)\frac{t}{2}\right]}{(x\pm\Delta)} \tag{6.2.8}$$

with $x = (E^W_{\vec{k}} - E^e_{\vec{q}} - \overline{\Omega}_{\vec{p}})$ are strongly peaked at $x \pm \Delta = 0$ with height t and width $\sim 2\pi/t$. In the infinite time limit, $f_{\pm}(x,t,\Delta) \to 2\pi\,\delta(x\pm\Delta)$ and therefore their product would vanish in this limit, leading to the vanishing of the coherence. This is the result obtained in Ref. [92]. However, at finite time t, they feature a non-vanishing overlap when $2\Delta \lesssim 2\pi/t$. We recognize this as the condition for oscillations. We note that $t \sim \pi/\Delta$ yields a macroscopically large time scale. The functions $f_{\pm}(x,t,\Delta)$ and their products are depicted in Figs. 33 and 34 for the values $\Delta = 0.1$, $t = \{40, 100\}$, respectively.

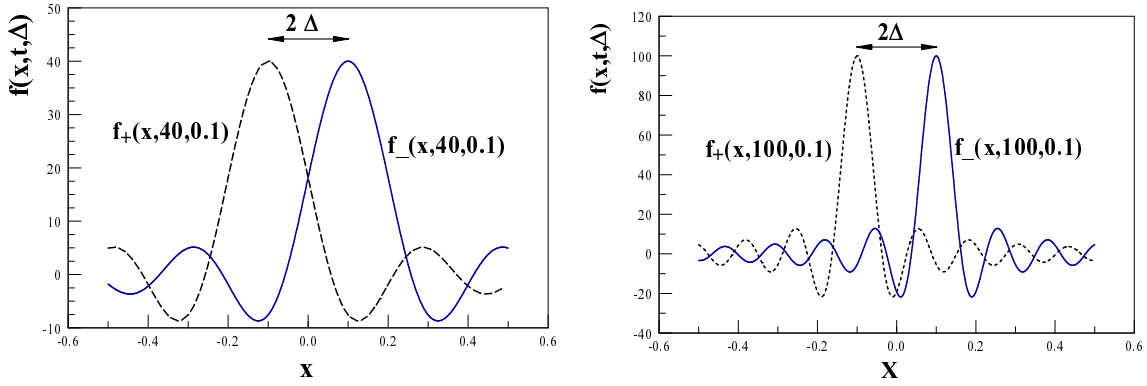

Figure 33: The functions $f_{\pm}(x,t,\Delta)$ vs. x for $t = \{40, 100\}$, $\Delta = 0.1$

It is straightforward to find

$$\begin{aligned} f_-(x,t,\Delta)f_+(x,t,\Delta) \;=\; & \frac{\sin(\Delta\,t)}{\Delta}\left[\frac{\sin[(x-\Delta)t]}{(x-\Delta)} + \frac{\sin[(x+\Delta)t]}{(x+\Delta)}\right] \\ & + 2\frac{\cos(\Delta\,t)}{\Delta}\left[\frac{\sin^2[(x-\Delta)\frac{t}{2}]}{(x-\Delta)} - \frac{\sin^2[(x+\Delta)\frac{t}{2}]}{(x+\Delta)}\right]. \end{aligned} \tag{6.2.9}$$

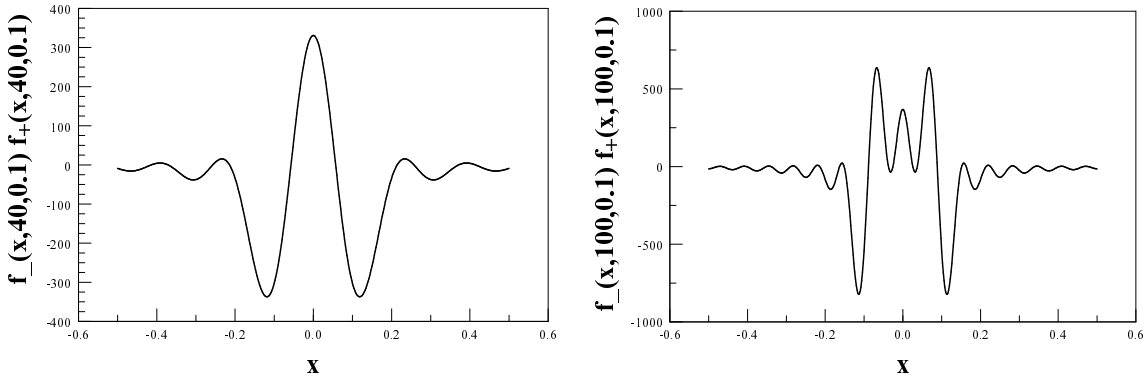

Figure 34: The products $f_-(x,t,\Delta)f_+(x,t,\Delta)$ vs. x for $t = \{40, 100\}$,$\Delta = 0.1$

In the long time limit, the terms in the first bracket yield a sum of delta functions at $x = \pm\Delta$. Upon integrating the product of f_-f_+ with functions of compact support, the contribution from the second line in (6.2.9) is negligible in the long time limit. Therefore, the long time limit of f_+f_- can be replaced by

$$f_-(x,t,\Delta)f_+(x,t,\Delta) = \pi\,\frac{\sin(\Delta\,t)}{\Delta}\Big[\delta(x-\Delta)+\delta(x+\Delta)\Big]. \tag{6.2.10}$$

During a time interval $t \ll 2\pi/\Delta$, the product $f_-(x,t,\Delta)f_+(x,t,\Delta) \sim \pi\,t[\delta(x-\Delta)+\delta(x+\Delta)]$ grows linearly in time until it begins to oscillate with frequency $2\pi/\Delta$ for $t > 2\pi/\Delta$. Therefore, we conclude that upon integration with a smooth density of states, the off-diagonal terms in the density matrix grow linearly in time for $t \ll t_{osc} = 2\pi/\Delta$, but feature a bound oscillatory behavior of frequency Δ for $t \gtrsim 2\pi/\Delta$.

The diagonal terms, *i.e.*, the first two terms in the reduced density matrix (6.2.7), are proportional to $4\sin^2(x\frac{t}{2})/x^2 \to 2\pi\ t\delta(x)$. This shows that the coherences or off diagonal terms are linear in time and of the same order as the diagonal elements for $t \lesssim t_{osc} = 2\pi/\Delta$, but are of $\mathcal{O}(1/\Delta t)$ and oscillate compared to the diagonal terms for $t \gg t_{osc}$. This behavior

is displayed in Figure 35, where as an example we consider a smooth density of states and the integral

$$I(t,\Delta) = \int_{-\infty}^{\infty} e^{-x^2} f_+(x,t,\Delta) f_-(x,t,\Delta) dx. \tag{6.2.11}$$

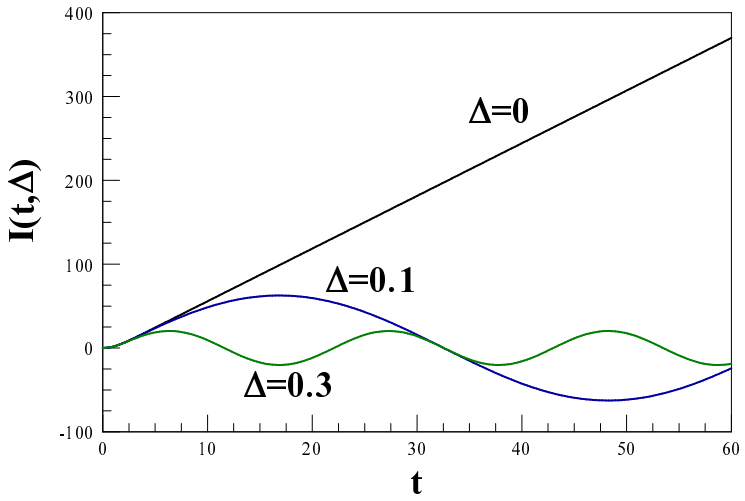

Figure 35: The integral $I(t,\Delta) = \int_{-\infty}^{\infty} e^{-x^2} f_+(x,t,\Delta) f_-(x,t,\Delta) dx$ vs. t for $\Delta = \{0, 0.1, 0.3\}$

The case $\Delta = 0$ describes either of the diagonal terms and is linearly secular in time. This figure clearly shows the slow oscillations for $t \gtrsim 1/\Delta$. Therefore, the approximation (6.2.10) is reliable in the long time limit and upon integration with functions of compact support. We see that for large t, but $t\Delta \ll 1$, $f_+(x,t,\Delta) f_-(x,t,\Delta) \to \pi t \big[\delta(x-\Delta) + \delta(x+\Delta)\big]$ and for $\Delta \to 0$, the product yields $2\pi t \delta(x)$.

The reduced density matrix (6.2.7) allows us to obtain the time evolution of the neutrino populations and coherence, namely

$$\begin{aligned} n_i(\vec{p},t) &= \mathrm{Tr}\, \rho_r(t) a_i^\dagger(\vec{p}) a_i(\vec{p}), \\ \mathcal{C}_{ij}(\vec{p},t) &= \mathrm{Tr}\, \rho_r(t) a_i^\dagger(\vec{p}) a_j(\vec{p}) \ , \ i \neq j \end{aligned} \tag{6.2.12}$$

where the annihilation and creation operators are in the Schrodinger picture. In the long time limit and using the results above, we find

$$n_1(\vec{p},t) = t\ \Gamma_1(\vec{p})\cos^2\theta, \qquad n_2(\vec{p},t) = t\ \Gamma_2(\vec{p})\sin^2\theta, \tag{6.2.13}$$

where

$$\Gamma_{1,2} = \frac{2\pi\, g^2}{8E^W_{\vec{k}}}\int \frac{d^3\vec{Q}}{(2\pi)^3\, E^e_{\vec{Q}}\,\Omega_{1,2}}\delta\big(E^W_{\vec{k}} - E^e_{\vec{Q}} - \Omega_{1,2}\big) \tag{6.2.14}$$

are the partial widths for the decay of the W into the charged lepton and the neutrino mass eigenstates. For the off-diagonal matrix elements or coherence we find,

$$\begin{aligned}\mathcal{C}_{12}(\vec{p},t) = \mathcal{C}^\dagger_{21}(\vec{p},t) \;\; &= \;\; \frac{2\pi\, g^2\sin 2\theta}{32E^W_{\vec{k}}}\ \frac{\sin[t\Delta]}{\Delta}\ e^{i\Delta t} \\ &\int \frac{d^3\vec{Q}}{(2\pi)^3\, E^e_{\vec{Q}}\,\sqrt{\Omega_1\,\Omega_2}}\Big[\delta\big(E^W_{\vec{k}} - E^e_{\vec{Q}} - \Omega_1\big) + \delta\big(E^W_{\vec{k}} - E^e_{\vec{Q}} - \Omega_2\big)\Big].\end{aligned} \tag{6.2.15}$$

$dn_i(\vec{p},t)/dt$ yields the production rate of the neutrino mass eigenstates from the decay of the W and the coherences $\mathcal{C}_{ij}$ are non-vanishing at any finite time. In Ref. [92], the coherences vanish as a consequence of the product of delta functions on the different mass shells of the mass eigenstates. The coherences vanish in the formal infinite time limit because of the oscillatory behavior averages out on time scales $t \gg 1/\Delta$ and they are of $\mathcal{O}\big(\sin(t\Delta)/t\Delta\big)$ with respect to the diagonal terms. However, we emphasize that experimentally, the time scales involved (or length scales) are of order $1/\Delta$ as these are the scales on which oscillatory phenomena are revealed. Taking $\Omega_1 \sim \Omega_2 \sim \overline{\Omega}$ in the denominators in (6.2.14) and (6.2.15), it follows that

$$\mathcal{C}_{12}(\vec{p},t) \simeq \frac{\sin 2\theta}{2}\frac{\sin[t\Delta]}{\Delta}\ e^{i\Delta t}\ \frac{1}{2}\big[\Gamma_1 + \Gamma_2\big]. \tag{6.2.16}$$

Therefore, the coherences are of the same order of the population terms on time scales $t \leq 1/\Delta$, but average out for $t \gg 1/\Delta$, showing that coherence persists over the oscillation time scale.

6.2.2 Disentangling the neutrino: a two-time measurement

As we have discussed above, a long baseline experiment is actually a *two-time measurement* process, as the charged lepton produced at the interaction vertex at the source is detected at the source or stopped and absorbed in a nearby "beam dump". This "measurement" of the charged lepton disentangles the neutrinos from the charged lepton in the quantum state (7.3.7) [92]. The detection of the charged lepton at the source (or its stopping at a nearby "beam dump") projects the quantum state (7.3.7) at the observation time t_S onto the single particle charged lepton state $e^{-iE^e_{\vec{Q}}t_S}\,\big|e_{\vec{Q}}\rangle$ disentangling the neutrino states into the "collapsed" state

$$\begin{aligned}
\big|\mathcal{V}_e(\vec{Q},t_S)\rangle \;&\equiv\; \langle e_{\vec{Q}}\big|\Psi(t_S)\rangle\; e^{iE^e_{\vec{Q}}t_S} \\
&=\; i\frac{g\; e^{-iE_S\frac{t_S}{2}}}{2\sqrt{2VE^W_{\vec{k}}E^e_{\vec{Q}}}}\left\{\frac{\sin\theta}{\sqrt{\Omega_{2,\vec{P}}}}\;|\nu_{2,\vec{P}}\rangle e^{-i\Omega_{2,\vec{P}}\frac{t_S}{2}}\left[\frac{\sin\left[\left(E_S-\Omega_{2,\vec{P}}\right)\frac{t_S}{2}\right]}{(E_S-\Omega_{2,\vec{P}})/2}\right]\right. \\
&\quad\left.+\;\frac{\cos\theta}{\sqrt{\Omega_{1,\vec{P}}}}\;|\nu_{1,\vec{P}}\rangle e^{-i\Omega_{1,\vec{P}}\frac{t_S}{2}}\left[\frac{\sin\left[\left(E_S-\Omega_{1,\vec{P}}\right)\frac{t_S}{2}\right]}{(E_S-\Omega_{1,\vec{P}})/2}\right]\right\},
\end{aligned} \tag{6.2.17}$$

where $E_S=E^W_{\vec{k}}-E^e_{\vec{Q}}$ and $\vec{P}=\vec{k}-\vec{Q}$. We note that up to a phase, the coefficient functions that multiply $\big|\nu_1\rangle$ and $\big|\nu_2\rangle$ are

$$\frac{\sin\left[(E_S-\Omega_1)\frac{t_S}{2}\right]}{(E_S-\Omega_1)/2}\quad,\quad\frac{\sin\left[(E_S-\Omega_2)\frac{t_S}{2}\right]}{(E_S-\Omega_2)/2}, \tag{6.2.18}$$

respectively. In the limit $t_S\to\infty$, they become $2\pi\delta(E_S-\Omega_1)$ and $2\pi\delta(E_S-\Omega_2)$, respectively. Therefore, in this limit, for a fixed E_S, one of the quantum states will be projected out. However, as we insist on keeping a finite time interval, we will keep t_S finite.

The state $\big|\mathcal{V}_e(\vec{Q},t_S)\rangle$ then evolves forward in time with the full Hamiltonian

$$\big|\mathcal{V}_e(\vec{Q},t)\rangle=e^{-iH_0t}U(t,t_S)e^{iH_0t_S}\big|\mathcal{V}_e(\vec{Q},t_S)\rangle. \tag{6.2.19}$$

The "free" evolution is obtained by setting to lowest order $U(t,t_S)=1$, leading to

$$\begin{aligned}\left|\mathcal{V}_e(\vec{Q},t)\right\rangle &= i\frac{g\; e^{-iE_S\frac{t_S}{2}}}{2\sqrt{2VE^W_{\vec{k}}E^e_{\vec{Q}}}}\left\{\frac{\sin\theta}{\sqrt{\Omega_{2,\vec{P}}}}\left|\nu_{2,\vec{P}}\right\rangle\left[\frac{\sin\left[\left(E_S-\Omega_{2,\vec{P}}\right)\frac{t_S}{2}\right]}{(E_S-\Omega_{2,\vec{P}})/2}\right]e^{-i\Omega_{2,\vec{P}}\frac{t_S}{2}}\;e^{-i\Omega_{2,\vec{P}}(t-t_S)}\right.\\ &+\left.\frac{\cos\theta}{\sqrt{\Omega_{1,\vec{P}}}}\left|\nu_{1,\vec{P}}\right\rangle\left[\frac{\sin\left[\left(E_S-\Omega_{1,\vec{P}}\right)\frac{t_S}{2}\right]}{(E_S-\Omega_{1,\vec{P}})/2}\right]e^{-i\Omega_{1,\vec{P}}\frac{t_S}{2}}\;e^{-i\Omega_{1,\vec{P}}(t-t_S)}\right\}. \qquad (6.2.20)\end{aligned}$$

The phase factors $e^{-i\Omega_j t_S/2}$ multiplying each mass eigenstate are the consequence of the phase build-up during the time evolution from the production vertex until the detection of the charged lepton and the collapse of the wave function. The expression (6.2.20) features the factors

$$\frac{\sin\left[\left(E_S-\Omega_j\right)\frac{t_S}{2}\right]}{(E_S-\Omega_j)/2}, \qquad (6.2.21)$$

which as $t_S\to\infty$ becomes $2\pi\,\delta(E_S-\Omega_j)$. These factors, which are a direct consequence of the neutrino state being produced by the decay of the "parent" particle (here the W) into an *entangled* quantum state, distinguish Eq. (6.2.20) from the familiar quantum mechanical description. These factors emerge from the (approximate) energy conservation at the decay vertex. Again, in the $t_S\to\infty$ limit, if the energy of the parent particle and the charged lepton are both certain, only one of the mass eigenstates will be produced but not both. However, writing $\Omega_{1,2}$ as in Eq. (6.2.5), it follows that for $t_S\ll 4\overline{\Omega}/\delta m^2$, the width of the "diffraction" functions is much larger than the frequency difference Δ and there is a substantial overlap between these "approximate" delta functions (see Figure 33.). Only for $t_S\geq t_{osc}=2\pi/\Delta$ are the two peaks at $E_S-\overline{\Omega}=\pm\Delta$ actually resolved, whereas for $t_S\ll t_{osc}$, the two peaks are unresolved, "blurred" into one broad peak at $\overline{\Omega}$. Thus for $t_S\ll 2\pi/\Delta$, we can use the approximation

$$\frac{\sin\left[\left(E_S-\Omega_1\right)\frac{t_S}{2}\right]}{(E_S-\Omega_1)/2}\simeq\frac{\sin\left[\left(E_S-\Omega_2\right)\frac{t_S}{2}\right]}{(E_S-\Omega_2)/2}\simeq\frac{\sin\left[\left(E_S-\overline{\Omega}\right)\frac{t_S}{2}\right]}{(E_S-\overline{\Omega})/2}\,. \qquad (6.2.22)$$

To illustrate the validity of the above approximation, let us consider the case in which the typical size of the source or beam dump is a few meters across. In a typical experiment, the charged lepton emerging from the interaction vertex travels this distance within a time scale $t_S\approx 10^{-8}$ s, leading to an energy uncertainty above $\delta E\sim\hbar/t_S\sim 10^{-7}\,\text{eV}$. Taking as an

example $\delta m^2 \sim 10^{-4}\,\mathrm{eV}^2$ and $\overline{\Omega} \sim E_S \sim 100\,\mathrm{MeV}$, it follows that $\delta m^2/\overline{\Omega} \sim 10^{-12}\,\mathrm{eV} \ll \delta E$. Therefore, the detection or absorption of the charged lepton near the source, on a time scale much smaller than $1/\Delta$ cannot resolve the energy difference between the mass eigenstates and the approximation (6.2.22) is justified.

Another approximation we can use in (6.2.17) is $\Omega_1 \simeq \Omega_2 \simeq \overline{\Omega}$, for $\overline{\Omega} \gg \Delta$. Absorbing the phase factors $e^{-i\Omega_j t_S/2}$ into the definition of the states $|\nu_j\rangle$, the time evolved disentangled state is then approximately given by

$$\begin{aligned} \left|\mathcal{V}_e(\vec{Q},t)\right\rangle \;\simeq\; & \frac{ig}{\sqrt{8VE^W_{\vec{k}}E^e_{\vec{Q}}\overline{\Omega}}}\left[\frac{\sin\left[\left(E_S-\overline{\Omega}\right)\frac{t_S}{2}\right]}{(E_S-\overline{\Omega})/2}\right] \\ & \left\{\sin\theta\,\left|\nu_{2,\vec{P}}\right\rangle\,e^{-i\Omega_{2,\vec{P}}(t-t_S)} + \cos\theta\,\left|\nu_{1,\vec{P}}\right\rangle\,e^{-i\Omega_{1,\vec{P}}(t-t_S)}\right\}, \end{aligned} \tag{6.2.23}$$

for $t_S \ll 2\pi/\Delta$. The state inside the brackets is identified as the usual quantum mechanical state that is time evolved from the "electron" neutrino state, which is prepared initially at t_S. From this analysis, we see that there are two conditions required for the disentangled neutrino state to be identified with the familiar quantum mechanical state: $\delta m^2/\overline{\Omega}^2 \ll 1$ and $t_S \ll t_{osc} \sim 2\pi\overline{\Omega}/\delta m^2$. The former is always satisfied for neutrinos with $\delta m^2 \sim 10^{-3} - 10^{-4}\,\mathrm{eV}^2$, $\overline{\Omega} >$ a few MeV, while the latter is fulfilled if the charged lepton produced at the source is either observed or stopped at a beam-dump near the production region in long-baseline experiments.

The latter condition implies that the neutrino state is disentangled before oscillations can occur. In a long-baseline experiment, this is achieved if the charged lepton, which is entangled with the neutrino at the production vertex, is measured or stopped near the production region. Therefore, we conclude that an important condition for the familiar quantum mechanical description of oscillations to be reliable is that the quantum state must be disentangled on time scales much shorter than the oscillation time. It is clear from this discussion that the precise value of t_S is irrelevant as long as $t_S \ll t_{osc}$. Experimentally, t_S is of the order of the time of flight of the charged lepton in the production region at the source namely a few $10^{-8}\,s$.

6.2.3 Transition amplitudes and event rates

The number of charged lepton events with momentum $\vec{Q}$ produced at the source, at time t_S is given by

$$n_e(\vec{Q},t_S)=\langle\Psi_e(t_S)|a_e^\dagger(\vec{Q})a_e(\vec{Q})|\Psi_e(t_S)\rangle=\langle\mathcal{V}_e(\vec{Q},t_S)\big|\mathcal{V}_e(\vec{Q},t_S)\rangle. \tag{6.2.24}$$

For $t_S\ll t_{osc}=2\pi/\Delta$ and $\overline{\Omega}\gg\Delta$, using the approximations leading to (6.2.23), we obtain the charged lepton differential detection rate at the source

$$\begin{aligned}(2\pi)^3\,\frac{dN_e^S}{d^4x\,d^3\vec{Q}} &= \frac{dn_e(\vec{Q},t_S)}{dt_S}\\ &= \frac{2g^2}{8VE_{\vec{k}}^W E_{\vec{Q}}^e\,\overline{\Omega}}\,\frac{\sin\Big[\big(E_S-\overline{\Omega}\big)t_S\Big]}{(E_S-\overline{\Omega})}\\ &\simeq \frac{2\pi g^2}{8VE_{\vec{k}}^W E_{\vec{Q}}^e\,\overline{\Omega}}\,\delta(E_S-\overline{\Omega}),\end{aligned} \tag{6.2.25}$$

where at the last step we have replaced the diffraction function by the delta function. This can be justified as follows. For $t_S\sim 10^{-8}\,\mathrm{s}$, the width of this function (the resolution) in energy is $\sim 10^{-7}\,\mathrm{eV}$. Since the typical energy in a long-baseline experiment is $\gtrsim 40-100\,\mathrm{MeV}$, the error incurred in replacing the diffraction function by a delta function is smaller than one part in 10^{15}.

6.3 INTERACTION AT THE FAR DETECTOR

We can also obtain the transition amplitude for the disentangled state to produce a final charged lepton and another W particle at the far detector at time t_D, where $t_D-t_S\sim L$ and L is the baseline. This is obtained from the time evolution of the disentangled state with the full Hamiltonian from the time of disentanglement t_S until the time t_D, at which the detection measurement is carried out by overlapping the time evolved state with the final state.

6.3.1 Transition amplitude and probabilities

The transition amplitude is given by

$$\begin{aligned}\mathcal{A}_{\alpha\to\beta} &= \langle W(\vec{k}_D), l_\beta(\vec{p}_D)\big|\, e^{-iH(t_D-t_S)}\,\big|\mathcal{V}_e(\vec{Q},t_S)\rangle \\ &= e^{-iE_D t_D}\,\langle W(\vec{k}_D), l_\beta(\vec{p}_D)\big|\, U(t_D,t_S)\, e^{iH_0 t_S}\,\big|\mathcal{V}_e(\vec{Q},t_S)\rangle. \end{aligned} \tag{6.3.1}$$

The disappearance and appearance amplitudes are then given by

$$\begin{aligned}\mathcal{A}_{e\to e} &= -g^2\,\Pi\,(2\pi)^3\delta(\vec{k}_S-\vec{p}_S-\vec{k}_D-\vec{p}_D)\,\times \\ &\left\{\frac{\cos^2\theta}{2\Omega_{1,\vec{P}}}e^{-i\Omega_{1,\vec{P}}\frac{t_D}{2}}\left[\frac{\sin\left[\left(E_S-\Omega_{1,\vec{P}}\right)\frac{t_S}{2}\right]}{(E_S-\Omega_{1,\vec{P}})/2}\right]\left[\frac{\sin\left[\left(E_D-\Omega_{1,\vec{P}}\right)\left(t_D-t_S\right)/2\right]}{(E_D-\Omega_{1,\vec{P}})/2}\right]\right. \\ &\left.+\frac{\sin^2\theta}{2\Omega_{2,\vec{P}}}e^{-i\Omega_{2,\vec{P}}\frac{t_D}{2}}\left[\frac{\sin\left[\left(E_S-\Omega_{2,\vec{P}}\right)\frac{t_S}{2}\right]}{(E_S-\Omega_{2,\vec{P}})/2}\right]\left[\frac{\sin\left[\left(E_D-\Omega_{2,\vec{P}}\right)\left(t_D-t_S\right)/2\right]}{(E_D-\Omega_{2,\vec{P}})/2}\right]\right\}\end{aligned} \tag{6.3.2}$$

and

$$\begin{aligned}\mathcal{A}_{e\to\mu} &= -g^2\,\Pi\,(2\pi)^3\delta(\vec{k}_S-\vec{p}_S-\vec{k}_D-\vec{p}_D)\,\frac{\sin 2\theta}{2}\,\times \\ &\left\{\frac{e^{-i\Omega_{1,\vec{P}}\frac{t_D}{2}}}{2\Omega_{1,\vec{P}}}\left[\frac{\sin\left[\left(E_S-\Omega_{1,\vec{P}}\right)\frac{t_S}{2}\right]}{(E_S-\Omega_{1,\vec{P}})/2}\right]\left[\frac{\sin\left[\left(E_D-\Omega_{1,\vec{P}}\right)\left(t_D-t_S\right)/2\right]}{(E_D-\Omega_{1,\vec{P}})/2}\right]\right. \\ &\left.-\frac{e^{-i\Omega_{2,\vec{P}}\frac{t_D}{2}}}{2\Omega_{2,\vec{P}}}\left[\frac{\sin\left[\left(E_S-\Omega_{2,\vec{P}}\right)\frac{t_S}{2}\right]}{(E_S-\Omega_{2,\vec{P}})/2}\right]\left[\frac{\sin\left[\left(E_D-\Omega_{2,\vec{P}}\right)\left(t_D-t_S\right)/2\right]}{(E_D-\Omega_{2,\vec{P}})/2}\right]\right\},\end{aligned} \tag{6.3.3}$$

with $\vec{P}=\vec{k}_S-\vec{p}_S$, and Π is given by

$$\Pi=\left[\frac{1}{16\;V^4\;E^W_{\vec{k}_S}\,E^W_{\vec{k}_D}\,E^l_{\vec{p}_S}\,E^l_{\vec{p}_D}}\right]^{\frac{1}{2}}\quad, \tag{6.3.4}$$

the labels D, S refer to (far) detector and source respectively. Implementing the same approximations leading to the factorized state (6.2.23), namely $\overline{\Omega} \gg \Delta$ and $t_S \Delta \ll 1$, we find the disappearance and appearance probabilities

$$\begin{aligned}
\mathcal{P}_{e\to e}(t_D) &= \Big(\frac{g^2\Pi}{2\overline{\Omega}_{\vec{P}}}\Big)^2 (2\pi)^3\, V\, \delta(\vec{k}_S - \vec{p}_S - \vec{k}_D - \vec{p}_D)\, 2\pi\, t_S\, \delta(E_S - \overline{\Omega}_{\vec{P}}) \\
&\quad \Big\{ \cos^4\theta\, f_+^2(x,t,\Delta) + \sin^4\theta\, f_-^2(x,t,\Delta) + \frac{\sin^2(2\theta)}{2} \cos(t\Delta) f_+(x,t,\Delta) f_-(x,t,\Delta) \Big\}, \\
\mathcal{P}_{e\to\mu}(t_D) &= \Big(\frac{g^2\Pi}{2\overline{\Omega}_{\vec{P}}}\Big)^2 (2\pi)^3\, V\, \delta(\vec{k}_S - \vec{p}_S - \vec{k}_D - \vec{p}_D)\, 2\pi\, t_S\, \delta(E_S - \overline{\Omega}_{\vec{P}})\, \frac{\sin^2 2\theta}{4} \\
&\quad \Big\{ f_+^2(x,t,\Delta) + f_-^2(x,t,\Delta) - 2\cos(t\Delta) f_+(x,t,\Delta) f_-(x,t,\Delta) \Big\},
\end{aligned} \tag{6.3.5}$$

where $t = t_D - t_S$ and $x = E_D - \overline{\Omega}_{\vec{P}}$. Here,

$$E_S = E^W_{\vec{k}_S} - E^e_{\vec{p}_S}, \qquad E_D = E^W_{\vec{k}_D} + E^l_{\vec{p}_D}, \tag{6.3.6}$$

and $f_\pm$ are given by Eq. (6.2.8).

In the long time limit, using $f_\pm(x,t,\Delta) \to 2\pi\, t\, \delta(x \pm \Delta)$, their product is given by (6.2.10), and we find

$$\begin{aligned}
\mathcal{P}_{e\to e}(t_D) &= \Big(\frac{g^2\Pi}{2\overline{\Omega}_{\vec{P}}}\Big)^2 (2\pi)^5\, V\, \delta(\vec{k}_S - \vec{p}_S - \vec{k}_D - \vec{p}_D)\; t_S\, \delta(E_S - \overline{\Omega}_{\vec{P}}) \\
&\quad \Big\{ \cos^4\theta\, t\, \delta(x+\Delta) + \sin^4\theta\, t\, \delta(x-\Delta) \\
&\quad + \frac{\sin^2(2\theta)}{2}\, \frac{\sin(2\,t\,\Delta)}{2\Delta}\, \frac{1}{2}\Big[\delta(x+\Delta) + \delta(x-\Delta)\Big] \Big\}, \\
\mathcal{P}_{e\to\mu}(t_D) &= \Big(\frac{g^2\Pi}{2\overline{\Omega}_{\vec{P}}}\Big)^2 (2\pi)^5\, V\, \delta(\vec{k}_S - \vec{p}_S - \vec{k}_D - \vec{p}_D)\; t_S\, \delta(E_S - \overline{\Omega}_{\vec{P}})\, \frac{\sin^2 2\theta}{4} \\
&\quad \Big\{ t\, \delta(x+\Delta) + t\, \delta(x-\Delta) - 2\, \frac{\sin(2\,t\,\Delta)}{2\Delta}\, \frac{1}{2}\Big[\delta(x+\Delta) + \delta(x-\Delta)\Big] \Big\}.
\end{aligned} \tag{6.3.7}$$

where $\vec{P} = \vec{k}_D + \vec{p}_D$. These transition probabilities feature the *two* time scales t_S and $t = t_D - t_S$ associated with the measurements at the near and far detector. They also feature energy conserving delta functions associated with the different mass eigenstates. There is a further simplification when $\overline{\Omega} \gg \Delta$. In this regime, when the probabilities (6.3.7) are integrated over a smooth density of states, the delta functions corresponding to the mass eigenstates yield the density of states at values $E_D = \overline{\Omega} \mp \Delta$. In typical experiments, where $\overline{\Omega} \sim 100\,\text{MeV}$ and $\delta m^2 \sim 10^{-3}\,\text{eV}^2$, the density of final states must vary dramatically near $\overline{\Omega}$ to resolve the small interval Δ, with $\Delta/\overline{\Omega} \lesssim 10^{-19}$. Therefore, understanding the probabilities as being integrated with a smooth final density of states insensitive to the mass difference, we can approximate $\delta(x \pm \Delta) \simeq \delta(x)$. In this case, we can approximate the above expressions by

$$\begin{aligned}
\mathcal{P}_{e\to e}(t_D) &= \left(\frac{g^2\Pi}{2\overline{\Omega}_{\vec{P}}}\right)^2 (2\pi)^5\, V\, \delta(\vec{k}_S - \vec{p}_S - \vec{k}_D - \vec{p}_D)\; t_S\, \delta(E_S - \overline{\Omega}_{\vec{P}})\, \delta(E_D - \overline{\Omega}_{\vec{P}}) \\
&\quad \left\{ t\Big[\cos^4\theta + \sin^4\theta\Big] + 2\cos^2\theta \sin^2\theta\, \frac{\sin(2\,t\,\Delta)}{2\Delta} \right\}, \qquad (6.3.8) \\
\mathcal{P}_{e\to\mu}(t_D) &= \left(\frac{g^2\Pi}{2\overline{\Omega}_{\vec{P}}}\right)^2 (2\pi)^5\, V\, \delta(\vec{k}_S - \vec{p}_S - \vec{k}_D - \vec{p}_D)\; t_S\, \delta(E_S - \overline{\Omega}_{\vec{P}})\, \delta(E_D - \overline{\Omega}_{\vec{P}})\, \frac{\sin^2 2\theta}{2} \\
&\quad \left\{ t - \frac{\sin(2\,t\,\Delta)}{2\Delta} \right\}. \qquad (6.3.9)
\end{aligned}$$

The product $\delta(E_S - \overline{\Omega}_{\vec{P}})\, \delta(E_D - \overline{\Omega}_{\vec{P}})$ is an *approximate* energy conservation at both production and detection vertices, where we have neglected Δ, which is twice the energy difference between the mass eigenstates.

6.3.2 Factorization of the event rates

Further insight can be gained by obtaining the phase space distribution of the number of charged leptons $l = \{e, \mu\}$ at the far detector

$$(2\pi)^3\, \frac{dN_l^{FD}}{d^3x\, d^3\vec{p}_D} = n_l(\vec{p}_D, t_D) = \langle \mathcal{V}_e(\vec{Q}, t_D, t_S) \big| a_l^\dagger(\vec{p}_D) a_l(\vec{p}_D) \big| \mathcal{V}_e(\vec{Q}, t_D, t_S) \rangle. \qquad (6.3.10)$$

Here,

$$\big|\mathcal{V}_e(\vec{Q},t_D,t_S)\rangle = e^{-iH_0 t_D} U(t_D,t_S) e^{iH_0 t_S} \big|\mathcal{V}_e(\vec{Q},t_S)\rangle \tag{6.3.11}$$

is the neutrino state disentangled at t_S near the source and has been time-evolved until it is detected at the far detector at time t_D. Not surprisingly, since we only keep terms that are up to order g^2, the time evolved state contains a single lepton Fock state. We find that

$$(2\pi)^3 \frac{dN_e^{FD}}{d^3x\, d^3\vec{p}_D} = \mathcal{P}_{e\to e}(t_D), \qquad (2\pi)^3 \frac{dN_\mu^{FD}}{d^3x\, d^3\vec{p}_D} = \mathcal{P}_{e\to\mu}(t_D), \tag{6.3.12}$$

with the probabilities $\mathcal{P}_{e\to e}(t_D)$ and $\mathcal{P}_{e\to\mu}(t_D)$ are given by (6.3.8) and (6.3.9).

Taking the time derivative with respect to t_D, we obtain the differential charged lepton event rates at the far detector

$$\begin{aligned}(2\pi)^3 \frac{dN_e^{FD}}{d^3x\, dt\, d^3\vec{p}_D} &= \left(\frac{g^2\Pi}{2\overline{\Omega}_{\vec{P}}}\right)^2 (2\pi)^5\, V\, \delta(\vec{k}_S - \vec{p}_S - \vec{k}_D - \vec{p}_D)\; t_S\, \delta(E_S - \overline{\Omega}_{\vec{P}})\, \delta(E_D - \overline{\Omega}_{\vec{P}}) \\ &\quad \left\{ \cos^4\theta + \sin^4\theta + 2\cos^2\theta \sin^2\theta\, \cos(2t\Delta) \right\},\end{aligned} \tag{6.3.13}$$

$$\begin{aligned}(2\pi)^3 \frac{dN_\mu^{FD}}{d^3x\, dt\, d^3\vec{p}_D} &= \left(\frac{g^2\Pi}{2\overline{\Omega}_{\vec{P}}}\right)^2 (2\pi)^5\, V\, \delta(\vec{k}_S - \vec{p}_S - \vec{k}_D - \vec{p}_D)\; t_S\, \delta(E_S - \overline{\Omega}_{\vec{P}})\, \delta(E_D - \overline{\Omega}_{\vec{P}})\, \frac{\sin^2 2\theta}{2} \\ &\quad \left\{ 1 - \cos(2t\Delta) \right\}.\end{aligned} \tag{6.3.14}$$

Remarkably, these rates can be simply written as

$$(2\pi)^3 \frac{dN_\beta^{FD}}{d^3x\, dt\, d^3\vec{p}_D} = (2\pi)^3 \frac{dN_\alpha^S}{d^3x\, d^3\vec{p}_s}\, P_{\alpha\to\beta}(t)\, d\Gamma_{\nu_\beta \to W\, l_\beta}, \tag{6.3.15}$$

where we have used the expression (6.2.25) for the differential charged lepton event rate at the source and integrated in t_S,

$$d\Gamma_{\nu_\beta \to W\, l_\beta} = \frac{(2\pi)^4\, g^2\, V}{8V^3 E^W_{\vec{k}_D} E^{l_\beta}_{\vec{p}_D} \overline{\Omega}_{\vec{P}}}\, \delta(\vec{k}_S - \vec{p}_S - \vec{k}_D - \vec{p}_D)\, \delta(E_D - \overline{\Omega}_{\vec{P}}) \tag{6.3.16}$$

is the charged lepton production rate from the reaction $\nu_\beta \to W\, l_\beta$ for a flavor neutrino of energy $\overline{\Omega}$ and $P_{\alpha\to\beta}(t)$ are the disappearance ($\alpha = \beta$) or appearance ($\alpha \neq \beta$) transition probabilities obtained from the usual quantum mechanical calculations of Rabi-oscillations.

One remarkable aspect of the final result (6.3.16) is the factorization of the different processes contributing to the far detector event rate, namely the number of events at the source multiplies the quantum mechanical transition probability which in turn multiplies the production rate at the vertex in the far detector. This factorization is a distinct consequence of the *two time* analysis, of the disentanglement of the neutrino near the production region along with the approximations invoked in the resolution of the energy conserving delta functions. We emphasize that the factorization in terms of the quantum mechanical transition probabilities $P_{\alpha\to\beta}(t)$ only applies to the detection rate defined by taking the time derivative. The total number of events per phase space volume also factorizes but not in terms of the quantum mechanical transition probabilities but in terms of their integral in time.

6.4 DISCUSSIONS

6.4.1 Possible corrections for short baseline experiments

This analysis also suggests that potentially important corrections may arise in short baseline experiments for much lower energy. In this case, it may occur that the time scale of disentanglement is of the same order as the oscillation scale $\overline{\Omega}/\delta m^2$ so that $t_S\delta m^2/\overline{\Omega}\sim 1$ and the sine functions cannot be factored out of the quantum state as in (6.2.23). In this case, the resulting disentangled state is

$$\left|\mathcal{V}_e(\vec{Q},t)\right\rangle \propto \left\{\sin\theta\,\left|\nu_{2,\vec{P}}\right\rangle\, e^{-i\Omega_{2,\vec{P}}(t-t_S)}\, f_-(x,t_S,\Delta) + \cos\theta\,\left|\nu_{1,\vec{P}}\right\rangle\, e^{-i\Omega_{1,\vec{P}}(t-t_S)}\, f_+(x,t_S,\Delta)\right\}, \tag{6.4.1}$$

which is not of the familiar quantum mechanical form of a coherent superposition of the mass eigenstates with the usual $\cos\theta,\sin\theta$ amplitudes but with the "diffraction functions" multiplying these factors. If the width of these functions is of order $2\pi/t_S \lesssim 2\Delta$, interference term in the probability will feature the product (6.2.10) which would lead to an extra interference terms of the form $\sin(t_S\Delta)/t_S\Delta$ multiplying the $\sin(2t\Delta)/2\Delta$ in (6.3.8) and (6.3.9). Such factor yields an *extra modulation with energy* which may yield phenomenologically interesting modifications in the interpretation and analysis of data. Although the typical time scale

t_S for disentanglement near the source region is approximately the same for short and long baseline experiments, this discussion applies to the possibility in which t_S is not too small compared to the oscillation time scale as could be the case in short-baseline experiments. For example at LSND the source region is a few meters across and the baseline is $\sim 30\,m$, and at KARMEN where the baseline is $\sim 17.5\,m$. The baseline and beam energy are designed so that at least an oscillation takes place along the baseline. However in these short-baseline experiments, the distance over which the neutrino state is disentangled from the charged lepton, a few meters, is not to much smaller than the baseline, consequently t_S may not be much smaller than an oscillation time.The potential phenomenological importance of these effects merit their further study.

6.4.2 Wave packet description

As mentioned earlier in the paper, we restricted ourselves to plane-wave states, the main reason being to discuss the essential concepts within the simplest setting. Although we postpone a thorough discussion of the more technical aspects including the wave packet description to further study, we can provide physical arguments that allow the extrapolation of the main results obtained above to the wave packet case.

Consider that the initial particle, the charged leptons measured at the near and far detectors and the final particle are all described by wave packets with a macroscopic localization length scale σ of the order of the typical scale of the detectors (a few meters) localized at the source and detectors respectively. These are sharply localized in momentum. The transition amplitudes between wave packets are now obtained from (6.3.1-6.3.3) by convolution with the wave functions of the initial state, the charged lepton measured near the source and those of the final state at the far detector.

The disentangled neutrino state (6.2.17) is now described as a propagating wave packet with a typical spatial localization length also of $\mathcal{O}(\sigma)$, namely of macroscopic scale. These mildly localized wave packets lead to both momentum and energy uncertainty of the same

order $\Delta E \sim \Delta p \sim \hbar/\sigma \sim \hbar/t_S \sim 10^{-7}\,\mathrm{eV}$. These uncertainties in energy and momentum are much larger than typical values for the neutrino energy differences $\delta m^2/\overline{\Omega} \sim 10^{-12}\,\mathrm{eV}$. As this wave packet propagates, the mass eigenstates will slowly separate because they feature different group velocities, and coherence will be maintained as long as the separation between the wave packets is much smaller than their localization lengths (neglecting dispersion). For a baseline L and typical energies $\overline{\Omega} \sim 100\,\mathrm{MeV}$, the separation at the far detector is $\propto (\Delta/\overline{\Omega})\, L \sim 10^{-20} L$. Therefore, coherence is always maintained for macroscopic localization lengths in terrestrial experiments. The detection amplitudes (6.3.2) and (6.3.3) and probabilities (6.3.8) and (6.3.9) vanish until the time when the front of the packet overlaps with the far detector, namely for $t_D - t_S \approx L$, with an uncertainty of $\mathcal{O}(\sigma)$, which for long-baseline experiments is always $\sigma \ll L$. The total number of events at the far detector is found by integrating the rate (6.3.16) from $t = L$, which is when the front of the wave packet overlaps with the detector until $t = L + \sigma$ when the wave packet has completely passed through the detector. For $L \gg \sigma$ and neglecting the separation of wave packets the total number of events at the far detector is obtained by replacing (6.3.15) by

$$\frac{dN_\beta^{FD}}{d^3x\, d^3\vec{p}_D} = \frac{dN_\alpha^S}{d^3x\, d^3\vec{p}_s}\, \left[P_{\alpha\to\beta}(L)\,\sigma\right]\, d\Gamma_{\nu_\beta \to W\, l_\beta}\,. \tag{6.4.2}$$

The delta functions will also be integrated with the wave packet profiles and volume factors are replaced by σ^3. Furthermore, at distances from the source $\gg \sigma$, the disentangled neutrino wave packet propagates as a spherical wave. Therefore, for far-detectors in the "radiation zone," the probability will be suppressed by a geometric flux factor $1/L^2$ [159, 160, 158, 119, 116, 118]. Obviously, there are uncertainties of $\mathcal{O}(\sigma)$ in this argument, but these are irrelevant for long-baselines $L \gg \sigma$. The σ multiplying the total number of events in (6.4.2) is expected: it is the "total interaction time" during which the wave packet interacts with the detector. Obviously, these factors modify the overall normalization. However, the distortion of the energy spectrum in disappearance and the appearance probabilities for long-baseline experiments are determined by $P_{\alpha\to\beta}(L, E)$ (for short baseline there are potential corrections as discussed above). While we deem these arguments describing the wave-packet scenario to be physically sound, we will provide a thorough technical

discussion of this case based on the results obtained above in the plane wave approximation in future work. The analysis presented above for the dynamics of disentanglement and propagation provides the fundamental basis to include the wave packet description, which is obtained from simple convolution of these results with wave packet wave functions.

6.5 CONCLUSION

In appearance and disappearance experiments, neutrinos produced by a charged current vertex at the source are entangled with the charged lepton. We study the dynamics of this quantum state directly as a function of time.

If the charged lepton (or daughter particle) produced at the source is not measured, tracing out this degree of freedom yields a density matrix for the neutrino. In the mass basis, the time evolution of the diagonal density matrix elements describe the production of mass eigenstates from the decay, whereas the off-diagonal density matrix elements exhibit the oscillations resulting from the interference of mass eigenstates and are a measure of coherence. We find that coherence remains up to a time of the order of the oscillation time scale during which diagonal and off diagonal matrix elements are of the same order.

The measurement of the charged lepton near the source (or its stopping at a nearby "beam dump") disentangles the neutrino state, and it is the further time evolution of this disentangled state with the total Hamiltonian that leads to the production of charged leptons at the far detector. Thus, the process of production and detection in long-baseline experiments involves two different time scales: the measurement of the charged lepton near the source determines the first time scale at which the neutrino state is disentangled, while the measurement of the charged lepton at the far detector is the second time scale, which is much longer than the first one in long-baseline experiments.

In this time dependent description, we establish that the usual quantum mechanical state

emerges if the disentanglement of the charged lepton produced with the neutrino occurs on time scales much shorter than the oscillation scale $\sim E/\delta m^2$. Under these circumstances, the event rate at the far detector factorizes in terms of the usual quantum mechanical probability if the final density of states is insensitive to the difference in the energies of the mass eigenstates in the ultrarelativistic limit $\delta m^2/E$.

Although in this article we focused on the study of the dynamics for the case of plane waves to exhibit the main results within the simplest setting, we provide physically motivated arguments to extrapolate the results to the case of wave packets, analyzing the effect of localization of the initial and final state wave functions at the near and far detector on the detection process. Combining the results obtained for plane waves with a wave packet description yields the total number of events detected in terms of the usual transition probability as a function of baseline. A deeper and more detailed analysis of wave packets and localization aspects will be provided in forthcoming work.

The analysis presented here also suggests that there could arise potentially interesting corrections in the case of short baseline experiments such as MiniBooNE and/or LSND with baselines of $\sim 500, \sim 30$ meters and typical energies ~ 1GeV; ~ 30MeV, respectively, wherein the disentanglement of the neutrino could occur on time scales of the same order as the oscillation scale. In this case, the disentangled state will differ from the usual quantum mechanical coherent superposition and this difference introduces extra modulation with energy and could be important in the final detection rate. Such possibility could be relevant in the interpretation and analysis of data, in particular masses and mixing angles and certainly merits further detailed study.

7.0 PART II: IS THE GSI ANOMALY DUE TO NEUTRINO OSCILLATIONS?

In this chapter, we apply the method developed in Chap. 6 to the "GSI anomaly", from which we examine whether neutrino mixing and oscillations could be responsible for time dependent modulations in the two-body decay rate. This study is reported in [287]. We first introduce the background of the GSI anomaly in Sec. 7.1, and then propose a model for it in Sec. 7.2, which captures the relevant physical ingredients while neglecting all unnecessary technical complications. In Sec. 7.3, we obtain the time evolved state emerging from the two-body decay of the parent particle. This is a quantum mechanically entangled state [92] between the daughter particle and the neutrino, whose time evolution determines completely the number densities of parent and daughter particles, unambiguously yielding the time dependence of their population. The result of this study confirms that interference between neutrino mass eigenstates is *not* responsible for any modulation in the parent or daughter population, therefore neutrino mixing is *not* the reason behind the GSI anomaly. Sec. 7.4 summarizes our conclusions and comments on more recent experimental results.

7.1 INTRODUCTION TO THE GSI ANOMALY

Recent experiments at the Experimental Storage Ring (ESR) at GSI in Darmstadt have revealed an unexpected time dependent modulation in the population of parent ions $^{140}\mathrm{Pr}^{58+}$ and $^{142}\mathrm{Pm}^{62+}$ from the Electron Capture (EC) decays $^{140}\mathrm{Pr}^{58+} \to {}^{140}\mathrm{Ce}^{58+} + \nu_e$ and $^{142}\mathrm{Pm}^{62+} \to {}^{142}\mathrm{Nd}^{62+} + \nu_e$ [205, 206], a phenomenon that has been dubbed the "GSI anomaly." In this experiment, changes of the ions' revolution frequencies are detected by the technique of time

resolved Schottky mass spectrometry. For a small number of stored ions, every decay can be resolved. Thus, a time distribution of EC decays of the parent ions can be measured. On top of the experimental decay curve, the GSI experiment observed an unexpected time modulation with a period of about $T \simeq 7s$. Such a behavior is summarized in Figs. 36 and 37 [205, 206].

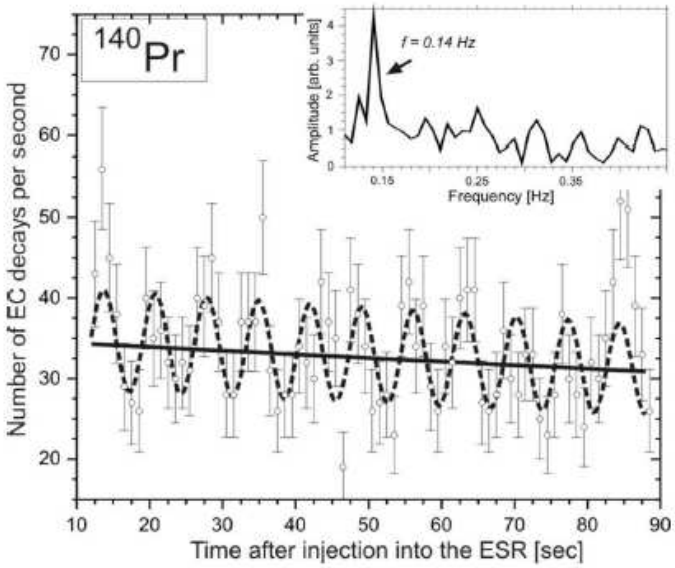

Figure 36: Figure 3 from [206]. Number of EC decays of H-like ^{140}Pr ions per second as a function of the time after the injection into the ring. The solid and dashed lines represent the fits according to Eq. 1 (without modulation) and Eq. 2 (with modulation) in [206], respectively. The inset shows the Fast Fourier Transform of these data. A clear frequency signal is observed at 0.14 Hz (laboratory frame).

A theoretical explanation of this time dependent modulation of the decay rate of the parent ion suggests that it is a consequence of the interference between the neutrino mass eigenstates in the final state of the two-body decay [205, 206, 175, 174, 173, 122, 204]. The authors in Refs. [175, 174, 173, 122] argue that the total amplitude of an EC decay is a coherent sum of contributions from difference neutrino mass eigenstates. The decay probability is obtained by squaring the total amplitude, thus the interference between neutrino mass eigenstates gives rise to the observed modulation feature as a consequence of their mixing

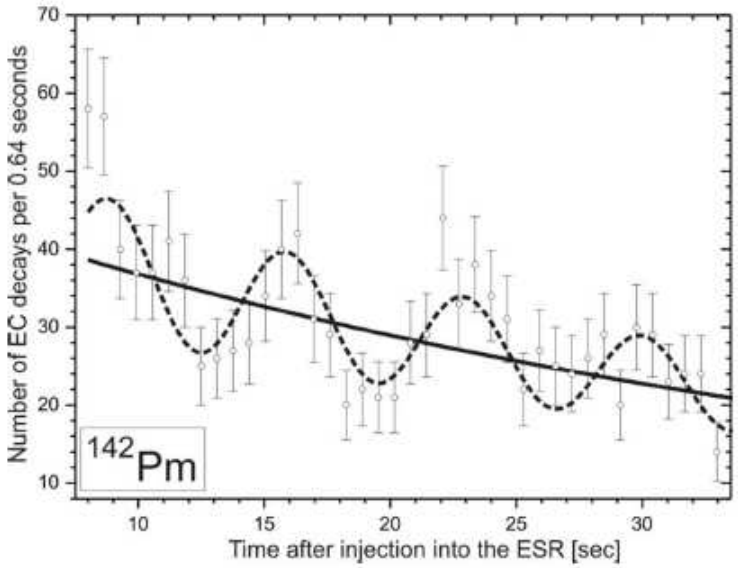

Figure 37: Figure 5 from [206]. A roomed-in plot of the number of EC decays of H-like ^{142}Pm ions per 0.64 second as a function of the time after the injection into the ring. The solid and dashed lines represent the fits according to Eq. 1 (without modulation) and Eq. 2 (with modulation) in [206], respectively. The inset shows the Fast Fourier Transform of these data. A clear frequency signal is observed at 0.14 Hz (laboratory frame).

and oscillations. If indeed periodic modulations of EC decay rates are a consequence of neutrino mixing, these experiments bring an interesting alternative to long-baseline neutrino experiments for the determination of neutrino mass differences.

However, this interpretation has been re-examined and criticized in Refs. [145, 146, 86, 188, 235] on the basis that it is not the amplitudes that must be summed coherently but the probabilities, corresponding to an incoherent addition of the contributions from the different mass eigenstates. This approach does not lead to any modulation as the probabilities for the decay channels into the different mass eigenstates do not interfere. The theoretical and experimental importance of understanding whether neutrino mixing and oscillations could lead to time dependent modulations in two body decays when neutrinos are a component of the final state warrants an alternative exploration of these questions.

Rather than focusing on any one of these approaches, either summing amplitudes or probabilities, in this study, we analyze the two-body decay process in a different way, by obtaining the time evolution of the population of the parent and daughter particles and considering explicitly the entanglement between the daughter particle and neutrino mass eigenstates. We apply the method developed in Ref. [286] to analyze the GSI anomaly. In this approach, we obtain the kinetic equations for the populations of the parent and daughter particles directly in real time without the necessity to invoke a coherent sum over amplitudes or a sum over probabilities, thereby bypassing the theoretical controversy.

If the time modulation is a consequence of neutrino mixing and oscillations, then this phenomenon is robust and does not depend on the details of the parent and daughter nuclei. Therefore a simple model of charged current interactions which incorporates neutrino mixing but is stripped off the peripheral complications of nuclear matrix elements should describe the essential physical phenomena.

7.2 A MODEL FOR THE GSI ANOMALY

The EC decays of heavy hydrogen-like particles are governed by charge current weak interactions, as shown in Figure 38(a). If the observed GSI anomaly is a direct consequence of interference between different neutrino mass eigenstates as proposed in Refs. [175, 174, 173, 122], the technical complications associated with the details of the interaction vertices, e.g., spin dependence of fermionic and gauge fields, are irrelevant. In order to simplify our calculation, we introduce a bosonic model that captures the main features of these EC decays without any unnecessary complication. The two body decay now can be represented by the process shown in Figure 38(b). Our model is specified by the following Lagrangian density

$$\mathcal{L} = \mathcal{L}_0[M, D] + \mathcal{L}_0[\nu] + \mathcal{L}_{\rm int}[M, D, \nu_e], \tag{7.2.1}$$

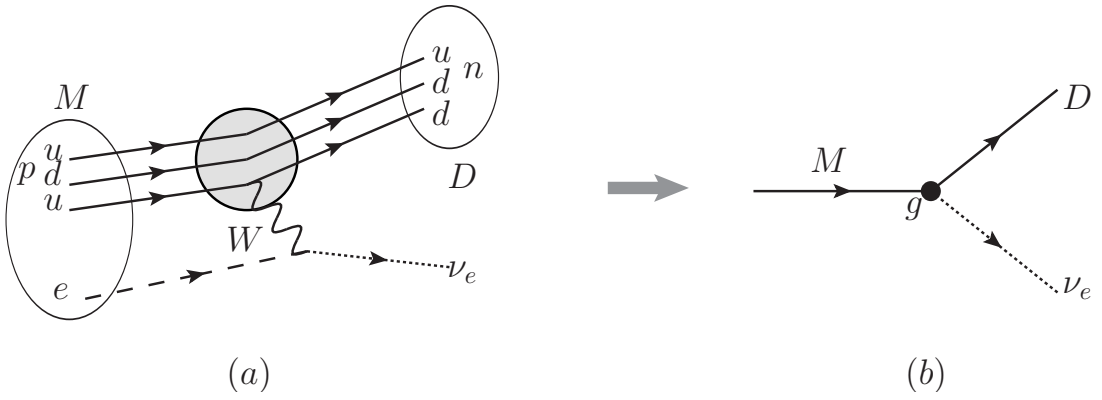

Figure 38: (a) exact interaction of EC decays of a parent particle, (b) approximated interaction of EC decays in our model.

with

$$\mathcal{L}_0[\nu] = \frac{1}{2}\left[\partial_\mu \Psi^T \partial^\mu \Psi - \Psi^T \mathbb{M} \Psi\right] , \tag{7.2.2}$$

where Ψ is a flavor doublet representing the neutrinos

$$\Psi = \begin{pmatrix} \nu_e \\ \nu_\mu \end{pmatrix}, \tag{7.2.3}$$

and $\mathbb{M}$ is the mass matrix

$$\mathbb{M} = \begin{pmatrix} m_{ee} & m_{e\mu} \\ m_{e\mu} & m_{\mu\mu} \end{pmatrix} . \tag{7.2.4}$$

Here, M and D represent the parent and daughter particles, respectively. Their free lagrangian density is specified by $\mathcal{L}_0[M, D]$. Also, we consider the simple case of only two neutrino flavors. The interaction Lagrangian is analogous to the charged current interaction of the standard model, namely

$$\mathcal{L}_{\text{int}}(\vec{x}, t) = g\, M(\vec{x}, t) D(\vec{x}, t)\, \nu_e(\vec{x}, t), \tag{7.2.5}$$

where g is the coupling constant proportional to the Fermi constant G_F. We note that only electron neutrinos enter the interaction because we are considering EC decays.

The mass matrix is diagonalized by a unitary transformation

$$U^{-1}(\theta)\,\mathbb{M}\,U(\theta) = \begin{pmatrix} m_1 & 0 \\ 0 & m_2 \end{pmatrix}, \quad U(\theta) = \begin{pmatrix} \cos\theta & \sin\theta \\ -\sin\theta & \cos\theta \end{pmatrix}. \tag{7.2.6}$$

In terms of the doublet of mass eigenstates, the flavor doublet can be expressed as

$$\begin{pmatrix} \nu_e \\ \nu_\mu \end{pmatrix} = U(\theta) \begin{pmatrix} \nu_1 \\ \nu_2 \end{pmatrix}. \tag{7.2.7}$$

In particular $\nu_e = \cos\theta\ \nu_1 + \sin\theta\ \nu_2$.

7.3 NUMBER DENSITIES OF THE PARENT AND THE DAUGHTER PARTICLES

Let us consider an initial parent particle state $\left|M(\vec{k})\right\rangle$ at time $t = 0$. For the GSI experiment, the parent ions are produced with a center velocity of 71% of the speed of light, and with a velocity spread $\Delta v/v \simeq 5 \times 10^{-7}$ [205, 206]. The evolution of the number density of parent (M) and daughter (D) particles is obtained from

$$\begin{aligned} N_M(t) &= \left\langle M(\vec{k})\right| e^{iHt}\ a_M^\dagger(\vec{k}) a_M(\vec{k})\ e^{-iHt} \left|M(\vec{k})\right\rangle, \\ n_D(t) &= \sum_{\vec{Q}} n_D(\vec{Q},t) = \sum_{\vec{Q}} \left\langle M(\vec{k})\right| e^{iHt}\ a_D^\dagger(\vec{Q}) a_D(\vec{Q})\ e^{-iHt} \left|M(\vec{k})\right\rangle, \end{aligned} \tag{7.3.1}$$

where $n_D(\vec{Q},t)$ is the number density of daughter particles with momentum $\vec{Q}$. Here, the annihilation and creation operators are in the Schroedinger picture. We note that $e^{-iHt} = e^{-iH_0 t}U(t,0)$ and that the number operators commute with the free field Hamiltonian. $U(t,0)$ is the time evolution operator in the interaction picture, namely,

$$U(t,0) = T\left[e^{i\int_0^t dt' d^3x\, \mathcal{L}_{\rm int}(\vec{x},t')}\right], \tag{7.3.2}$$

where T is the time-ordering operator.

Expanding $U(t,0)$ perturbatively, we obtain $U(t,0)\big|M\rangle = \big|M\rangle + \big|\Psi_D(t)\rangle^{(1)} + \big|\Psi_D(t)\rangle^{(2)} + \cdots$, where

$$\big|\Psi_D(t)\rangle^{(1)} = ig\int_0^t dt_1 \int d^3x_1 \Big[M(\vec{x}_1,t_1)D(\vec{x}_1,t_1)\nu_e(\vec{x}_1,t_1)\big)\Big]\big|M(\vec{k})\rangle, \tag{7.3.3}$$

and

$$\begin{aligned}\big|\Psi_D(t)\rangle^{(2)} \;=\; -g^2\int_0^t dt_1 \int d^3x_1 \int_0^{t_1} dt_2 \int d^3x_2 \Big[M(\vec{x}_1,t_1)D(\vec{x}_1,t_1)\nu_e(\vec{x}_1,t_1)\big)\Big] \\ \Big[M(\vec{x}_2,t_2)D(\vec{x}_2,t_2)\nu_e(\vec{x}_2,t_2)\big)\Big]\big|M(\vec{k})\rangle,\end{aligned} \tag{7.3.4}$$

with $\nu_e = \cos\theta\,\nu_1 + \sin\theta\,\nu_2$. Since $\big|\Psi_D(t)\rangle^{(1)}$ creates one daughter particle and the initial state has none, it is clear that to lowest order, the number of daughter particles is

$$n_D(\vec{Q},t) = {}^{(1)}\langle\Psi_D(t)\big|a_D^\dagger(\vec{Q})a_D(\vec{Q})\big|\Psi_D(t)\rangle^{(1)}\,. \tag{7.3.5}$$

The calculation of the parent population is slightly more involved. The first order state has contributions from Fock states with zero or two parent particles M, however the state with two parent particles does not conserve energy and its phase varies very rapidly in time and averages out in short time scales of order of the inverse mass of the parent particle. Therefore to obtain a non-vanishing contribution to the parent population we must consider the second order state (7.3.4).

To second order, there are several contributions, but the only one that is relevant is the process in which the first vertex at $(\vec{x_2},t_2)$ annihilates the initial M creating the intermediate state with one (D,ν_e) entangled pair, while the second interaction vertex at $(\vec{x}_1,t_1)$ *annihilates* this (D,ν_e) pair in the intermediate state and creates the M, which has non-vanishing overlap with $\big|M\rangle$. This process is depicted in Figure 39 and is recognized as the self-energy of the parent particle.

Thus to lowest order in g,

$$N_M(t) = 1 + 2\,\mathrm{Re}\Big[\langle M\big|\Psi_D(t)\rangle^{(2)}\Big]. \tag{7.3.6}$$

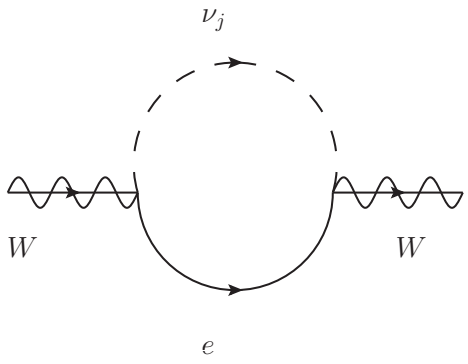

Figure 39: Self-energy of the parent particle M, the neutrino line corresponds to a propagator of a mass eigenstate.

7.3.1 Number Density of Daughter Particles

As pointed out previously, for the number density of daughter particles, we only need to consider the interaction Lagrangian up to the first order, namely, Eq. (7.3.3). Expanding the field ν_e in terms of the fields that create or annihilate the mass eigenstates ν_1 and ν_2, and carrying out a standard quantum field theory calculation, we obtain

$$\begin{aligned}
\big|\Psi_D(t)\big\rangle^{(1)} \;\simeq\; & \frac{g}{\sqrt{8VE^M_{\vec{k}}E^D_{\vec{q}}}} \\
& \sum_{\vec{q}}\left\{\frac{\sin\theta}{\sqrt{\Omega_{2,\vec{p}}}}e^{(E^M_{\vec{k}}-E^D_{\vec{q}}-\Omega_{2,\vec{p}})\frac{t}{2}}\big|\nu_{2,\vec{p}},D_{\vec{q}}\big\rangle\left[\frac{\sin\left((E^M_{\vec{k}}-E^D_{\vec{q}}-\Omega_{2,\vec{p}})\frac{t}{2}\right)}{(E^M_{\vec{k}}-E^D_{\vec{q}}-\Omega_{2,\vec{p}})/2}\right]\right. \\
& \left.+\frac{\cos\theta}{\sqrt{\Omega_{1,\vec{p}}}}e^{i(E^M_{\vec{k}}-E^D_{\vec{q}}-\Omega_{1,\vec{p}})\frac{t}{2}}\big|\nu_{1,\vec{p}},D_{\vec{q}}\big\rangle\left[\frac{\sin\left((E^M_{\vec{k}}-E^D_{\vec{q}}-\Omega_{1,\vec{p}})\frac{t}{2}\right)}{(E^M_{\vec{k}}-E^D_{\vec{q}}-\Omega_{1,\vec{p}})/2}\right]\right\},
\end{aligned} \tag{7.3.7}$$

in which the daughter particle and the neutrinos are *entangled* [286]. Momentum conservation, a consequence of translational invariance manifest in the Lagrangian density (7.2.1), enforces $\vec{p}+\vec{q}=\vec{0}$, where $\vec{p}$ and $\vec{q}$ label the momenta of the neutrinos and the daughter particle. Also, $E^M_{\vec{k}}$ and $E^D_{\vec{q}}$ are the energies of the parent and daughter particles with momentum

$\vec{k}$ and $\vec{q}$, respectively. $\Omega_{1,\vec{p}}$ and $\Omega_{2,\vec{p}}$ are the energies of the neutrino mass eigenstates with momentum $\vec{p}$. In other words,

$$E^M_{\vec{k}} = \sqrt{k^2 + m^2_M}, \quad E^D_{\vec{q}} = \sqrt{q^2 + m^2_D}, \quad \Omega_{1,\vec{p}} = \sqrt{p^2 + m^2_1}, \quad \Omega_{2,\vec{p}} = \sqrt{p^2 + m^2_2}. \tag{7.3.8}$$

In order to manifestly study the time evolution of the populations and possible time dependent phenomena resulting from the mixing of mass eigenstates, we keep the finite time-dependence explicitly. As is familiar from Fermi's Golden rule, taking t to infinity results in replacing

$$\left.\frac{\sin\left((E^M_{\vec{k}} - E^D_{\vec{q}} - \Omega_{i,\vec{p}})\frac{t}{2}\right)}{(E^M_{\vec{k}} - E^D_{\vec{q}} - \Omega_{i,\vec{p}})/2}\right|_{t\to\infty} \simeq \pi\delta(E^M_{\vec{k}} - E^D_{\vec{q}} - \Omega_{i,\vec{p}}), \tag{7.3.9}$$

which leads to the standard S-matrix result with the energy conservation at each vertex. Here $i = 1, 2$ stand for the neutrino mass eigenstates.

It is straightforward to calculate (7.3.5) with the state (7.3.7). We find

$$n_D(\vec{Q}, t) = \frac{g^2}{8V\, E^M_{\vec{k}} E^D_{\vec{Q}}}\left[\frac{\cos^2\theta}{\Omega_1}\frac{\sin^2\left[(E^M_{\vec{k}} - E^D_{\vec{Q}} - \Omega_1)\frac{t}{2}\right]}{(E^M_{\vec{k}} - E^D_{\vec{Q}} - \Omega_1)^2/4} + \frac{\sin^2\theta}{\Omega_2}\frac{\sin^2\left[(E^M_{\vec{k}} - E^D_{\vec{Q}} - \Omega_2)\frac{t}{2}\right]}{(E^M_{\vec{k}} - E^D_{\vec{Q}} - \Omega_2)^2/4}\right], \tag{7.3.10}$$

where $\Omega_{1,2} = \sqrt{|\vec{k} - \vec{Q}|^2 + m^2_{1,2}}$, corresponding to the specific momentum $\vec{Q}$ of the daughter particle. The result (7.3.10) is a consequence of the orthogonality of the Fock states associated with the mass eigenstates. The production rate of the daughter particle is given by

$$\frac{dn_D(\vec{Q}, t)}{dt} = \frac{g^2}{8V\, E^M_{\vec{k}} E^D_{\vec{Q}}}\left[\frac{\cos^2\theta}{\Omega_1}\frac{2\sin\left[(E^M_{\vec{k}} - E^D_{\vec{Q}} - \Omega_1)t\right]}{(E^M_{\vec{k}} - E^D_{\vec{Q}} - \Omega_1)} + \frac{\sin^2\theta}{\Omega_2}\frac{2\sin\left[(E^M_{\vec{k}} - E^D_{\vec{Q}} - \Omega_2)t\right]}{(E^M_{\vec{k}} - E^D_{\vec{Q}} - \Omega_2)}\right]. \tag{7.3.11}$$

The time scale of the GSI experiment is about $10 - 100$ seconds, corresponding to an energy uncertainty $\Delta E \sim \hbar/t \simeq 10^{-16} - 10^{-17} eV$. Therefore, we can safely take the long time limit (7.3.9), leading to the a constant production rate of daughter particles, and the total number of daughter particles produced as a function of time is given by

$$n_D(t) = \sum_{\vec{Q}} n_D(\vec{Q}, t) = \left[\Gamma_1\, \cos^2\theta + \Gamma_2\, \sin^2\theta\right] t, \tag{7.3.12}$$

where

$$\Gamma_{1,2} = \frac{2\pi\, g^2}{8E^M_{\vec{k}}} \int \frac{d^3\vec{Q}}{(2\pi)^3\, E^D_{\vec{Q}}\, \Omega_{1,2}} \delta\big(E^M_{\vec{k}} - E^D_{\vec{Q}} - \Omega_{1,2}\big). \tag{7.3.13}$$

$\Gamma_{1,2}$ are the partial widths, while $\cos^2\theta$ and $\sin^2\theta$ are the probabilities (or branching ratios) associated with each neutrino mass eigenstate.

From the rate (7.3.11), we see that there is no interference between the mass eigenstates. This is a *consequence of the orthogonality of the Fock states associated with mass eigenstates.* The parent particle decays through two channels, either $|\nu_1\rangle$ or $|\nu_2\rangle$ with probabilities $\cos^2\theta$ and $\sin^2\theta$ respectively, without interference between them. Obviously when the masses of the neutrino vanish the result reduces to the "standard model" decay rate, since $\Gamma_1 = \Gamma_2$. This argument becomes clearer upon considering the process of disentanglement of the state (7.3.3). The entangled state is disentangled by the measurement resulting in the "collapsed" state [286]

$$\begin{aligned} |\mathcal{V}_D(\vec{Q},t)\rangle \;=\; & \frac{g}{\sqrt{8V E^M_{\vec{k}} E^D_{\vec{Q}}}} \left\{ \frac{\sin\theta}{\sqrt{\Omega_2}} e^{(E^M_{\vec{k}} - E^D_{\vec{Q}} - \Omega_2)\frac{t}{2}} |\nu_{2,\vec{P}}\rangle \left[\frac{\sin\left((E^M_{\vec{k}} - E^D_{\vec{Q}} - \Omega_2)\frac{t}{2}\right)}{(E^M_{\vec{k}} - E^D_{\vec{Q}} - \Omega_2)/2} \right] \right. \\ & \left. + \frac{\cos\theta}{\sqrt{\Omega_1}} e^{i(E^M_{\vec{k}} - E^D_{\vec{Q}} - \Omega_1)\frac{t}{2}} |\nu_{1,\vec{P}}\rangle \left[\frac{\sin\left((E^M_{\vec{k}} - E^D_{\vec{Q}} - \Omega_1)\frac{t}{2}\right)}{(E^M_{\vec{k}} - E^D_{\vec{Q}} - \Omega_1)/2} \right] \right\}, \end{aligned} \tag{7.3.14}$$

where $\vec{P} = \vec{k} - \vec{Q}$. It is straightforward to confirm that

$$n_D(t) = \sum_{\vec{Q}} \langle \mathcal{V}_D(\vec{Q},t) \big| \mathcal{V}_D(\vec{Q},t)\rangle\,. \tag{7.3.15}$$

Because $|\nu_{1,\vec{P}}\rangle$ and $|\nu_{2,\vec{P}}\rangle$ are orthogonal with each other, there is no interference between these two mass eigenstates.

We can further confirm our previous result of the number density of daughter particles from the density matrix. The entangled state $\left|\Psi_D(t)\right\rangle^{(1)}$ is produced from the decay of a parent particle, correspondingly the density matrix describing this entangled state is

$$\begin{aligned}
\hat{\rho}(t) &= \left|\Psi_D(t)\right\rangle^{(1)(1)}\left\langle\Psi_D(t)\right| \\
&= \frac{g^2}{8VE^M_{\vec{k}}}\sum_{\vec{q}}\frac{1}{E^D_{\vec{q}}}\Bigg\{\frac{\sin^2\theta}{\Omega_{2,\vec{p}}}\left|D_{\vec{q}},\nu_{2,\vec{p}}\right\rangle\left\langle D_{\vec{q}},\nu_{2,\vec{p}}\right|\left[\frac{\sin\left(\left(E^M_{\vec{k}}-E^D_{\vec{q}}-\Omega_{2,\vec{p}}\right)\frac{t}{2}\right)}{\left(E^M_{\vec{k}}-E^D_{\vec{q}}-\Omega_{2,\vec{p}}\right)/2}\right]^2 \\
&\quad+\frac{\cos^2\theta}{\Omega_{1,\vec{p}}}\left|D_{\vec{q}},\nu_{1,\vec{p}}\right\rangle\left\langle D_{\vec{q}},\nu_{1,\vec{p}}\right|\left[\frac{\sin\left(\left(E^M_{\vec{k}}-E^D_{\vec{q}}-\Omega_{1,\vec{p}}\right)\frac{t}{2}\right)}{\left(E^M_{\vec{k}}-E^D_{\vec{q}}-\Omega_{1,\vec{p}}\right)/2}\right]^2 \\
&\quad+\frac{\sin 2\theta}{2\sqrt{\Omega_{2,\vec{p}}\,\Omega_{1,\vec{p}}}}\left[\frac{\sin\left(\left(E^M_{\vec{k}}-E^D_{\vec{q}}-\Omega_{2,\vec{p}}\right)\frac{t}{2}\right)}{\left(E^M_{\vec{k}}-E^D_{\vec{q}}-\Omega_{2,\vec{p}}\right)/2}\right]\left[\frac{\sin\left(\left(E^M_{\vec{k}}-E^D_{\vec{q}}-\Omega_{1,\vec{p}}\right)\frac{t}{2}\right)}{\left(E^M_{\vec{k}}-E^D_{\vec{q}}-\Omega_{1,\vec{p}}\right)/2}\right] \\
&\quad\times\left[e^{-i\frac{\delta m^2}{4\bar{\Omega}}t}\left|D_{\vec{q}},\nu_{2,\vec{p}}\right\rangle\left\langle D_{\vec{q}},\nu_{1,\vec{p}}\right|+e^{i\frac{\delta m^2}{4\bar{\Omega}}t}\left|D_{\vec{q}},\nu_{1,\vec{p}}\right\rangle\left\langle D_{\vec{q}},\nu_{2,\vec{p}}\right|\right]\Bigg\},
\end{aligned} \tag{7.3.16}$$

where $\delta m^2 = m_2^2 - m_1^2$, and $\bar{\Omega} = \sqrt{p^2 + (m_2^2+m_1^2)/2}$ is the average energy. The density matrix contains both diagonal terms, which describe the time evolution of the populations, and off-diagonal terms, which display the interference between the two neutrino massive eigenstates [286]. In the GSI experiment, these neutrinos are not measured, therefore, to calculate the number density of daughter particles, we trace out the neutrino states, namely

$$n_D(t) = \mathrm{Tr}\left[\hat{\rho}(t)\sum_{\vec{Q}} a^\dagger_D(\vec{Q})a_D(\vec{Q})\right]. \tag{7.3.17}$$

Only diagonal terms contribute to the trace. Therefore, the number density of daughter particles has nothing to do with the interference between neutrino mass eigenstates, which is manifest in the off diagonal density matrix elements (coherence). This is consistent with the arguments in [188] stating that the GSI experiment must be described by an incoherent sum over different neutrino states. Once again, the answer is Eq. (7.3.11) in the long time limit.

7.3.2 Number Density of Parent Particles

Now, let us consider the number density of the parent particles, which follows the same line of argument. It proves more convenient to calculate $dN_M(\vec{k},t)/dt$, for which we find[1]

$$\frac{dN_M(\vec{k},t)}{dt} = -\frac{g^2}{4E^M_{\vec{k}}}\int\frac{d^3\vec{Q}}{(2\pi)^3\,E^D_{\vec{Q}}} \left\{\frac{\cos^2\theta}{\Omega_1}\,\frac{\sin\Big[\big(E^M_{\vec{k}}-E^D_{\vec{Q}}-\Omega_1\big)t\Big]}{\big(E^M_{\vec{k}}-E^D_{\vec{Q}}-\Omega_1\big)} + \frac{\sin^2\theta}{\Omega_2}\,\frac{\sin\Big[\big(E^M_{\vec{k}}-E^D_{\vec{Q}}-\Omega_2\big)t\Big]}{\big(E^M_{\vec{k}}-E^D_{\vec{Q}}-\Omega_2\big)}\right\}. \tag{7.3.18}$$

In the long time limit this becomes

$$\frac{dN_M(\vec{k},t)}{dt} = -\Big[\Gamma_1\,\cos^2\theta + \Gamma_2\,\sin^2\theta\Big]. \tag{7.3.19}$$

Clearly, $dN_M(\vec{k},t)/dt = -dn_D(t)/dt$ as the decay of the parent population results in the growth of the daughter population with the same rate. This is a consequence of unitarity and we can see this by substituting (7.3.15) and (7.3.6) into the unitarity condition

$$1 = \langle M(\vec{k})\big|U^\dagger(t,0)U(t,0)\big|M(\vec{k})\rangle = 1 + {}^{(1)}\langle\Psi_D(t)\big|\Psi_D(t)\rangle^{(1)} + 2\,\mathrm{Re}\Big[\langle M\big|\Psi_D(t)\rangle^{(2)}\rangle\Big] + \mathcal{O}(g^3) \tag{7.3.20}$$

Although we have used plane waves to describe our parent and daughter particles, our main result, the lack of interference of mass eigenstates in the final state, is a direct consequence of the orthogonality of the mass eigenstates, and this generalizes straightforwardly to the case of wave packets. In particular, according to Refs. [174, 175, 173], the wave-packet aspect of the parent and daughter nuclei is emphasized as an important ingredient to allow the neutrino mixing. It is straightforward to show that a wave-packet is a superposition of plane wave components, namely,

$$|\Psi(\vec{X}_0,\vec{P}_0;\vec{x},t=0)\rangle = \int d^3p\, f(\vec{x},\vec{X}_0;\vec{p},\vec{P}_0)\,e^{i\vec{p}\cdot\vec{x}}|\vec{p}\rangle \tag{7.3.21}$$

at an initial time $t=0$. Here, $\vec{X}_0$, $\vec{P}_0$ are the center position and momentum of wave packet, respectively, while $\vec{x}$, $\vec{p}$ and E_p are the position, momentum and energy, respectively. The

[1] Effectively, we are obtaining the Boltzmann equation for the parent particle, neglecting the build-up of the population.

function $f(\vec{x}, \vec{X}_0; \vec{p}, \vec{P}_0)$ specifies the wave function of the particle. In our calculation, we obtain the time evolution of each plane wave component $|\vec{p}\rangle$, from which it follows that,

$$n_\Psi(t) = \int d^3p \left| f(\vec{x}, \vec{X}_0; \vec{p}, \vec{P}_0) \right|^2 \; n_\Psi(\vec{p}, t), \tag{7.3.22}$$

where $n_\Psi(\vec{p}, t)$ is the parent or daughter population for plane waves obtained above. The distribution function f just weights each plane wave component. As demonstrated by our calculation in section 7.3, the populations $n_\Psi(\vec{p}, t)$ do not feature oscillations because of the orthogonality of the mass eigenstates. Therefore, interference between different neutrino mass eigenstates does not appear either in wave packet treatment, as shown in (7.3.22). Again, this is a consequence of the orthogonality of neutrino mass eigenstates. Obviously, this conclusion is independent of whether the parent or daughter particles are described by plane waves or wave packets.

A complementary pathway to the same conclusion is provided by the interpretation of (7.3.19) in terms of the Feynman diagram depicted in Figure 39. This also manifestly leads to the conclusion of lack of interference between mass eigenstates because the decay rate of the parent particle is the imaginary part of the self-energy. Since the correct propagating degrees of freedom are the neutrino mass eigenstates, the total self energy is the sum of self-energies with the neutrino mass eigenstates in the intermediate state. As a result, the usual Cutkosky rules indicate that the total decay width is the sum of the partial decay widths into the mass eigenstates without interference. The real time calculations of the decay and production rates presented above confirm this result directly from the evolution of the parent and daughter populations.

Therefore, we confirm the analysis of Refs. [146, 145, 188, 86, 235] that there is no interference of mass eigenstates and we conclude that the GSI anomaly cannot be explained in terms of the interference of mass eigenstates in the decay.

7.4 CONCLUSION AND DISCUSSIONS

In this chapter, we re-examine the GSI anomaly within a framework that is different from and complementary to previous work of various groups [174, 175, 173, 122, 204, 146, 145, 188, 86, 235]. The controversy in the literature on the theoretical analysis of the GSI anomaly mainly focuses on whether probabilities must be summed incoherently [146, 145, 188, 86, 235] or amplitudes must be summed coherently [174, 175, 173, 122, 204]. We offer a completely different alternative to study this phenomenon: we obtain directly the time evolution of the population of parent and daughter particles taking into account that the quantum state arising from the decay of the parent particle is an entangled state of the neutrino mass eigenstates and the daughter particle. Our method bypasses the issue of summing amplitudes or probabilities and exhibits directly the time evolution of the parent and daughter populations.

Recognizing that if the time modulation of the parent and daughter populations is a result of interference phenomena between neutrino mass eigenstates, hence a fairly robust consequence is independent of the complexities of the parent and daughter nuclei, we introduce a simple bosonic model that captures reliably the relevant charged current interaction process for EC and manifestly includes neutrino mixing. This allows us to extract the relevant aspects without the peripheral complications associated with spinors, nuclear wave-functions, etc. We generalize our previous work [286] to analyze the GSI anomaly by studying the evolution of the distribution functions of the parent and daughter particles directly in time. Our starting point is the time evolution of the daughter-neutrino entangled state produced by the decay of the parent particle. This treatment also allows us to study the dynamics of the daughter particle from the density matrix upon tracing the unobserved neutrino degrees of freedom. We show that both the decay rate of the parent particle and the production rate of the daughter particle *do not feature* oscillations arising from the interference of mass eigenstates in the final state. This is a direct consequence of the orthogonality of the mass eigenstates.

Furthermore, we provide an alternative field theoretical explanation in terms of the

imaginary part of the self-energy diagram of the parent particle. The propagator of the intermediate neutrino states is that of mass eigenstates, therefore Cutkosky rules immediately lead to the conclusion that the decay rate is an incoherent sum of probabilities of decay into each different mass eigenstate (channels), complementing and confirming our previous analysis. Simple arguments based on superposition clearly show that a wave packet treatment of parent and daughter particles yields the same result, namely no time modulation since there is no interference between mass eigenstates in the final state, again a direct consequence of orthogonality of mass eigenstates. Our work confirms the result of Refs. [146, 145, 188, 86, 235] that if the GSI anomaly is a real effect, it cannot be explained from the interference of neutrino mass eigenstates.

More recently, independent experimental efforts have addressed the GSI anomaly: in Ref. [123] the EC decay of ^{180}Re is studied and no modulation of the decay rate is observed. However, this experiment is different from the one at GSI not only because of the very short-lived initial state, but also more importantly because the daughter particle moves in a lattice and is restricted to transfer crystal momentum to phonons. Another EC-decay experiment with ^{142}Pm and an earlier EC-decay experiment with ^{142}Eu re-analyzed by Vetter *et.al.* [270] did not observe the modulation in the rates reported by the GSI experiment.

In summary, we conclude that our work supports the conclusion against an explanation of the GSI anomaly as a consequence of neutrino mixing in agreement with previous work [146, 145, 188, 86, 235]. These theoretical results, combined with emerging independent experimental evidence seem to suggest that even if the GSI time modulation anomaly is a real phenomenon, its cause is probably associated with the details of the GSI experiment or perhaps internal nuclear degrees of freedom of the parent particle in such an experiment, but not a consequence of neutrino mixing.

8.0 CONCLUSION OF THE THESIS

Finally, in this last chapter, we briefly summarize all the work we have done in this thesis and highlight our main results.

8.1 STERILE NEUTRINO PRODUCED AT THE ELECTROWEAK SCALE

To study the properties of keV sterile neutrinos as a WDM candidate, we first study their production in the early universe at a temperature regime near the electroweak scale. By introducing a Lagrangian beyond the SM, sterile neutrinos can be produced by the decays of the Higgs-like scalar beyond the SM and of the charged and neutral vector bosons of the SM. By applying the non-equilibrium finite temperature field theory, we obtain an effective Dirac-equation for both active and sterile neutrinos, which contains the self-energies corrections in the medium. The real part of the self-energy determines the dispersion relations and mixing angles between active and sterile neutrinos in the medium, and the imaginary part determines the production rates. We analyze and compare the contributions from both decay channels to the mixing angles, dispersion relations and production rates, thereby facilitating the analysis of different situations.

Most interestingly, we discovery two narrow MSW resonances. One of them is the usual MSW resonance driven by a small lepton asymmetry in the neutrino sector; however, the other one is a new type of MSW resonance in the absence of a lepton asymmetry, and it happens in the temperature regime $T \gtrsim M_W$ for $k/T \lesssim 1$. We find that the difference in the

propagating frequencies vanishes exactly at the position of the resonance, with a concomitant breakdown of the adiabaticity. We obtain simple expressions for the production rates of active and sterile neutrinos that are valid in a wide range of temperatures and clearly displays the contribution from SM and BSM interactions.

Finally, we apply our results and observations to an expanding universe. Because of the MSW resonances, we expect a highly non-thermal distribution function for sterile neutrinos with an enhancement at the low momentum region $k < T$ both. Therefore, sterile neutrinos should feature a smaller free streaming length and larger power spectrum at small scales as compared to the DW mechanism [113, 61].

8.2 LINEAR STRUCTURE GROWTH IN THE WDM SCENARIO

Then, we follow the previous chapter by a semi-analytical study on the linear structure growth of WDM candidates in a radiation-matter cosmology for arbitrary distribution function and mass around keV scale. We divide the time evolution of density perturbations of WDM particles into three stages and solve the corresponding collision-less Boltzmann equation individually. Stages I) and II) describe the time evolution of density fluctuations during the RD era when the particles are relativistic and non-relativistic respectively, and stage III refers to the time evolution of the density fluctuations of non-relativistic WDM particles in the MD era. We connect these piece-wise solutions smoothly and obtain the transfer function and the power spectrum of WDM particles under the Born approximation. Unlike the CDM situation where the transfer function only depends on k_{eq} (the wave vector at matter-radiation equality), we find the transfer function of WDM is also characterized by the free-streaming wave vector k_{fs}, which is inversely proportional to the distance traveled by the WDM particles from matter-radiation equality to today. Moreover, we find that $1/k_{fs}$ also of the same order as the size of the comoving horizon when the WDM particles become non-relativistic.

In stages I), the acoustic oscillations in the gravitational potential leads to an ISW effect that amplifies WDM density perturbations, on scales larger than $1/k_{fs}$. This amplification translates in a prolonged plateau in the transfer function for perturbation scales larger than $1/k_{fs}$. Moreover, we discover an WDM acoustic oscillation from the transfer function of WDM particles at small scales roughly about $k \geq 2k_{fs}$, which might suggest interesting observational signals. Also, we compare our semi-analytical transfer function and power spectrum with the results from Boltzmann codes [165, 1, 274], and reach an excellent agreement within 5% error. Finally, we discuss the quasi-degeneracy between mass, distribution function and decoupling temperature of WDM particles and comment on the caveats of the constraints on the mass of sterile neutrinos from current Lyman-α forest data.

8.3 DYNAMICS OF DISENTANGLEMENT AND COHERENCE IN NEUTRINO OSCILLATION

Since this chapter, we switch to a new research topic, where we discuss some subtle aspects of the theory of neutrino oscillations.

By observing that in neutrino oscillation experiments, neutrinos produced by a charged current vertex are entangled with the charged lepton, we propose a field theoretical model to study the dynamics of this entangled state directly as a function of time. We aim to investigate the influence of this dynamics on the neutrino oscillation formulas. To simplify our calculation, we assume that all the particles are described by plane waves in this study. We evolve the entangled state until the charged lepton is measured at t_S, yielding a disentangled neutrino state. This disentangled neutrino state is evolved further and eventually gets measured at the far detector at t_D. By carrying out this two-time measurement calculation, we obtain the transition amplitude and probability for neutrino oscillation phenomena.

We find that the transition amplitude depends on both time scales t_S and t_D, and it is in general different from the standard formulas of neutrino oscillations. However, under the

long time limit, the transition rate of long baseline neutrino oscillations, defined as the time derivative of the transition probability, factorizes in terms of the usual quantum mechanical probability.

Moreover, our result suggests that there could arise interesting corrections in the case of short baseline experiments such as MiniBooNE and/or LSND, wherein t_S and t_D are both of the same order as the oscillation scale. In this case, the dynamics of dis-entanglement may introduce extra modulation with energy. Such possibility could be relevant in the interpretation and analysis of data.

8.4 IS THE GSI ANOMALY DUE TO NEUTRINO OSCILLATIONS?

Finally, as an application of our plane wave calculations, we consider the GSI anomaly, investigating the interpretation of GSI anomaly as a result of neutrino oscillations. Following the method developed in the previous study, we obtain the time evolution of the population of parent and daughter particles directly in real time, considering explicitly the quantum entanglement between the daughter particle and neutrino mass eigenstates in the two-body decay. We confirm that the decay rate of the parent particle and the growth rate of the daughter particle do *not* feature a time modulation from interference of neutrino mass eigenstates. The lack of interference is a consequence of the orthogonality of the mass eigenstates. This result also follows from the density matrix obtained by tracing out the unobserved neutrino states. We confirm this result by providing a complementary explanation based on Cutkosky rules applied to the Feynman diagram of the self-energy of the parent particle.

APPENDIX A

APPENDIX FOR STERILE NEUTRINO PRODUCTION

A.1 STANDARD MODEL (SM) VECTOR BOSON EXCHANGE

The SM self-energy contributions with the exchange of a vector boson are given by the spectral representation (3.2.5) with the imaginary part given by Eq. (3.2.14) of the form

$$Im\Sigma_{sm}(\omega,\vec{k}) = \frac{\pi g_{sm}^2}{4}\int \frac{d^3p}{(2\pi)^3\, p\, W_{\vec{p}+\vec{k}}}\Big[\gamma^0\,\Pi^0_{sm}(\omega,\vec{p},\vec{k}) - \vec{\gamma}\cdot\hat{k}\,\Pi^1_{sm}(\omega,\vec{p},\vec{k})\Big]\,. \tag{A.1.1}$$

Neglecting the mass of the neutrinos and charged leptons we find

$$\begin{aligned}
&\Pi^0_{sm}(\omega,\ \vec{p},\ \vec{k}) \\
=\ &\Big[1-n_F(p)+N_B(W_{\vec{p}+\vec{k}})\Big]\Big[p\big(1+\frac{2W^2_{\vec{p}+\vec{k}}}{M^2}\big)+\frac{2W_{\vec{p}+\vec{k}}}{M^2}\big(p^2+\vec{k}\cdot\vec{p}\big)\Big]\ \delta\big(\omega-p-W_{\vec{p}+\vec{k}}\big) \\
&+\Big[1-\overline{n}_F(p)+N_B(W_{\vec{p}+\vec{k}})\Big]\Big[p\Big(1+\frac{2W^2_{\vec{p}+\vec{k}}}{M^2}\Big)+\frac{2W_{\vec{p}+\vec{k}}}{M^2}\Big(p^2+\vec{k}\cdot\vec{p}\Big)\Big]\ \delta\Big(\omega+p+W_{\vec{p}+\vec{k}}\Big) \\
&+\Big[n_F(p)+N_B(W_{\vec{p}+\vec{k}})\Big]\Big[p\Big(1+\frac{2W^2_{\vec{p}+\vec{k}}}{M^2}\Big)-\frac{2W_{\vec{p}+\vec{k}}}{M^2}\Big(p^2+\vec{k}\cdot\vec{p}\Big)\Big]\ \delta\Big(\omega-p+W_{\vec{p}+\vec{k}}\Big) \\
&+\Big[\overline{n}_F(p)+N_B(W_{\vec{p}+\vec{k}})\Big]\Big[p\Big(1+\frac{2W^2_{\vec{p}+\vec{k}}}{M^2}\Big)-\frac{2W_{\vec{p}+\vec{k}}}{M^2}\Big(p^2+\vec{k}\cdot\vec{p}\Big)\Big]\ \delta\Big(\omega+p-W_{\vec{p}+\vec{k}}\Big)
\end{aligned} \tag{A.1.2}$$

and

$$
\begin{aligned}
&\Pi^1_{sm}(\omega,\vec{p},\vec{k}) \\
= \;& \Big[1-n_F(p)+N_B(W_{\vec{p}+\vec{k}})\Big]\Big[-\hat{k}\cdot\vec{p}+\frac{2\Big(k+\hat{k}\cdot\vec{p}\Big)}{M^2}\Big(p\,W_{\vec{p}+\vec{k}}+p^2+\vec{k}\cdot\vec{p}\Big)\Big]\;\delta\big(\omega-p-W_{\vec{p}+\vec{k}}\big) \\
& -\Big[1-\overline{n}_F(p)+N_B(W_{\vec{p}+\vec{k}})\Big]\Big[-\hat{k}\cdot\vec{p}+\frac{2\Big(k+\hat{k}\cdot\vec{p}\Big)}{M^2}\Big(p\,W_{\vec{p}+\vec{k}}+p^2+\vec{k}\cdot\vec{p}\Big)\Big]\;\delta\big(\omega+p+W_{\vec{p}+\vec{k}}\big) \\
& +\Big[n_F(p)+N_B(W_{\vec{p}+\vec{k}})\Big]\Big[-\hat{k}\cdot\vec{p}+\frac{2\Big(k+\hat{k}\cdot\vec{p}\Big)}{M^2}\Big(-p\,W_{\vec{p}+\vec{k}}+p^2+\vec{k}\cdot\vec{p}\Big)\Big]\;\delta\big(\omega-p+W_{\vec{p}+\vec{k}}\big) \\
& -\Big[\overline{n}_F(p)+N_B(W_{\vec{p}+\vec{k}})\Big]\Big[-\hat{k}\cdot\vec{p}+\frac{2\Big(k+\hat{k}\cdot\vec{p}\Big)}{M^2}\Big(-p\,W_{\vec{p}+\vec{k}}+p^2+\vec{k}\cdot\vec{p}\Big)\Big]\;\delta\big(\omega+p-W_{\vec{p}+\vec{k}}\big)\;. \qquad \text{(A.1.3)}
\end{aligned}
$$

A.2 BEYOND STANDARD MODEL (BSM) SCALAR EXCHANGE

For scalar boson exchange, we find

$$
\mathrm{Im}\Sigma_{bsm}(\omega,\vec{k})=\frac{\pi Y^2}{4}\int\frac{d^3p}{(2\pi)^3\,W_{\vec{p}+\vec{k}}}\Big[\gamma^0\,\Pi^0_{bsm}(\omega,\vec{p},\vec{k})-\vec{\gamma}\cdot\hat{k}\;\Big(\hat{k}\cdot\hat{p}\Big)\;\Pi^1_{bsm}(\omega,\vec{p},\vec{k})\Big]\;, \quad \text{(A.2.1)}
$$

where

$$
\begin{aligned}
\Pi^0_{bsm}(\omega,\vec{p},\vec{k}) \;=\;& \Big[1-n_F(p)+N_B(W_{\vec{p}+\vec{k}})\Big]\;\delta\big(\omega-p-W_{\vec{p}+\vec{k}}\big) \\
& +\Big[1-\overline{n}_F(p)+N_B(W_{\vec{p}+\vec{k}})\Big]\;\delta\Big(\omega+p+W_{\vec{p}+\vec{k}}\Big) \\
& +\Big[n_F(p)+N_B(W_{\vec{p}+\vec{k}})\Big]\;\delta\big(\omega-p+W_{\vec{p}+\vec{k}}\big) \\
& +\Big[\overline{n}_F(p)+N_B(W_{\vec{p}+\vec{k}})\Big]\;\delta\big(\omega+p-W_{\vec{p}+\vec{k}}\big)\;, \qquad \text{(A.2.2)}
\end{aligned}
$$

$$
\begin{aligned}
\Pi^1_{bsm}(\omega,\vec{p},\vec{k}) \;=\;& \Big[1-n_F(p)+N_B(W_{\vec{p}+\vec{k}})\Big]\;\delta\big(\omega-p-W_{\vec{p}+\vec{k}}\big) \\
& -\Big[1-\overline{n}_F(p)+N_B(W_{\vec{p}+\vec{k}})\Big]\;\delta\Big(\omega+p+W_{\vec{p}+\vec{k}}\Big) \\
& +\Big[n_F(p)+N_B(W_{\vec{p}+\vec{k}})\Big]\;\delta\big(\omega-p+W_{\vec{p}+\vec{k}}\big) \\
& -\Big[\overline{n}_F(p)+N_B(W_{\vec{p}+\vec{k}})\Big]\;\delta\big(\omega+p-W_{\vec{p}+\vec{k}}\big)\;. \qquad \text{(A.2.3)}
\end{aligned}
$$

APPENDIX B

NUMERICAL MANIPULATION OF $I_1(K,U)$

According to the definition of the inhomogeneous source term $I_1(k,u)$ in Eq. (4.6.8), we have

$$I_1(k,u) = -\frac{8k^2}{\alpha k_{eq}^2}\int_{u_{NR}}^{u_{eq}} du'\tilde{a}^2(k,u')\phi_r(k,u')\int dyy\tilde{f}_0(y)\sin\left[\alpha y(u-u')\right]. \quad \text{(B.0.1)}$$

Recall the gravitational potential ϕ_r in the RD era, which gives

$$\phi_r(k,u) = -3\phi_i\,\frac{x\cos x-\sin x}{x^3} = -\frac{3\phi_i}{x}\frac{d}{dx}\left(\frac{\sin x}{x}\right), \quad \text{(B.0.2)}$$

where $x = k\eta/\sqrt{3}$ as defined before. By rewriting I_1 in terms of x, we can integrate by parts and optimize the integrand of $I_1(k,u)$ for numerical computation. Making use of Eqs.(4.1.8) and (4.4.6), we find

$$u = \frac{1}{2}\ln\left(\frac{\frac{x}{2x_*}}{2+\frac{x}{2x_*}}\right), \quad \text{(B.0.3)}$$

$$du = \frac{dx}{2x(1+\frac{x}{4x_*})}, \quad \text{(B.0.4)}$$

where $x_* = k\eta_*/\sqrt{3}$. In terms of x, the integral $I_1(k,u)$ becomes

$$I_1(k,u) = (-3\phi_i)\left(-\frac{6}{\alpha}\right)\int dyy\tilde{f}_0(y)\int_{x_{NR}}^{x_{eq}} dx'\left[\frac{d}{dx'}\left(\frac{\sin x'}{x'}\right)\right]\left(1+\frac{x'}{4x_*}\right)\sin\left[\alpha yh(x')\right], \quad \text{(B.0.5)}$$

where $h(x') = u + \frac{1}{2}\ln(1+\frac{4x_*}{x'})$. Integrating by parts over x', we find

$$\begin{aligned} I_1(k,u) &= (-3\phi_i)\left(-\frac{6}{\alpha}\right)\int dyy\tilde{f}_0(y) \\ &\left\{ \left(1+\frac{x'}{4x_*}\right)\frac{\sin x'}{x'}\sin\left[\alpha y h(x')\right]\Big|_{x_{NR}}^{x_{eq}} \right. \\ &\left. -\frac{1}{4x_*}\int_{x_{NR}}^{x_{eq}} dx'\ \frac{\sin x'}{x'}\sin\left[\alpha y h(x')\right] + \frac{\alpha y}{2}\int_{x_{NR}}^{x_{eq}} dx'\ \frac{\sin x'}{x'^2}\cos\left[\alpha y h(x')\right] \right\}. \end{aligned} \tag{B.0.6}$$

Plugging in the value of x_{NR} and x_{eq}, and note that

$$x_* = \frac{k\eta_*}{\sqrt{3}} = \sqrt{\frac{2}{3}}\frac{k}{k_{eq}} \gg 1 \tag{B.0.7}$$

for perturbation modes we are interested in. Correspondingly, $\frac{x_{NR}}{x_*} = \frac{\eta_{NR}}{\eta_*} \ll 1$ and $x_{eq} = 2(\sqrt{2}-1)x_* = 0.8294\ x_*$. We thus neglect terms proportional to $\frac{1}{x_*}$ and $\frac{x_{NR}}{x_*}$, getting

$$\begin{aligned} I_1(k,u) \simeq (-3\phi_i)\left(-\frac{6}{\alpha}\right)\int dyy\tilde{f}_0(y)\Bigg\{ & \left(1+\frac{x_{eq}}{4x_*}\right)\frac{\sin(x_{eq})}{x_{eq}}\sin\left[\alpha y\left(u+\ln(1+\frac{4x_*}{x_{eq}})\right)\right] \\ & -\frac{\sin(x_{NR})}{x_{NR}}\sin\left[\alpha y\left(u+\frac{1}{2}\ln(1+\frac{4x_*}{x_{NR}})\right)\right] \\ & +\frac{\alpha y}{2}\int_{x_{NR}}^{x_{eq}} dx'\ \frac{\sin x'}{x'^2}\cos\left[\alpha y\left(u+\frac{1}{2}\ln(1+\frac{4x_*}{x'})\right)\right]\Bigg\} \end{aligned} \tag{B.0.8}$$

Based on the above approximations, $I_1(k,u)$ becomes a one-dimensional integral except for the last term, which will be our focus. Define

$$I_{1a} = \int_{x_{NR}}^{x_{eq}} dx'\ \frac{\sin x'}{x'^2}\cos\left[\alpha y\left(u+\frac{1}{2}\ln(1+\frac{4x_*}{x'})\right)\right]. \tag{B.0.9}$$

Since $\frac{\sin x'}{x'^2}$ decays rapidly as x' increases, contributions to I_{1a} are mainly from small x'. On the other hand, however, $\frac{\sin x'}{x'^2}$ diverges as $x' \to 0$, which could be the case for large

scale perturbations that correspond to a very small x_{NR}. To avoid the potential problem in numerical evaluation, we divide I_{1a} into two pieces

$$\begin{aligned} I_{1a} &= \int_{x_{NR}}^{x_{eq}} dx' \left(\frac{\sin x'}{x'^2} - \frac{1}{x'}\right) \cos\left[\alpha y \left(u + \frac{1}{2}\ln(1 + \frac{4x_*}{x'})\right)\right] \\ &+ \int_{x_{NR}}^{x_{eq}} dx' \frac{1}{x'} \cos\left[\alpha y \left(u + \frac{1}{2}\ln(1 + \frac{4x_*}{x'})\right)\right]. \end{aligned} \tag{B.0.10}$$

The singularity has been removed from the first piece, and for the second one, it follows again that small x' contributes most to the integral. At small x', $\frac{x_*}{x'} \gg 1$, thus $\ln(1+\frac{4x_*}{x'}) \simeq \ln(\frac{4x_*}{x'})$ for small x'. Consequently, the second piece of integration is analytically doable, which gives

$$\begin{aligned} I_{1a} &= \int_{x_{NR}}^{x_{eq}} dx' \left(\frac{\sin x'}{x'^2} - \frac{1}{x'}\right) \cos\left[\alpha y \left(u + \frac{1}{2}\ln(1 + \frac{4x_*}{x'})\right)\right] \\ &+ \frac{2}{\alpha y}\left\{\sin\left[\alpha y \left(u + \frac{1}{2}\ln(\frac{4x_*}{x_{NR}})\right)\right] - \sin\left[\alpha y \left(u + \frac{1}{2}\ln(\frac{4x_*}{x_{eq}})\right)\right]\right\}. \end{aligned} \tag{B.0.11}$$

Plugging the expression of I_{1a} in (B.0.11) back to Eq. (B.0.8), we finally obtain

$$\begin{aligned} \tilde{I}_1(k,u) &= -\frac{I_1(k,u)}{3\phi_i} \\ &\simeq \left(-\frac{6}{\alpha}\right)\int dyy\tilde{f}_0(y)\Bigg\{\frac{\alpha y}{2}\int_{x_{NR}}^{x_{eq}} dx' \left(\frac{\sin x'}{x'^2} - \frac{1}{x'}\right)\cos\left[\alpha y\left(u + \frac{1}{2}\ln(1+\frac{4x_*}{x'})\right)\right] \\ &\quad + \left(1 + \frac{x_{eq}}{4x_*}\right)\frac{\sin(x_{eq})}{x_{eq}}\sin\left[\alpha y\left(u + \frac{1}{2}\ln(1+\frac{4x_*}{x_{eq}})\right)\right] \\ &\quad - \frac{\sin(x_{NR})}{x_{NR}}\sin\left[\alpha y\left(u + \frac{1}{2}\ln(1+\frac{4x_*}{x_{NR}})\right)\right] \\ &\quad + \sin\left[\alpha y\left(u + \frac{1}{2}\ln(\frac{4x_*}{x_{NR}})\right)\right] - \sin\left[\alpha y\left(u + \frac{1}{2}\ln(\frac{4x_*}{x_{eq}})\right)\right]\Bigg\} \end{aligned} \tag{B.0.12}$$

BIBLIOGRAPHY

[1] K. Abazajian. Linear cosmological structure limits on warm dark matter. *Phys. Rev.*, D73:063513, 2006.

[2] K. Abazajian. Production and evolution of perturbations of sterile neutrino dark matter. *Phys. Rev.*, D73:063506, 2006.

[3] K. Abazajian, G. M. Fuller, and M. Patel. Sterile neutrino hot, warm, and cold dark matter. *Phys. Rev.*, D64:023501, 2001.

[4] K. N. Abazajian and G. M. Fuller. Bulk QCD thermodynamics and sterile neutrino dark matter. *Phys. Rev.*, D66:023526, 2002.

[5] K. N. Abazajian, M. Markevitch, S. M. Koushiappas, and R. C. Hickox. Limits on the radiative decay of sterile neutrino dark matter from the unresolved cosmic and soft X-ray backgrounds. *Phys. Rev.*, D75:063511, 2007.

[6] J. N. Abdurashitov et al. Measurement of the solar neutrino capture rate by the Russian-American gallium solar neutrino experiment during one half of the 22-year cycle of solar activity. *J. Exp. Theor. Phys.*, 95:181–193, 2002.

[7] K. Abe et al. Indication of Electron Neutrino Appearance from an Accelerator-produced Off-axis Muon Neutrino Beam. *Phys. Rev. Lett.*, 107:041801, 2011.

[8] Abramowitz and Stegun. *Handbook of Mathematical Functions With Formulas, Graphs, and Mathematical Tables*. National Bureau of Standards, 1972.

[9] P. Adamson et al. Measurement of Neutrino Oscillations with the MINOS Detectors in the NuMI Beam. *Phys. Rev. Lett.*, 101:131802, 2008.

[10] P. Adamson et al. Search for active neutrino disappearance using neutral- current interactions in the MINOS long-baseline experiment. *Phys. Rev. Lett.*, 101:221804, 2008.

[11] A. A. Aguilar-Arevalo et al. Event Excess in the MiniBooNE Search for $\bar{\nu}_\mu \to \bar{\nu}_e$ Oscillations. *Phys. Rev. Lett.*, 105:181801, 2010.

[12] B. Aharmim et al. Electron energy spectra, fluxes, and day-night asymmetries of B-8 solar neutrinos from the 391-day salt phase SNO data set. *Phys. Rev.*, C72:055502, 2005.

[13] M. H. Ahn et al. Indications of Neutrino Oscillation in a 250 km Long- baseline Experiment. *Phys. Rev. Lett.*, 90:041801, 2003.

[14] M. H. Ahn et al. Search for electron neutrino appearance in a 250-km long- baseline experiment. *Phys. Rev. Lett.*, 93:051801, 2004.

[15] E. K. Akhmedov and J. Kopp. Neutrino oscillations: Quantum mechanics vs. quantum field theory. *JHEP*, 04:008, 2010.

[16] E. K. Akhmedov and A. Y. Smirnov. Paradoxes of neutrino oscillations. *Phys. Atom. Nucl.*, 72:1363–1381, 2009.

[17] E. K. Akhmedov and A. Y. Smirnov. Neutrino oscillations: Entanglement, energy-momentum conservation and QFT. *arXiv:1008.2077*, 2010.

[18] E. Aliu et al. Evidence for muon neutrino oscillation in an accelerator- based experiment. *Phys. Rev. Lett.*, 94:081802, 2005.

[19] W. W. M. Allison et al. Neutrino oscillation effects in Soudan-2 upward-stopping muons. *Phys. Rev.*, D72:052005, 2005.

[20] M. Altmann et al. GNO solar neutrino observations: Results for GNO I. *Phys. Lett.*, B490:16–26, 2000.

[21] M. Ambrosio et al. Matter effects in upward-going muons and sterile neutrino oscillations. *Phys. Lett.*, B517:59–66, 2001.

[22] M. Ambrosio et al. Atmospheric neutrino oscillations from upward throughgoing muon multiple scattering in MACRO. *Phys. Lett.*, B566:35–44, 2003.

[23] M. Apollonio et al. Initial Results from the CHOOZ Long Baseline Reactor Neutrino Oscillation Experiment. *Phys. Lett.*, B420:397–404, 1998.

[24] M. Apollonio et al. Limits on Neutrino Oscillations from the CHOOZ Experiment. *Phys. Lett.*, B466:415–430, 1999.

[25] M. Apollonio et al. Search for neutrino oscillations on a long base-line at the CHOOZ nuclear power station. *Eur. Phys. J.*, C27:331–374, 2003.

[26] T. Araki et al. Measurement of neutrino oscillation with KamLAND: Evidence of spectral distortion. *Phys. Rev. Lett.*, 94:081801, 2005.

[27] F. Ardellier et al. Letter of intent for double-CHOOZ: A search for the mixing angle theta(13). *arXiv:hep-ex/0405032*, 2004.

[28] F. Ardellier et al. Double Chooz: A search for the neutrino mixing angle theta(13). *arXiv:hep-ex/0606025*, 2006.

[29] T. Asaka, S. Blanchet, and M. Shaposhnikov. The nuMSM, dark matter and neutrino masses. *Phys. Lett.*, B631:151–156, 2005.

[30] T. Asaka, M. Laine, and M. Shaposhnikov. On the hadronic contribution to sterile neutrino production. *JHEP*, 06:053, 2006.

[31] T. Asaka, M. Laine, and M. Shaposhnikov. Lightest sterile neutrino abundance within the nuMSM. *JHEP*, 01:091, 2007.

[32] T. Asaka and M. Shaposhnikov. The nuMSM, dark matter and baryon asymmetry of the universe. *Phys. Lett.*, B620:17–26, 2005.

[33] T. Asaka, M. Shaposhnikov, and A. Kusenko. Opening a new window for warm dark matter. *Phys. Lett.*, B638:401–406, 2006.

[34] Y. Ashie et al. A Measurement of Atmospheric Neutrino Oscillation Parameters by Super-Kamiokande I. *Phys. Rev.*, D71:112005, 2005.

[35] C. Athanassopoulos et al. Candidate events in a search for anti-muon-neutrino $\rightarrow$ anti-electron-neutrino oscillations. *Phys. Rev. Lett.*, 75:2650–2653, 1995.

[36] C. Athanassopoulos et al. Evidence for anti-nu/mu –¿ anti-nu/e oscillation from the LSND experiment at the Los Alamos Meson Physics Facility. *Phys. Rev. Lett.*, 77:3082–3085, 1996.

[37] C. Athanassopoulos et al. Evidence for neutrino oscillations from muon decay at rest. *Phys. Rev.*, C54:2685–2708, 1996.

[38] C. Athanassopoulos et al. Evidence for nu/mu –¿ nu/e neutrino oscillations from LSND. *Phys. Rev. Lett.*, 81:1774–1777, 1998.

[39] C. Athanassopoulos et al. Evidence for nu/mu –¿ nu/e oscillations from pion decay in flight neutrinos. *Phys. Rev.*, C58:2489–2511, 1998.

[40] V. Avila-Reese, P. Colin, O. Valenzuela, E. D'Onghia, and C. Firmani. Formation and structure of halos in a warm dark matter cosmology. *Astrophys. J.*, 559:516–530, 2001.

[41] J. N. Bachall. *Neutrino Astrophysics*. Cambridge University Press, NY, 1989.

[42] J. N. Bahcall, N. A. Bahcall, and G. Shaviv. Present status of the theoretical predictions for the *cl*37 solar-neutrino experiment. *Phys. Rev. Lett.*, 20(21):1209–1212, May 1968.

[43] J. M. Bardeen, J. R. Bond, N. Kaiser, and A. S. Szalay. The Statistics of Peaks of Gaussian Random Fields. *Astrophys. J.*, 304:15–61, 1986.

[44] G. Battaglia et al. The kinematic status and mass content of the Sculptor dwarf spheroidal galaxy. *arXiv:0802.4220*, 2008.

[45] R. Becker-Szendy, C. B. Bratton, D. Casper, S. T. Dye, W. Gajewski, M. Goldhaber, T. J. Haines, P. G. Halverson, D. Kielczewska, W. R. Kropp, J. G. Learned, J. M. LoSecco, S. Matsuno, G. McGrath, C. McGrew, R. Miller, L. R. Price, F. Reines, J. Schultz, H. W. Sobel, J. L. Stone, L. R. Sulak, and R. Svoboda. Electron- and muon-neutrino content of the atmospheric flux. *Phys. Rev. D*, 46(9):3720–3724, Nov 1992.

[46] H. A. Bethe. Possible explanation of the solar-neutrino puzzle. *Phys. Rev. Lett.*, 56(12):1305–1308, Mar 1986.

[47] M. Beuthe. Towards a unique formula for neutrino oscillations in vacuum. *Phys. Rev.*, D66:013003, 2002.

[48] M. Beuthe. Oscillations of neutrinos and mesons in quantum field theory. *Phys. Rept.*, 375:105–218, 2003.

[49] P. L. Biermann and A. Kusenko. Relic keV sterile neutrinos and reionization. *Phys. Rev. Lett.*, 96:091301, 2006.

[50] P. L. Biermann and F. Munyaneza. Dark matter and sterile neutrinos. *arXiv:astro-ph/0702173*, 2007.

[51] S. M. Bilenky and B. Pontecorvo. *Sov. J. Nucl. Phys.*, 24:316–319, 1976.

[52] S. M. Bilenky and B. Pontecorvo. *Nuovo Cim. Lett.*, 17:569, 1976.

[53] S. M. Bilenky and B. Pontecorvo. *Phys. Rep.*, 41:225, 1978.

[54] P. Bode, J. P. Ostriker, and N. Turok. Halo Formation in Warm Dark Matter Models. *Astrophys. J.*, 556:93–107, 2001.

[55] F. Boehm et al. Results from the Palo Verde neutrino oscillation experiment. *Phys. Rev.*, D62:072002, 2000.

[56] F. Boehm et al. Search for Neutrino Oscillations at the Palo Verde Nuclear Reactors. *Phys. Rev. Lett.*, 84:3764–3767, 2000.

[57] F. Boehm et al. Final results from the Palo Verde Neutrino Oscillation Experiment. *Phys. Rev.*, D64:112001, 2001.

[58] J. R. Bond, G. Efstathiou, and J. Silk. Massive neutrinos and the large-scale structure of the universe. *Phys. Rev. Lett.*, 45:1980–1984, 1980.

[59] D. Boyanovsky. Neutrino collective excitations in the standard model at high temperature. *Phys. Rev.*, D72:033004, 2005.

[60] D. Boyanovsky. Production of a sterile species via active-sterile mixing: an exactly solvable model. *Phys. Rev.*, D76:103514, 2007.

[61] D. Boyanovsky. Clustering properties of a sterile neutrino dark matter candidate. *Phys. Rev.*, D78:103505, 2008.

[62] D. Boyanovsky, K. Davey, and C. M. Ho. Particle abundance in a thermal plasma: Quantum kinetics vs. Boltzmann equation. *Phys. Rev.*, D71:023523, 2005.

[63] D. Boyanovsky, H. J. de Vega, D. S. Lee, Y. J. Ng, and S.-Y. Wang. Fermion damping in a fermion-scalar plasma. *Phys. Rev.*, D59:105001, 1999.

[64] D. Boyanovsky, H. J. de Vega, and N. Sanchez. Constraints on dark matter particles from theory, galaxy observations and N-body simulations. *Phys. Rev.*, D77:043518, 2008.

[65] D. Boyanovsky, H. J. de Vega, and N. G. Sanchez. The dark matter transfer function: free streaming, particle statistics and memory of gravitational clustering. *Phys. Rev.*, D78:063546, 2008.

[66] D. Boyanovsky and C. M. Ho. Charged lepton mixing and oscillations from neutrino mixing in the early Universe. *Astropart. Phys.*, 27:99–112, 2007.

[67] D. Boyanovsky and C. M. Ho. Sterile neutrino production via active-sterile oscillations: the quantum Zeno effect. *JHEP*, 07:030, 2007.

[68] D. Boyanovsky and J. Wu. Small scale aspects of warm dark matter : power spectra and acoustic oscillations. *Phys. Rev.*, D83:043524, 2011.

[69] A. Boyarsky, J. W. den Herder, A. Neronov, and O. Ruchayskiy. Search for the light dark matter with an X-ray spectrometer. *Astropart. Phys.*, 28:303–311, 2007.

[70] A. Boyarsky et al. Searching for dark matter in X-rays: how to check the dark matter origin of a spectral feature. *arXiv:1001.0644*, 2010.

[71] A. Boyarsky, D. Iakubovskyi, O. Ruchayskiy, and V. Savchenko. Constraints on decaying Dark Matter from XMM-Newton observations of M31. *Mon. Not. Roy. Astron. Soc.*, 387:1361, 2008.

[72] A. Boyarsky, J. Lesgourgues, O. Ruchayskiy, and M. Viel. Lyman-alpha constraints on warm and on warm-plus-cold dark matter models. *JCAP*, 0905:012, 2009.

[73] A. Boyarsky, J. Lesgourgues, O. Ruchayskiy, and M. Viel. Realistic sterile neutrino dark matter with keV mass does not contradict cosmological bounds. *Phys. Rev. Lett.*, 102:201304, 2009.

[74] A. Boyarsky, D. Malyshev, A. Neronov, and O. Ruchayskiy. Constraining DM properties with SPI. *Mon. Not. Roy. Astron. Soc.*, 387:1345, 2008.

[75] A. Boyarsky, A. Neronov, O. Ruchayskiy, and M. Shaposhnikov. Constraints on sterile neutrino as a dark matter candidate from the diffuse X-ray background. *Mon. Not. Roy. Astron. Soc.*, 370:213–218, 2006.

[76] A. Boyarsky, A. Neronov, O. Ruchayskiy, and M. Shaposhnikov. Restrictions on parameters of sterile neutrino dark matter from observations of galaxy clusters. *Phys. Rev.*, D74:103506, 2006.

[77] A. Boyarsky, A. Neronov, O. Ruchayskiy, M. Shaposhnikov, and I. Tkachev. How to find a dark matter sterile neutrino? *Phys. Rev. Lett.*, 97:261302, 2006.

[78] A. Boyarsky, J. Nevalainen, and O. Ruchayskiy. Constraints on the parameters of radiatively decaying dark matter from the dark matter halo of the milky way and ursa minor. *Astron. Astrophys.*, 471:51–57, 2007.

[79] A. Boyarsky, O. Ruchayskiy, and D. Iakubovskyi. A lower bound on the mass of Dark Matter particles. *JCAP*, 0903:005, 2009.

[80] A. Boyarsky, O. Ruchayskiy, and M. Markevitch. Constraints on parameters of radiatively decaying dark matter from the galaxy cluster 1E0657-56. *Astrophys. J.*, 673:752–757, 2008.

[81] A. Boyarsky, O. Ruchayskiy, and M. Shaposhnikov. The role of sterile neutrinos in cosmology and astrophysics. *Ann. Rev. Nucl. Part. Sci.*, 59:191–214, 2009.

[82] E. Braaten and R. D. Pisarski. DEDUCING HARD THERMAL LOOPS FROM WARD IDENTITIES. *Nucl. Phys.*, B339:310–324, 1990.

[83] E. Braaten and R. D. Pisarski. Soft Amplitudes in Hot Gauge Theories: A General Analysis. *Nucl. Phys.*, B337:569, 1990.

[84] J. S. Bullock et al. Profiles of dark haloes: evolution, scatter, and environment. *Mon. Not. Roy. Astron. Soc.*, 321:559–575, 2001.

[85] J. S. Bullock et al. Dwarf Galaxies in 2010: Revealing Galaxy Formation's Threshold and Testing the Nature of Dark Matter. *arXiv:0902.3492*, 2009.

[86] H. Burkhardt, J. Lowe, G. J. Stephenson, Jr., T. Goldman, and B. H. J. McKellar. Oscillations in the GSI electron capture experiment. *arXiv:0804.1099*, 2008.

[87] R. R. Caldwell and M. Kamionkowski. The Physics of Cosmic Acceleration. *Ann. Rev. Nucl. Part. Sci.*, 59:397–429, 2009.

[88] C. Y. Cardall. Coherence of neutrino flavor mixing in quantum field theory. *Phys. Rev.*, D61:073006, 2000.

[89] D. Casper, R. Becker-Szendy, C. B. Bratton, D. R. Cady, R. Claus, S. T. Dye, W. Gajewski, M. Goldhaber, T. J. Haines, P. G. Halverson, T. W. Jones, D. Kielczewska, W. R. Kropp, J. G. Learned, J. M. LoSecco, C. McGrew, S. Matsuno, J. Matthews, M. S. Mudan, L. Price, F. Reines, J. Schultz, D. Sinclair, H. W. Sobel, J. L. Stone, L. R. Sulak, R. Svoboda, G. Thornton, and J. C. van der Velde. Measurement of atmospheric neutrino composition with the imb-3 detector. *Phys. Rev. Lett.*, 66(20):2561–2564, May 1991.

[90] B. T. Cleveland, T. Daily, R. Davis, Jr., J. R. Distel, K. Lande, C. K. Lee, P. S. Wildenhain, and J. Ullman. Measurement of the Solar Electron Neutrino Flux with the Homestake Chlorine Detector. *Astrophys. J.*, 496:505–+, Mar. 1998.

[91] D. Clowe et al. A direct empirical proof of the existence of dark matter. *Astrophys. J.*, 648:L109–L113, 2006.

[92] A. G. Cohen, S. L. Glashow, and Z. Ligeti. Disentangling Neutrino Oscillations. *Phys. Lett.*, B678:191–196, 2009.

[93] P. Colin, A. A. Klypin, A. V. Kravtsov, and A. M. Khokhlov. Evolution of bias in different cosmological models. *Astrophys. J.*, 523:32, 1999.

[94] S. Colombi, S. Dodelson, and L. M. Widrow. Large scale structure tests of warm dark matter. *Astrophys. J.*, 458:1, 1996.

[95] J. J. Dalcanton and C. J. Hogan. Halo Cores and Phase Space Densities: Observational Constraints on Dark Matter Physics and Structure Formation. *Astrophys. J.*, 561:35–45, 2001.

[96] G. Danby, J.-M. Gaillard, K. Goulianos, L. M. Lederman, N. Mistry, M. Schwartz, and J. Steinberger. Observation of high-energy neutrino reactions and the existence of two kinds of neutrinos. *Phys. Rev. Lett.*, 9(1):36–44, Jul 1962.

[97] R. Davis. Solar neutrinos. ii. experimental. *Phys. Rev. Lett.*, 12(11):303–305, Mar 1964.

[98] R. Davis. A review of the Homestake solar neutrino experiment. In A. Faessler, editor, *Neutrinos in Cosmology, in Astro, Particle and Nuclear Physics*, pages 13–32, 1994.

[99] R. Davis, D. S. Harmer, and K. C. Hoffman. Search for neutrinos from the sun. *Phys. Rev. Lett.*, 20(21):1205–1209, May 1968.

[100] W. J. G. de Blok et al. High-Resolution Rotation Curves and Galaxy Mass Models from THINGS. *arXiv:0810.2100*, 2008.

[101] A. de Gouvea. Neutrino physics. *arXiv:hep-ph/0411274*, 2004.

[102] A. De Gouvea. Neutrinos Have Mass - So What? *Mod. Phys. Lett.*, A19:2799–2813, 2004.

[103] A. de Gouvea. GeV Seesaw, Accidentally Small Neutrino Masses, and Higgs Decays to Neutrinos. *arXiv:0706.1732*, 2007.

[104] A. de Gouvea. Neutrino Masses and Mixing - Theory. *arXiv:0902.4656*, 2009.

[105] A. de Gouvea, J. Jenkins, and N. Vasudevan. Neutrino phenomenology of very low-energy seesaws. *Phys. Rev.*, D75:013003, 2007.

[106] H. J. de Vega and N. G. Sanchez. Model independent analysis of dark matter points to a particle mass at the keV scale. *Mon. Not. Roy. Astron. Soc.*, 404:885, 2010.

[107] F. Di Lodovico and f. t. T. Collaboration. T2K Results and Future Plans. *arXiv:1110.5382*, 2011.

[108] J. Diemand et al. Clumps and streams in the local dark matter distribution. *Nature*, 454:735–738, 2008.

[109] J. Diemand, M. Kuhlen, and P. Madau. Dark matter substructure and gamma-ray annihilation in the Milky Way halo. *Astrophys. J.*, 657:262–270, 2007.

[110] J. Diemand, M. Kuhlen, and P. Madau. Formation and evolution of galaxy dark matter halos and their substructure. *Astrophys. J.*, 667:859–877, 2007.

[111] J. Diemand, M. Zemp, B. Moore, J. Stadel, and M. Carollo. Cusps in CDM halos. *Mon. Not. Roy. Astron. Soc.*, 364:665, 2005.

[112] S. Dodelson. *Modern Cosmology*. Oxford University Press, 2008.

[113] S. Dodelson and L. M. Widrow. Sterile Neutrinos as Dark Matter. *Phys. Rev. Lett.*, 72:17–20, 1994.

[114] A. D. Dolgov. Cosmological implications of neutrinos. *Surveys High Energ. Phys.*, 17:91–114, 2002.

[115] A. D. Dolgov. Neutrinos in cosmology. *Phys. Rept.*, 370:333–535, 2002.

[116] A. D. Dolgov et al. Oscillations of neutrinos produced and detected in crystals. *Nucl. Phys.*, B729:79–94, 2005.

[117] A. D. Dolgov and S. H. Hansen. Massive sterile neutrinos as warm dark matter. *Astropart. Phys.*, 16:339–344, 2002.

[118] A. D. Dolgov, O. V. Lychkovskiy, A. A. Mamonov, L. B. Okun, and M. G. Schepkin. Neutrino wave function and oscillation suppression. *Eur. Phys. J.*, C44:431–434, 2005.

[119] A. D. Dolgov, L. B. Okun, M. V. Rotaev, and M. G. Schepkin. Oscillations of neutrinos produced by a beam of electrons. *arXiv:hep-ph/0407189*, 2004.

[120] J. Dubinski and R. G. Carlberg. The Structure of cold dark matter halos. *Astrophys. J.*, 378:496, 1991.

[121] S. Eliezer and A. R. Swift. *Nucl. Phys.*, B105:45, 1976.

[122] M. Faber. Kinematics and Quantum Field Theory of the Neutrino Oscillations Observed in the Time-modulated Orbital Electron Capture Decay in an Ion Storage Ring. *arXiv:0801.3262*, 2008.

[123] T. Faestermann et al. Could the GSI Oscillations be Observed in a Standard Electron Capture Decay Experiment? *Phys. Lett.*, B672:227–229, 2009.

[124] J. L. Feng. Dark Matter Candidates from Particle Physics and Methods of Detection. *Ann. Rev. Astron. Astrophys.*, 48:495, 2010.

[125] B. D. Fields and S. Sarkar. Big Bang Nucleosynthesis. *Phys. Lett.*, B667:228–231, 2008.

[126] R. A. Flores and J. R. Primack. Observational and theoretical constraints on singular dark matter halos. *Astrophys. J.*, 427:L1–4, 1994.

[127] G. L. Fogli, E. Lisi, A. Marrone, A. Palazzo, and A. M. Rotunno. Evidence of theta(13)¿0 from global neutrino data analysis. *arXiv:1106.6028*, 2011.

[128] J. Frenkel and J. C. Taylor. High Temperature Limit of Thermal QCD. *Nucl. Phys.*, B334:199, 1990.

[129] P. Fritzsch. J amd Minkowski. *Phys. Lett.*, B62:72, 1976.

[130] Y. Fukuda et al. Evidence for oscillation of atmospheric neutrinos. *Phys. Rev. Lett.*, 81:1562–1567, 1998.

[131] Y. Fukuda et al. Measurement of a small atmospheric nu/mu / nu/e ratio. *Phys. Lett.*, B433:9–18, 1998.

[132] M. Fukugita and T. Yanagida. *Physics of Neutrinos and Applications to Astrophysics.* Springer-Verlag Berlin Heidelberg, 2003.

[133] G. M. Fuller, A. Kusenko, I. Mocioiu, and S. Pascoli. Pulsar kicks from a dark-matter sterile neutrino. *Phys. Rev.*, D68:103002, 2003.

[134] A. Gando et al. Constraints on θ_{13} from A Three-Flavor Oscillation Analysis of Reactor Antineutrinos at KamLAND. *Phys. Rev.*, D83:052002, 2011.

[135] G. Gentile, A. Burkert, P. Salucci, U. Klein, and F. Walter. The dwarf galaxy DDO 47: testing cusps hiding in triaxial halos. *Astrophys. J.*, 634:L145–L148, 2005.

[136] G. Gentile, P. Salucci, U. Klein, D. Vergani, and P. Kalberla. The cored distribution of dark matter in spiral galaxies. *Mon. Not. Roy. Astron. Soc.*, 351:903, 2004.

[137] G. Gentile, C. Tonini, and P. Salucci. LambdaCDM Halo Density Profiles: where do actual halos converge to NFW ones? *Astron. Astrophys.*, 467:925–931, 2007.

[138] S. Ghigna et al. Density profiles and substructure of dark matter halos: converging results at ultra-high numerical resolution. *Astrophys. J.*, 544:616, 2000.

[139] G. Gilmore. Dark Matter on small scales: Telescopes on large scales. *arXiv:astro-ph/0703370*, 2007.

[140] G. Gilmore et al. Observed Properties of Dark Matter: dynamical studies of dSph galaxies. *Nucl. Phys. Proc. Suppl.*, 173:15–18, 2007.

[141] G. Gilmore et al. The Observed properties of Dark Matter on small spatial scales. *Astrophys. J.*, 663:948–959, 2007.

[142] G. Gilmore et al. What is a galaxy? How Cold is Cold Dark Matter? Recent progress in Near Field Cosmology. *arXiv:0804.1919*, 2008.

[143] C. Giunti. Neutrino wave packets in quantum field theory. *JHEP*, 11:017, 2002.

[144] C. Giunti. The phase of neutrino oscillations. *Phys. Scripta*, 67:29–33, 2003.

[145] C. Giunti. Comment on the Neutrino-Mixing Interpretation of the GSI Time Anomaly. *arXiv:0801.4639*, 2008.

[146] C. Giunti. Rates of Processes with Coherent Production of Different Particles and the GSI Time Anomaly. *Phys. Lett.*, B665:92–94, 2008.

[147] C. Giunti and C. W. Kim. Coherence of neutrino oscillations in the wave packet approach. *Phys. Rev.*, D58:017301, 1998.

[148] C. Giunti and C. W. Kim. *Fundamentals of Neutrino Physics and Astrophysics*. Oxford University Press, Oxford, 2007.

[149] C. Giunti, C. W. Kim, J. A. Lee, and U. W. Lee. On the treatment of neutrino oscillations without resort to weak eigenstates. *Phys. Rev.*, D48:4310–4317, 1993.

[150] C. Giunti, C. W. Kim, and U. W. Lee. When do neutrinos really oscillate?: Quantum mechanics of neutrino oscillations. *Phys. Rev.*, D44:3635–3640, 1991.

[151] C. Giunti, C. W. Kim, and U. W. Lee. Remarks on the weak states of neutrinos. *Phys. Rev. D*, 45(7):2414–2420, Apr 1992.

[152] C. Giunti, C. W. Kim, and U. W. Lee. When do neutrinos cease to oscillate? *Phys. Lett.*, B421:237–244, 1998.

[153] N. Y. Gnedin and A. J. S. Hamilton. Matter Power Spectrum from the Lyman-Alpha Forest: Myth or Reality? *Mon. Not. Roy. Astron. Soc.*, 334:107–116, 2002.

[154] D. Gorbunov, A. Khmelnitsky, and V. Rubakov. Constraining sterile neutrino dark matter by phase-space density observations. *JCAP*, 0810:041, 2008.

[155] V. Gribov and B. Pontecorvo. Neutrino astronomy and lepton charge. *Physics Letters B*, 28:493–496, Jan. 1969.

[156] W. Grimus. Neutrino physics: Theory. *Lect. Notes Phys.*, 629:169–214, 2004.

[157] W. Grimus, S. Mohanty, and P. Stockinger. Field-theoretical treatment of neutrino oscillations. *arXiv:hep-ph/9904340*, 1999.

[158] W. Grimus, S. Mohanty, and P. Stockinger. Field theoretical treatment of neutrino oscillations: The strength of the canonical oscillation formula. *arXiv:hep-ph/9909341*, 1999.

[159] W. Grimus and P. Stockinger. Real Oscillations of Virtual Neutrinos. *Phys. Rev.*, D54:3414–3419, 1996.

[160] W. Grimus, P. Stockinger, and S. Mohanty. The field-theoretical approach to coherence in neutrino oscillations. *Phys. Rev.*, D59:013011, 1999.

[161] E. J. Groth and P. J. E. Peebles. Closed-form solutions for the evolution of density perturbations in some cosmological models. *Astr. Astroph*, 41:143–145, June 1975.

[162] X. Guo et al. A precision measurement of the neutrino mixing angle theta(13) using reactor antineutrinos at Daya Bay. *arXiv:hep-ex/0701029*, 2007.

[163] R. G. Hamish Robertson. Neutrino Oscillations and Entanglement. *arXiv:1004.1847*, 2010.

[164] W. Hampel, J. Handt, G. Heusser, J. Kiko, T. Kirsten, M. Laubenstein, E. Pernicka, W. Rau, M. Wojcik, Y. Zakharov, R. von Ammon, K. H. Ebert, T. Fritsch, D. Heidt, E. Henrich, L. Stieglitz, F. Weirich, M. Balata, M. Sann, F. X. Hartmann, E. Bellotti, C. Cattadori, O. Cremonesi, N. Ferrari, E. Fiorini, L. Zanotti, M. Altmann, F. von Feilitzsch, R. Mössbauer, S. Wanninger, G. Berthomieu, E. Schatzman, I. Carmi, I. Dostrovsky, C. Bacci, P. Belli, R. Bernabei, S. D'Angelo, L. Paoluzi, M. Cribier, J. Rich, M. Spiro, C. Tao, D. Vignaud, J. Boger, R. L. Hahn, J. K. Rowley, R. W. Stoenner, and J. Weneser. GALLEX solar neutrino observations: results for GALLEX IV. *Physics Letters B*, 447:127–133, Feb. 1999.

[165] S. H. Hansen, J. Lesgourgues, S. Pastor, and J. Silk. Closing the window on warm dark matter. *Mon. Not. Roy. Astron. Soc.*, 333:544–546, 2002.

[166] W. C. Haxton. The solar neutrino problem. *Ann. Rev. Astron. Astrophys.*, 33:459–503, 1995.

[167] W. C. Haxton. Neutrino oscillations and the solar neutrino problem. *arXiv:nucl-th/0004052*, 2000.

[168] W. C. Haxton. Neutrino Astrophysics. *arXiv:0808.0735*, 2008.

[169] K. S. Hirata, T. Kajita, M. Koshiba, M. Nakahata, S. Ohara, Y. Oyama, N. Sato, A. Suzuki, M. Takita, Y. Totsuka, T. Kifune, T. Suda, K. Nakamura, K. Takahashi, T. Tanimori, K. Miyano, M. Yamada, E. W. Beier, L. R. Feldscher, E. D. Frank, W. Frati, S. B. Kim, A. K. Mann, F. M. Newcomer, R. van Berg, W. Zhang, and B. G. Cortez. Experimental study of the atmospheric neutrino flux. *Physics Letters B*, 205:416–420, Apr. 1988.

[170] C. M. Ho and D. Boyanovsky. Space-time propagation of neutrino wave packets at high temperature and density. *Phys. Rev.*, D73:125014, 2006.

[171] C. M. Ho, D. Boyanovsky, and H. J. de Vega. Neutrino oscillations in the early universe: A real-time formulation. *Phys. Rev.*, D72:085016, 2005.

[172] W. Hu and N. Sugiyama. Small scale cosmological perturbations: An Analytic approach. *Astrophys. J.*, 471:542–570, 1996.

[173] A. N. Ivanov and P. Kienle. On the time modulation of the K-shell electron capture decay rates of H-like heavy ions at GSI experiments. *Phys. Rev. Lett.*, 103:062502, 2009.

[174] A. N. Ivanov, E. L. Kryshen, M. Pitschmann, and P. Kienle. On the Time-Modulation of the *beta*$^+$-Decay Rate of H-like 140Pr58+ Ion. *arXiv:0806.2543*, 2008.

[175] A. N. Ivanov, R. Reda, and P. Kienle. On the time–modulation of the K–shell electron capture decay of H-like $^{140}Pr^{58+}$ ions produced by neutrino–flavour mixing. *arXiv:0801.2121*, 2008.

[176] N. Jarosik et al. Seven-Year Wilkinson Microwave Anisotropy Probe (WMAP) Observations: Sky Maps, Systematic Errors, and Basic Results. *Astrophys. J. Suppl.*, 192:14, 2011.

[177] S. Jha, A. G. Riess, and R. P. Kirshner. Improved Distances to Type Ia Supernovae with Multicolor Light Curve Shapes: MLCS2k2. *Astrophys. J.*, 659:122–148, 2007.

[178] M. K. R. Joung, R. Cen, and G. Bryan. Galaxy Size Problem at z=3: Simulated Galaxies Are Too Small. *Astrophys. J. Lett.*, 692:L1–L4, 2009.

[179] G. Kauffmann, S. D. M. White, and B. Guiderdoni. The Formation and Evolution of Galaxies Within Merging Dark Matter Haloes. *Mon. Not. Roy. Astron. Soc.*, 264:201, 1993.

[180] B. Kayser. On the Quantum Mechanics of Neutrino Oscillation. *Phys. Rev.*, D24:110, 1981.

[181] B. Kayser. Neutrino physics: Where do we stand, and where are we going? The theoretical-phenomenological perspective. *Nucl. Phys. Proc. Suppl.*, 118:425–437, 2003.

[182] B. Kayser. Neutrino Mass, Mixing, and Flavor Change. *arXiv:0804.1497*, 2008.

[183] B. Kayser. Neutrino Oscillation Phenomenology. *arXiv:0804.1121*, 2008.

[184] B. Kayser, J. Kopp, R. G. H. Roberston, and P. Vogel. On a theory of neutrino oscillations with entanglement. *Phys. Rev.*, D82:093003, 2010.

[185] E. Kearns. Experimental measurements of atmospheric neutrinos. *Nucl. Phys. Proc. Suppl.*, 70:315–323, 1999.

[186] B. D. Keister and W. N. Polyzou. Relativistic quantum theories and neutrino oscillations. *Phys. Scripta*, 81:055102, 2010.

[187] R. Kessler et al. First-year Sloan Digital Sky Survey-II (SDSS-II) Supernova Results: Hubble Diagram and Cosmological Parameters. *Astrophys. J. Suppl.*, 185:32–84, 2009.

[188] H. Kienert, J. Kopp, M. Lindner, and A. Merle. The GSI anomaly. *J. Phys. Conf. Ser.*, 136:022049, 2008.

[189] C. W. Kim and A. Pevsner. *Neutrinos in Physics and Astrophysics*. Harwood Academic Publishers, Chur, Switzerland, 1993.

[190] J. T. Kleyna, M. I. Wilkinson, N. W. Evans, and G. Gilmore. Dark Matter in Dwarf Spheroidals II: Observations and Modelling of Draco. *Mon. Not. Roy. Astron. Soc.*, 330:792, 2002.

[191] A. A. Klypin, A. V. Kravtsov, O. Valenzuela, and F. Prada. Where are the missing galactic satellites? *Astrophys. J.*, 522:82–92, 1999.

[192] A. Knebe, J. E. G. Devriendt, B. K. Gibson, and J. Silk. Top-Down Fragmentation of a Warm Dark Matter Filament. *Mon. Not. Roy. Astron. Soc.*, 345:1285, 2003.

[193] A. Knebe, J. E. G. Devriendt, A. Mahmood, and J. Silk. Merger Histories in Warm Dark Matter Structure Formation Scenario. *Mon. Not. Roy. Astron. Soc.*, 329:813, 2002.

[194] E. Kolb and M. Turner. *The Early Universe*. Westview Press, 1994.

[195] E. Komatsu et al. Seven-Year Wilkinson Microwave Anisotropy Probe (WMAP) Observations: Cosmological Interpretation. *arXiv:1001.4538*, 2010.

[196] A. V. Kravtsov. Dark matter substructure and dwarf galactic satellites. *arXiv:0906.3295*, 2009.

[197] M. Kuhlen, J. Diemand, P. Madau, and M. Zemp. The Via Lactea INCITE Simulation: Galactic Dark Matter Substructure at High Resolution. *J. Phys. Conf. Ser.*, 125:012008, 2008.

[198] A. Kusenko. Sterile neutrinos, dark matter, and the pulsar velocities in models with a Higgs singlet. *Phys. Rev. Lett.*, 97:241301, 2006.

[199] A. Kusenko. Sterile neutrinos. *AIP Conf. Proc.*, 917:58–68, 2007.

[200] A. Kusenko. Detecting sterile dark matter in space. *Int. J. Mod. Phys.*, D16:2325–2335, 2008.

[201] M. Laine and M. Shaposhnikov. Sterile neutrino dark matter as a consequence of nuMSM- induced lepton asymmetry. *JCAP*, 0806:031, 2008.

[202] D. Larson et al. Seven-Year Wilkinson Microwave Anisotropy Probe (WMAP) Observations: Power Spectra and WMAP-Derived Parameters. *arXiv:1001.4635*, 2010.

[203] A. Lewis and S. Bridle. Cosmological parameters from CMB and other data: a Monte-Carlo approach. *Phys. Rev.*, D66:103511, 2002.

[204] H. J. Lipkin. Theoretical Analysis Supports Darmstadt Oscillations Crucial Roles of Wave Function Collapse and Dicke Superradiance. *arXiv:0910.5049*, 2009.

[205] Y. A. Litvinov et al. Measurement of the β^+ and orbital electron-capture decay rates in fully-ionized, hydrogen-like, and helium- like ^{140}Pr ions. *Phys. Rev. Lett.*, 99:262501, 2007.

[206] Y. A. Litvinov et al. Observation of Non-Exponential Orbital Electron Capture Decays of Hydrogen-Like ^{140}Pr and ^{142}Pm Ions. *Phys. Lett.*, B664:162–168, 2008.

[207] A. Loeb and M. Zaldarriaga. The small-scale power spectrum of cold dark matter. *Phys. Rev.*, D71:103520, 2005.

[208] M. Loewenstein and A. Kusenko. Dark Matter Search Using Chandra Observations of Willman 1, and a Spectral Feature Consistent with a Decay Line of a 5 keV Sterile Neutrino. *Astrophys. J.*, 714:652–662, 2010.

[209] M. Loewenstein, A. Kusenko, and P. L. Biermann. New Limits on Sterile Neutrinos from Suzaku Observations of the Ursa Minor Dwarf Spheroidal Galaxy. *Astrophys. J.*, 700:426–435, 2009.

[210] J. M. Losecco. Muon Oscillations. *arXiv:0902.2752*, 2009.

[211] J. M. Losecco. Pion Oscillations. *arXiv:0912.0900*, 2009.

[212] C.-P. Ma and E. Bertschinger. Cosmological perturbation theory in the synchronous and conformal Newtonian gauges. *Astrophys. J.*, 455:7–25, 1995.

[213] A. V. Maccio' and F. Fontanot. How cold is Dark Matter? Constraints from Milky Way Satellites. *arXiv:0910.2460*, 2009.

[214] Z. Maki, M. Nakagawa, and S. Sakata. *Prog. Theor. Phys.*, 28:870, 1962.

[215] P. McDonald et al. The Lyman-alpha Forest Power Spectrum from the Sloan Digital Sky Survey. *Astrophys. J. Suppl.*, 163:80–109, 2006.

[216] S. S. McGaugh, W. J. G. de Blok, J. M. Schombert, R. K. de Naray, and J. H. Kim. The Rotation Velocity Attributable to Dark Matter at Intermediate Radii in Disk Galaxies. *Astrophys. J.*, 659:149–161, 2007.

[217] P. Meszaros. The behaviour of point masses in an expanding cosmological substratum. *Astr. Astroph*, 37:225–228, Dec. 1974.

[218] S. P. Mikheev and A. Y. Smirnov. Resonance enhancement of oscillations in matter and solar neutrino spectroscopy. *Sov. J. Nucl. Phys.*, 42:913–917, 1985.

[219] P. Minkowski. μ–eγ at a rate of one out of 10^9 muon decays? *Phys. Lett. B*, 67:421–428, 1977.

[220] R. N. Mohapatra et al. Theory of neutrinos. *arXiv:hep-ph/0412099*, 2004.

[221] R. N. Mohapatra et al. Theory of neutrinos: A white paper. *Rept. Prog. Phys.*, 70:1757–1867, 2007.

[222] R. N. Mohapatra and P. B. Pal. *Massive Neutrinos in Physics and Astrophysics*. World Scientific, Singapore, 2004.

[223] R. N. Mohapatra and G. Senjanovic. Neutrino mass and spontaneous parity nonconservation. *Physical Review Letters*, 44:912–915, Apr. 1980.

[224] R. N. Mohapatra and G. Senjanović. Neutrino mass and spontaneous parity nonconservation. *Phys. Rev. Lett.*, 44(14):912–915, Apr 1980.

[225] B. Moore. The Nature of dark matter. *arXiv:astro-ph/9402009*, 1994.

[226] B. Moore et al. Dark matter substructure within galactic halos. *Astrophys. J.*, 524:L19–L22, 1999.

[227] B. Moore, T. R. Quinn, F. Governato, J. Stadel, and G. Lake. Cold collapse and the core catastrophe. *Mon. Not. Roy. Astron. Soc.*, 310:1147–1152, 1999.

[228] J. F. Navarro, C. S. Frenk, and S. D. M. White. The Structure of Cold Dark Matter Halos. *Astrophys. J.*, 462:563–575, 1996.

[229] J. F. Navarro, C. S. Frenk, and S. D. M. White. A Universal Density Profile from Hierarchical Clustering. *Astrophys. J.*, 490:493–508, 1997.

[230] D. Notzold and G. Raffelt. Neutrino Dispersion at Finite Temperature and Density. *Nucl. Phys.*, B307:924, 1988.

[231] S. Nussinov. *Phys. Lett.*, B63:201–203, 1976.

[232] S.-H. Oh, W. J. G. de Blok, F. Walter, E. Brinks, and R. C. Kennicutt, Jr. High-resolution dark matter density profiles of THINGS dwarf galaxies: Correcting for non-circular motions. *arXiv:0810.2119*, 2008.

[233] A. Palazzo, D. Cumberbatch, A. Slosar, and J. Silk. Sterile neutrinos as subdominant warm dark matter. *Phys. Rev.*, D76:103511, 2007.

[234] S. Perlmutter et al. Measurements of Omega and Lambda from 42 High-Redshift Supernovae. *Astrophys. J.*, 517:565–586, 1999.

[235] M. Peshkin. Comment on 'New method for studying neutrino mixing and mass differences'. *arXiv:0804.4891*, 2008.

[236] K. Petraki. Small-scale structure formation properties of chilled sterile neutrinos as dark matter. *Phys. Rev.*, D77:105004, 2008.

[237] K. Petraki and A. Kusenko. Dark-matter sterile neutrinos in models with a gauge singlet in the Higgs sector. *Phys. Rev.*, D77:065014, 2008.

[238] R. D. Pisarski. Computing Finite Temperature Loops with Ease. *Nucl. Phys.*, B309:476, 1988.

[239] R. D. Pisarski. How to Compute Scattering Amplitudes in Hot Gauge Theories. *Physica*, A158:246–250, 1989.

[240] R. D. Pisarski. Scattering Amplitudes in Hot Gauge Theories. *Phys. Rev. Lett.*, 63:1129, 1989.

[241] B. Pontecorvo. On the quantum mechanics of neutrino oscillation. *Sov. Phys. JETP*, 6:427, 1957.

[242] B. Pontecorvo. The Neutrino and its Importance in Astrophysics. In Y. G. Shafer, editor, *Cosmic Rays and Problems of Space Physics*, pages 20–+, 1967.

[243] B. Pontecorvo. Neutrino Experiments and the Problem of Conservation of Leptonic Charge. *Soviet Journal of Experimental and Theoretical Physics*, 26:984–+, May 1968.

[244] J. R. Primack. Cosmology: small scale issues revisited. *arXiv:0909.2247*, 2009.

[245] A. Refregier. Weak Gravitational Lensing by Large-Scale Structure. *Ann. Rev. Astron. Astrophys.*, 41:645–668, 2003.

[246] J. A. Regan, M. G. Haehnelt, and M. Viel. Numerical Simulations of the Lyman-alpha forest - A comparison of Gadget-2 and Enzo. *Mon. Not. Roy. Astron. Soc.*, 374:196–205, 2007.

[247] J. Rich. The Quantum mechanics of neutrino oscillations. *Phys. Rev.*, D48:4318–4325, 1993.

[248] A. G. Riess et al. Observational Evidence from Supernovae for an Accelerating Universe and a Cosmological Constant. *Astron. J.*, 116:1009–1038, 1998.

[249] A. G. Riess et al. New Hubble Space Telescope Discoveries of Type Ia Supernovae at $z > 1$: Narrowing Constraints on the Early Behavior of Dark Energy. *Astrophys. J.*, 659:98–121, 2007.

[250] V. C. Rubin and W. K. Ford, Jr. Rotation of the Andromeda Nebula from a Spectroscopic Survey of Emission Regions. *Astrophys. J.*, 159:379–+, Feb. 1970.

[251] V. C. Rubin, W. K. J. Ford, and N. . Thonnard. Rotational properties of 21 SC galaxies with a large range of luminosities and radii, from NGC 4605 /R = 4kpc/ to UGC 2885 /R = 122 kpc/. *Astrophys. J.*, 238:471–487, June 1980.

[252] M. C. Sanchez et al. Observation of atmospheric neutrino oscillations in Soudan 2. *Phys. Rev.*, D68:113004, 2003.

[253] T. Sawala, Q. Guo, C. Scannapieco, A. Jenkins, and S. D. M. White. What is the Matter with Dwarf Galaxies? *arXiv:1003.0671*, 2010.

[254] U. Seljak, A. Makarov, P. McDonald, and H. Trac. Can sterile neutrinos be the dark matter? *Phys. Rev. Lett.*, 97:191303, 2006.

[255] U. Seljak and M. Zaldarriaga. A Line of Sight Approach to Cosmic Microwave Background Anisotropies. *Astrophys. J.*, 469:437–444, 1996.

[256] M. Shaposhnikov. Dark matter: The case of sterile neutrino. *arXiv:astro-ph/0703673*, 2007.

[257] M. Shaposhnikov. The nuMSM, leptonic asymmetries, and properties of singlet fermions. *JHEP*, 08:008, 2008.

[258] M. Shaposhnikov and I. Tkachev. The nuMSM, inflation, and dark matter. *Phys. Lett.*, B639:414–417, 2006.

[259] X.-D. Shi and G. M. Fuller. A new dark matter candidate: Non-thermal sterile neutrinos. *Phys. Rev. Lett.*, 82:2832–2835, 1999.

[260] A. Silvestri and M. Trodden. Approaches to Understanding Cosmic Acceleration. *Rept. Prog. Phys.*, 72:096901, 2009.

[261] V. Simha and G. Steigman. Constraining The Universal Lepton Asymmetry. *JCAP*, 0808:011, 2008.

[262] J. D. Simon and M. Geha. The Kinematics of the Ultra-Faint Milky Way Satellites: Solving the Missing Satellite Problem. *Astrophys. J.*, 670:313–331, 2007.

[263] M. B. Smy et al. Precise Measurement of the Solar Neutrino Day/Night and Seasonal Variation in Super-Kamiokande-I. *Phys. Rev.*, D69:011104, 2004.

[264] M. Tegmark et al. Cosmological parameters from SDSS and WMAP. *Phys. Rev.*, D69:103501, 2004.

[265] T. Theuns, A. Leonard, G. Efstathiou, F. R. Pearce, and P. A. Thomas. P3M-SPH simulations of the Lyman-alpha Forest. *Mon. Not. Roy. Astron. Soc.*, 301:478–502, 1998.

[266] A. Tikhonov and A. Klypin. The emptiness of voids: yet another over-abundance problem for the LCDM model. *arXiv:0807.0924*, 2008.

[267] A. V. Tikhonov, S. Gottloeber, G. Yepes, and Y. Hoffman. The sizes of mini-voids in the local universe: an argument in favor of a warm dark matter model? *arXiv:0904.0175*, 2009.

[268] S. Tremaine and J. E. Gunn. Dynamical role of light neutral leptons in cosmology. *Phys. Rev. Lett.*, 42(6):407–410, Feb 1979.

[269] J. A. Tyson, G. P. Kochanski, and I. P. Dell'Antonio. Detailed Mass Map of CL0024+1654 from Strong Lensing. *Astrophys. J.*, 498:L107, 1998.

[270] P. A. Vetter et al. Search for Oscillation of the Electron-Capture Decay Probability of ^{142}Pm. *Phys. Lett.*, B670:196–199, 2008.

[271] M. Viel et al. How cold is cold dark matter? Small scales constraints from the flux power spectrum of the high-redshift Lyman- alpha forest. *Phys. Rev. Lett.*, 100:041304, 2008.

[272] M. Viel and M. G. Haehnelt. Cosmological and astrophysical parameters from the SDSS flux power spectrum and hydrodynamical simulations of the Lyman-alpha forest. *Mon. Not. Roy. Astron. Soc.*, 365:231–244, 2006.

[273] M. Viel, M. G. Haehnelt, and V. Springel. Testing the accuracy of the Hydro-PM approximation in numerical simulations of the Lyman-alpha forest. *Mon. Not. Roy. Astron. Soc.*, 367:1655–1665, 2006.

[274] M. Viel, J. Lesgourgues, M. G. Haehnelt, S. Matarrese, and A. Riotto. Constraining warm dark matter candidates including sterile neutrinos and light gravitinos with WMAP and the Lyman- alpha forest. *Phys. Rev.*, D71:063534, 2005.

[275] M. Viel, J. Lesgourgues, M. G. Haehnelt, S. Matarrese, and A. Riotto. Can sterile neutrinos be ruled out as warm dark matter candidates? *Phys. Rev. Lett.*, 97:071301, 2006.

[276] M. G. Walker et al. A Universal Mass Profile for Dwarf Spheroidal Galaxies. *Astrophys. J.*, 704:1274–1287, 2009.

[277] M. G. Walker, S. S. McGaugh, M. Mateo, E. Olszewski, and R. K. de Naray. Comparing the Dark Matter Halos of Spiral, Low Surface Brightness and Dwarf Spheroidal Galaxies. *arXiv:1004.5228*, 2010.

[278] S.-Y. Wang, D. Boyanovsky, H. J. de Vega, D. S. Lee, and Y. J. Ng. Damping rates and mean free paths of soft fermion collective excitations in a hot fermion-gauge-scalar theory. *Phys. Rev.*, D61:065004, 2000.

[279] C. R. Watson, J. F. Beacom, H. Yuksel, and T. P. Walker. Direct X-ray constraints on sterile neutrino warm dark matter. *Phys. Rev.*, D74:033009, 2006.

[280] S. Weinberg. Cosmological fluctuations of short wavelength. *Astrophys. J.*, 581:810–816, 2002.

[281] S. Weinberg. *Cosmology*. Academic Press, 2003.

[282] B. Willman, F. Governato, J. J. Dalcanton, D. Reed, and T. R. Quinn. The Observed and Predicted Spatial Distribution of Milky Way Satellite Galaxies. *Mon. Not. Roy. Astron. Soc.*, 353:639–646, 2004.

[283] L. Wolfenstein. Neutrino oscillations in matter. *Phys. Rev.*, D17:2369–2374, 1978.

[284] W. M. Wood-Vasey et al. Observational Constraints on the Nature of the Dark Energy: First Cosmological Results from the ESSENCE Supernova Survey. *Astrophys. J.*, 666:694–715, 2007.

[285] J. Wu, C.-M. Ho, and D. Boyanovsky. Sterile neutrinos produced near the EW scale I: mixing angles, MSW resonances and production rates. *Phys. Rev.*, D80:103511, 2009.

[286] J. Wu, J. A. Hutasoit, D. Boyanovsky, and R. Holman. Dynamics of disentanglement, density matrix and coherence in neutrino oscillations. *Phys. Rev. D*, 82:013006, 2010.

[287] J. Wu, J. A. Hutasoit, D. Boyanovsky, and R. Holman. Is the GSI anomaly due to neutrino oscillations? - A real time perspective -. *Phys. Rev.*, D82:045027, 2010.

[288] R. F. G. Wyse and G. Gilmore. Observed Properties of Dark Matter on Small Spatial Scales. *arXiv:0708.1492*, 2007.

[289] H. Yuksel, J. F. Beacom, and C. R. Watson. Strong Upper Limits on Sterile Neutrino Warm Dark Matter. *Phys. Rev. Lett.*, 101:121301, 2008.

[290] M. Zaldarriaga and U. Seljak. CMBFAST for spatially closed universes. *Astrophys. J. Suppl.*, 129:431–434, 2000.

[291] M. Zaldarriaga, U. Seljak, and E. Bertschinger. Integral Solution for the Microwave Background Anisotropies in Non-flat Universes. *Astrophys. J.*, 494:491–502, 1998.

[292] A. R. Zentner and J. S. Bullock. Inflation, CDM, and the central density problem. *Phys. Rev.*, D66:043003, 2002.

[293] A. R. Zentner and J. S. Bullock. Halo Substructure And The Power Spectrum. *Astrophys. J.*, 598:49, 2003.

[294] F. Zwicky. Die Rotverschiebung von extragalaktischen Nebeln. *Helvetica Physica Acta*, 6:110–127, 1933.

[295] F. Zwicky. On the Masses of Nebulae and of Clusters of Nebulae. *Astrophys. J.*, 86:217–+, Oct. 1937.